

1-1-2011

A hybrid approach to characterization and life assessment of trilayer assemblies of dissimilar materials under thermal cycles

Alireza Shirazi
Ryerson University

Follow this and additional works at: <http://digitalcommons.ryerson.ca/dissertations>



Part of the [Mechanical Engineering Commons](#)

Recommended Citation

Shirazi, Alireza, "A hybrid approach to characterization and life assessment of trilayer assemblies of dissimilar materials under thermal cycles" (2011). *Theses and dissertations*. Paper 728.

This Dissertation is brought to you for free and open access by Digital Commons @ Ryerson. It has been accepted for inclusion in Theses and dissertations by an authorized administrator of Digital Commons @ Ryerson. For more information, please contact bcameron@ryerson.ca.

**A HYBRID APPROACH TO CHARACTERIZATION AND LIFE
ASSESSMENT OF TRILAYER ASSEMBLIES OF DISSIMILAR
MATERIALS UNDER THERMAL CYCLES**

By

Alireza Shirazi

B.Sc., Iran University of Science and Technology, Iran, Tehran, 1999

M.A.Sc., Ryerson University, Toronto, Ontario, 2006

**A dissertation
presented to Ryerson University
in partial fulfillment of the
requirement for the degree of**

Doctor of Philosophy

**in the Program of
Mechanical Engineering in**

Toronto, Ontario, Canada, 2011

© Alireza Shirazi, 2011

AUTHOR'S DECLARATION

I hereby declare that I am the sole author of this thesis.

I authorize the Ryerson University to lend this thesis to other institutions or individuals for the purpose of scholarly research.

Alireza Shirazi

I further authorize the Ryerson University to reproduce this thesis by photocopying or by other means, in total or in part, at the request of other institutions or individuals for the purpose of scholarly research.

Alireza Shirazi

ABSTRACT

A hybrid approach to characterization and life assessment of trilayer assemblies of dissimilar materials under thermal cycles

Doctor of Philosophy, 2011

Alireza Shirazi

Mechanical Engineering

Ryerson University

The current study puts forward non-local closed-form solutions for interfacial peel and shear stress, as well as warpage deformation, of trilayer structures under thermal cycling. Based on the solution, a hybrid experimental-analytical inverse method (HEAIM) has been proposed for characterizing the constitutive behaviour of the trilayer constituents. The method is applied to optimize the correlation between the experimentally measured thermal warpage of a trilayer structure and the analytically solved warpage.

Furthermore, a localized analytical and experimental method is suggested for characterizing the stress-strain relation of a joint alloy at the interfacial level in the trilayer structure. The resulted viscoelastoplastic model of the joint alloy is further employed in predicting the life of a trilayer structure that consists of a failure dominant adhesive layer made of the same joint material. A method for the thermal fatigue life prediction is proposed, which applies critical plane-energy fatigue damage parameter in combination with a modified Coffin-Manson life model.

The experimental evaluation of the proposed models and approaches for the characterization of thermally induced trilayer structure deformation and stress, as well as the fatigue life prediction is conducted on several custom-made trilayer structures as well as real microelectronics. In the study if trilayer structure reliability and durability, experimental validation of numerical and

analytical modeling has been rare. The current study has obtained good agreement between the measured trilayer warpage and the predicted one using the thermomechanical properties of the trilayer constituents determined by HEAIM, owing to its more accurate prediction for the creep behaviour of the joint alloy. The study of thermal fatigue of the trilayer structure follows a new method that involves the critical plane-energy fatigue damage parameter. The resulted fatigue life prediction has been promising.

ACKNOWLEDGEMENTS

Writing a thesis can be considered as a solitary work, but research and implementation are clearly collaborative. Therefore, I first would like to thank all the people that contribute in a variety of ways to make the completion of this work possible.

My deepest thanks go to my co-supervisors, Professors H. Lu and A. Varvani-Farahani, for their support, encouragement and advice through my PhD program in the Department of Mechanical and Industrial Engineering at Ryerson University. They guided me through this work with clear-sightedness, drove me into very fruitful discussions and definitely contributed to the success of this work.

Further, I am thankful to Professors M. Papini and V. Venkatkrishnan for their guidance and valuable discussions throughout the research.

The help of Ms. M. Zhou, Mr. D. Onstrom, Mr. A. Machin, Mr. J. Amankrah, Mr. Q. Li and Mr. A. Heim from the Department of Mechanical and Industrial Engineering, Ryerson University were invaluable for the completion of this thesis.

I sincerely appreciate Ms. I. De Sousa from IBM Canada, Mr. A. Chen, Mr. B. Gray, Mr. J. Bragg, Mr. J. Keeping from Celestica Company in providing guidance and support associated with the design of experiments.

Further, I would like to thank Mr. M. Bijand, Mr. H. Kapadia, Mr. N. Malakootikhah, Mr. A. Mansouri, Mr. K. Chow, Mr. J. Giancola, Mr. D. Kam and Mr. S. Troung for their help with sample preparations, experiments, data processing and graphical drawing.

The Financial support of Ontario Center of Excellence, Celestica, IBM through Professor H. Lu and Natural Sciences and Engineering Research Council (NSERC) through Professor A. Varvani-Farahani of the Department of Mechanical and Industrial Engineering, Ryerson

University and the Ontario Government for financial support in the form of a Graduate Scholarship in Science and Technology (OGSST) are greatly appreciated.

My gratitude goes to my love Jananeh who patiently encouraged and accompanied me during all the moments of my studies. This work undoubtedly owes a lot to her love, presence and support.

I have a special appreciation for my parents who directed me on this path and undoubtedly without their mercy nothing could have been done.

And, Thanks to God for all the blessings he has given me.

Alireza Shirazi, 2011

TABLE OF CONTENTS

AUTHOR’S DECLARATION	II
ABSTRACT.....	III
ACKNOWLEDGEMENTS	V
TABLE OF CONTENTS	VII
LIST OF TABLES	XI
LIST OF FIGURES	XII
NOMENCLATURE.....	XVII
CHAPTER ONE	1
INTRODUCTION.....	1
1.1 OBJECTIVE AND SCOPE OF THE THESIS	1
1.2 PREFACE	2
CHAPTER TWO	4
LITERATURE REVIEW	4
2.1 ANALYTICAL MODELING OF TRILAYER STRUCTURES UNDER THERMAL LOADING.....	4
2.2 THERMAL AND MECHANICAL PROPERTIES OF JOINT LAYER MATERIALS	8
2.2.1 ADHESIVE LAYER.....	8
2.2.2 SOLDER JOINT ALLOY	9
2.2.2.1 SOLDER JOINTS CONSTITUTIVE MODELS	11
2.2.2.2 PARTITIONED CONSTITUTIVE MODEL.....	12
2.2.2.2.1 ELASTIC RESPONSE	12
2.2.2.2.2 PLASTIC RESPONSE	14
2.2.2.2.3 CREEP RESPONSE	17
2.2.2.2.3.1 CREEP TESTING PROCEDURES.....	19
2.3 PREDICTION MODELS FOR THERMAL FATIGUE OF TRILAYER.....	19
2.4 CHAPTER SUMMARY	24

CHAPTER THREE	26
ANALYTICAL METHODS FOR TESTING OF RELIABILITY AND DURABILITY OF TRILAYER STRUCTURE	26
3.1 INTERFACIAL MODELING OF TRILAYER STRUCTURES UNDER THERMAL LOADING	26
3.1.1 INTERFACIAL SHEAR STRESS	34
3.1.2 INTERFACIAL PEEL STRESS	37
3.1.3 WARPAGE	44
3.2 INVERSE METHOD IN CHARACTERIZATION OF TRILAYER CONSTITUENTS	46
3.3 METHOD IN APPROXIMATION OF NOTCH STRESSES AND STRAINS UNDER CREEP CONDITIONS.	50
3.4 PROPOSED METHOD FOR THERMAL FATIGUE LIFE PREDICTION	52
CHAPTER FOUR	57
EXPERIMENTAL METHODS IN TESTING RELIABILITY AND DURABILITY OF TRILAYER STRUCTURE	57
4.1 TRILAYER SAMPLE UNDER THERMAL CYCLING	57
4.1.1 TRILAYER SAMPLES DESIGN AND PREPARATION	57
4.1.2 THERMAL CHAMBER	60
4.1.3 SAMPLE TEMPERATURE CONTROL	61
4.1.4 WARPAGE MEASUREMENTS OF THE TRILAYER	62
4.1.4.1 TESTING TEMPERATURE CONDITION IN WARPAGE MEASUREMENT	62
4.1.4.2 PHASE SHIFTED SHADOW MOIRÉ	62
4.1.4.3 VIRTUAL REFERENCE PLANE	65
4.1.5 IN-PLANE STRAIN OF SIDE-SECTION OF TRILAYER	68
4.1.5.1 TESTING TEMPERATURE CONDITION IN IN-PLANE STRAIN MEASUREMENT	69
4.1.5.2 DIGITAL SPECKLE CORRELATION METHOD	70
4.1.5.3 IMAGE RECORDING AND DATA PROCESSING	74
4.2 STEADY-STATE CREEP TESTS OF SOLDER ALLOY	74
4.2.1 SAMPLES AND TESTING PROCEDURES	75
4.2.1.1 SAMPLES PREPARATION	76

4.2.1.1.1	CASTING SETUP	76
4.2.1.2	CREEP DEAD-WEIGHT TENSILE TEST	78
4.2.1.2.1	TESTSETUP	78
4.3	ACCELERATED THERMAL CYCLING TEST	81
4.3.1	ACCELERATED THERMAL CYCLING (ATC) TEST AT ASSEMBLY LEVEL	81
4.3.1.1	ACCELERATED THERMAL CYCLING TEST CONDITION	83
4.3.2	LOCAL TESTING METHOD	84
4.3.2.1	SOLDER STRAIN MEASUREMENTS UNDER ACCELERATED THERMAL CYCLING CONDITION USING DSC	85
CHAPTER FIVE		88
EXPERIMENTAL AND ANALYTICAL RESULTS AND DISCUSSIONS		88
5.1	WARPAGE OF TRILAYER SAMPLE UNDER THERMAL CYCLING	88
5.1.1	PROPOSED INVERSE METHOD AND TRILAYER CONSTITUTIVE PROPERTIES	89
5.1.2	WARPAGE MODELS COMPARISONS	96
5.1.3	INTERFACIAL STRESSES AND STRAINS	98
5.1.3.1	IN-PLANE STRAIN MEASUREMENTS RESULTS OF SIDE-SECTION OF TRILAYER	98
5.1.3.2	INTERFACIAL STRESSES RESULTS BASED ON ANALYTICAL MODELING	99
5.1.3.3	RESULTS OF COMPARISONS BETWEEN ANALYTICAL AND EXPERIMENTAL PEEL STRAINS ..	101
5.1.3.4	INTERFACIAL PEEL STRESS-MODELS COMPARISONS	103
5.2	VISCOELASTOPLASTIC BEHAVIOUR OF SAC305 INTERFACIAL ALLOY	104
5.2.1	MICROSTRUCTURAL ASSESSMENT OF SAMPLES	105
5.2.2	TEST MATRIX	107
5.2.3	STEADY-STATE CREEP CONSTITUTIVE BEHAVIOUR	108
5.2.4	ELASTIC-PLASTIC BEHAVIOUR	112
5.3	FATIGUE LIFE PREDICTION OF TRILAYER STRUCTURE UNDER THERMAL CYCLING	114
5.3.1	ACCELERATED THERMAL CYCLING TEST AND WEIBULL DISTRIBUTIONS	115
5.3.2	THE PROCEDURE OF FATIGUE LIFE ASSESSMENT OF TRILAYER STRUCTURE	116
5.3.2.1	CRITICAL JOINT OF DISCRETE LAYER OF JOINS	117
5.3.2.1.1	CRITICAL CORNER OF THE CRITICAL JOINT	117
5.3.2.1.2	CRITICAL PLANE OF THE CRITICAL CORNER	118

5.3.2.2 ENERGY-CRITICAL PLANE DAMAGE PARAMETER	118
CHAPTER SIX	131
CONCLUSIONS, CONTRIBUTIONS AND SUGGESTIONS FOR FUTURE WORK...	131
6.1 CONCLUSIONS	131
6.2 COTRIBUTIONS	132
6.3 SUGGESTIONS FOR FUTURE WORK	134
REFERENCES.....	135
APPENDIX1:INTERFACIAL SHEAR STRESS MODEL FOR TRILAYER STRUCTURE.....	145
APPENDIX2: INTERFACIAL PEEL STRESS MODEL FOR TRILAYER STRUCTURE	158
APPENDIX3: PROGRAM OF INVERSE METHOD	171
APPENDIX4:WARPAGE OF TRILAYER STRUCTURE- EXPERIMENTAL RESULTS	177
APPENDIX5: INVERSE MODELING RESULTS AND WARPAGE PREDICTION.....	189
APPENDIX6:INTERFACIAL STRESSES AND STRAINS, EXPERIMENTAL AND ANALYTICAL RESULTS AND COMPARISONS.....	197
APPENDIX7: CAST DETAILED DRAWINGS.....	234
APPENDIX8: MICRO-TESTER DESIGN DRAWINGS	238
APPENDIX9: CREEP TENSILE TEST RESULTS	252
APPENDIX10: FATIGUE DAMAGE RESULTS.....	269

LIST OF TABLES

Table 1: Elastic Modulus for different compositions of SAC solder alloy tested at different strain rates.	13
Table 2: Elastic-plastic model of leadfree solder alloy as cast	16
Table 3: Plastic model parameters of leadfree solder alloys.....	16
Table 4: Creep models of leadfree solder alloys.....	18
Table 5: Parameters for leadfree solder for plastic and creep strain range of shear and Von Mises model.....	21
Table 6: Engelman fitted model parameters	22
Table 7: Parameters for leadfree solder alloy for plastic and creep strain energy density model	22
Table 8: Mechanical Properties of Trilayer Constituents	59
Table 9: Schematic of the test specimen.....	76
Table 10: Classification Casting Temperature Profile.....	78
Table 11 - Description of samples used in this study.	82
Table 12 – Location of DSC measurement (critical joint) for each sample	87
Table 13: Matrix of the trilayer samples design	91
Table 14: Bilinear material properties of the trilayer constituents determined using HEAIM.....	95
Table 15: Maximum peel stresses determined using present analytical model for different..... samples.....	100
Table 16: Test matrix for monotonic loading creep tests.	108
Table 17: SAC305 solder alloy Garofalo hyperbolic sine law constitutive model constants.....	111
Table 18: Thermal Cycling Results of Accelerated Thermal Cycling Test.....	115
Table 19: SAC305 solder alloy viscoelastoplastic constitutive properties	123
Table 20: Durability model fitting results for SAC305 board-level solder joint under thermal..... cycling and mechanical bending conditions	129
Table 21: Predicted damage parameter for samples following critical plane damage modeling	129
Table 22: Comparison between predicted and experimental fatigue life N_{f50} for samples	130

LIST OF FIGURES

Figure 1: (a) Shear stresses along the interface, (b) peel stresses around the edges and along the interface [6].	5
Figure 2: Schematically illustrates a trilayer structure where the warpage that can be measured on top or bottom surfaces with the cross-section line in X (A-A') and Ψ (D-D') direction [13].	6
Figure 3: Schematic cross-section diagram of a plastic ball grid array (PBGA) package used for microelectronic applications.	10
Figure 4: Comparison of the elastic modulus of lead-free solders [34].	14
Figure 5: Trilinear elastic-plastic approximation for solder alloy.	15
Figure 6: Strain vs. time behaviour during creep under constant load, hence constant engineering stress, and the three stages of creep [51].	17
Figure 7: Schematic of trilayer structure with geometries related to Engelmaier model [70].	21
Figure 8: Free-body diagram, Shear and peel stresses along the interface, axial and shear forces and bending moments across the layer thickness.	27
Figure 9: Trilayer structure considered as 2D elemental strip under plane-stress (edge cross-section) and plane-strain (mid-cross section) with the width of unity ($t=1$), thickness as h and the length of $2l$ in the plane of XZ [9].	28
Figure 10: Flowchart of proposed inverse method	47
Figure 11: (a) Strain history, strain path and strain and stress Mohr's circle with stress and strain components of the critical plane-energy model, for in-phase strain path [89].	53
Figure 12: The procedure of fatigue damage analysis based on the critical plane damage parameter.	56
Figure 13: Schematic of the test sample with silicone balls of 0.35mm diameter before assembly.	60
Figure 14: Typical trilayer sample: a) after manufacturing process, b) trilayer final shape.	60
Figure 15: Warpage test temperature profile	62
Figure 16: Phase-shifted shadow moiré set-up [93].	64
Figure 17: Phase-shifted shadow moiré current set-up (Experimental Mechanics Laboratory, Dept. of Mechanical and Industrial Engineering, Ryerson University).	64
Figure 18: Phase-shifted shadow moiré fringe patterns [93].	65

Figure 19: The virtual datum plane presented in a) convex-down surface b) concave-up surface.	65
Figure 20: Side side-section of trilayer sample before speckling	69
Figure 21: Detail of strain measurement location.....	69
Figure 22: In-Plane strain measurement test temperature profile	70
Figure 23: Schematic of DSC system setup.....	71
Figure 24: DSC system current set-up (Experimental Mechanics Laboratory, Dept. of Mechanical and Industrial Engineering, Ryerson University).....	71
Figure 25: Test specimen a) Bulk sample of SAC305, b) Schematic of the test specimen [88]. .	75
Figure 26: Casting device a) Current setup, b) Mould top piece with riser and thermocouple probes place, c) Mould with cavities for four samples, d) Mould bottom piece with end-holes-inserter,.....	77
Figure 27: Casting temperature profile	78
Figure 28: Test setup presented in, a) Schematic of micro-tester structure, b) Current state of the micro-tester in tensile test, c) Current state of the micro-tester in creep-tensile-test while measuring strain using high-speed digital camera under load and temperature condition.	80
Figure 29 –Samples prepared for ATC Test with types presented in Table 11 as: a) Type A, b) Type B c) Type D and d) Type D.....	82
Figure 30 – Configurations of samples of: a) Type A, b) Type B, c) Type D and d) Type D [2] with cut along a BGA diagonal.....	83
Figure 31- Design of daisy chain, shown from BGA side view [29].	84
Figure 32 - DSC measurement steps presented at a) the diagonal cut of the sample, b) the location of critical corner joint, c) area of the measurement of critical joint in higher magnification and d) the solder joint after being speckled.	86
Figure 33 –Thermal profile of the pre-cycling condition of samples before DSC measurement.	86
Figure 34 –Thermal profile of cycling condition of samples during DSC measurements.	87
Figure 35: Typical image showing the thickness measurement of underfill layer using Buehler ViewMet Inverted Laboratory Metallograph.....	90
Figure 36: Typical 3-D graphical representation of measured warpage at temperature for sample#17 diagonal lines along LTRB (left-top to right-bottom) and LBRT (left-bottom to right-top).	94

Figure 37: Typical results of predicted relative warpage over the length of the module using HAEIM compared with experimental measurements for (a) Sample#3 at $\Delta T=35^{\circ}\text{C}$ (20°C to 55°C), (b) Sample#5 at $\Delta T=57^{\circ}\text{C}$ (160°C to 217°C), (c) Sample#11 at $\Delta T=35^{\circ}\text{C}$ (20°C to 55°C), (d) Sample#13 at $\Delta T=35^{\circ}\text{C}$ (20°C to 55°C), (e) Sample#17 at $\Delta T=30^{\circ}\text{C}$ (100°C to 130°C).....	95
Figure 38: HAEIM predicted mechanical properties versus temperatures a) Underfill materials Elastic Modulus, b) Substrate Elastic Modulus c) Substrate CTE.....	96
Figure 39: Typical results of comparison between the warpage obtained from experiments and analysis using present model and Suhir models a) Sample#3, b) Sample#5, c) Sample#11, d) Sample#13 and e) Sample#17.	97
Figure 40: Typical contour pattern of strain measurements at $T=125^{\circ}\text{C}$	98
Figure 41: Typical plot of modeled peel stress along the mid-cross section of trilayer structure	100
Figure 42: Typical plot of modeled shear stress along the mid-cross section of trilayer structure.....	100
Figure 43: Plots of average measured strain versus temperature for a) sample#3, b) sample#5, c) sample#11 and d) sample#13	103
Figure 44: Typical results of comparison between the peel stresses obtained from analysis using present model and Suhir model a) Sample#3, b) Sample#5, c) Sample#11 and d) Sample#13	104
Figure 45: Microstructures of Sn3.5Ag0.5Cu solder view indicating examples of various regions of Sn, Ag_3Sn , Cu_6Sn_5 and $\text{Sn} + \text{Ag}_3\text{Sn} + \text{Cu}_6\text{Sn}_5$ using: a) secondary electron image (SEI) for real solder joint, b) back scattered electron composition (BEC) for real solder joint, c) SEI for as cast solder and d) BEC for as cast solder.....	106
Figure 46: Summary of weights and atomic percent of elemental composition of the analyzed volume of phases of Sn, Ag_3Sn and Cu_6Sn_5 of SAC305 using EDS in: a) real solder joint, b) as casted solder alloy, c) as casted solder alloy and d) as casted solder alloy.	107
Figure 47: Typical strain vs. time behaviour during creep under constant temperature of 0°C and constant load, hence constant engineering stress, and the steady-state of creep.....	109
Figure 48: Typical elastic-plastic-creep curve for SAC305 solder alloy under constant stress and temperature.....	110

Figure 49: Normalized steady-state behaviour of Sn3Ag0.5Cu (SAC305) solder alloy.	110
Figure 50: Normalized steady-state behaviour of Sn3Ag0.5Cu solder alloy.	111
Figure 51: Comparison of Temperature dependent Young's modulus of SAC305 solder alloy measured in this study with the ones reported in literature [34] for SAC solder alloys.	113
Figure 52: Comparison of measured strains with predicted elastic-plastic strains for SAC305 solder alloy under various temperatures.	113
Figure 53: Comparison of temperature dependent elastic-plastic behaviour of SAC305 solder alloy with measured strains.	114
Figure 54: Weibull plots followed JEDEC ATC testing for four samples types [29].	116
Figure 55: The location of solder joints along diagonal line under the die shadow region.	119
Figure 56: Typical results of crack length measurements of solder joints along the diagonal line, after 4400 cycles of ATC test, for sample#36.	119
Figure 57: The FEM results in a) trilayer structure under multiaxial loading during thermal loading, b) Von Mises equivalent strain during thermal loading within critical joints (left-end joint under die shadow, c) Von Mises equivalent strain during thermal loading within critical joints (right-end joint under die shadow-joint), mapping the direction of the initiation of microcracks.	120
Figure 58: Von Mises-strain contour using DSC strain measurement system mapping the direction of the initiation of microcracks during thermal loading within critical joints (right-end joint under die shadow-joint with location of AA-21).	121
Figure 59: : Von Misses-strain contour using strain measurement results of DSC, mapping direction of the initiation of microcracks during thermal loading within critical joints (left-end joint under die shadow-joint with location of AN-33).	121
Figure 60: Mapping the ratio between the shear and tensile strains within the surface of the critical corner for a) sample#309 with critical joint at location of AA-21, b) sample#212 with critical joint at location of AN-33, c) sample#36 with critical joint at location of AN-33 and d) sample#344 with critical joint at location of AN-33.	122
Figure 61: Typical stress-strain hysteresis behaviour of stabilized loop (seventh cycle) in tensile and shear conditions.	122
Figure 62: Typical results of proportional loading of tensile and shear with indication of peak point of loading (P) and unloading (Q).	124

Figure 63: Typical results of shear and tensile strains with in-phase strain path with indication of peak point of loading (P) and unloading (Q).....	124
Figure 64: Typical stress Mohr's circle for in-phase path with mean-stress during loading and un-loading of stabilized loop.	125
Figure 65: Typical strain Mohr's circle for in-phase path with mean-strain during loading and un-loading of stabilized loop.	125
Figure 66: Strain Mohr's circle representing stress components of damage parameters for in-phase path for sample#36 during loading and un-loading of stabilized loop.	126
Figure 67: Stress Mohr's circle representing stress components of damage parameters for in-phase path for sample#36 during loading and un-loading of stabilized loop.	126
Figure 68: Durability curves and experiment data points for SAC305 solder joint tested under 25°C and 125°C temperatures [106].....	127
Figure 69: Assessment of critical plane damage parameter life prediction capability for SAC305 solder joint allot under thermal cycling of 25-125°C.....	130

NOMENCLATURE

Acronym	Definition
ATC	accelerated thermal cycling
BEC	back scattered electron composition
BGA	ball grid array
CTE	coefficients of thermal expansion
C4	controlled collapse chip connection
DSC	digital speckle correlation
EDS	energy dispersive spectroscopy
FC	flip chip
FEA	finite element analysis
HEAIM	hybrid experimental analytical inverse method
Pb	lead
PBGA	plastic ball grid array
PCB	printed circuit board
SAC	Sn-Ag-Cu (Tin-Silver-Copper)
SEI	secondary electron image
SEM	scanning electron microscope
Si	silicon chip
SnPb	Tin-Lead

Symbol	Definition
A	peel stress differential equation first constant
B	shear stress differential equation first constant
C_{pl}	strength coefficient
D	flexural rigidity in either plan-stress or plane-strain condition
$D_{damage-parameter}$	fatigue damage parameter
E_i	modulus of elasticity
E	peel stress differential equation second constant

F	shear stress differential equation second constant
h	thickness of the strip
G	peel stress differential equation third constant
k	universal gas constant
m	hardening exponent
L_d	distance to the neutral point
l	half length of the assembly
M	bending moment
N_0	crack initiation life
N_a	crack propagation life
N_f	failure life
$N_{50\%}$	number of cycles to failure of half of the population
p	shear stress Case-I first coefficient
$P(x)$	peel stress
q	shear stress Case-I second coefficient
Q	activation energy
$T(x)$	longitudinal axial force
T	temperature
T_{sj}	medium cyclic temperature
t_{dwell}	dwel time at the maximum temperature
ΔT	temperature range
u	displacement in longitudinal direction
$V(x)$	transverse shear force
Δw_{in}	total strain energy
x,y,z	Cartesian coordinate sytem

Greek Symbol	Definition
α	coefficients of thermal expansion
ε_x	unit elongation of a fibre at X-direction

ε_y	unit elongation of a fibre at Y-direction
ε_t	total strain
ε_e	elastic strain
ε_p	rate-independent strain
ε_{pl}	plastic strain
ε_c	rate-dependent creep strain
ε_{scr}	equivalent strain
$\Delta\varepsilon_{in}$	inelastic strain range
σ	normal stress
$\tau(x)$	shear stress
Γ	shear stress Case-II first coefficient
Ω	shear stress Case-II second coefficient
γ	shear strain
Φ	peel stress Case-I first coefficient
Π	peel stress Case-I second coefficient
Θ	peel stress Case-II first coefficient
Ψ	peel stress Case-II second coefficient
$\Delta\gamma$	total shear strain range
ν_i	poisson's ratio
μ_i	shear compliance
λ_i	axial compliance
γ_i	transversal shear compliance
η_i	through thickness compliance
ψ	diagonal direction
$\rho(x)$	radius of the curvature of the assembly
α_i	coefficients of thermal expansion
w	warp (deflection)
ε'_f	fatigue ductility coefficient
σ'_f	axial fatigue strength coefficient

τ'_f	shear fatigue strength coefficient
γ'_f	shear fatigue ductility coefficient

CHAPTER ONE

Introduction

1.1 Objective and scope of the thesis

Adhesively bonded trilayer structures are commonly used in many technology sectors including aerospace, electronics and optical networks. These structures are bodies made of a large variety of dissimilar materials. Due to the coefficients of thermal expansion (CTE) mismatches between and temperature gradients within the layers of structures, thermally induced interaction becomes a typical type of load for these joints. For instance, in microelectronic packages, the thermal stresses and strains at the interfaces of adhesive and solder joints are the cause of the most common package failures. The proposed study of the thermal stress-strain behaviour, as well as the fatigue life prediction of the multi-material joints, is thus of academic interests as well as practical importance.

The objective of the proposed study is to develop a unique yet simple method combining analytical and experimental approaches for the evaluation of reliability and durability of an adhesively bonded trilayer of dissimilar materials under thermal cycling.

This research has two major phases. Phase one is to characterize the trilayer structure under thermal cycling for its constituent thermomechanical properties, interfacial stress and strains, as well as the warpage deformation of the structure. An analytical method is developed to solve for thermally induced stresses and strains at the interface level as well the warpage deformation of the structure at the global level. The applications of the warpage model will be within an inverse method. This method employs the experimentally determined warpage deformation of the

trilayer structure to further determine the thermomechanical properties of the structure's constituents.

In the second phase, the fatigue life of the trilayer structure under thermal cycling is predicted. The damage criterion based on the energy method using the critical plane-energy fatigue damage parameter, is computed through a stress/strain hysteresis loop of a stabilized cycle. The stress-strain data of the stabilized cycle is determined using the developed viscoelastoplastic model of the joint layer. The resulting damage parameter is further evaluated with the experimentally determined characteristic life. The proposed life model can be applied to a class of trilayer structures with the same joint material.

1.2 Preface

The following provides a brief description of materials covered in the chapters of this thesis.

Chapter 2 covers a review of the analytical models of trilayer structures under thermal loads. The available methods of determining constitutive behaviour of viscous interfacial adhesive alloys are presented. Also life prediction methods of structures under thermal loadings are listed.

Chapter 3 presents 1) the interfacial peel and shear stress and warpage models of the trilayer structure under thermal cycling; 2) the inverse method for characterizing the constitutive behaviour of the trilayer constituents; 3) the analytical and experimental methods for characterizing the viscoelastoplastic joint alloy; 4) the method for predicting the characteristic fatigue life of the trilayer structures.

Chapter 4 presents a detailed description of the experiments carried out in this research. First, the development of the trilayer structure is discussed, followed by a description of optical experimental methods to measure in-plane and out-of-plane deformations under a thermal cycle. A description of digital image post-processing obtained through measurements is also presented. A creep dead-weight tensile testing procedure and set up, as well as sample preparation, are

described. The chapter concludes with a description of accelerated thermal cycling tests performed on a local level (single solder joint) and a global level (array of joints) in a real scale microelectronic prototype/test vehicle.

Chapter 5 presents the results of thermal cycling and creep tests carried out in this research. Results of each set of experiments are separately discussed. The analytical results, related to a hybrid experimental analytical inverse method (HEAIM) and interfacial stress-strain of the trilayer samples at different temperatures, are presented. The interfacial peel strains are evaluated against the experimental results. Parameters related to the secondary creep stage of the solder alloy constitutive behaviour are examined and compared with the literature data. Accelerated thermal cycling test results at the local level (single solder joint) and the global level (array of joints) have been demonstrated, followed by the results of the life prediction method and its comparison with the experimental data.

Chapter 6 summarizes the conclusions obtained from this study. It gives the key points related to the trilayer structure thermal stress and deformation under cycling, fatigue life prediction of the trilayer structure and includes a series of recommendations for future work at the end.

CHAPTER TWO

Literature Review

In this chapter, a literature review is presented. Analytical models of trilayer structures under thermal loads are reviewed. The available methods of determining the constitutive behaviour of viscous interfacial adhesive alloys are presented. Finally, life predictions methods of structures under thermal loadings are listed.

2.1 Analytical modeling of trilayer structures under thermal loading

Thermal loading can take place during the normal operation of the system, as well as during its fabrication, testing or storage. Induced thermal stresses and strains can be the major contributor to the finite service life of multilayered structures. The stresses can be caused by combination of elastic (reversible), plastic (residual, irreversible), or time dependent effects, such as creep, stress relaxation, viscoelastic or viscoplastic phenomena.

Many researchers have studied the failure mechanisms in multilayered structures. Timoshenko [1] pioneered the study of stresses in bi-material thermostats. He employed a simple perfect beam theory of elasticity to obtain the curvature of a bimetallic beam due to a uniform temperature change. Chen and Nelson [2] used force and moment equilibrium equations to understand the stress distribution in a bonded joint induced by thermal expansion of dissimilar materials, and Suhir [3, 4, 5] improved Timoshenko's beam theory with relatively simple calculations using longitudinal and transverse interfacial compliances.

The first linear elastic closed-form solution developed by Suhir [3] has been employed or extended by many studies to analyze the warpage of a trilayer structure and interfacial stresses

subjected to thermal cycles [6, 7, 8, 9, 10]. The interfacial compliances for the plane-strain and plane-stress conditions have been introduced to Suhir's solution by Ghorbani and Spelt [7]. Interfacial stresses evaluated in Suhir's analysis, included shear and transverse normal (peel) stresses taking place in the vicinity of the layers' interfaces and were accountable for the cohesive and adhesive strength of the mid layer [3].

In the analysis the layers were considered homogenous and isotropic with small deflections so the engineering theory of bending plates would be applicable. Uniform temperature distribution and constant radius of curvature have been considered through the layers' thicknesses. The adhesive layer was only under the shear deformation so its coefficient of thermal expansion has not been accounted for.

Although the shear stress calculated by Suhir [3] excludes the zero shear stress state at the end corners and the peel stress fails to satisfy a self-equilibrating condition, yet Suhir's stress model was a reliable approach to estimate actual stress values up to the end corners (within the region of $x/l < 0.98$) [7,8,11]. Within this region shear and peel stresses were the same at upper and lower interfaces [12] (Refer to Figure 1).

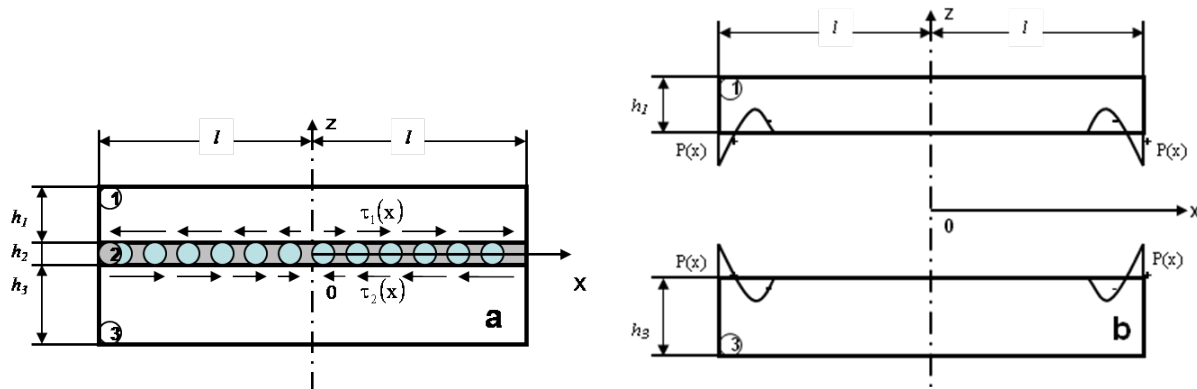


Figure 1: (a) Shear stresses along the interface, (b) peel stresses around the edges and along the interface [6].

The next linear elastic closed-form solution by Suhir [4] analyzed the warpage of a trilayer structure at micro-level thickness. The method was applied within a limited temperature period (ΔT) to consider the nonlinear behaviour of the constituent materials of structure [13]. For a trilayer beam structure, Suhir's strip model [4] provided some simple, closed-form mathematical

equations governing the system response. The closed-form model was applicable to general micro-level structures. The structure contained layers with CTE, stiffness and thicknesses not negligible relative to each other [4].

This model complements the warpage model presented in early study by Suhir for bimaterial strips [3] which is mainly applicable to structures with thin and compliant adhesive layers such as flip-chip plastic ball grid array packages (FC-PBGA) [6,14] as a result of a more rigorous analytical model [4]. The proposed analysis in later study by Suhir, further accounts for the CTE of all three layers opposed to only the top and the bottom layers.

The equations for both plane-strain and plane-stress conditions for the warpage model have been demonstrated in [6]. The interfacial compliances for the plane-strain and plane-stress conditions [6] have been introduced to Suhir's solution. The trilayer structure consists of three layers, top, middle (core) and bottom respectively, denoted by subscripts 1, 2, and 3. (Refer to Figure 2).

In later analysis by Suhir [4], the layers were considered homogenous and isotropic with small deflections so the engineering theory of bending plates was applicable. Uniform temperature distribution has been also considered throughout the thicknesses of the layers. Assuming spherical bending, the curvature has also been considered constant through the thickness and directly related to the bending moment [1].

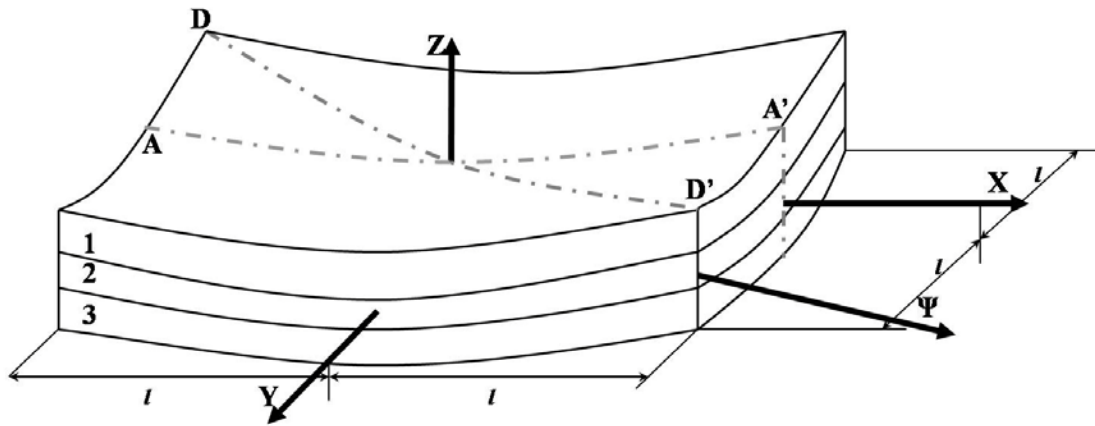


Figure 2: Schematically illustrates a trilayer structure where the warpage that can be measured on top or bottom surfaces with the cross-section line in X (A-A') and Ψ (D-D') direction [13].

The equations of shear and peel based on the later analysis of Suhir [4] have addressed the self-equilibrating peel but not the zero shear stress at the end. Also these stresses have been determined based on two separate conditions by assuming the different deflections amongst the assembly members to obtain the peel stresses, where the shear stresses were found assuming the same radius of curvature for the layers [7].

The analytical model presented based on the work by Valisetty [15] with emphasis on the stress behaviour along the interfaces between layers of composite laminates due to isothermal loading has been extended by Wen and Basaran [16] by implementing the orthotropic material properties, interfacial compliances as well as thermal loading in the model. Although they have found reasonable results in predicting the interfacial strains in comparison with experimentally measured strains (using Moiré interferometry) and peel stresses self-equilibrating but failed to predict shear stresses zero at the free ends.

Ru [17], by using the non-local Winkler models of thin elastic foundations by Kerr [18], successfully addressed the zero condition of shear stress at the end. However, the resulting self-equilibrating peel stresses were found based on an assumption which includes the beams with small deflections and subjected only to lateral loads.

Ghorbani and Spelt [19] using the structural mechanics approach, implemented more accurate compliances based on the linear viscoelasticity. Although their model predicted peel stresses self-equilibrating and shear stresses zero at the ends, there is no closed form solution presented. Also due to the approximate nature of first order finite difference solutions employed in solving the differential equations, there are some deviations existing from the exact solutions [20].

On the other hand, finite element analysis (FEA) has been widely used to address these complexities [21]; however, the mesh dependency and singularity of the FEA which results at free ends, where cracks often initiate, have generated some drawbacks in utilizing this method for real industrial applications including trilayer structures where geometries and loading conditions are not complex.

Hence, there is a need for closed-form solutions to predict the warpage and interfacial stresses of trilayer structures under thermal loads without involving high degrees of approximation and loss of generality. Besides, few experimental approaches have been reported [16] for the validation of the numerical modeling results as well as the analytical solutions.

2.2 Thermal and mechanical properties of joint layer materials

2.2.1 Adhesive layer

A reliable design of a trilayer structure is very much dependent on the close evaluation of thermal-mechanical behaviour of trilayer structure. Most materials exhibit behaviours that are highly dependent on their geometric scale, manufacturing process and service environment [22]. In addition, the material behaviours generally deviate from those of their generic counterparts as the result of their physical or metallurgical interconnection to neighbouring materials [23]. As such, relevant laws governing these behaviours are complex to prescribe [24]; related parameters are difficult to determine for a specific application [25], and book values of the properties as published, show wide ranges of variation [6,26].

The above facts constitute a dilemma and pose challenges to practical structure modeling attempts [14]. Hence the ability to predict the thermal and mechanical properties of the constituent materials is important to the structure design and development [27,28] and eventually their service lives [29].

The system thermal response parameters are key factors that further affect the multilayer structure manufacturing process. A valid evaluation of a trilayer structure's performance and the causes of its failure cannot be reached without thorough knowledge of thermal and mechanical behaviour of the package elements and materials. For instance for a microelectronics multilayer structure such as flip-chip plastic ball grid array (FC-PBGA), it is known that the behaviour of the organic substrate and in particular that of the die attachment are generally uncertain. The situation is attributable to the thin thickness, discrete and mixed underfill and solders materials,

and the effect of processing conditions, etc. [8, 12, 30]. These uncertainties contribute to the complexity of modeling and thus hamper the structure reliability evaluation.

What can be obtained with sufficient confidence, however, is the package's warpage variation with temperature. The latter can be measured by using optical methods such as shadow moiré. The thermal warpage assessment is popularly applied, and is becoming a part of the routine evaluation for FC-PBGA reliability. A review of the past research [4, 5, 17, 31] reveals that little existing modeling work has adequately emphasized the verification of results using experimentally measured structure actual deformation.

Hence, it is worth noting that there is need of a method that is generally applicable to the analysis of manufacturing induced stresses in adhesively bonded trilayer structures regardless of the prior knowledge of the manufacturing process, the materials' microstructure and the geometric scale effect on the materials' behaviour.

2.2.2 Solder joint alloy

Rapid advance in micro-structures such as those found in microelectronics applications during the past two decades has pushed the reliability concerns of the electronic systems and components to the front. For some new products, the field returned statistics show a rate of failure as high as 20%, among which the thermo-mechanical related failures account for over 65% of the total failures. The leadfree Sn-Ag-Cu (SAC) solder joints are at the core of the reliability related issues that call for a more thorough investigation. Demand for time and cost effective methodologies for reliability assessment as alternatives to the current time-consuming numerical approaches is rising.

There is a motivation for solder reliability modeling in transition to lead-free in microelectronic industries. There has been long-term, successful use of tin-lead solders in terms of electronics manufacturing and solder processing. In an electronic package, components that are joined together have different coefficients of thermal expansion (CTE) and rigidities within thermal strains when the package undergoes a temperature change. These thermally induced strains are

often cyclic in nature and result in fatigue failure of the solder joints and an open circuit. In many cases the joint is cycled at a high homologous temperature so the cyclic deformation that causes fatigue is predominantly creep. Although plastic deformation may also cause irreversible damage in solders, it is negligible over time compared to that produced by creep.

Figure 3 schematically demonstrates a cross-section of a plastic ball grid array (PBGA) package utilized for microelectronic applications. This figure demonstrates the most common type of the module in surface mount technology assemblies as flip chip (FC). There are two different solder joints highlighted. Type one is C4 (controlled collapse chip connection) solder joint, or bumps, which connect a silicon chip (Si) to an Epoxy-based laminate chip carrier (substrate) at the Module level and other one is BGA solder joint (ball), connecting the module to a PCB (Board-level).

The typical dimensions of the C4/flip-chip solder joints are of the order of 100 μm in diameter and 200 μm or less in pitch, and are usually made of high lead (Pb) SnPb solder alloy (melting point over 300°C) while the BGA solder balls, with typical dimensions of the order of 600 to 900 μm in diameter, are joined to a module (chip on the board) or substrate by reflowing the solder paste deposited onto a PCB (printed circuit board). The subject of the current study is reliability of the board level solders (BGA) where it can be extended to consider the reliability of a module as a separate case study of an adhesively bonded multilayer structure.

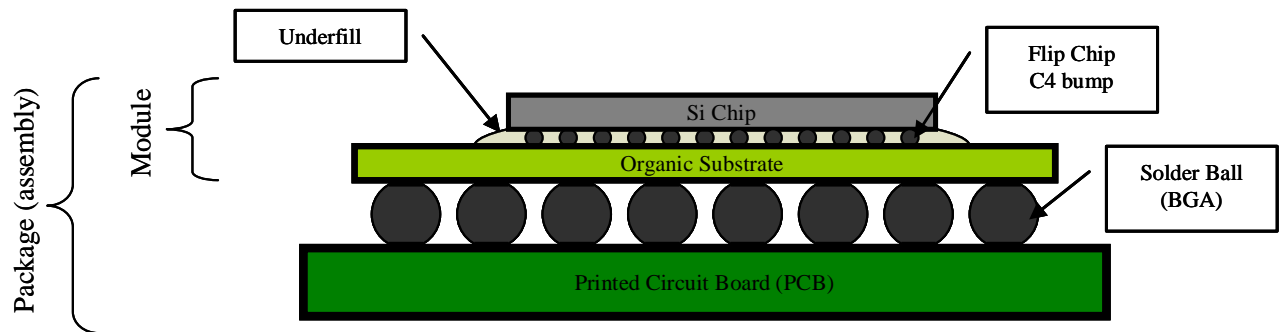


Figure 3: Schematic cross-section diagram of a plastic ball grid array (PBGA) package used for microelectronic applications.

The latest worldwide environmental legislations restricting the use of lead (Pb)-contained solders have presented new and imminent challenges to the microelectronics industry. The higher melting temperature of most of the promising Pb-free solders results in an increase in board assembly processing temperature. For instance, the most NEMI (National Electronic Manufacturing Initiative) preferred replacement SnAgCu, for the reflow process has a melting point of 217°C, which is 34°C higher than the conventional solder joint Sn37Pb. If the reflow time is maintained, this higher peak temperature can mean severe thermal induced stresses due to higher heat-up and cool-down rate in the components.

Studies have shown that many leadfree solder alloys have higher strength and creep resistance compared with the SnPb solder [32, 33, 34]. The increase in the strength and creep resistance should result in more fatigue-resisted solder joints. But the higher strength and creep resistance also give rise to a higher level of stresses in solder joints and the interfaces.

With the combination of the higher assembly temperature, the higher strength and less stress relaxation of most of the Pb-free solders, increased failures at interfaces are anticipated for the Pb-free solders. The leadfree substitutes such as Sn–3.5Ag–0.5Cu (SAC305) alloy has only limited database of the thermal-mechanical properties for any reliable modeling. Hence, the proposed research considers mechanical and thermal fatigue-properties of these joints at the interfacial level.

2.2.2.1 Solder joints constitutive models

The total deformation of the solder material consists of elastic, rate-independent plastic and rate-dependent creep components. The constitutive models discussed in this study each weighted elastic, plastic and creep deformations differently. At low stresses SAC solder alloys were found to be creep resistant, whereas at higher stresses, the influence of different microstructures disappears as matrix-creep dominates in this region. Thus, the proper constitutive model requires all the three ingredients of the elastic, the creep, and the time-independent plastic data for different stress levels to effectively predict the hysteresis behaviour of the SAC solder alloys [35].

2.2.2.2 Partitioned constitutive model

The total deformation of a solder material consists of elastic, plastic and creep components. The partitioning constitutive law is expressed as:

$$\varepsilon_t = \varepsilon_e + \varepsilon_{pl} + \varepsilon_c \quad (1)$$

where ε_t is the total strain, ε_e is the elastic strain, ε_{pl} is the rate-independent plastic strain, ε_c is the rate-dependent steady-state creep strain. According to the Von-Mises (distortion-energy theory) failure criterion, at the onset of a material's yielding, the shear stress reached in a pure shear test is $\sqrt{3}$ times lower than the tensile stress in a simple tension test. Hence the critical shear stress/strain and critical normal stress/strain in the respective pure shear and simple tension test have the following simple relationships:

$$\sigma = \tau\sqrt{3} \quad (2)$$

$$\varepsilon = \frac{1}{\sqrt{3}}\gamma \quad (3)$$

Terms σ and ε are the normal stress and strain components, respectively, and τ and γ are the shear stress and strain terms, respectively.

2.2.2.2.1 Elastic response

The elastic response of a solder joint and the corresponding modulus of elasticity are calculated and determined from the linear portion of stress-strain curve of solder materials. There are discrepancies between reported values for the Young's modulus since it is found that strain rate has a direct impact on the results.

Due to contributions from creep, slow strain rates produce lower modulus of elasticity where at high strain rates almost no effect of the creep behaviour of solder joints are noticed on the

measured Young's modulus [36]. Hence, it is recommended that solders with high creep rates must be tested at higher loading rates for measuring elastic properties [36].

Table 1 provides the Elastic Modulus for different compositions of SAC solder alloy tested at different strain rates [37]. The variations of the elastic modulus versus temperatures have been also shown in comparisons between different studies [34] (Refer to Figure 4).

Table 1: Elastic Modulus for different compositions of SAC solder alloy tested at different strain rates [34].

SAC Solder Alloy	Elastic modulus, E (GPa)	Strain rate (1/s)	Specimen preparation/type	Testing method	References
Sn3.9Ag0.5Cu	50.3	4.2×10^{-5}	machined/cylindrical	Compression	[38, 39]
Sn3.8Ag0.7Cu	45	6.68×10^{-4}	cast/cylindrical	Tension	[40]
	50	1.67×10^{-3}	cast/cylindrical	Tension	[41]
	44.4	5.6×10^{-4}	cast/dog-bone	Tension	[42]
	46	1×10^{-3}	cast/dog-bone	Tension	[43]
	41	1×10^{-3}	cast/dog-bone	Tension	[44]
Sn4.1Ag0.5Cu	43	6.86×10^{-4}	cast/cylindrical	Tension	[40]
Sn3.0Ag0.5Cu	54	4×10^{-3}	machined/cylindrical	Tension	[45]
	37.4	4×10^{-4}	cast/dog-bone	Tension	[46]
Sn3.1Ag0.5Cu	45	6.86×10^{-4}	Cast/cylindrical	Tension	[40]

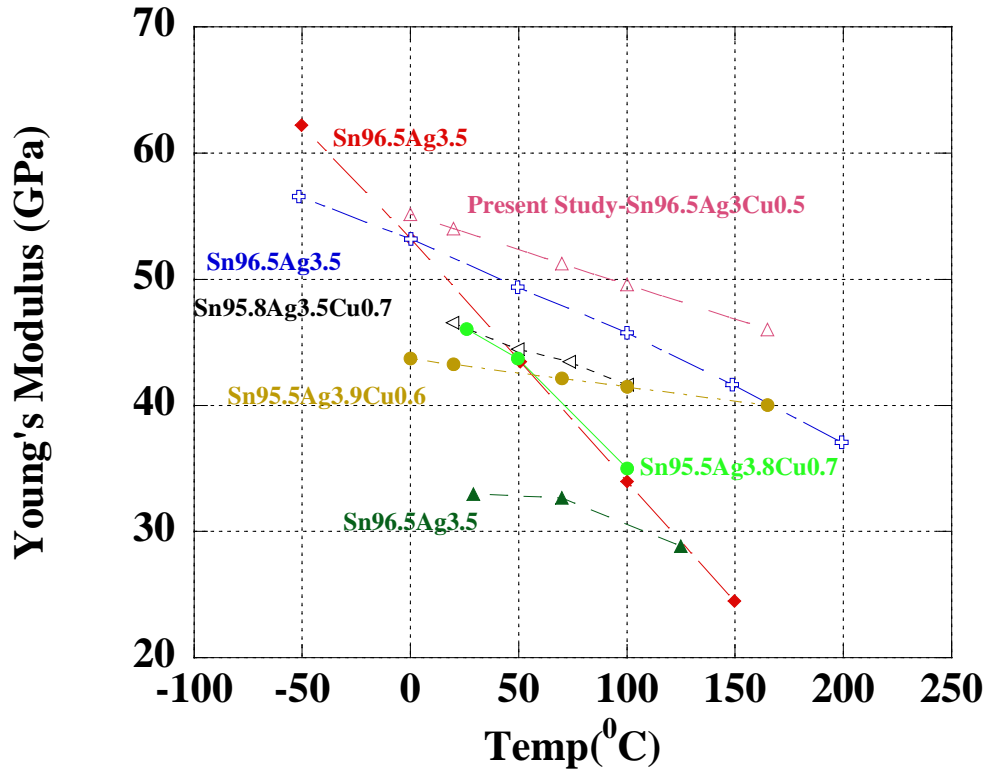


Figure 4: Comparison of the elastic modulus of lead-free solders [34]

2.2.2.2.2 Plastic response

Plastic behaviour of the SAC solder alloy has been reported in many studies by a tri-linear approximation of elastic-plastic behaviour [34, 47]. The approximations were achieved by fitting simulation results to experimental data, and resulted in either five (ϵ_1 , ϵ_2 , σ_1 , σ_2 , σ_3) or six (ϵ_1 , ϵ_2 , ϵ_f , σ_1 , σ_2 , σ_3) parameters, as shown in Figure 5. The ultimate strain (ϵ_f) has been treated as a criterion to determine the failure of a bulk material [47]. In Figure 5, the first line represents the elastic behaviour, the second line describes the initial plasticity and the third one refers to saturated plasticity [36]. These parameters for some leadfree solders at different testing conditions are given in Table 2

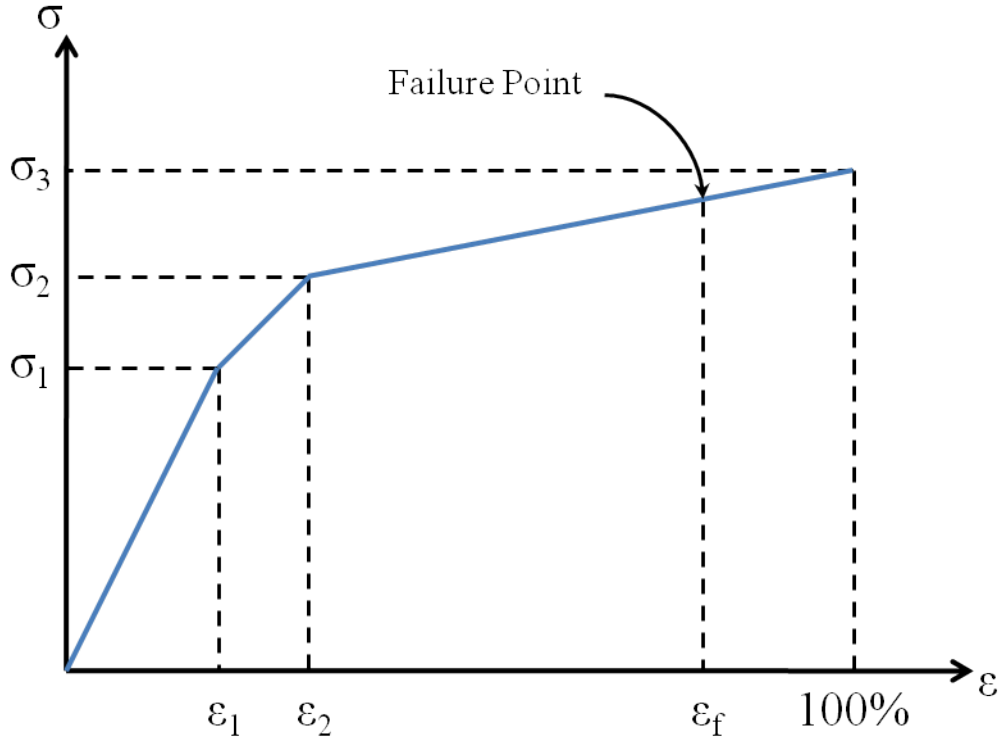


Figure 5: Trilinear elastic-plastic approximation for solder alloy.

There are also studies that have characterized the rate-independent plastic deformation of the leadfree solder alloy by measuring the instantaneous inelastic deformation beyond the yield point [36, 48, 49, 50]. Such plastic behaviour is usually described by a power law relationship such as follows [48]:

$$\varepsilon_{pl} = C_{pl}(\sigma)^m \quad (4)$$

where σ is the stress, ε_{pl} is the plastic strain, C_{pl} and m are the strength coefficient and the hardening exponent, respectively. There is very little plastic data for SAC305 solders reported in the literature. Table 3 refers to the available plastic model parameters for leadfree alloy. The plastic properties of the eutectic Sn3.5Ag solder were studied by Darveaux and Banerji [48]. They found that at low temperatures, Sn3.5Ag experiences a larger plastic deformation as compared with eutectic SnPb solders at the same stress magnitude. At high temperatures Sn3.5Ag solders undergo smaller plastic deformation than those of SnPb solders subjected to

stresses beyond 13 MPa. Stress-strain hysteresis responses of solder joints using complete and incomplete constitutive models have been studied in the literature [33, 34, 36, 48]. Complete models [33] include both the elastoplastic and creep deformations of solder materials, while incomplete models [34] are capable of evaluating elastic and creep deformations disregarding the effect of plastic deformation.

Table 2: Elastic-plastic model of leadfree solder alloy as cast

Leadfree solder alloy	Temp. (K)	ε_1 (%)	ε_2 (%)	ε_f (%)	σ_1 (MPa)	σ_2 (MPa)	σ_3 (MPa)	References
SAC305	298	0.14	0.40	38	55.3	76	2200	[47]
Sn4Ag0.5Cu	278	0.14	0.40	-	57.4	80	2500	[34]
	323	0.14	0.40	-	53.2	72	1900	[34]
Sn3.5Ag	278	0.10	0.40	-	41	64	700	[34]
	323	0.10	0.40	-	38	57.4	400	[34]

Table 3: Plastic model parameters of leadfree solder alloys

Solder	C_{pl}	m	References
Sn3.9Ag0.6Cu	$141.8-0.307T(K)$	$0.651-0.0015T(K)$	[50]
Sn3.5Ag	$286.0-0.579T(K)$	$0.000203T(K)-0.03998$	[49]
Sn3.9Ag0.6Cu	$121.6-0.4T(^{\circ}C)$	$0.29-0.00046T(^{\circ}C)$	[36]
Sn3.5Ag	$1.03 \times 10^{10} \left(\frac{1}{19.3 - 0.07T(^{\circ}C)} \right)^{4.39}$	4.39	[48]

2.2.2.2.3 Creep response

Creep deformation has been known as the most common and important micromechanical inelastic deformation mechanism in solder joints since solder joints are subjected to operating temperatures higher than half melting temperature. A typical constant-load creep deformation curve is composed of primary, secondary, and tertiary creep sections. The secondary creep or the steady state creep at minimum strain rate is generally expressed as the main part of inelastic deformation of the solder joint materials. The behaviour observed on a graph of strain versus time is usually similar to Figure 6.

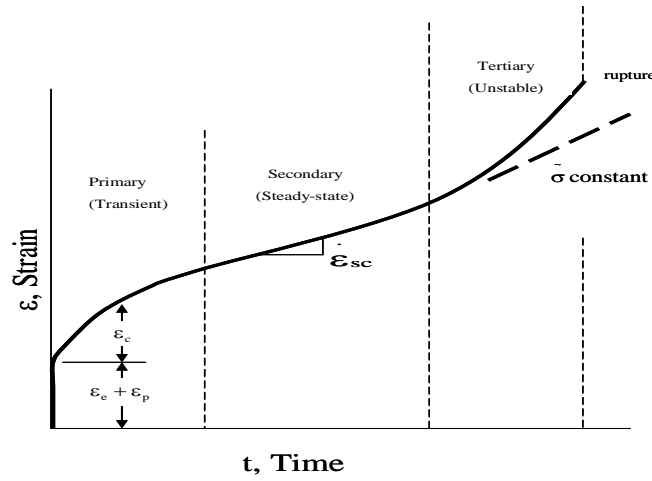


Figure 6: Strain vs. time behaviour during creep under constant load, hence constant engineering stress, and the three stages of creep. [51]

During past years, many researchers have explored the constitutive response of the SnAgCu solder during the creep [34, 35, 36]. It is expected from the physics point of view that the rate of a thermally activated process during the steady state to be governed with Arrhenius equations [51] as generally has been reported in literatures [33] in two consecutive forms:

$$\frac{d\epsilon_{scr}}{dt} = A \left(\frac{\sigma^n}{T} \right) \exp \left(-\frac{Q}{kT} \right) \quad (5)$$

$$\frac{d\epsilon_{scr}}{dt} = A \left[\sinh(\alpha\sigma) \right]^n \exp \left(-\frac{Q}{kT} \right) \quad (6)$$

Where σ is the applied stress, ϵ_{scr} is the strain, k is the universal gas constant ($k = 8.31451 \text{ m}^2 \text{ kg/s}^2 \text{ K mol}$), T is the temperature in Kelvin, Q is an activation energy in J/mol, A and n are model constants. Equation (5) is a simplified form of Dorn's creep law, which includes the temperature dependence of the hardening mechanism. Equation (6) is the Garofalo or hyperbolic sine creep law, which can represent two different creep mechanisms at different stress levels [36,48,52,53,54,55,56]. Wiese et al. [34] described the steady state creep of solders by using the power law (Equation (5)) to formulate the climb-controlled behaviour at low stress magnitudes and the combined glide/climb behaviour at high stress values.

While other studies [33, 35, 36, 48] have presented the creep behaviour of leadfree solder alloy in the form of Equation (6), Schubert et al. [35] defined the high stress region as a power law breakdown region using the hyperbolic sine law. Zhang [36] and Darveaux and Banerji [48] modeled the steady state creep behaviour using hyperbolic sine function postulating power law breakdown at high stress value. Table 4 presents the creep models for several leadfree solder alloys through different studies based on the two presented creep models (Equations (5) and (6)) [57].

Table 4: Creep models of leadfree solder alloys

Constitutive models	Leadfree Solder alloy	Constants				Specimen/testing method	Reference
		A	α (MPa) ⁻¹	n	Q (kJ/mol)		
Equation(5)	Sn3.5Ag	5×10^{-6}	-	11	79.8	Flip-chip/Tensile	[34]
		9.44×10^{-6}	-	6.05	61.1	Bulk/Tensile	[58]
	Sn4.0Ag0.5Cu	2×10^{-21}	-	18	83.1	Flip-chip/Tensile	[34]
Equation(6)	Sn3.5Ag	178.5	0.115	4.75	57.1	Bulk/Tensile	[34]
		23.17	0.059	5.04	41.6	Bulk/Tensile	[58]
		8.18×10^{11}	0.0266	8.67	77.4	Lap-joint, Shear	[58]
		2.46×10^5	0.0913	5.5	72.5	Lap-joint, Shear	[48, 58]
	Sn3.0Ag0.5Cu	2631	0.0453	5.0	52.4	-	[38]
	Sn3.9Ag0.6Cu	0.184	0.221	2.89	62.0	Cast bulk/Tensile	[59]
	Sn3.9Ag0.6Cu	4.41×10^5	0.005	4.2	45	Bulk/Compression	[60]
		3.49×10^4	0.005	4.3	43.13	Bulk/Compression	[39]
		248.4	0.188	3.79	62.3	Lap-joint/Tensile	[36]
	Sn3.8Ag0.7Cu	3.2×10^4	0.037	5.1	65.3	Bulk/Tensile	[42]
		2.78×10^5	0.0245	6.41	54.2	-	[35]
	SAC	7.93×10^5	0.0356	5	67.9	-	[58]

2.2.2.2.3.1 Creep testing procedures

Test specimens used in studies on creep behaviours of leadfree solder alloys can be divided into two groups: bulk, cast specimens and small solder joint either in the form of real joints (flip chip) or lap shear joint type specimens (Refer to Table 4). Lap joint type test specimens were five different solder joint type specimens: double lap shear [48], single lap shear [58], Iosipescu [50], modified single lap shear [49] and flip-chip samples [34].

It was found that in experimental methods of characterizing solder alloys cross-head displacements [34,48, 50] or total displacements [35, 36, 43] of the joints were commonly used along with the recorded far field applied loads which have direct impacts on the accuracy and reproducibility of the test results. The use of displacement and load in computing strain and stress requires uniform distribution of stress and strain within samples as well as rigid body motions of the gripping structures, which otherwise introduces some errors to the measurements. To eliminate the errors and determine the solder deformations out of total displacements, the calibration methods were often proposed [36,50], which also involves some degree of approximations [36]. Hence there is a need for a more accurate strain-stress measurement system to measure local strain and stress at the failure location.

2.3 Prediction models for thermal fatigue of trilayer

Trilayer structures such as flip chip plastic ball grid array (FC-PBGA) packages are bodies made of a large variety of dissimilar materials. Due to the coefficients of thermal expansion (CTE) mismatches between and temperature gradients within the layers, thermally induced interaction becomes a typical type of the loads for the joint layer [6]. For interconnects in microelectronic packages, thermal stresses and strains at the interfaces of adhesive and solder joints are the cause for solder joint fatigue failures, which account of the most common package failures [61].

Hence, thermal fatigue behaviour of leadfree solder interconnections is an important property for fatigue life prediction of the trilayer structures subjected to thermal cycling. Typically, thermal

cycling test failures under accelerated modes are precipitated over 1000 to 10,000 cycles [62]. There are two types of approaches to evaluate the fatigue life under thermal cycling. The total life approach [62], in which cycles to failure can be depicted using Coffin-Manson [63,64] or one its variants is perhaps the best-known and most widely used approach today [65], and the fracture mechanics approach [66], which is based on calculating the accumulated damage caused by crack propagation, and where the fatigue life is the number of cycles to propagate the crack to its critical size [48,65].

The total life approach for leadfree solder alloys can be divided into two major methods based on the damage parameter used to characterize the thermal fatigue process. These two parameters are (a) strain range-based and (b) energy-based [62,65,66].

The strain range-based fatigue approach can be further divided into plastic strain range [67], creep strain range [68] and total strain range [69]. Plastic strain deformation focuses on the time-independent plastic effect, creep strain accounts for the time-dependent effects and total strain range considers the total elastic, plastic and creep strains [65; 70]. The mean life of the solder joints (number of cycles to failure of half of the population, $N_{50\%}$) can be expressed as a function of the inelastic strain range per cycle using the Coffin-Manson equation [66]:

$$N_f = B(\Delta\epsilon_{in})^{-m} \quad (6)$$

where B and m are empirical constants that depend on the type of the solder alloy and $\Delta\epsilon_{in}$ is inelastic (plastic, creep or plastic plus creep) strain range (shear strain range or Von Mises strain range) per cycle. The values for B and m are presented in Table 5 for leadfree solder alloy for plastic and creep strain of shear and Von Mises range.

The Engelmaier model [70] given in Equation (7) relates the total number of cycles to failure to the total shear strain of the midlayer within a trilayer structure using the following equations as:

$$N_f = \frac{1}{2} \left(\frac{\Delta\gamma}{2\varepsilon'_f} \right)^{1/c} \quad (7)$$

$$c = c_0 + c_1 T_{sj} + c_2 \ln \left(1 + \frac{360}{t_{dwell}} \right) \quad (8)$$

$$\Delta\gamma = F \left(\frac{L_d (\alpha_t - \alpha_b) \Delta T}{h} \right) \quad (9)$$

where $\Delta\gamma$ is the total strain range, ε'_f is the fatigue ductility coefficient and c is the variable exponent, which is a function of T_{sj} (medium cyclic temperature) and t_{dwell} (the dwell time at the maximum temperature); c_0 , c_1 and c_2 are constants presented in Table 6 for SAC leadfree alloy. L_d in Equation (9) is the distance to the neutral point over which the expansion due to thermal cycling occurs, α_t and α_b are the coefficients of thermal expansion of the top layer and bottom layer in trilayer structure h is the effective height of the joint, F is a model calibration constant and ΔT is the temperature range of thermal cycling (Refer to Figure 7).

Table 5: Parameters for leadfree solder for plastic and creep strain range of shear and Von Mises model [66].

Strain range type	Shear		Von Mises	
	B	m	B	m
Plastic	14.35	0.5066	1.7857	0.8063
Creep	2.0×10^{-5}	2.7655	0.0002	2.425

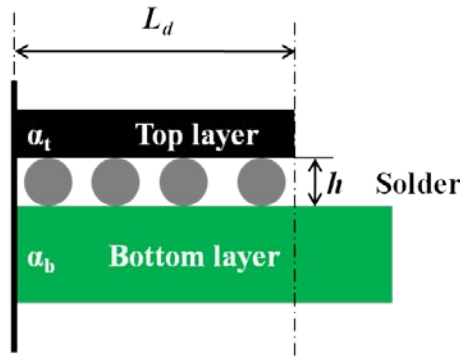


Figure 7: Schematic of trilayer structure with geometries related to Engelmaier model [70].

Table 6: Engelmaier fitted model parameters [69]

	c_0	c_1	c_2	\mathcal{E}'_f
SAC	-0.347	-1.74×10^{-3}	7.83×10^{-3}	3.47

The energy-based fatigue models include both stress and strain (hysteresis energy) information. The total number of cycles to failure, N_f is depicted as being dependent on the inelastic (plastic or creep) strain energy density per cycle. A simple form of the energy-based fatigue models used to predict fatigue failure based on hysteresis energy or volume-weighted average inelastic (plastic or creep) work density [62,66] is presented as follows:

$$N_f = w_0 (\Delta w_{in})^{-k} \quad (10)$$

where N_f is the mean cycles to failure, Δw_{in} is the total strain energy, w_0 and k are fatigue coefficients. These coefficients are presented in Table 7 for leadfree solder alloy for plastic and creep strain energy density.

Table 7: Parameters for leadfree solder alloy for plastic and creep strain energy density model [66].

Strain energy density type	w_0	k
Plastic	159.70	0.5473
Creep	12.251	2.1937

On the other hand the crack initiation and propagation approach predicts the fatigue life with a pre-existing crack. The fatigue life is the number of cycles to propagate this crack to its critical size. Darveaux [71] used strain energy to predict crack initiation and crack growth following the equations given as follows:

$$N_0 = k_1 (\Delta w_{in})^{k_2} \quad (11)$$

$$da/dN = k_3 (\Delta w_{in})^{k_4} \quad (12)$$

where Δw_{in} is strain energy, k_1 , k_2 , k_3 and k_4 are material constants and are defined based on the correlation existing between the measured cycles to crack initiation and the rate of propagation to the calculated strain energy density in the solder joint [66, 71]. The material constants for SAC solder alloy have been reported to be about $k_1 = 47.6$, $k_2 = 1$, $k_3 = 4.2 \times 10^{-5}$ and $k_4 = 1.76$ [66]. The predicted characteristic life ($N_{50\%}$) is finally obtained using the following relation:

$$N_{50\%} = N_0 + a \left(da/dN \right) \quad (13)$$

where a is the solder joint length.

The results of the comparison between experimental life (characteristic life ($N_{50\%}$)) and the predicted life using the presented strain based and energy based fatigue models for SAC solder alloy within trilayer structures with different designs are described below.

In a study by Michael Osterman and Michael Pecht [69], it was found that using the Coffin-Manson fatigue life relationship with a strain range-based damage parameter, the predicted fatigue life of different structures with SAC solder alloy falls within a factor of 4.71~(-1.18), as compared with the experimental fatigue life data. Qi [66] reviewed a number of different methods for the fatigue life prediction of SAC solder alloy under (0-100°C) temperature condition within the same structure and found a factor ranging from about 1.11~ (-1.20) for applying plastic strain range, 1.03~1.07 for creep strain range, 1.19~1.353 for plastic Von Mises strain range and about 1.04 for creep Von Mises strain range to the Coffin-Manson relationship.

By employing inelastic strain energy density with the Coffin-Manson relationship, Qi [66] found factors ranging from 1.2~1.6 for plastic and factors ranging from 1.06~1.22 for creep strain

energy density accumulation. Within energy based fatigue life prediction methods, modified Darveaux fatigue mode was applied to SAC solder joint [66] and found factors ranging from about 1.19~1.32. The results demonstrate that using strain energy density as the damage parameter provides a better life prediction in comparison with the strain range-based damage parameter. It is also evident that using the creep strain energy density outperforms the plastic strain energy density.

However, performing an in-depth material characterization of SnAgCu alloy along with the interfacial metallurgy has shown that damage propagation at SnAgCu solder joints at the interface with the neighbouring materials are reported to be the dominant failure mechanism [72, 73]. This suggests that damage localizes at the bonding interfaces with a well distinguished behaviour that can be only referred to as biaxial state of stress under monotonous shear and tension [72]. The highest values of damage also appear in the corners of the solder joints, where both shear and tensile strains are maximum [73]. The phenomenon corresponds to the typical failure positions observed in flip chip plastic ball grid array packages. Hence there is a need for a damage model to predict the life based on the combination of shear and tensile strain energy density.

2.4 Chapter summary

The literature review suggests that there is a need for closed-form solutions to predict the warpage and interfacial stresses of trilayer structures under thermal loads without involving high degrees of approximation and losing generality. Besides, few experimental approaches have been reported for the validation of the numerical modeling results, as well as the analytical solutions.

In regards to characterizing the joint materials, an accurate strain-stress measurement approach is required with the aim to measure local strain and stress at the failure locations. A more accurate material constitutive model further leads to a finer fatigue life prediction of the materials.

In order to advance the understanding of fatigue damage of solder materials, a novel approach is necessary to consider the localized damage of the joint materials at the dominant corners where the damage most likely initiates. With this consideration, the current research implemented localized strain measurements systems to characterize the solder alloy to quantify the stress and strain evolving at the onset of failure. Next, the theory of the strain energy-based fatigue model extended to cover the biaxial state of stress at the critical joints of the joint material (solder joint) and in the critical corner of the joint located on the critical plane (the most damaging plane), using a damage parameter which is based on shear and tensile stress and strain components acting on the critical plane.

CHAPTER THREE

Analytical Methods for Testing of Reliability and Durability of Trilayer Structure

This chapter presents 1) the interfacial peel and shear stresses and warpage models of the trilayer structure under thermal cycling, 2) the inverse method in characterizing the constitutive behaviour of the trilayer constituents, 3) the analytical and experimental methods in characterizing the viscoelastoplastic joint alloys as the primary material employed in the midlayer (bonding layer) within trilayer structure and 4) the method for predicting the characteristic fatigue life of the trilayer structures.

3.1 Interfacial modeling of trilayer structures under thermal loading

Figure 8 schematically shows three layers of a warped trilayer structure with three distinct materials as (a) top layer (die), (b) midlayer (adhesive layer) and (c) bottom layer (substrate). These materials with different coefficients of thermal expansion (CTE) and stiffness are joined together to form the trilayer. In analysis of deformation of a uniformly heated trilayer structure, the layers are considered homogenous and isotropic with small deflections so the engineering theory of bending plates is applicable. The adhesive layer is considered compliant. The bonded layers are under flexural load as the assembly is exposed uniform heat, and thus the assembly shape changes and the internal stresses/forces develop [5,16].

Two adherend layers expand unequally under change of the temperature due to the difference between their thermal expansion coefficients. This phenomenon causes the layers to bend and elongate and to develop internal forces and moments that are in equilibrium since there are no

external forces acting on layers [6,9,10,13,26,74,75]. The natural tendency of the whole structure to bend together further develops stresses near the end at the interfaces due to the differences in flexural rigidity of the layers [1,75,76].

The stresses at the interfacial level can be determined implying compatibility of axial and transverse displacements of upper and lower interfaces of the adhesive layer with adherends. The behaviour of the interfacial layer has been closely investigated in earlier studies of foundation analysis [17, 18,19]. This study puts forward the outcome of the foundation deformation analysis to follow the continuity at the interfaces and compatibility of vertical and transverse displacements.

The following closed-form solution was derived based on the mechanics of materials and non-local foundation analysis. Uniform temperature distribution and spherical bending shape were assumed, and the curvature was considered constant through the layer thickness. The small slope change was also assumed, which implies that the variation of the vertical deformation within each layer is constant. Deflection and longitudinal displacements of the contact layers were modeled to be dominantly subjected to the higher degree of the derivative of the forces. Based on the foundation of the spring type layers, however, there is no need for a higher order of derivation for the vertical deformation of the layers [17].

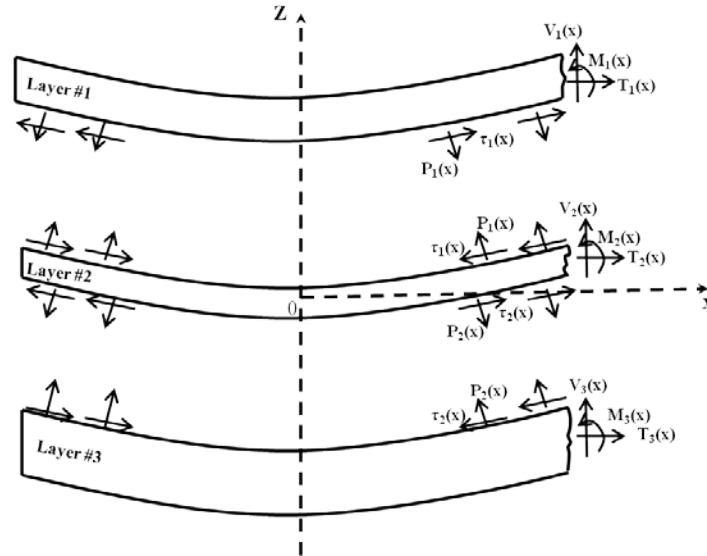


Figure 8: Free-body diagram, Shear and peel stresses along the interface, axial and shear forces and bending moments across the layer thickness.

The interfacial compliances for the plane-strain and plane-stress conditions have been introduced [6,13,26]. These compliances have been obtained for both plane strain and plane stress conditions using Ribière solution for a long-and-narrow strip [7,16,76].

Based on the theory of beams, the cross section of the bar remains rectangular during bending, so there is only rotation with respect to the neutral axis. The flexure formula is developed on the assumption of pure bending. This is done, however, to eliminate the complicating effects of shear force in the development.

From the study of pure bending, there is a relation between the radius of curvature and the applied bending moment. This relation was achieved after combining the two definitions of curvature resulting from analytical geometry [77] and mechanics of materials [76] (Equations (14) and (15), respectively) for both plane stress and plane strain conditions as follows:

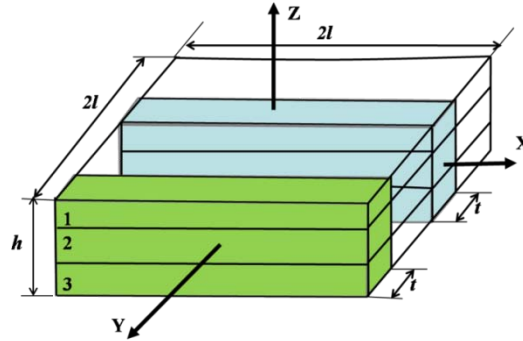


Figure 9: Trilayer structure considered as 2D elemental strip under plane-stress (edge cross-section) and plane-strain (mid-cross section) with the width of unity ($t=1$), thickness as h and the length of $2l$ in the plane of XZ [9].

A classic expression for curvature under bending moment is given as:

$$\frac{I}{\rho(x)} = - \frac{\frac{d^2 w}{dx^2}}{\left[1 + \left(\frac{dw}{dx} \right)^2 \right]^{3/2}} \quad (14)$$

where ρ is the radius of curvature and w is the vertical deflection. If the slope of the curve describing the loaded beam at all points is small relative to unity, one can set the denominator of the expression (Equation (14)) for curvature equal to one. As a result, one obtains the approximate relation as follows:

$$\frac{1}{\rho(x)} = -\frac{d^2 w}{dx^2} \quad (15)$$

Both plane-strain and plane-stress conditions have been considered in the analysis (Refer to Figure 9). The unit elongation ε_x of a fibre at X-direction at a distance z from midplane for a single beam at mid-cross section layer is defined as:

$$\varepsilon_x = -z(\rho(x))^{-1} \quad (16)$$

On the other hand the strain along X-direction in terms of stress and Poisson's ratio for plane-strain condition with stress in Z-direction being negligible is expressed as:

$$\varepsilon_x = \frac{\sigma_x}{E} - \frac{\nu \sigma_y}{E} \quad (17)$$

For plain-strain condition, strain in Y-direction is:

$$\varepsilon_y = \frac{\sigma_y}{E} - \frac{\nu \sigma_x}{E} = 0 \quad (18)$$

hence

$$\sigma_y = \nu \sigma_x \quad (19)$$

Substituting Equation (19) into Equation (17):

$$\varepsilon_x = \frac{(1 - \nu^2) \sigma_x}{E} \quad (20)$$

Solving Equation (20) for σ_x and substituting for ε_x from Equation (16), yields:

$$\sigma_x = \frac{E\varepsilon_x}{1-\nu^2} = -\frac{Ez}{1-\nu^2}(\rho(x))^{-1} \quad (21)$$

The bending moment at x is defined per unit width as:

$$M(x) = \int_{-h/2}^{h/2} \sigma_x z dz = -\int_{-h/2}^{h/2} \frac{Ez^2}{1-\nu^2} (\rho(x))^{-1} dz = -\frac{Eh^3}{12(1-\nu^2)} (\rho(x))^{-1} = -D(\rho(x))^{-1} \quad (22)$$

where under plane-strain condition

$$D = \frac{Eh^3}{12(1-\nu^2)} \quad (23)$$

and is referred to as the flexural rigidity for plane-strain condition within the plane of XZ and having an elongation of zero in the Y-direction.

For a plane-stress condition with stress in the Z-direction being negligible, strain along the X-direction in terms of stress is expressed as:

$$\varepsilon_x = \frac{\sigma_x}{E} \quad (24)$$

Once again substituting for ε_x from Equation (16) yields:

$$\sigma_x = E\varepsilon_x = -Ez(\rho(x))^{-1} \quad (25)$$

The bending moment at x is reached as:

$$M(x) = \int_{-h/2}^{h/2} \sigma_x z dz = - \int_{-h/2}^{h/2} E z^2 (\rho(x))^{-1} dz = - \frac{Eh^3}{12} (\rho(x))^{-1} = -D(\rho(x))^{-1} \quad (26)$$

where under plane-stress condition

$$D = \frac{Eh^3}{12} \quad (27)$$

and is referred to as flexural rigidity for plane-stress condition within the plane of XZ and having a stress of zero in Y-direction. As the derivation implies, the beam equation in this form only holds for beams that at all points have small slope angles. This restriction can be removed by avoiding the approximation and using the full expression for curvature, but this is not necessary for many applications that result in only small changes in the shape of the beam.

Consequently, based on the earlier Equation (15) one finds the following relation between the moment and the vertical deflection for both plane-stress and plane-strain conditions as:

$$M = -D \frac{d^2 w}{dx^2} \quad (28)$$

In analysis, the sense of arrows is chosen such that the longitudinal forces and moments are positive if the product of $\Delta\alpha \times \Delta T$ is positive. The transverse forces are positive if these forces cause tensile stresses in the beams. Equilibrium of forces and moments per unit width lead to:

1) Equilibrium of horizontal forces:

$$T_i(x) = \int_{-l}^x \tau_i(\zeta) d\zeta \quad i=1, 2, 3 \quad (29)$$

It is assumed that T_1 and T_3 , forces in the horizontal direction, (Refer to Figure 8) are equal; hence, T_2 vanishes [2, 3, 7, and 17].

2) Equilibrium of vertical forces:

$$V_i(x) = - \int_{-l}^x p_i(\zeta) d\zeta \quad i=1, 2, 3 \quad (30)$$

It is also assumed that V_1 and V_3 , forces in the vertical direction, (Refer to Figure 8) are equal; hence, V_2 vanishes [7].

3) Equilibrium of bending moments:

Based on the earlier assumption in regards to vertical and horizontal forces within each layer, the bending moments of layer-1 and layer-3 are as follows for layer-1 and layer-3 (No bending moment for layer-2):

$$M_1(x) = - \int_{-l}^x V(\zeta) d\zeta + \frac{h_1}{2} T(x) \quad (31)$$

$$M_3(x) = \int_{-l}^x V(\zeta) d\zeta + \frac{h_3}{2} T(x) \quad (32)$$

where

$$M_i(x) = - \frac{D_i}{\rho_i(x)} \quad i=1, 3 \quad (33)$$

Next displacements of the layers at each interface have been derived respective to the origin. These displacements are mainly due to the thermal expansion, the resultant longitudinal force at the centre of the layer and the bending of the layer with respect to its middle plane.

1) Longitudinal displacements

$$u_l(x) = x\alpha_l^* \Delta T + \lambda_l \int_0^x T(\zeta) d\zeta + \frac{h_l}{2} \int_0^x \frac{d\zeta}{\rho_l(\zeta)} - \mu_l(\tau(x) - \beta_l \tau''(x)) \quad (34)$$

$$u_3(x) = x\alpha_3^* \Delta T - \lambda_3 \int_0^x T(\zeta) d\zeta - \frac{h_3}{2} \int_0^x \frac{d\zeta}{\rho_3(\zeta)} + \mu_3 (\tau(x) - \beta_3 \tau''(x)) \quad (35)$$

where $\lambda_i = \frac{(1+\nu_i)(1-2\nu_i)}{(1-\nu_i)E_i h_i}$ (i=1, 3) (axial compliance) [6,7] and $\alpha_i^* = \alpha_i(1+\nu_i)$ (CTE of the layers) for the plane-strain condition and $\lambda_i = \frac{(1-\nu_i^2)}{E_i h_i}$ (i=1, 3) [6,7] and $\alpha_i^* = \alpha_i$ for the plane-stress condition. Also $\mu_i = \frac{h_i}{3G_i}$ (i=1, 3) (shear compliance) is the same for both plane-stress and plane-strain [6, 7], and best results are found to be based on $\beta_i = \frac{h_i^2}{3}$ (i=1, 3) [17] as well as ΔT is temperature change.

2) Vertical deflection

The deflections of the adherends due to the transverse deformation and flexural deflection are presented as follows:

$$w_1(x) = \gamma_1 \int_{-l}^x V(\zeta) d\zeta + \eta_1 p(x) + \int_0^x \int_0^x \frac{d\zeta}{\rho_1(\zeta)} \quad (36)$$

$$w_3(x) = \gamma_3 \int_{-l}^x V(\zeta) d\zeta - \eta_3 p(x) + \int_0^x \int_0^x \frac{d\zeta}{\rho_3(\zeta)} \quad (37)$$

where $\gamma_i = \frac{1}{G_i h_i}$ (i=1,3) (transversal shear compliance) is the same for both the plane-stress and

the plane-strain condition [6, 7], $\eta_i = \frac{(1-2\nu_i)(1+\nu_i)}{3(1-\nu_i)} \frac{h_i}{E_i}$ (i=1,3) (through thickness compliance) for

plane strain and $\eta_i = \frac{(1-\nu_i^2)}{3} \frac{h_i}{E_i}$ (i=1,3) for plane-stress.

3) Compatibility of displacements

$$u_3(x) - u_1(x) = \mu_2(\tau(x) - \beta_2 \tau''(x)) \quad (38)$$

$$w_3(x) - w_1(x) = \eta_2 p(x) \quad (39)$$

where $\mu_2 = \frac{h_2}{3G_2}$ is same for plane-stress and plane-strain, $\eta_2 = \frac{(1-2\nu_2)(1+\nu_2)}{3(1-\nu_2)} \frac{h_2}{E_2}$ for plane-strain; $\eta_2 = \frac{(1-\nu_2^2)}{3} \frac{h_2}{E_2}$ for plane-stress and $\beta_2 = \frac{h_2^2}{3}$.

For the final solutions of the stresses proper boundary conditions are employed. For region $-l \leq x \leq l$ it is evident that the shear stresses that also have antisymmetric nature will vanish at each end. The longitudinal force is zero at the ends. The peel stress has a symmetric distribution with respect to the plane of symmetry perpendicular to the layers and is also self-equilibrating over the region. There are transverse forces due to the interlaminar peel stresses acting at the mid-plane of adherends that are zero at the free ends. Bending moments due to both the shear and peel stresses are also zero at both ends [19].

3.1.1 Interfacial shear stress

Compatibility of longitudinal displacements and substituting the Equations (34) and (35) into Equation (38) leads to:

$$\begin{aligned} & -x\alpha_1^* \Delta T - \lambda_1 \int_0^x T(\zeta) d\zeta - \frac{h_1}{2} \int_0^x \frac{d\zeta}{\rho_1(\zeta)} + x\alpha_3^* \Delta T - \lambda_3 \int_0^x T(\zeta) d\zeta - \frac{h_3}{2} \int_0^x \frac{d\zeta}{\rho_3(\zeta)} \\ & + \mu_1(\tau(x) - \beta_1 \tau''(x)) + \mu_3(\tau(x) - \beta_3 \tau''(x)) - \mu_2(\tau(x) - \beta_2 \tau''(x)) = 0 \end{aligned} \quad (40)$$

Considering the assumption of small deflections and assuming that the transverse stresses are the same at upper and lower interfaces, the variation of the vertical deformations for both upper and lower layers are counted equal, hence:

$$w'_l(x) = w'_3(x) \quad (41)$$

yields:

$$\begin{aligned} & -x\alpha_l^* \Delta T - \lambda_l \int_0^x T(\zeta) d\zeta - \left(\frac{h_l}{2} + \frac{h_3}{2} \right) w'(x) + x\alpha_3^* \Delta T - \lambda_3 \int_0^x T(\zeta) d\zeta + \\ & \mu_l (\tau(x) - \beta_l \tau''(x)) + \mu_3 (\tau(x) - \beta_3 \tau''(x)) - \mu_2 (\tau(x) - \beta_2 \tau''(x)) = 0 \end{aligned} \quad (42)$$

By differentiating Equation (42) one finds:

$$\begin{aligned} & -\alpha_l^* \Delta T - \lambda_l \int_0^x \tau(\zeta) d\zeta - \left(\frac{h_l}{2} + \frac{h_3}{2} \right) w''(x) + \alpha_3^* \Delta T - \lambda_3 \int_0^x \tau(\zeta) d\zeta + \\ & \mu_l (\tau'(x) - \beta_l \tau'''(x)) + \mu_3 (\tau'(x) - \beta_3 \tau'''(x)) - \mu_2 (\tau'(x) - \beta_2 \tau'''(x)) = 0 \end{aligned} \quad (43)$$

Differentiating Equation (43) leads to a 4th order equation for shear stress which further leads to determination of shear stress. On the other hand, from equilibrium of bending moments Equations (31-33) it is revealed that:

$$w''(x) = w'_l(x) = w''_3(x) = \frac{I}{D_l} \int_{-l}^x V(\zeta) d\zeta - \frac{h_l}{2D_l} T(x) = \frac{-I}{D_3} \int_{-l}^x V(\zeta) d\zeta - \frac{h_3}{2D_3} T(x) \quad (44)$$

Equation (44) further results in:

$$(D_l + D_3) w'''(x) = - \left(\frac{h_l}{2} + \frac{h_3}{2} \right) \tau(x) \quad (45)$$

By using Equation (45) and substituting for the third order of deflection in once differentiated Equation (43) yields:

$$\left[(\lambda_l + \lambda_3) + \frac{I}{(D_l + D_3)} \left(\frac{h_l}{2} + \frac{h_3}{2} \right)^2 \right] \tau(x) - (\mu_l - \mu_2 + \mu_3) \tau''(x) + (\mu_l \beta_l - \mu_2 \beta_2 + \mu_3 \beta_3) \tau'''(x) = 0 \quad (46)$$

It is realized after differentiating Equation (43) some of the terms disappear. This equation can be written with new notation as:

$$\tau(x) - F\tau''(x) + B\tau'''(x) = 0 \quad (47)$$

where

$$F = \frac{\mu_1 - \mu_2 + \mu_3}{\left[(\lambda_1 + \lambda_3) + \frac{1}{(D_1 + D_3)} \left(\frac{h_1}{2} + \frac{h_3}{2} \right)^2 \right]} \quad (48)$$

and

$$B = \frac{\mu_1\beta_1 - \mu_2\beta_2 + \mu_3\beta_3}{\left[(\lambda_1 + \lambda_3) + \frac{1}{(D_1 + D_3)} \left(\frac{h_1}{2} + \frac{h_3}{2} \right)^2 \right]} \quad (49)$$

Next presents the solutions for shear stress for different cases after using the proper boundary conditions (presented in Appendix 1).

Case-I ($F^2 - 4B < 0$):

Solution for shear stress, after using the proper boundary conditions (presented in Appendix 1), addresses many trilayer structures with thin and compliant adhesive layer represented as:

$$\tau(x) = C_{11} \sinh(px) \cos(qx) + C_{22} \cosh(px) \sin(qx) \quad (50)$$

where $p = \frac{1}{2\sqrt{B}} \sqrt{\sqrt{4B} + F}$, $q = \frac{1}{2\sqrt{B}} \sqrt{\sqrt{4B} - F}$, $C_{11} = \frac{\Delta\alpha\Delta T \cosh(pl) \sin(ql)}{\Sigma}$ and

$$C_{22} = \frac{-\Delta\alpha\Delta T \sinh(pl) \cos(ql)}{\Sigma} \text{ where } \Sigma = p\sqrt{B} \cos(ql) \sin(ql) + q\sqrt{B} \cosh(pl) \sinh(pl).$$

Case-II ($F^2 - 4B > 0$):

The solution of shear stress is given:

$$\tau(x) = C_{11}(\sinh \Gamma x) + C_{22}(\sinh \Omega x) \quad (51)$$

$$\text{where, } \Gamma = \frac{I}{\sqrt{2B}} \sqrt{F + \sqrt{F^2 - 4B}}, \Omega = \frac{I}{\sqrt{2B}} \times \sqrt{F - \sqrt{F^2 - 4B}}, C_{11} = \frac{\Delta\alpha\Delta T \sinh(\Omega l)}{\Sigma I} \text{ and}$$

$$C_{22} = \frac{-\Delta\alpha\Delta T \sinh(\Gamma l)}{\Sigma I} \text{ where}$$

$$\Sigma I = \Gamma \left\{ \left(\frac{F}{2} \left(1 - \sqrt{1 - 4 \frac{B}{F^2}} \right) \right) \right\} \left(\cosh \Gamma l \sinh(\Omega l) \right) - \Omega \left\{ \left(\frac{F}{2} \left(1 + \sqrt{1 - 4 \frac{B}{F^2}} \right) \right) \right\} \left(\cosh \Gamma l \sinh(\Omega l) \right).$$

The complete solution to Equation (47) has been presented in Appendix 1.

3.1.2 Interfacial peel stress

The equation related to peel stress was determined by referring to vertical deflection compatibility presented in Equation (39) and substituting for the deflection equivalents from Equations (36) and (37) as:

$$-\gamma_1 \int_{-l}^x V(\zeta) d\zeta - \int_0^x \int_0^x \frac{d\zeta}{\rho_1(\zeta)} + \gamma_3 \int_{-l}^x V(\zeta) d\zeta + \int_0^x \int_0^x \frac{d\zeta}{\rho_3(\zeta)} = \eta p(x) \quad (52)$$

where $\eta = \eta_1 + \eta_2 + \eta_3$.

After differentiating Equation (52) twice and substituting for transverse forces using Equation (30), it leads to:

$$\gamma_1 p(x) - \frac{I}{\rho_1(x)} - \gamma_3 p(x) + \frac{I}{\rho_3(x)} = \eta p''(x) \quad (53)$$

where

$$\frac{I}{\rho_1(x)} = \frac{I}{D_1} \int_{-l}^x V(\zeta) d\zeta - \frac{h_1}{2D_1} T(x) \quad (54)$$

and

$$\frac{I}{\rho_3(x)} = \frac{-I}{D_3} \int_{-l}^x V(\zeta) d\zeta - \frac{h_3}{2D_3} T(x) \quad (55)$$

Implementing Equations (54) and (55) into Equation (53) results in:

$$\gamma_1 p(x) + \frac{h_1}{2D_1} T(x) - \frac{I}{D_1} \int_{-l}^x V(\zeta) d\zeta - \frac{h_3}{2D_3} T(x) - \frac{I}{D_3} \int_{-l}^x V(\zeta) d\zeta - \gamma_3 p(x) = \eta p''(x) \quad (56)$$

Differentiating Equation (56) gives:

$$\gamma_1 p'(x) + \frac{h_1}{2D_1} \tau(x) - \frac{I}{D_1} V(x) - \frac{h_3}{2D_3} \tau(x) - \frac{I}{D_3} V(x) - \gamma_3 p'(x) = \eta p'''(x) \quad (57)$$

Equation (57) is re-differentiated to be arranged in a format having peel stress as a governing function:

$$-(\gamma_1 - \gamma_3) p''(x) - \left[\frac{h_1}{2D_1} - \frac{h_3}{2D_3} \right] \tau'(x) + \left[\frac{I}{D_3} + \frac{I}{D_1} \right] p(x) + \eta p^{IV}(x) = 0 \quad (58)$$

Equation (58) is a 4th order nonhomogeneous linear differential equation and can be rewritten as:

$$p(x) - Ep''(x) + Ap^{IV}(x) = G\tau'(x) \quad (59)$$

where $E = \frac{(\gamma_3 - \gamma_1)}{\left[\frac{1}{D_3} + \frac{1}{D_1}\right]}$, $A = \frac{\eta}{\left[\frac{1}{D_3} + \frac{1}{D_1}\right]}$ and $G = \frac{\left[\frac{h_3}{2D_3} - \frac{h_1}{2D_1}\right]}{\left[\frac{1}{D_3} + \frac{1}{D_1}\right]}$.

Next presents the solutions for peel stress for different cases after using the proper boundary conditions (presented in Appendix 1).

The solution for peel stress for Case-I of shear stress ($F^2 - 4B < 0$) and Case-I of peel stress ($E^2 - 4A < 0$) is as follows:

$$p(x) = C_I \cosh(\Phi x) \cos(\Pi x) + C_{II} \sinh(\Phi x) \sin(\Pi x) \quad (60)$$

where

$$\Phi = \frac{1}{2\sqrt{A}} \sqrt{\sqrt{4A} + E}$$

$$\Pi = \frac{1}{2\sqrt{A}} \sqrt{\sqrt{4A} - E}$$

and

$$C_I = - \frac{\left(\frac{h_1}{2D_1} - \frac{h_3}{2D_3} \right) \frac{\left[\frac{\Delta \alpha \Delta T \cosh(pl) \sin(ql)}{\Sigma} \sinh(pl) \cos(ql) - \frac{\Delta \alpha \Delta T \sinh(pl) \cos(ql)}{\Sigma} \cosh(pl) \sin(ql) \right]}{\eta}}{\left[\begin{array}{l} \frac{(\gamma_1 - \gamma_3)}{\eta} \cosh(\Phi l) \cos(\Pi l) \\ - (\Phi^2 - \Pi^2) \cosh(\Phi l) \cos(\Pi l) \\ + 2\Phi \Pi \sinh(\Phi l) \sin(\Pi l) \end{array} \right] - \left[\begin{array}{l} \frac{(\gamma_1 - \gamma_3)}{\eta} \sinh(\Phi l) \sin(\Pi l) \\ - (\Phi^2 - \Pi^2) \sinh(\Phi l) \sin(\Pi l) \\ - 2\Phi \Pi \cosh(\Phi l) \cos(\Pi l) \end{array} \right]} \left[\begin{array}{l} \frac{(\gamma_1 - \gamma_3)}{\eta} (\Phi \sinh(\Phi l) \cos(\Pi l) - \Pi \cosh(\Phi l) \sin(\Pi l)) \\ - (\Phi^2 - \Pi^2) \Phi \sinh(\Phi l) \cos(\Pi l) \\ + (\Phi^2 - \Pi^2) \Pi \cosh(\Phi l) \sin(\Pi l) \\ + 2\Phi^2 \Pi \cosh(\Phi l) \sin(\Pi l) \\ + 2\Phi \Pi^2 \sinh(\Phi l) \cos(\Pi l) \end{array} \right] \left[\begin{array}{l} \frac{(\gamma_1 - \gamma_3)}{\eta} (\Phi \cosh(\Phi l) \sin(\Pi l) + \Pi \sinh(\Phi l) \cos(\Pi l)) \\ + (\Phi^2 - \Pi^2) \Phi \cosh(\Phi l) \sin(\Pi l) \\ + (\Phi^2 - \Pi^2) \Pi \sinh(\Phi l) \cos(\Pi l) \\ + 2\Phi^2 \Pi \sinh(\Phi l) \cos(\Pi l) \\ - 2\Phi \Pi^2 \cosh(\Phi l) \sin(\Pi l) \end{array} \right]$$

$$C_{II} = \frac{\left(\frac{h_1}{2D_1} - \frac{h_3}{2D_3} \right) \left[\frac{\Delta\alpha\Delta T \cosh(pl)\sin(ql)}{\Sigma} \sinh(pl)\cos(ql) + \frac{-\Delta\alpha\Delta T \sinh(pl)\cos(ql)}{\Sigma} \cosh(pl)\sin(ql) \right] * \text{Cons tan } t1}{\text{Cons tan } t2 * \text{Cons tan } t3 - \text{Cons tan } t1 * \text{Cons tan } t4}$$

where

$$\text{Constant } t1 = \begin{bmatrix} \frac{(\gamma_1 - \gamma_3)}{\eta} \cosh(\Phi l) \cos(\Pi l) \\ -(\Phi^2 - \Pi^2) \cosh(\Phi l) \cos(\Pi l) \\ +2\Phi\Pi \sinh(\Phi l) \sin(\Pi l) \end{bmatrix} \quad \text{Constant } t2 = \begin{bmatrix} \frac{(\gamma_1 - \gamma_3)}{\eta} \sinh(\Phi l) \sin(\Pi l) \\ -(\Phi^2 - \Pi^2) \sinh(\Phi l) \sin(\Pi l) \\ -2\Phi\Pi \cosh(\Phi l) \cos(\Pi l) \end{bmatrix}$$

$$\text{Constant } t3 = \begin{bmatrix} \frac{(\gamma_1 - \gamma_3)}{\eta} \left(\Phi \sinh(\Phi l) \cos(\Pi l) \right) \\ -\Pi \cosh(\Phi l) \sin(\Pi l) \\ -(\Phi^2 - \Pi^2) \Phi \sinh(\Phi l) \cos(\Pi l) \\ +(\Phi^2 - \Pi^2) \Pi \cosh(\Phi l) \sin(\Pi l) \\ +2\Phi^2 \Pi \cosh(\Phi l) \sin(\Pi l) \\ +2\Phi \Pi^2 \sinh(\Phi l) \cos(\Pi l) \end{bmatrix} \quad \text{Constant } t4 = \begin{bmatrix} \frac{(\gamma_1 - \gamma_3)}{\eta} \left(\Phi \cosh(\Phi l) \sin(\Pi l) \right) \\ +\Pi \sinh(\Phi l) \cos(\Pi l) \\ +(\Phi^2 - \Pi^2) \Phi \cosh(\Phi l) \sin(\Pi l) \\ +(\Phi^2 - \Pi^2) \Pi \sinh(\Phi l) \cos(\Pi l) \\ +2\Phi^2 \Pi \sinh(\Phi l) \cos(\Pi l) \\ -2\Phi \Pi^2 \cosh(\Phi l) \sin(\Pi l) \end{bmatrix}$$

The solution for the peel stress in Case-II of shear stress ($F^2 - 4B > 0$) and Case-I of peel stress ($E^2 - 4A < 0$) follows Equation (59) with new sets of coefficients (C_I , C_{II}), where:

$$C_I = - \frac{\left(\frac{h_1}{2D_1} - \frac{h_3}{2D_3} \right) \left[\frac{\Delta\alpha\Delta T \sinh(\Omega l)}{\Sigma l} (\sinh \Gamma l) \right]}{\eta \left[- \frac{\Delta\alpha\Delta T \sinh(\Gamma l)}{\Sigma l} (\sinh \Omega l) \right]}$$

$$\left[\begin{array}{l} \left(\frac{\gamma_1 - \gamma_3}{\eta} \right) (\Phi \sinh(\Phi l) \cos(\Pi l) - \Pi \cosh(\Phi l) \sin(\Pi l)) \\ - (\Phi^2 - \Pi^2) \Phi \sinh(\Phi l) \cos(\Pi l) \\ + (\Phi^2 - \Pi^2) \Pi \cosh(\Phi l) \sin(\Pi l) \\ + 2\Phi^2 \Pi \cosh(\Phi l) \sin(\Pi l) \\ + 2\Phi \Pi^2 \sinh(\Phi l) \cos(\Pi l) \end{array} \right] - \left[\begin{array}{l} \left(\frac{\gamma_1 - \gamma_3}{\eta} \right) \cosh(\Phi l) \cos(\Pi l) \\ - (\Phi^2 - \Pi^2) \cosh(\Phi l) \cos(\Pi l) \\ + 2\Phi \Pi \sinh(\Phi l) \sin(\Pi l) \\ \left(\frac{\gamma_1 - \gamma_3}{\eta} \right) \sinh(\Phi l) \sin(\Pi l) \\ - (\Phi^2 - \Pi^2) \sinh(\Phi l) \sin(\Pi l) \\ - 2\Phi \Pi \cosh(\Phi l) \cos(\Pi l) \end{array} \right] \left[\begin{array}{l} \left(\frac{\gamma_1 - \gamma_3}{\eta} \right) (\Phi \cosh(\Phi l) \sin(\Pi l) + \Pi \sinh(\Phi l) \cos(\Pi l)) \\ - (\Phi^2 - \Pi^2) \Phi \cosh(\Phi l) \sin(\Pi l) \\ - (\Phi^2 - \Pi^2) \Pi \sinh(\Phi l) \cos(\Pi l) \\ - 2\Phi^2 \Pi \sinh(\Phi l) \cos(\Pi l) \\ + 2\Phi \Pi^2 \cosh(\Phi l) \sin(\Pi l) \end{array} \right]$$

$$C_{II} = \frac{\left(\frac{h_1}{2D_1} - \frac{h_3}{2D_3} \right) \left[\frac{\Delta\alpha\Delta T \sinh(\Omega l)}{\Sigma l} (\sinh \Gamma l) \right]}{\eta \left[- \frac{\Delta\alpha\Delta T \sinh(\Gamma l)}{\Sigma l} (\sinh \Omega l) \right]} \text{Cons tan } t1$$

$$\text{Cons tan } t2 * \text{Cons tan } t3 - \text{Cons tan } t1 * \text{Cons tan } t4$$

where

$$\text{Constant } t1 = \left[\begin{array}{l} \left(\frac{\gamma_1 - \gamma_3}{\eta} \right) \cosh(\Phi l) \cos(\Pi l) \\ - (\Phi^2 - \Pi^2) \cosh(\Phi l) \cos(\Pi l) \\ + 2\Phi \Pi \sinh(\Phi l) \sin(\Pi l) \end{array} \right] \text{Constant } t2 = \left[\begin{array}{l} \left(\frac{\gamma_1 - \gamma_3}{\eta} \right) \sinh(\Phi l) \sin(\Pi l) \\ - (\Phi^2 - \Pi^2) \sinh(\Phi l) \sin(\Pi l) \\ - 2\Phi \Pi \cosh(\Phi l) \cos(\Pi l) \end{array} \right]$$

$$\text{Constant } t3 = \left[\begin{array}{l} \left(\frac{\gamma_1 - \gamma_3}{\eta} \right) \left(\Phi \sinh(\Phi l) \cos(\Pi l) \right) \\ - \Pi \cosh(\Phi l) \sin(\Pi l) \\ - (\Phi^2 - \Pi^2) \Phi \sinh(\Phi l) \cos(\Pi l) \\ + (\Phi^2 - \Pi^2) \Pi \cosh(\Phi l) \sin(\Pi l) \\ + 2\Phi^2 \Pi \cosh(\Phi l) \sin(\Pi l) \\ + 2\Phi \Pi^2 \sinh(\Phi l) \cos(\Pi l) \end{array} \right] \text{Constant } t4 = \left[\begin{array}{l} \left(\frac{\gamma_1 - \gamma_3}{\eta} \right) \left(\Phi \cosh(\Phi l) \sin(\Pi l) \right) \\ + \Pi \sinh(\Phi l) \cos(\Pi l) \\ + (\Phi^2 - \Pi^2) \Phi \cosh(\Phi l) \sin(\Pi l) \\ + (\Phi^2 - \Pi^2) \Pi \sinh(\Phi l) \cos(\Pi l) \\ + 2\Phi^2 \Pi \sinh(\Phi l) \cos(\Pi l) \\ - 2\Phi \Pi^2 \cosh(\Phi l) \sin(\Pi l) \end{array} \right]$$

Following is the solution for peel stress under the Case-I of shear stress ($F^2 - 4B < 0$) and Case-II of peel stress ($E^2 - 4A > 0$) conditions:

$$p(x) = C_I (\cosh \Theta x) + C_{II} (\cosh \Psi x) \quad (61)$$

where

$$\Theta = \frac{1}{\sqrt{2A}} \sqrt{E + \sqrt{E^2 - 4A}}$$

$$\Psi = \frac{1}{\sqrt{2A}} \times \sqrt{E - \sqrt{E^2 - 4A}}$$

and

$$C_I = - \frac{\left(\frac{h_1}{2D_1} - \frac{h_3}{2D_3} \right) \left[\frac{\Delta \alpha \Delta T \cosh(pl) \sin(ql)}{\Sigma} \sinh(pl) \cos(ql) + \frac{-\Delta \alpha \Delta T \sinh(pl) \cos(ql)}{\Sigma} \cosh(pl) \sin(ql) \right]}{\left[\frac{(\gamma_1 - \gamma_3)}{\eta} \Theta \sinh \Theta l \right] - \left[\frac{(\gamma_1 - \gamma_3)}{\eta} \cosh \Theta l - \Theta^2 \cosh \Theta l \right] \left[\frac{(\gamma_1 - \gamma_3)}{\eta} \Psi (\sinh \Psi l) \right] - \left[\frac{(\gamma_1 - \gamma_3)}{\eta} \cosh \Psi l - \Psi^2 \cosh \Psi l \right] \left[-\Psi^3 (\sinh \Psi l) \right]}$$

$$C_{II} = \frac{\left(\frac{h_1}{2D_1} - \frac{h_3}{2D_3} \right) \left[\frac{\Delta \alpha \Delta T \cosh(pl) \sin(ql)}{\Sigma} \sinh(pl) \cos(ql) + \frac{-\Delta \alpha \Delta T \sinh(pl) \cos(ql)}{\Sigma} \cosh(pl) \sin(ql) \right] * \text{Cons tan } t1_case2}{[\text{Cons tan } t2_case2 * \text{Cons tan } t3_case2] - [\text{Cons tan } t1_case2 * \text{Cons tan } t4_case2]}$$

where

$$\begin{aligned}
\text{Cons tan } t1_case2 &= \left[\frac{(\gamma_1 - \gamma_3)}{\eta} \cosh \Theta l - \Theta^2 \cosh \Theta l \right] \\
\text{Cons tan } t2_case2 &= \left[\frac{(\gamma_1 - \gamma_3)}{\eta} \cosh \Psi l - \Psi^2 \cosh \Psi l \right] \\
\text{Cons tan } t3_case2 &= \left[\frac{(\gamma_1 - \gamma_3)}{\eta} \Theta \sinh \Theta l \right. \\
&\quad \left. - \Theta^3 (\sinh \Theta l) \right] \\
\text{Cons tan } t4_case2 &= \left[\frac{(\gamma_1 - \gamma_3)}{\eta} \Psi (\sinh \Psi l) \right. \\
&\quad \left. - \Psi^3 (\sinh \Psi l) \right]
\end{aligned}$$

And lastly is the solution for the peel stress in Case-II of shear stress ($F^2 - 4B > 0$) and Case-II of peel stress ($E^2 - 4A > 0$) follows Equation (61) with new sets of coefficients (C_I , C_{II}) where:

$$\begin{aligned}
C_I &= - \frac{\left(\frac{h_1}{2D_1} - \frac{h_3}{2D_3} \right) \left[\frac{\Delta \alpha \Delta T \sinh(\Omega l)}{\Sigma 1} (\sinh \Gamma l) \right.}{\eta \left[- \frac{\Delta \alpha \Delta T \sinh(\Gamma l)}{\Sigma 1} (\sinh \Omega l) \right]} \\
&\quad \left[\frac{(\gamma_1 - \gamma_3)}{\eta} \Theta (\sinh \Theta l) \right. \\
&\quad \left. - \Theta^3 (\sinh \Theta l) \right] - \frac{\left[\frac{(\gamma_1 - \gamma_3)}{\eta} (\cosh \Theta l) \right.}{\left[\frac{(\gamma_1 - \gamma_3)}{\eta} (\cosh \Psi l) \right.} \left[\frac{(\gamma_1 - \gamma_3)}{\eta} \Psi (\sinh \Psi l) \right. \\
&\quad \left. - \Theta^2 (\cosh \Theta l) \right] \left[- \Psi^3 (\sinh \Psi l) \right] \\
&\quad \left. - \Psi^2 (\cosh \Psi l) \right] \\
C_{II} &= \frac{\left(\frac{h_1}{2D_1} - \frac{h_3}{2D_3} \right) \left[\frac{\Delta \alpha \Delta T \sinh(\Omega l)}{\Sigma 1} (\sinh \Gamma l) \right.}{\eta \left[- \frac{\Delta \alpha \Delta T \sinh(\Gamma l)}{\Sigma 1} (\sinh \Omega l) \right]} * \text{Cons tan } t1_case2 \\
&\quad \left[\text{Cons tan } t2_case2 * \text{Cons tan } t3_case2 \right] - \left[\text{Cons tan } t1_case2 * \text{Cons tan } t4_case2 \right]
\end{aligned}$$

$$\begin{aligned}
Constant1_case2 &= \left[\frac{(\gamma_1 - \gamma_3)}{\eta} \cosh \Theta l - \Theta^2 \cosh \Theta l \right] \\
Constant2_case2 &= \left[\frac{(\gamma_1 - \gamma_3)}{\eta} \cosh \Psi l - \Psi^2 \cosh \Psi l \right] \\
Constant3_case2 &= \left[\frac{(\gamma_1 - \gamma_3)}{\eta} \Theta \sinh \Theta l \right] \quad Constant4_case2 = \left[\frac{(\gamma_1 - \gamma_3)}{\eta} \Psi (\sinh \Psi l) \right] \\
&\quad \left[-\Theta^3 (\sinh \Theta l) \right] \quad \left[-\Psi^3 (\sinh \Psi l) \right]
\end{aligned}$$

The details of the solutions to Equation (59) are presented in Appendix 2.

3.1.3 Warpage

After solving for shear stress the warpage equation can be found using Equation (45). For Case-I ($F^2 - 4B < 0$) of shear stress Equation (50) leads to:

$$\begin{aligned}
w(x) &= \frac{1}{(D_1 + D_3)} \left(\frac{h_1}{2} + \frac{h_3}{2} \right) \left[\frac{C_{11}}{2} \left\{ \frac{e^{px}}{(p^2 + q^2)^3} (p^3 \cos(qx) + 3p^2 q \sin(qx) - 3pq^2 \cos(qx) - q^3 \sin(qx)) + \right. \right. \\
&\quad \left. \frac{e^{-px}}{(p^2 + q^2)^3} (p^3 \cos(qx) - 3p^2 q \sin(qx) - 3pq^2 \cos(qx) - q^3 \sin(qx)) \right\} + \\
&\quad \frac{C_{22}}{2} \left\{ \frac{e^{px}}{(p^2 + q^2)^3} (p^3 \sin(qx) - 3p^2 q \cos(qx) - 3pq^2 \sin(qx) + q^3 \cos(qx)) + \right. \\
&\quad \left. \frac{e^{-px}}{(p^2 + q^2)^3} (-p^3 \sin(qx) - 3p^2 q \cos(qx) + 3pq^2 \sin(qx) + q^3 \cos(qx)) \right\} \right] \\
&+ C1(x^2) + C2(x) + C3
\end{aligned} \tag{62}$$

where

$$C1 = -\frac{l}{(D_1 + D_3)} \left(\frac{h_1}{2} + \frac{h_3}{2} \right) \left(\frac{C_{11}}{2} \left(\frac{e^{pl}}{p^2 + q^2} (q \sin(ql) + p \cos(ql)) \right) - \frac{C_{22}}{2} \left(\frac{e^{-pl}}{p^2 + q^2} (p \sin(ql) - q \cos(ql)) \right) \right) + \left(\frac{C_{11}}{2} \left(\frac{e^{-pl}}{p^2 + q^2} (q \sin(ql) - p \cos(ql)) \right) - \frac{C_{22}}{2} \left(\frac{e^{pl}}{p^2 + q^2} (p \sin(ql) + q \cos(ql)) \right) \right)$$

$$C2 = 0$$

$$C3 = -\frac{l}{(D_1 + D_3)} \left(\frac{h_1}{2} + \frac{h_3}{2} \right) \left[\frac{C_{11}}{(p^2 + q^2)^3} (p^3 - 3pq^2) + \frac{C_{22}}{(p^2 + q^2)^3} (q^3 - 3p^2q) \right]$$

Further the warpage model that was determined for Case-II of shear ($F^2 - 4B > 0$) based on Equation (51) leads to:

$$w(x) = \frac{l}{D1 + D3} \left(\frac{h1}{2} + \frac{h2}{2} \right) \left[C11 \frac{\cosh(\Gamma x)}{\Gamma^3} + C22 \frac{\cosh(\Omega x)}{\Omega^3} \right] + C1(x^2) + C2(x) + C3 \quad (63)$$

where

$$C1 = -\frac{l}{D1 + D3} \left(\frac{h1}{2} + \frac{h2}{2} \right) \left[C11 \frac{\cosh(\Gamma l)}{\Gamma} + C22 \frac{\cosh(\Omega l)}{\Omega} \right]$$

$$C2 = 0$$

$$C3 = -\frac{l}{D1 + D3} \left(\frac{h1}{2} + \frac{h2}{2} \right) \left(\frac{C11}{\Gamma^3} + \frac{C22}{\Omega^3} \right)$$

3.2 Inverse method in characterization of trilayer constituents

It is realized that the thermal-mechanical behaviour of real size material components can be substantially different from that of bulk size test samples due to differences in geometric scales, environmental and loading conditions (e.g., humidity, temperature, temperature rate, and holding time) [23]. On the other hand, certain system response parameters, such as warpage, can be determined experimentally with sufficient confidence [78].

The warpage response of the trilayer is normally obtained in a temperature interval (ΔT) to account for nonlinear/bilinear behaviour of the constituent layers, containing polymeric composite materials in organic trilayer structures [79]. Correlation between the experimentally measured system response parameter and the theoretically predicted one is done through the steps of the proposed inverse method, hybrid experimental analytical inverse method (HEAIM), which leads to determination of any unknown system parameters as well as to the evaluation of the thermal-mechanical cyclic response of any trilayer structure.

The flowchart of the HEAIM method is presented in Figure 10. The basic procedural steps are as follows: (i) Measuring strain/deformation, (ii) formulating a system of equations based on closed-form solutions for deformation, (iii) identifying known and unknown material parameters, (iv) solving the system of equations using an iterative method, (v) calculating the difference between the predicted and the measured deformation and finally (vi) continuing the iterative processing until reaching the maximum correlation and the predicted parameters are optimized.

The material response is very much influenced by the uniformity of the layers. Assuming a uniform and symmetrical structure, it is expected that the properties will be consistently distributed parallel to X, Y and Ψ -axes. This can be further verified by comparing the properties resulting for each cross-section line. Figure 2 schematically illustrates a warped trilayer structure where the warpage is measured on the top or bottom surface. These data are further used to compare results of modeled warpage along the cross-section line parallel to X (A-A') or Ψ -axis (D-D') as shown in Figure 2.

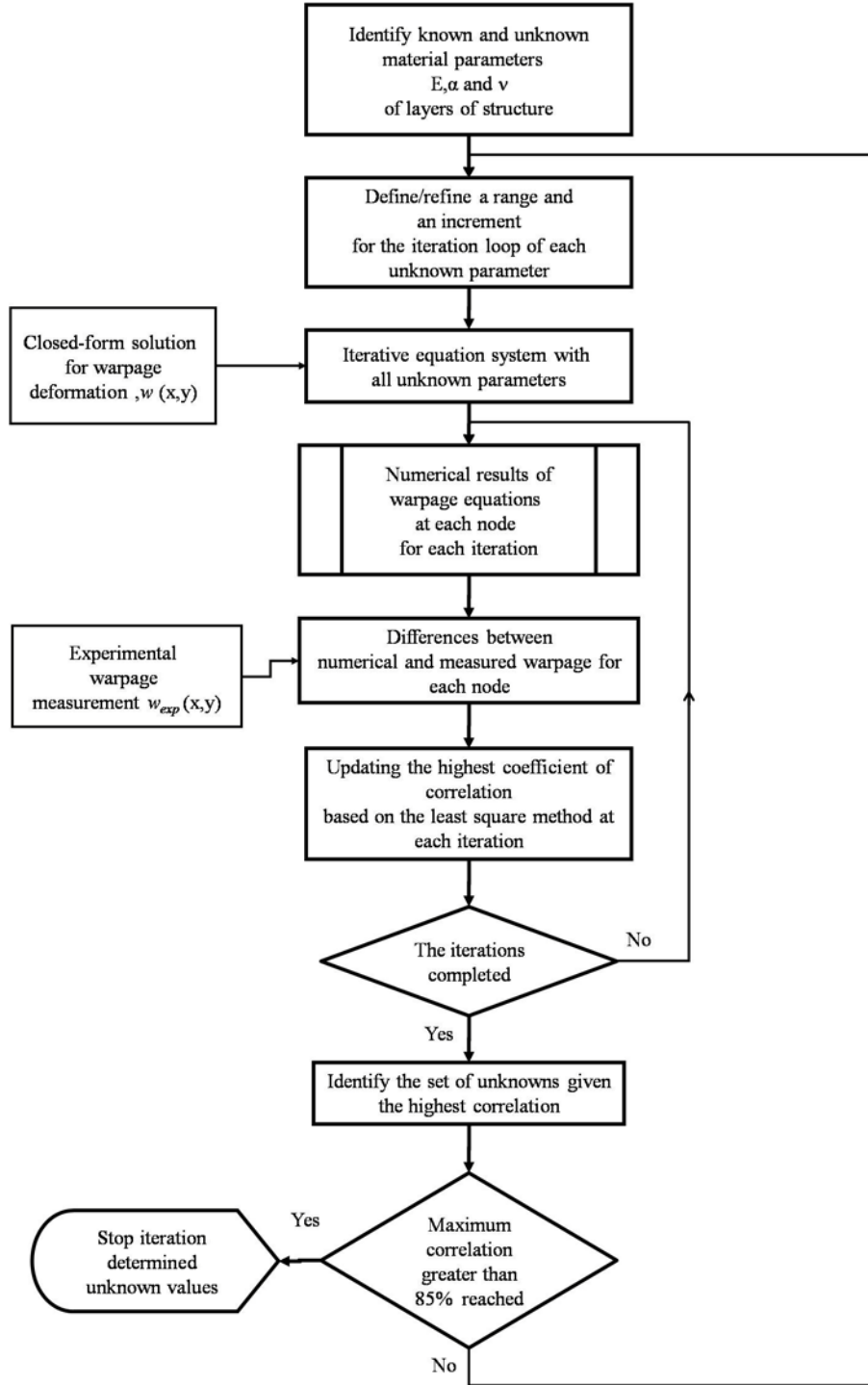


Figure 10: Flowchart of proposed inverse method

The comparison between the experimentally measured and the model predicted warpage at each node within the top or bottom surface of the structure along the cross-section line is taken in a

search loop for highest correlation coefficient ($\max(R_r^2)$). The total variance $SSerr_r$ which is the sum of the squares of the differences between the measured warpage and the warpage predicted at the r^{th} iteration ($r = 1 \dots t$) at each node along the cross-section line (x_i, y_i):

$$SSerr_r = \sum_{i=1}^n \left(w_{exp}(x_i, y_i) - w_{comp}(x_i, y_i) \Big|_r \right)^2 \quad (64)$$

The total variability SS_{tot} is the sum of the squares of the differences between the measured warpage at each node and the average of the measured warpage along the cross-section line (x_i, y_i), $i = 1 \dots n$, for all the nodes along the cross-section line:

$$SS_{tot} = \sum_{i=1}^n \left[w_{exp}(x_i, y_i) - \frac{\sum_{i=1}^n w_{exp}(x_i, y_i) \Big|_r}{n} \right]^2 \quad (65)$$

The maximum number of the iteration t is dependent on the number of unknown material parameters as well as the range and the search increment for each parameter (Figure 3). In Equations (64) and (65) $w_{exp}(x_i, y_i)$ and $w_{comp}(x_i, y_i) \Big|_r$ represent the measured and the calculated warpage (for r^{th} iteration), respectively, at the i^{th} node point (x_i, y_i) along the cross-section line. While $SSerr_r$ indicates the total difference between the measured and the predicted warpage along the line, SS_{tot} reflects the overall curve non-flatness that can be regarded as an experimentally evaluated parameter characterizing the extent of the deflection along the line. R_r^2 in Equation (66) is defined based on the method of least squares difference (LSD) as an index representing the reliability of the model prediction as verified with the experimentally measured data [6,13,80].

$$R_{r|l \rightarrow n}^2 = 1 - \frac{SSerr_r}{SS_{tot}} \quad (66)$$

Given that the ratio of $SSerr_r$ to SS_{tot} is a positive number normally smaller than unity, (for each loop), $R_r^2 = 1$ represents an ideal situation of a perfect match between the experimental and predicted warpage, whereas a small R_r^2 close to zero indicates that the discrepancy between the predicted and the measured warpage is greater than the overall measured warpage itself and therefore the model predication is barely credible. Term n in Equation (65) refers to the number of the nodes along the cross-section line, which is the same for X,Y and Ψ -axes in the case of a square-shaped structure. For such a structure it is apparent that nodes along the Ψ -axis have $x_i = y_i$, and along the mid-line parallel to the X-axis, $y_i = l$ (l is the half length of the side dimension of the structure (Figure 2)).

The result of the search loop is compared with the set criterion (recommended maximum squared correlation coefficient greater than 85% [6]). If the criterion is not met, the search loop will be refined with the finer steps and ranges for each parameter (Refer to Figure 10). After satisfying the set criterion, the matrix representing the corresponding material parameters is identified. These parameters are employed to predict the temperature dependent warpage of the structure.

The uniqueness of the materials parameters determined using HEAIM is addressed by characterizing the laminate warpage with a single parameter, the peak-to-trough warpage versus temperature. Such representation is applied to both the warpage obtained using the analytical solution and the experimentally measured values [13]. The analytical results obtained from HEAIM lead to the prediction of the temperature dependent warpage behavior of the trilayer structure constituents using a reference temperature referred to stress-free-state or reticulation temperature for polymeric based composites [13].

This approach follows the fact that for a thermoelastic material the thermal warpage at a given temperature depends on the thermal warpage at the stress-free-state and warpage change between the temperature at the stress-free-state (reticulation temperature) and the given temperature [6]. Later warpage change between the temperatures is obtained using the accurately determined properties of the constituents using the direct method.

3.3 Method in approximation of notch stresses and strains under creep conditions

After presenting the inverse method for determination of any unknown thermomechanical parameters of trilayer structure under the thermal cyclising, this section presents the proposed direct method for viscoelastoplastic characterization of interfacial layer of trilayer structure constituent alloy. Of those interfacial alloys, may refer to Sn–3.0Ag–0.5Cu (SAC305) lead-free solder alloy which is being widely used in advanced microelectronics applications.

The experimental method is proposed to ensure accurate time-dependent strain and stress data can be obtained during a simple tension test. By employing a notched sample, the measurement can be concentrated only at the notch root to surely capture the stress and strain that are localized in that small scale area, thus to facilitate the analysis of solder constitutive behaviour including the linear-elastic and the creep model. The proposed solution is an extension of Neuber's rule used for the case of time-independent plasticity.

In the traditional local strain approach, the stress or strain at the notch tip is determined using empirical methods such as Neuber's rule to estimate the elastic-plastic response at a notch-tip on the basis of elastic solutions [81]. Tabulations of the theoretical stress concentration factors for a variety of notch geometry and loading configurations have been documented in handbooks [82,83] .

This section presents a method of predicting the stress for a notched body with the theoretical stress concentration factor of K_σ . The notched body is under an elastic-creep tensile condition, and then, the total strain rate is thus expressed by the sum of the elastic, plastic and creep strain versus time. The geometry chosen is a double edge-notched flat plate with V-notches. The plate is subjected to uniformly applied tensile load at its end. Plane-stress condition was applied for creep analysis.

The K field (the elastic-plastic notch-tip Field [82]) is expected to provide an accurate representation of the stress field close to the crack tips in an elastic-plastic material. Satisfactory solutions have also been obtained through the use of the reference stress to estimate the

amplitude of the crack-tip stress in conjunction with the K field. The use of Neuber's approach directly to predict the maximum principal stress in the plane of the crack provides a non-conservative prediction [82, 83].

$$k_t = \sqrt{k_\sigma k_\varepsilon} \Rightarrow k_t = \left(\frac{\sigma}{S} \right) \left(\frac{\varepsilon}{e} \right) \quad (67)$$

where $\sigma, S, \varepsilon, e, k_\sigma, k_\varepsilon$ are maximum stress, nominal stress, maximum strain, nominal strain, stress concentration and strain concentration respectively. Stress concentration (k_σ) and strain concentration (k_ε) for stresses below the yield stress are given as:

$$k_\sigma = \left(\frac{\sigma}{S} \right) \quad (68)$$

and

$$k_\varepsilon = \left(\frac{\varepsilon}{e} \right) \quad (69)$$

Hence, the maximum stress at the tip of the notch under the plane-stress condition can be calculated as:

$$\sigma_y = \sigma = S k_\sigma \quad (70)$$

where $\sigma_x = \sigma_z = 0$.

In the plane-stress condition, a uniaxial stress state exists at the notch tip and therefore uniaxial stress-strain relations can be used [84].

$$\begin{aligned} \varepsilon_t &= \varepsilon_e + \varepsilon_{pl} + \varepsilon_c \\ \varepsilon_e &= \frac{\sigma_t}{E(T)} \\ \varepsilon_{pl} &= C_{pl} (\sigma_t)^m \\ \varepsilon_c &= C [\sinh(\alpha \sigma_t)]^n \exp\left(\frac{-Q}{kT}\right) \end{aligned} \quad (71)$$

where k is the universal gas constant, T is the temperature in Kelvin, σ is the local stress, α and C are material dependent constants, n is the stress exponent, Q is the activity energy, ε_t is the total strain being measured at the notch root, ε_e elastic strain, ε_{pl} is plastic strain and ε_c is creep strain.

It is recognized that the local stress in Equations (71), depends upon the total strains, loading system, global geometry of the notched body and the local notch geometry which translates into the stress concentration factor [84]. It has been indicated in the past that the stress concentration factor, K_t during transient condition (creep steady-state) stays constant versus time [85, 86]. Hence the stress concentration factor for the transient creep stage can be approximately taken as what has been reported in literature for V-notch $60^\circ \pm 5$ configurations [87]. The employed stress concentration factors in this study are listed in Appendix 9.

The total strains at the notch root are measured using a high accuracy digital speckle correlation system (DSC) (Refer to following chapter for more details). The test methods followed the ASTM E-292-09 standard [88] in determination of the time for rupture of notched specimens under conditions of constant load and temperature. These test methods also include the essential requirements for testing equipment, which is demonstrated in the following chapter.

3.4 Proposed method for thermal fatigue life prediction

For the purpose of considering both the normal and shear energies in fatigue damage of the critical corner of the interfacial solder joint, the critical plane-energy fatigue damage parameter is employed. This method was initially introduced by Varvani [89]. In this method the critical-energy damage parameter is defined based on the largest strain and stress Mohr's circles during the reversals of the stabilized cycle.

The model constants of tensorial stress and strain range are maximum shear stress $\Delta\tau_{max}$ and shear strain $\Delta\left(\frac{\gamma_{max}}{2}\right)_{max}$ as well the related normal stress range $\Delta\sigma_n$ and the normal strain range

$\Delta\epsilon_n$ that are found from the largest stress and strain Mohr's circle for loading and unloading during the first and second reversals of a loading cycle on the critical plane (Refer to Figure 11).

Both the normal and shear strain energies are weighted by the axial and shear fatigue properties, respectively. The effect of the mean stress also has been implemented into the model. The most damaging plane has been introduced through experimental results in the following chapter. For proportional loading and shear stress with the in-plane phase, this plane rests at 45° with respect to the parallel axis. Varvani's fatigue damage parameter which contributes to the normal and shear energies acting on the most damaging plane is expressed as [89]:

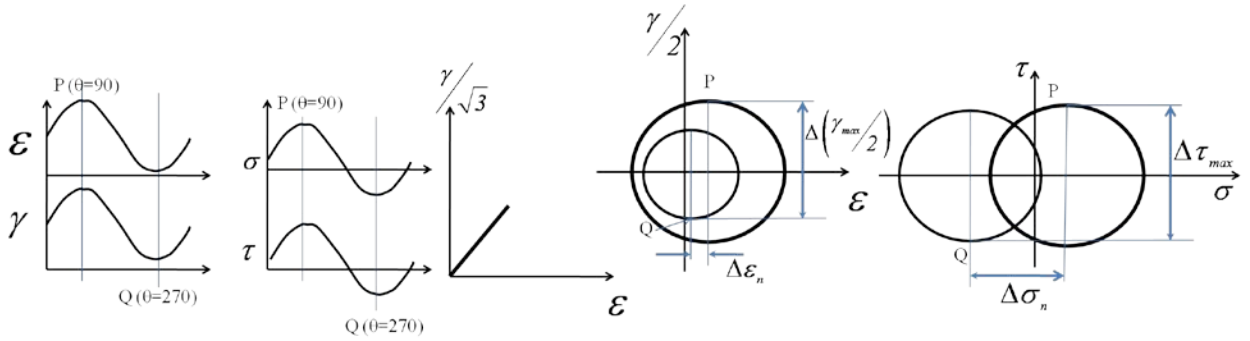


Figure 11: (a) Strain history, strain path and strain and stress Mohr's circle with stress and strain components of the critical plane-energy model, for in-phase strain path [89].

$$D_{damage-parameter} = \frac{1}{(\sigma'_f \epsilon'_f)} (\Delta\epsilon_n \times \Delta\sigma_n) + \frac{\left(1 + \frac{\sigma_n^m}{\sigma'_f}\right)}{(\tau'_f \gamma'_f)} \left(\Delta\left(\frac{\gamma_{max}}{2}\right) \times \Delta\tau_{max} \right) \quad (72)$$

where σ'_f and ϵ'_f are the axial fatigue strength and ductility coefficients, respectively, and τ'_f and γ'_f are the shear fatigue strength and ductility coefficients, respectively.

The axial fatigue strength and ductility coefficients are found from the strain-life response of the materials under cyclic loading. The shear fatigue strength and ductility coefficients can be approximated using the following expressions [90]:

$$\begin{cases} \sigma'_f = \sqrt{3}\tau'_f \\ \gamma'_f = \sqrt{3}\varepsilon'_f \end{cases} \quad (73)$$

The ranges of maximum shear stress $\Delta\tau_{max}$ and shear strain $\Delta\left(\frac{\gamma_{max}}{2}\right)$ are calculated as (Refer to Figure 11):

$$\Delta\tau_{max} = \left(\frac{\sigma_1 - \sigma_3}{2}\right)_{loading(P, \theta=90^\circ)} - \left(\frac{\sigma_1 - \sigma_3}{2}\right)_{unloading(Q, \theta=270^\circ)} \quad (74)$$

$$\Delta\left(\frac{\gamma_{ma}}{2}\right) = \left(\frac{\varepsilon_1 - \varepsilon_3}{2}\right)_{loading(P, \theta=90^\circ)} - \left(\frac{\varepsilon_1 - \varepsilon_3}{2}\right)_{unloading(Q, \theta=270^\circ)} \quad (75)$$

In addition the ranges for normal stress $\Delta\sigma_n$ and shear strain $\Delta\varepsilon_n$ are calculated as (Refer to Figure 11):

$$\Delta\sigma_n = \left(\frac{\sigma_1 + \sigma_3}{2}\right)_{loading(P, \theta=90^\circ)} - \left(\frac{\sigma_1 + \sigma_3}{2}\right)_{unloading(Q, \theta=270^\circ)} \quad (76)$$

$$\Delta\varepsilon_n = \left(\frac{\varepsilon_1 + \varepsilon_3}{2}\right)_{loading(P, \theta=90^\circ)} - \left(\frac{\varepsilon_1 + \varepsilon_3}{2}\right)_{unloading(Q, \theta=270^\circ)} \quad (77)$$

where σ_1, σ_3 are the maximum and minimum principle stresses and $\varepsilon_1, \varepsilon_3$ are the maximum and minimum principle strains from loading (90°) and unloading (270 °) reversals of a cycle and they are calculated for plane-stress conditions from the Mohr's circle (See Figure 11) as follows:

$$\begin{cases} \varepsilon_1 = (I - \nu)\frac{\varepsilon_{ap}}{2} + \frac{I}{2} \left[\varepsilon_{ap}^2 (I + \nu)^2 + 4 \left(\frac{\gamma_{ap}}{2} \right)^2 \right]^{1/2} \\ \varepsilon_2 = -\nu\varepsilon_{ap} \\ \varepsilon_3 = (I - \nu)\frac{\varepsilon_{ap}}{2} - \frac{I}{2} \left[\varepsilon_{ap}^2 (I + \nu)^2 + 4 \left(\frac{\gamma_{ap}}{2} \right)^2 \right] \end{cases} \quad (78)$$

and

$$\begin{cases} \sigma_1 = \frac{\sigma_{ap}}{2} + \frac{I}{2} [\sigma_{ap}^2 + 4\tau^2]^{1/2} \\ \sigma_2 = 0 \\ \sigma_3 = \frac{\sigma_{ap}}{2} - \frac{I}{2} [\sigma_{ap}^2 + 4\tau^2]^{1/2} \end{cases} \quad (79)$$

where σ_{ap} is the applied stress in normal direction, τ is the applied shear stress, ε_{ap} total strain in normal direction and γ_{ap} is total shear strain. The present study correlates Varvani's fatigue damage parameter (Equation 72) to the modified Coffin–Manson equation [90] to predict the fatigue life of trilayer structure. Varvani's damage parameter follows the energy-based method, which accumulates the fatigue damage over the entire life of a component as the number of cycles progresses. Since the presented damage parameter was developed based on shear and axial stress and strain components acting on the critical plane, then the Coffin–Manson modified equation for both axial and shear fatigue components was implemented.

$$\begin{aligned} & \left[\frac{\sigma'_f}{E(T)} (2N_f)^{b_{axial}} + \varepsilon'_f (2N_f)^{c_{axial}} \right] + \left[\frac{\tau'_f}{G(T)} (2N_f)^{b_{shear}} + \gamma'_f (2N_f)^{c_{axial}} \right] = \\ & \frac{I}{(\sigma'_f \varepsilon'_f)} (\Delta \varepsilon_n \times \Delta \sigma_n) + \frac{\left(I + \frac{\sigma_n^m}{\sigma'_f} \right)}{(\tau'_f \gamma'_f)} \left(\Delta \left(\frac{\gamma_{max}}{2} \right) \times \Delta \tau_{max} \right) \end{aligned} \quad (80)$$

The LHS (left hand side) of the Equation (80) represents the fatigue life cycles based on the modified Coffin-Manson equation which correlates with the fatigue life, N_f , of components to the total damage accumulated over the life cycles, versus the RHS (right hand side) which holds cyclic stress and strain terms and materials properties/coefficients, which quantifies the fatigue damage over the fatigue life cycle. Figure 12 demonstrates the step-by-step procedure required to calculate the fatigue damage and to predict the fatigue life of a trilayer structure using an energy-based critical plane approach. The detail of the results in investigating the critical plane and the damage parameters are presented in the following chapter.

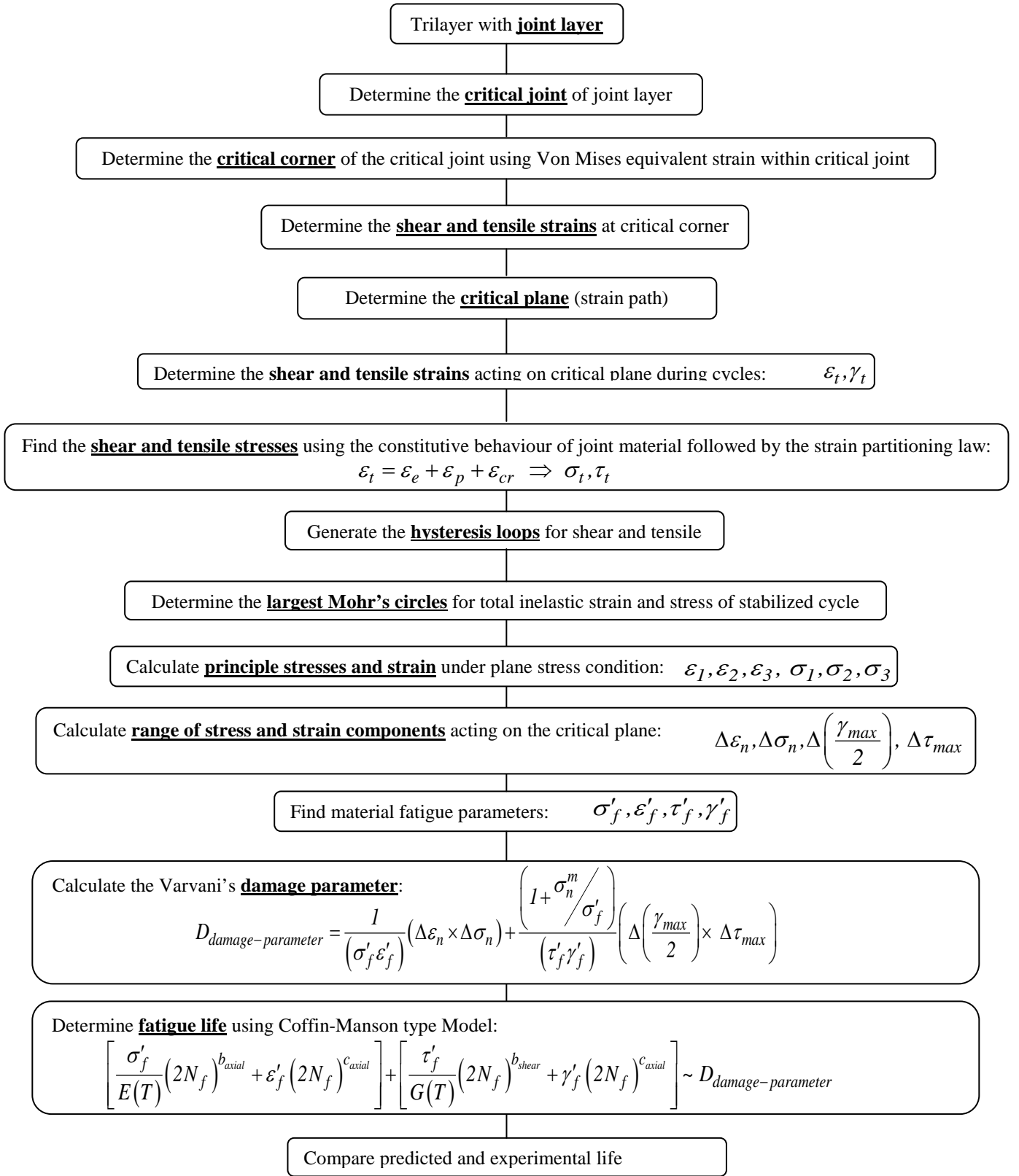


Figure 12: The procedure of fatigue damage analysis based on the critical plane damage parameter

CHAPTER FOUR

Experimental Methods in Testing Reliability and Durability of Trilayer Structure

This chapter presents a detailed description of the experiments carried out in this research. First, the development of the trilayer structure is discussed, followed by a description of optical experimental methods to measure in-plane and out-of-plane deformations under thermal cycling. A description of digital image post-processing obtained through measurements is also presented. The creep dead-weight tensile testing procedure and set up, as well as sample preparation, as part of viscoelastoplastic characterization procedure of trilayer structure midlayer solder material, are described. The chapter concludes with a description of accelerated thermal cycling tests performed on a local level (single solder joint) and global level (array of joints) in a real scale microelectronic prototype/test vehicle.

4.1 Trilayer sample under thermal cycling

4.1.1 Trilayer samples design and preparation

The trilayer test specimens were designed with the intent of simulating the real modules, structures with small aspect ratio and materials with high thermal expansion and high rigidity mismatch, in microelectronics devices. As a result, the samples included features such as the top layer consisting of silicon die square; the bottom layer of organic substrate made of *woven* E-glass fabric epoxy composite lamina, and the mid layer of adhesive layer formally known as underfill. The sample geometries were inspired by the real module design currently used in the industry.

Like traditional samples, the samples were designed using capillary flow, rather than a no-flow underfill process. This feature enhanced the repeatability of manufacturing sample results, since sample misalignment, which potentially contributes to the variation of underfill thickness was avoided. The sample geometry was designed such that the aspect ratio (ratio of the thickness of the sample to its length) was 0.0645~0.0685 to follow the small deflections and the engineering theory of bending of plates with small aspect ratio [5, 91].

In order to ensure a uniform thickness of the underfill layer, five high precision miniature silicone balls (with diameter of 0.30 mm to 0.55mm) have been entrapped between the die at the top and substrate layer at the bottom, while four balls were placed at each corner and one in the centre of the bottom layer (substrate), prior to the application of underfill to the gap. First, the bottom layer was designed with larger dimensions compared with the top layer. Once the manufacturing process was finished the bottom layer was cut to follow the sizes of the top layer in order to generate a trilayer with the same square dimensions. The square dimension helps to minimize variations from ideal symmetrical trilayer structure.

The substrate laminate was cut into 50mm squares from the sheet of composite laminate with dimensions of 215.9 x 279.4 x 0.720 mm using Shear Cutting Machine (Dept. of Mechanical and Industrial Engineering, Ryerson University). The silicon dies were precisely cut into 25.4mm squares from prime wafers, with diameters of 100mm, thickness of $525 \pm 25 \mu\text{m}$, orientation of $\langle 100 \rangle$, single side polished and the backside seal of nitride. The cuts were made using micro-dicing machine (Centre for Emerging Device Technology, McMaster University)

Underfills have been chosen from a selection of materials designed for use as capillary flow, with a rheology allowing the penetration of gaps as small as 25 μm ., rapid curing while featuring low coefficient of thermal expansion properties that make them suitable to be used in manufacturing of chip size packages. For best results, the substrate was placed on a levelled ceramic top hot plate and pre-heated (90 to 100 °C for about 20 seconds) to allow fast capillary flow and facilitate levelling. The dispense nozzle was also pre-heated (30 to 50 °C maximum) to further increase capillary flow.

To ensure optimal flow conditions for the underfill, it was dispensed at moderate speed (2.5 to 12.7 mm/s) while ensuring the needle tip was about 0.1 mm from substrate surface and from chip edge. The dispense pattern was an "L" pattern along two sides, focused at the corner. Application was started at the location furthest away from the chip centre to help ensure a void-free fill underneath the die. Each leg of the "L" pattern was about 80% of the length of each die edge being dispensed. In some cases a second or third application of the underfill product was necessary. With all the selected underfills, the hot plate was used as the optimum tool to reach the fastest curing while following suggested cure conditions as general guidelines to obtain satisfactory results.

An isometric view of the layer of the trilayer before the assembly process is shown in Figure 13. The final samples after each assembly process and trilayer final shape are indicated in Figures 14a-b. Material properties including elastic modulus E , Poisson's ratio ν and coefficient of thermal expansion α as well as glass transition temperature (T_g) of substrates and underfills and curing conditions of underfills are presented in Table 8.

Table 8: Mechanical Properties of Trilayer Constituents

Materials Properties		Substrate Laminate		Underfill			Silicon Die
		VT-47	GETEK	LOCTITE 3593	LOCTITE 3536	HYSOL FP4531	
Tensile Elastic Modulus (GPa)		24.5	N/A	2	N/A	N/A	98
Coefficient of Linear expansion (ppm/ $^{\circ}$ C)	pre- T_g	11	13	50	63	28	2.6
	Post- T_g	13	14	160	178	104	
Poisson's ratio		0.18-0.19	N/A	N/A	N/A	N/A	0.22-0.28
$T_g(^{\circ}$ C)		175-185	180	110	53	161	-
Curing Condition		N/A	N/A	3 minutes@ 165 $^{\circ}$ C	5 minutes@ 120 $^{\circ}$ C	7 minutes@ 160 $^{\circ}$ C	-

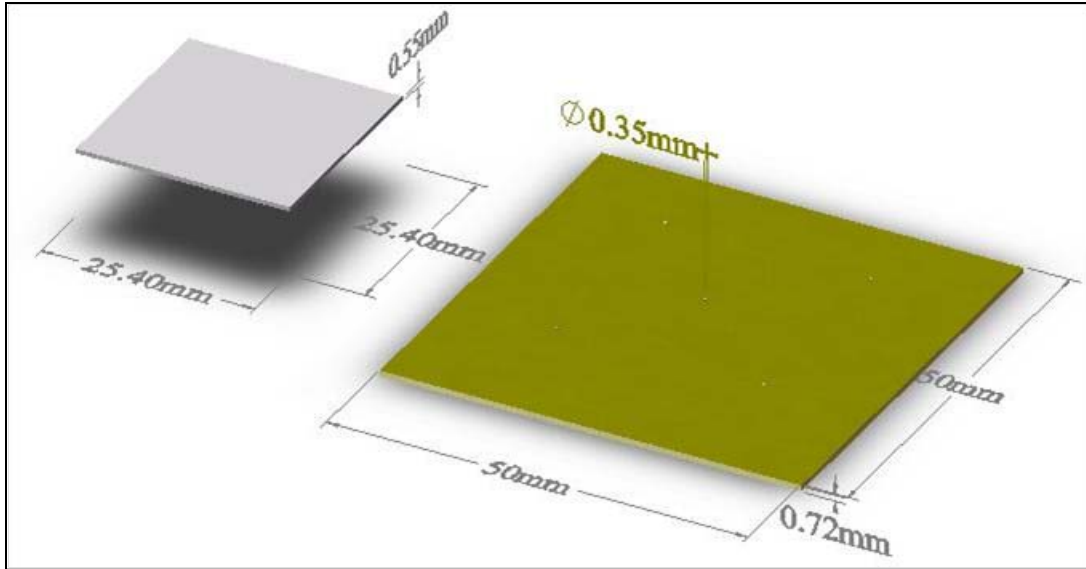


Figure 13: Schematic of the test sample with silicone balls of 0.35mm diameter before assembly.

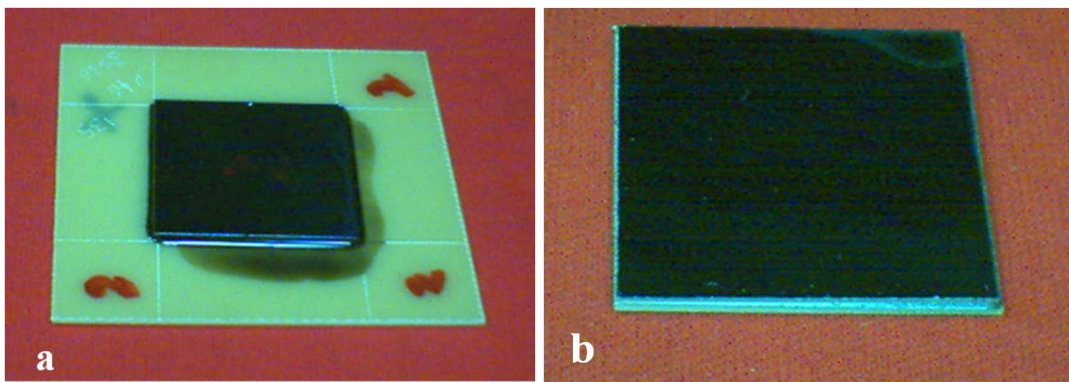


Figure 14: Typical trilayer sample: a) after manufacturing process, b) trilayer final shape.

4.1.2 Thermal chamber

The thermal chamber used in this research is INSTRON SFL 3119-005(Experimental Mechanics Laboratory, Dept. of Mechanical and Industrial Engineering, Ryerson University), which has capability from -50 to 250°C with an automatic control at the accuracy of $\pm 1^{\circ}\text{C}$. The ramp rate can be preset and go up to 8°C/min. The chamber is constructed using a mild steel frame with removable painted mild steel panels. A perforated stainless steel frame surrounds the door aperture and supports a stainless steel

inner chamber. The inner chamber is insulated with glass fiber and/or Microtherm insulation, which are retained by painted panels. A re-circulating fan in the chamber is used to distribute the heat uniformly using the process of natural convection through thermal cycles.

4.1.3 Sample temperature control

There is a temperature lag in the sample with respect to the oven air. The chamber temperature sensor is at the intake of the ventilation with a distance from the sample. During testing, two additional thermal couples are attached to the sample stand in the vicinity of the sample to monitor the sample temperature. The sample temperature is also calibrated before the formal testing and is found to slightly lag behind the chamber reading.

At the high temperature, the difference between the chamber and sample temperature can go up to 10°C, whereas no significant difference is recorded at low temperatures. Due to the high optical magnification used during measurements the system vibration may disturb image recording. To avoid this, the fan is turned off at the image recording time. When the chamber is set at the automatic temperature holding mode, the turn-off will cause a temperature drop of a few degrees depending upon the duration of the off time and the heating rate.

The automatic temperature holding works well only at the sensor location and the sample temperature will experience a slight but continued rise due to delayed heat transfer. This problem is solved using manual control, which can keep the sample temperature stable at one or two degrees fluctuation.

4.1.4 Warpage measurements of the trilayer

4.1.4.1 Testing temperature condition in warpage measurement

The temperature profile is plotted in Figure 15. All the tests start at room temperature (21°C) and the sample temperature increases at a constant rate of 7.5°C/min during ramp up until 220°C. The ramp down was achieved at a rate of 4.65°C/min down to 110 °C and 1.85°C/min from 110 °C until reaching the room temperature.

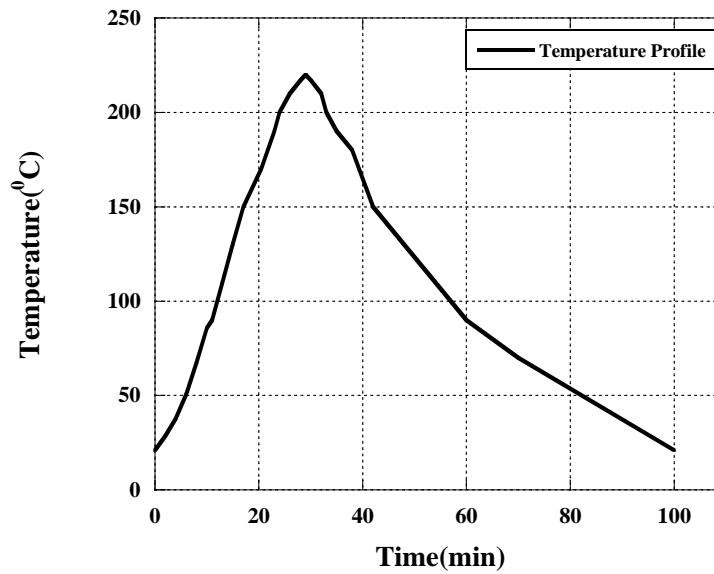


Figure 15: Warpage test temperature profile

4.1.4.2 Phase shifted shadow moiré

Phase-shifted Shadow Moiré method has been employed in this study. This method has long been used in studying thermal warpage of Printed Circuit Boards (PCB) in microelectronics [78, 79, 92, 93, 94]. Figures 16 and 17 schematically demonstrate a detail of the system set-up with its present configuration (Experimental Mechanics Laboratory, Dept. of Mechanical and Industrial Engineering, Ryerson University). As a light beam illuminates the surface through a glass grating, it interferes with the grating's

shadow, producing a fringe pattern. The fringe pattern on the surface due to light interferences shows the surface height contour.

The recorded fringe pattern registers the light intensity distribution over the surface, phase variation as well as the light amplitude. Later phase shifting is introduced to bring a constant phase change to the light wave, which is realized by adjusting the distance between the surface and the glass grating. The Phase-shifted shadow moiré involves multiple sets of phase-shifted fringe patterns. Fringe patterns in a set are recorded under identical conditions but with different phase-shifts, as shown in Figure 18 the optical phase variation over the surface is extracted upon digitally processing the set.

Since the surface height is simply proportional to the optical phase, the phase shifted shadow moiré realizes full measurement automation. Meanwhile, the measurement resolution and accuracy are much improved. Due to an inverse trigonometric operation involved in the fringe processing, the originally solved phase term is but the principal values of the true phase wrapped in a $(-\pi, \pi]$ interval. Phase unwrapping is a necessary step to add a proper multiple of 2π to the wrapped phase term where appropriate.

The current study uses an improved shadow moiré method that employs a cos/sin averaging filtering and an un-weighted least squares phase unwrapping [78]. The latter belongs to a family of least squares unwrapping methods that include the Fast Fourier Transform (FFT) and Discrete Cosine Transform (DCT). The least squares fitting approach is formulated to minimize the sum of the squared differences between the gradients of the unwrapped phase solution and those of the wrapped phase. The improved shadow moiré method exerts no restriction on the sizes of the wrapped phase arrays, and it is proved that the measurements are more accurate than those obtained by using conventional algorithms [78].

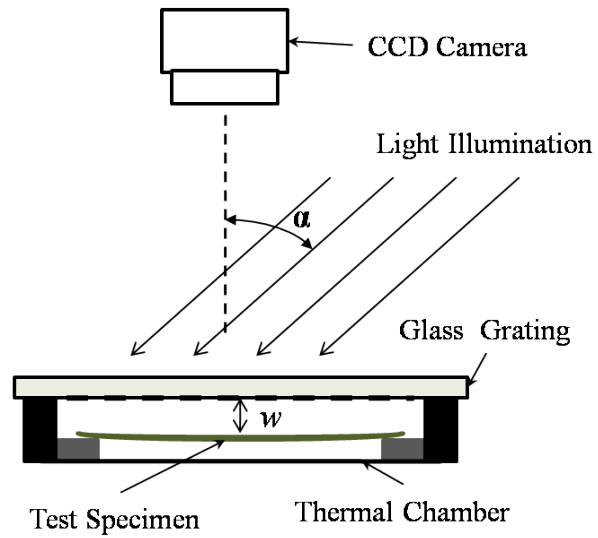


Figure 16: Phase-shifted shadow moiré set-up [93].

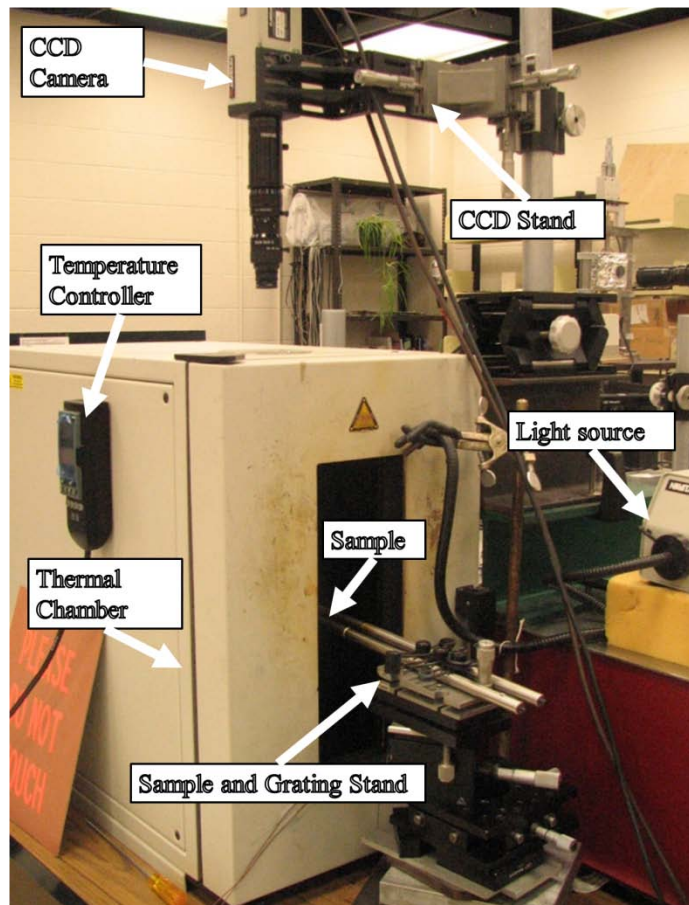


Figure 17: Phase-shifted shadow moiré current set-up (Experimental Mechanics Laboratory, Dept. of Mechanical and Industrial Engineering, Ryerson University).

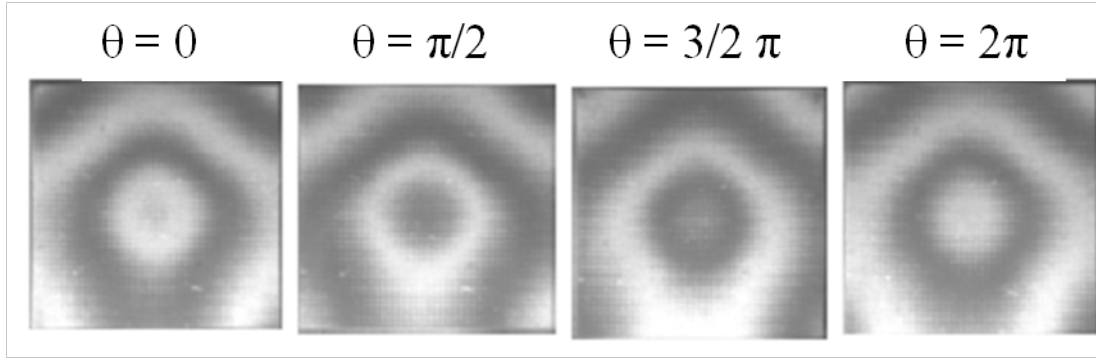


Figure 18: Phase-shifted shadow moiré fringe patterns. [93]

4.1.4.3 Virtual reference plane

As indicated in Figure 16 the warpage data w originally obtained from a fringe processing is expressed as the distance from a surface point to the glass grating. The peak-to-trough warpage as an important surface characteristic parameter can differ depending on how the surface lies under the grating [78]. A virtual datum plane (reference plane) is proposed in this study to overcome this uncertainty. The proposed plane is determined by using the least square difference (LSD) method using raw warpage values at whole points of array, as illustrated in Figure 19.

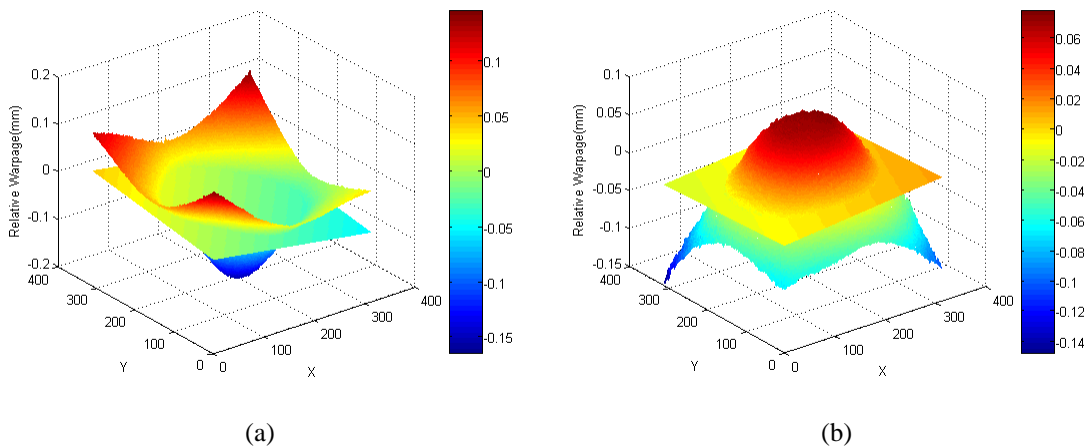


Figure 19: The virtual datum plane presented in a) convex-down surface b) concave-up surface.

The transformation of reference coordinates is performed to convert the raw warpage data from the natural datum plane to the virtual reference plane. The virtual reference plane is as if the unwrapped surface is at this surface and as a result the surface warpage is presented regardless of the orientation and deformation of the surface placed under the grating [78].

The general form of the equation of the reference plane (regression plane) is:

$$Z(x_i, y_i) = ax_i + by_i + c \quad (81)$$

where Z is the dependent variable and x_i and y_i are the independent variables within the matrix of the surface area of interest with $n \times n$ nodes. a , b and c are the regression parameters or partial regression coefficients yet to be defined. The regression parameters are defined based on the classical regression analysis (CRA) and using the least-squares method (LSM). The least-square method is used to obtain the best fitting equation for given set of calibration (experimentally measured data) as $w_{\text{exp}i}(x_i, y_i)$. The deviations from the calibration data are referred to as:

$$d_i = (w_{\text{exp}} - Z)_i \quad (82)$$

An approximation measure of the goodness of fit f is such that the deviations are minimum and is given by:

$$f = \sum_{i=1}^{n \times n} d_i^2 \quad (83)$$

For f to be minimum it requires that:

$$\frac{\partial f}{\partial a} = \frac{\partial f}{\partial b} = \frac{\partial f}{\partial c} = 0 \quad (84)$$

Ultimately these relations lead to a set of equations in the form of:

$$\begin{bmatrix} \sum x_i^2 & \sum x_i y_i & \sum x_i \\ \sum x_i y_i & \sum y_i^2 & \sum y_i \\ \sum x_i & \sum y_i & n \times n \end{bmatrix} \begin{bmatrix} a \\ b \\ c \end{bmatrix} = \begin{bmatrix} \sum x_i z_i \\ \sum y_i z_i \\ \sum z_i \end{bmatrix} \quad (85)$$

After substituting the defined a , b and c regression parameters into the equation of the proposed reference plane, the distance between the raw data and this plane is obtained as follows:

$$w(x_i, y_i) = \frac{|ax_i + by_i - w_{exp}(x_i, y_i) + c|}{\sqrt{a^2 + b^2 + 1}} \quad (86)$$

noting that $w(x_i, y_i)$ values at the surface of the datum plane area are always zero and letting the positive w -axis be upward. Hence, within an array of w where the edge values of warpage are smaller than the peak value represents a concave-up surface and peak value as the maximum warpage. On the other hand, an array with edge values greater than the peak value represents a convex-down area, as seen in Figure 19. Parametric studies of the warpage leads to two main parameters as maximum warpage w_{\max} which is defined as the maximum (in magnitude) w in an area, and Peak-to-valley warpage Δw , which is defined as the algebraic maximum warpage subtracted by the algebraic minimum in a surface area [78].

As for most BGA components, the signs of w_{\max} are indicative of the feature of substrate inflection. A positive w_{\max} characterizes a concave surface and a negative w_{\max} corresponds to a convex one, while a close-to-zero w_{\max} indicates a nearly flat surface [78]. Both w_{\max} and Δw conveniently characterize the feature of a warped surface with a single parameter. The former may apply to surfaces with a single dominant peak/trough whereas the latter to multi-peak wavy surfaces [78].

A plot of w_{\max} vs. temperature shows the trend of warpage variation over a temperature range. Warpage characteristics of the surface such as the net warpage change between two temperatures, the stress-free condition temperature (the temperature of inflection change) and the warpage change after a temperature cycle, etc. can all be determined from that graph, as the primary subject of this study.

The accuracy of shadow moiré measurement depends on the system internal and external factors such as the environment stability, the measurement sensitivity and the pixel reading repeatability of the digital camera [78]. The accuracy is restricted by the measurement repeatability though the sensitivity is claimed to reach 1 μm [93]. This study employs the results of the peak-to-trough warpage measurements of the given surface with the standard deviation less than 10 μm at room temperature and 20 μm at elevated temperatures.

4.1.5 In-plane strain of side-section of trilayer

The trilayer test specimens were measured under thermal cycle for their in-plane strains at the layer interfacial region. As seen in Figure 20, the samples includes features such as layer-1 silicon die square; layer-2, the mid layer of underfill and layer-3 *woven* E-glass fabric epoxy composite laminate. The location of strain measurements at the interfacial layers is focused at the centre of the side-section with the intent of measuring the V-displacement at the free edge which later leads to the value of the maximum peel strain (strain in Z-direction) of points along the X-direction. The interested location of measurement is presented in Figure 20 in more detail. Figure 21-a presents the isometric view of the trilayer sample and the location of measurement, Figure 21-b demonstrates the right-view of the trilayer sample with the location of the measurements at the interfacial layer with the points along the Y and Z axes and Figure 21-c demonstrates the typical digital image processing area showing the U-V displacements coordinate system.

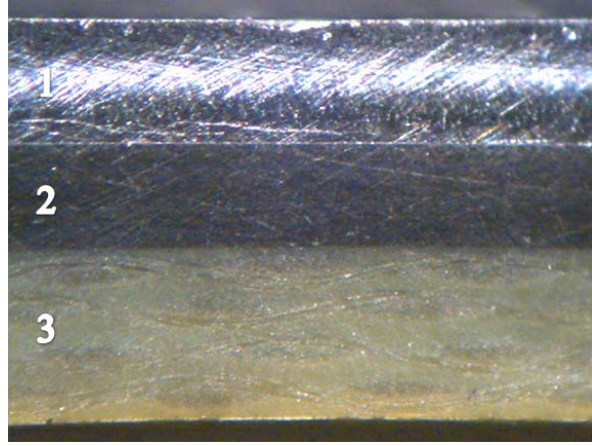


Figure 20: Side side-section of trilayer sample before speckling

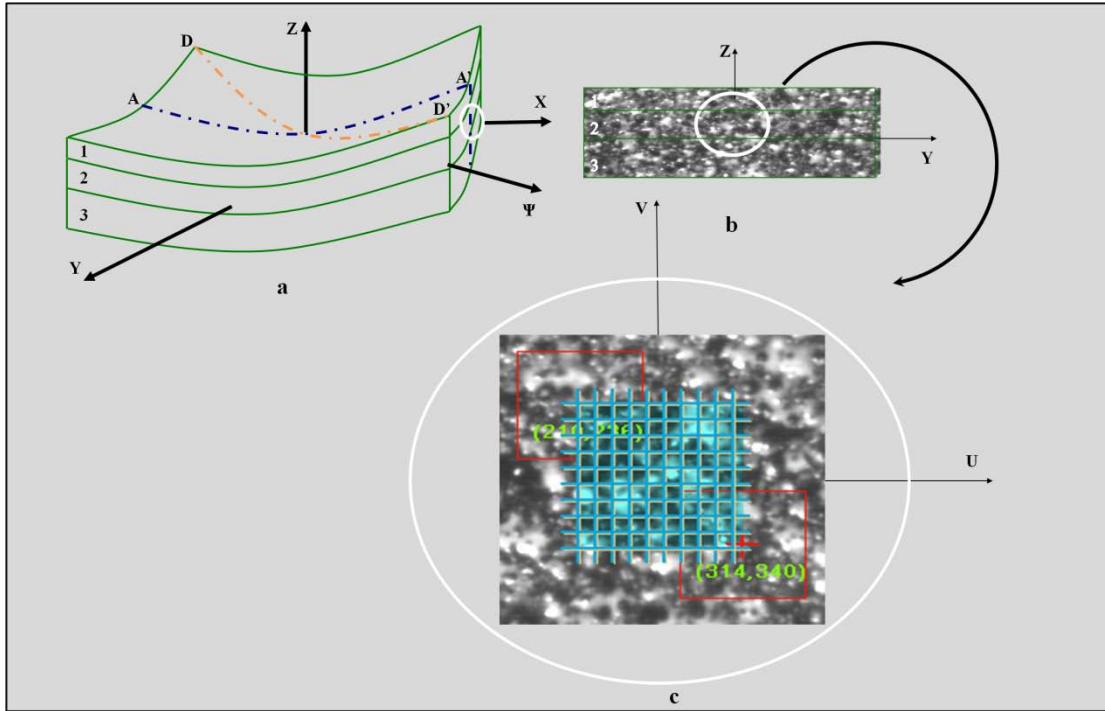


Figure 21: Detail of strain measurement location.

4.1.5.1 Testing temperature condition in in-plane strain measurement

For tests of in-plane strains at the side of trilayer structure, the samples have been thermally tested following a temperature profile (Refer to Figure 22). All tests were started at room temperature (21 °C) and the sample temperature increases at a constant

rate of 3.5°C/min. The ramp up finishes at 125°C. In testing the trilayer samples, the cooling process results from natural convection. Cooling starts immediately after at a rate of 4.8°C/min, reaching 85°C, continues at a rate of 1.3°C/min between 85-49°C and finishes at a rate of 0.2°C/min while arriving at room temperature.

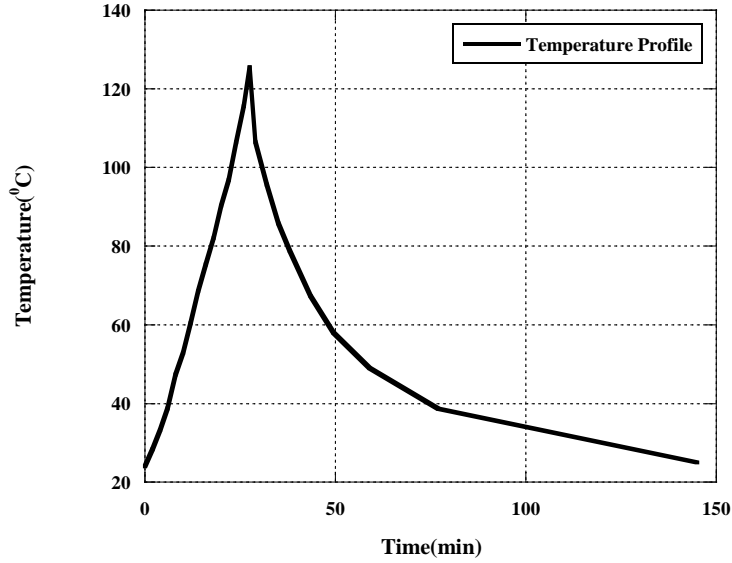


Figure 22: In-Plane strain measurement test temperature profile

4.1.5.2 Digital speckle correlation method

As the system schematic in Figure 23 illustrates, DSC is a computer vision technique. An application using DSC for strain measurement includes two main steps: image acquisition during the test and image processing after the test. The latter, based on theories of digital image processing and correlation, determines the strains and displacements of the surface in a multiple-scale, full field and computer-automated manner. The features of the method include being non-contact and remote sensing, which make the technique suitable for high temperature applications [95].

The advantages lie mainly in that the technique does not need to attach physical gauges or sensors (mechanical, optical, or electric, etc) to testing samples, even though it does

require a sample surface with sufficient variation of light reflectivity. As a computer vision technique, DSC generates results in a matter of minutes after the completion of testing, thus being advantageous for applications that require full-field measurement at up to several dozen different temperatures. Figure 24 demonstrates a detail of the system set-up with its present configuration (Experimental Mechanics Laboratory, Dept. of Mechanical and Industrial Engineering, Ryerson University)

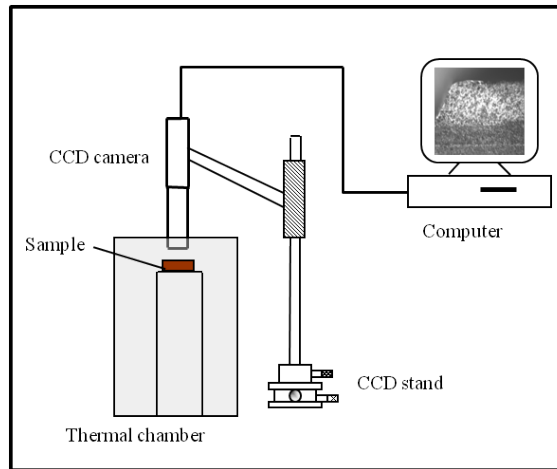


Figure 23: Schematic of DSC system setup

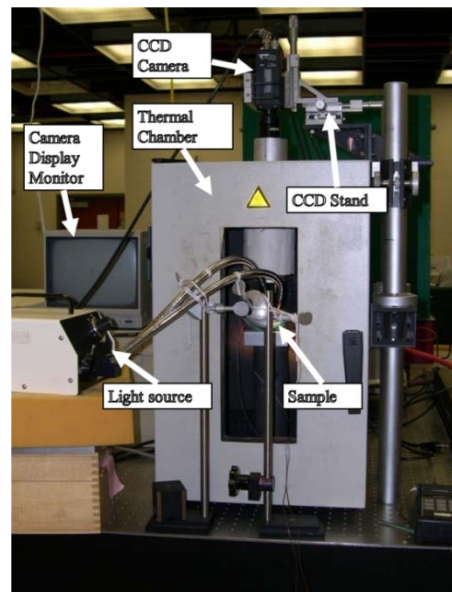


Figure 24: DSC system current set-up (Experimental Mechanics Laboratory, Dept. of Mechanical and Industrial Engineering, Ryerson University).

The image processing is performed by comparing a pair of digital image subsets of a sample surface that are recorded respectively before and after the surface is deformed. To explain briefly the theory, let such pair be given as follows: the subset of the non-deformed image, also referred to as a “reference image”, is represented by a light intensity distribution function $f(x, y)$ while the deformed one is given by $g^*(x^*, y^*)$. (x, y) represents a pixel location of the CCD camera used in the image recording. A decorrelation or dissimilarity factor S is defined for the image pair as follows:

$$S(u, v, \partial u / \partial x, \partial u / \partial y, \partial v / \partial x, \partial v / \partial y) = 1 - \frac{\sum f(x, y) g^*(x^*, y^*)}{\sqrt{\sum f^2(x, y) \sum g^{*2}(x^*, y^*)}} \quad (87)$$

It is assumed that the surface deformation is the sole cause of the image decorrelation. The displacements and the displacement gradients ($u, v, \partial u / \partial x, \partial u / \partial y, \partial v / \partial x, \partial v / \partial y$) are independent variables of the S function, which are defined at the centre point of the image subset. These parameters are obtained through solving $S = 0$ for the root. To explain briefly: the image processing routine examines the image decorrelation by calculating the S with initially estimated deformation parameters. The estimates come from a prior routine of “coarse search.” Upon obtaining the S value, the estimated deformation parameters are upgraded as the result of a Newton-Raphson algorithm that finds the approximate root of the S function. The subsequent iteration generates progressively reduced S values and the improved deformation parameters. Normally the S value will converge and reduce to a pre-determined minimal (very close to zero) after a few rounds of calculation. The attainment of the convergence criterion signifies that the parameters (the measurements) have approached acceptable quality at the termination of the process. After the image processing, the strains are calculated with the obtained displacement gradients via the following equations:

$$\varepsilon_x = \sqrt{1 + 2 \frac{\partial u}{\partial x} + \left(\frac{\partial u}{\partial x} \right)^2 + \left(\frac{\partial v}{\partial x} \right)^2} - 1 \quad (88)$$

$$\varepsilon_y = \sqrt{1 + 2\frac{\partial v}{\partial y} + \left(\frac{\partial v}{\partial y}\right)^2 + \left(\frac{\partial u}{\partial y}\right)^2} - 1 \quad (89)$$

$$\gamma_{xy} = \arcsin \frac{\frac{\partial u}{\partial y} + \frac{\partial v}{\partial x} + \frac{\partial u}{\partial x} \frac{\partial u}{\partial y} + \frac{\partial v}{\partial x} \frac{\partial v}{\partial y}}{(1 + \varepsilon_x)(1 + \varepsilon_y)} \quad (90)$$

or if the deformation is small, using the following equations:

$$\varepsilon_x = \frac{\partial u}{\partial x} \quad (91)$$

$$\varepsilon_y = \frac{\partial v}{\partial y} \quad (92)$$

$$\gamma_{xy} = \frac{\partial u}{\partial y} + \frac{\partial v}{\partial x} \quad (93)$$

For applications that involve temperature changes, the measured strains are so-called “total strains” or the sum of the mechanical strain and the thermal expansion. For thermally isotropic materials responding linearly to the temperature change ΔT with a constant coefficient of thermal expansion α , the measured total strains, mechanical strains and thermal expansion terms are related by the following equations:

$$\varepsilon_x = \sqrt{1 + 2\frac{\partial u}{\partial x} + \left(\frac{\partial u}{\partial x}\right)^2 + \left(\frac{\partial v}{\partial x}\right)^2} - 1 + \alpha \cdot \Delta T \quad (94)$$

$$\varepsilon_y = \sqrt{1 + 2\frac{\partial v}{\partial y} + \left(\frac{\partial v}{\partial y}\right)^2 + \left(\frac{\partial u}{\partial y}\right)^2} - 1 + \alpha \cdot \Delta T \quad (95)$$

$$\gamma_{xy} = \arcsin \frac{\frac{\partial u}{\partial y} + \frac{\partial v}{\partial x} + \frac{\partial u}{\partial x} \frac{\partial u}{\partial y} + \frac{\partial v}{\partial x} \frac{\partial v}{\partial y}}{(1 + \varepsilon_x)(1 + \varepsilon_y)} \quad (96)$$

or if the deformation is small, with the following equations:

$$\varepsilon_x = \frac{\partial u}{\partial x} - \alpha \cdot \Delta T \quad (97)$$

$$\varepsilon_y = \frac{\partial v}{\partial y} - \alpha \Delta T \quad (98)$$

$$\gamma_{xy} = \frac{\partial u}{\partial y} + \frac{\partial v}{\partial x} \quad (99)$$

4.1.5.3 Image recording and data processing

A series of about 24 images at different temperatures are taken during the thermal cycle. The time interval between two consecutive images is approximately two minutes. The area chosen for processing is shown in Figure 21, which covers a portion of the interfacial layer between layer 1 and 3 at the centre of the side-section of the sample. The processing follows a grid of 104 (horizontal) by 104 (vertical) points that cover the boxed area. The rectangular area has a dimension of 0.257mm by 0.257mm. This area is chosen because it is located at the corner of the cross-section line along the X-direction ((A-A') as seen in Figure 21), where maximum peel stress along the X-direction exists.

4.2 Steady-state creep tests of solder alloy

As it mentioned earlier in chapter 3, this study puts forward a direct method for viscoelastoplastic characterization of interfacial layer of trilayer structure constituent alloy, Sn–3.0Ag–0.5Cu (SAC305) lead-free solder, measuring localized stress-strain. In

the following section the creep dead-weight tensile testing procedure and set up, as well as the sample preparation are described.

4.2.1 Samples and testing procedures

Sn–3.0Ag–0.5Cu (SAC305) lead-free solder alloy specimen with a flat dog-bone shape is used in this work. Figures 25(a-b) show the solder specimen and its dimensions. The dog-bone notch samples have been designed based on the standard test for conducting time-for-rupture notch tension tests [88]. The detail of the geometries is presented in Table 9.

A comparison of microstructural behaviour between cast samples and real SAC solder joints is carried out. A total of 40 samples have been casted. Ten randomly selected of samples have been tested to verify the repeatability of the casting procedure with a confidence level of 90%. The samples were mounted in epoxy resin, ground with silicon carbide papers, and polished with alumina slurry. The final polish was done with colloidal silica. Samples were examined using energy dispersive x-ray spectroscopy (EDS) in conjunction with a scanning electron microscope (SEM) (Dept. of Mechanical and Industrial Engineering, Ryerson University).

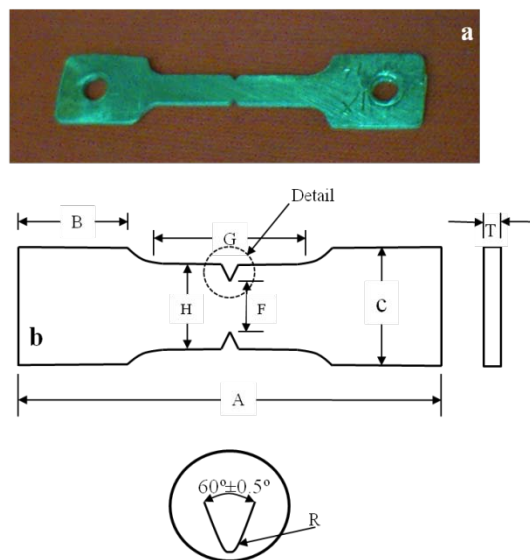


Figure 25: Test specimen a) Bulk sample of SAC305, b) Schematic of the test specimen [88].

Table 9: Schematic of the test specimen

Geometries	Values (mm)
<i>F</i> -Notch ligament (Width)	2.23±0.025
<i>H</i> -Major width	4±0.08
<i>R</i> -Radius of notch tip	0.17±0.03
<i>G</i> -Gage length	20
<i>C</i> -Shoulder width	10
<i>T</i> - Thickness	1±0.05
<i>A</i> -Sample length	50
<i>B</i> -Shoulder length	12

4.2.1.1 Samples preparation

4.2.1.1.1 Casting setup

The samples were cast inside a flat mould made of aluminum, which was heated to about 260 °C approximately 40 °C above the melting temperature of the SAC305 solder alloy. The samples were cast in a specially designed casting tool consisting of a mould, a feeder, four risers and a temperature sensing system. The casting device is described in more detail in Figures 26(a, b, c, d and e). SAC305 has a melting point close to 220 °C (solidus temperature of 217 °C and liquidus temperature of 220 °C) [32].

The mould was cooled by air cooling natural and forced convection (slow cooling rate) until the solidification stage. Within the solid state the cooling carried on using the water-quenching bath. The measured water temperature was 20 °C. It has been reported that the mechanical properties of both, the water-quenched and air-cooled tensile specimens, are similar [3]. Figure 27 represents the following temperature profile. The detail of the temperature profile is listed in Table 10.

Thermocouples implanted in the mould allowed the specimens temperature to be measured within millimeters from the specimen gauge section, at the risers of the cast. The temperatures were measured with an accuracy of about 1°C/s. The cooling rates used

in this study were about 1°C/s above solidus temperature and slightly above 4°C/s just below solidus temperature. The cooling rates are within the range that is followed by the electronics manufacture in reflow of FC-PBGA assemblies [29].

The geometries of the mould are presented in the Appendix 7. The solder alloys were melted and maintained 40°C above their respective melting point for 10 minutes. All the steps were in accordance with recommendations from the National Center for Manufacturing Sciences (NCMS) [96].

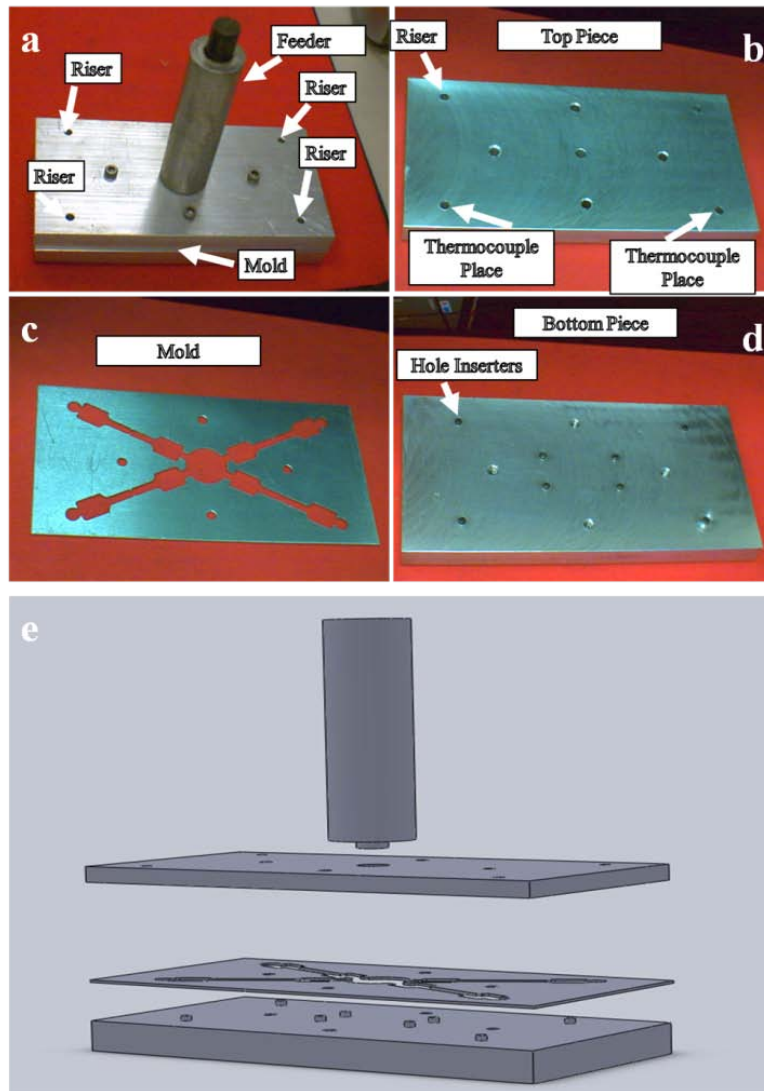


Figure 26: Casting device a) Current setup, b) Mould top piece with riser and thermocouple probes place, c) Mould with cavities for four samples, d) Mould bottom piece with end-holes-inserter, e) Schematic of the disassembled casting device

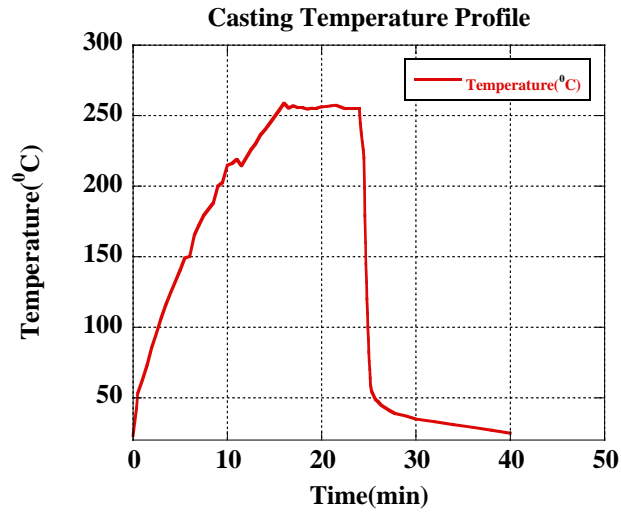


Figure 27: Casting temperature profile

Table 10: Classification Casting Temperature Profile

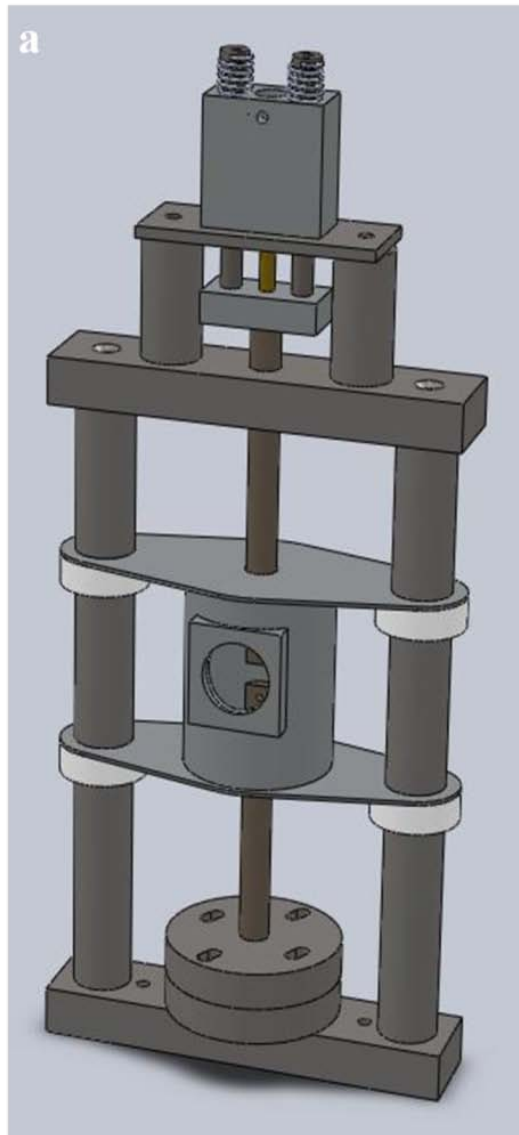
Profile Feature	SAC305
Average ramp-up Rate	1°C/second max.
Peak Temperature	255±2 °C
Time marinated Peak Temperature	10min max.
Time 25 °C to Peak Temperature	15 minutes max.
Average ramp-down Rate before Solidus Temperature	1.13°C/second max.
Average ramp-down Rate after Solidus Temperature	4.25°C/second max.

4.2.1.2 Creep dead-weight tensile test

4.2.1.2.1 Test setup

Figures 28(a-c) demonstrate the schematic and current status of testing set up. DSC system has been used to measure the total strain at the notch root. Isothermal load control tensile tests (dead-weight tensile creep) have been carried out. The creep tests were performed at several temperatures: 0°C, 25°C, 70°C, 100°C and 165 °C; and the load

conditions: 2kg 3kg, 4kg, 6 kg, 8 kg, 10 kg and 12 kg, in order to obtain temperature dependent steady-state strain rate of solder alloy versus tensile stress. The samples temperature is measured using a thermocouple at neighbouring of the specimen gauge length. Two other thermocouples are used to monitor the oven environment temperature. A closed-loop control system has been designed using LabView8.0 to control the heating and cooling system. The cooling system was designed using CO₂ gas, channelled into the oven. The heating system was fabricated using three flexible heaters that were formed inside the wall of the oven. The detailed drawings of the micro-tester components are presented in the Appendix 8.



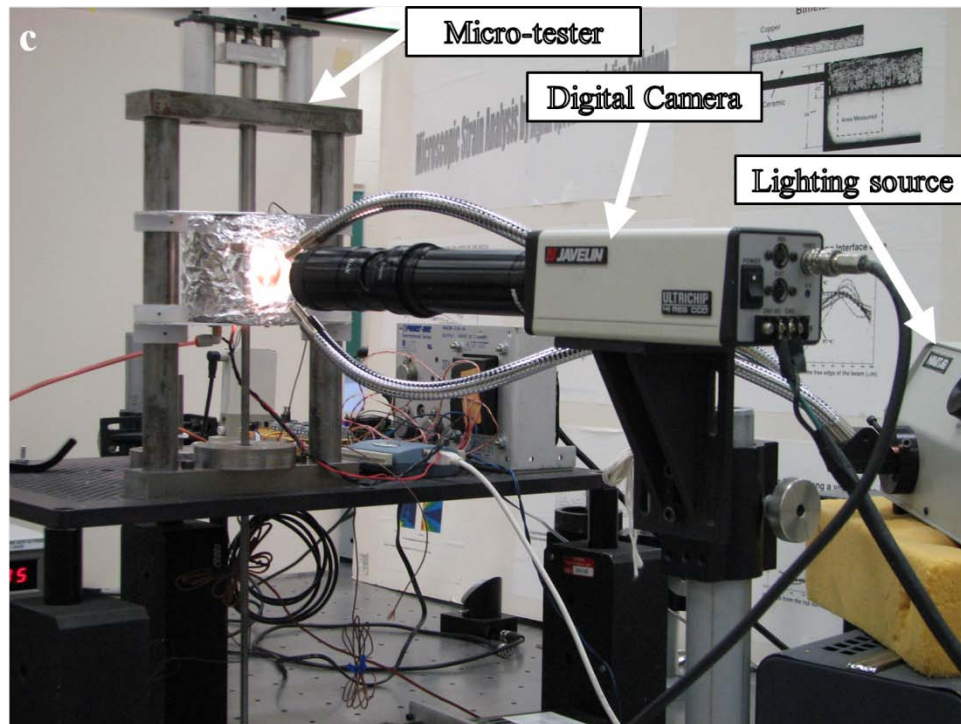
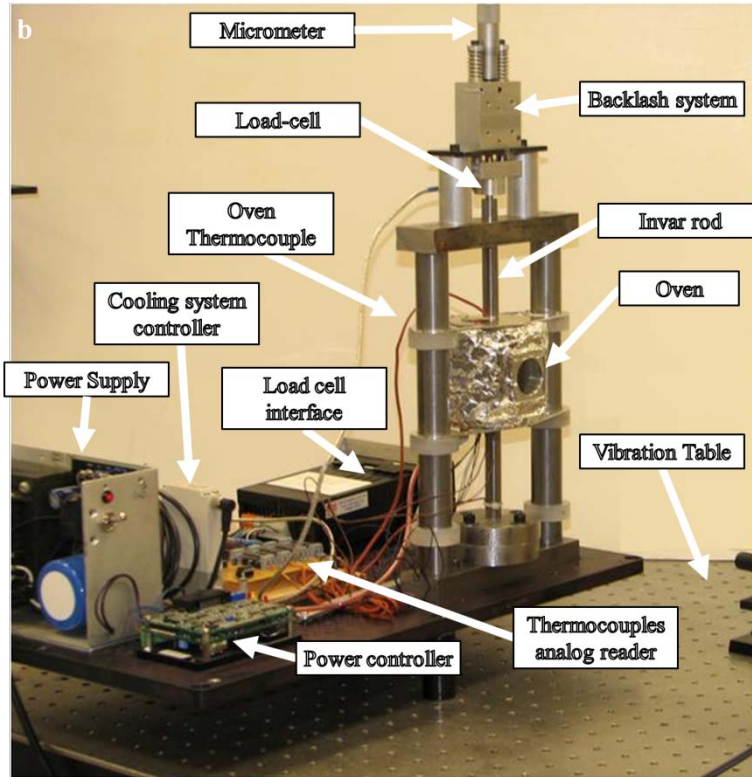


Figure 28: Test setup presented in, a) Schematic of micro-tester structure, b) Current state of the micro-tester in tensile test, c) Current state of the micro-tester in creep-tensile-test while measuring strain using high-speed digital camera under load and temperature condition.

4.3 Accelerated thermal cycling test

This section represents the detail of experimental procedures that have been carried out in this study for life assessment of trilayer structures under accelerated thermal cycling condition. The trilayer structures with dominant joint layer, are found in many applications such as microelectronics assemblies. Life assessment in general suggests the analysis of life data from a sampling of units operated under normal conditions. For a variety of reasons, the life assessment of trilayer structures involves faster process in determining life data than those obtained under normal operating conditions.

As an alternative, the quantitative accelerated life tests are performed to capture life data under accelerated stress conditions that will cause the products to fail more quickly without introducing unrealistic failure mechanisms. In the following section, the method of the accelerated thermal cycling tests is described.

The thermal cycling test has been carried out following the requirements of JEDEC JESD22-A104C [97] industry standard. The present work studies the life of the prototypes with different designs consisting of trilayer structures joined together with a discrete layer of lead (Pb)-free solder joints. Prototypes represent some real applications of advanced microelectronics technology as flip chip plastic ball grid array (FC-PBGA).

This section includes a description of accelerated thermal cycling tests performed at the global level [2], testing the whole structure with detecting the failures at the joints, followed by a local level (single solder joint) strain measurements test.

4.3.1 Accelerated thermal cycling (ATC) test at assembly level

Four different types of samples with different designs were subjected to accelerated thermal cycling condition. The samples have solder balls of Sn3Ag0.5Cu (SAC305) with a sphere size of 600 μ m, 1 mm pitch array. Table 11 represents the details of the

structures of the samples in terms of the size of the Die and thicknesses of lid and the printed circuit board (PCB).

Table 11 - Description of samples used in this study.

Sample#	Module Type	Lid Thick. (mm)	Die size (mm)	PCB (mm)
1B	A	2.0	19	3.2
2A	B	0.5	19	2.4
4	D	Lidless	19	2.4
6A	F	1.0	19	3.2

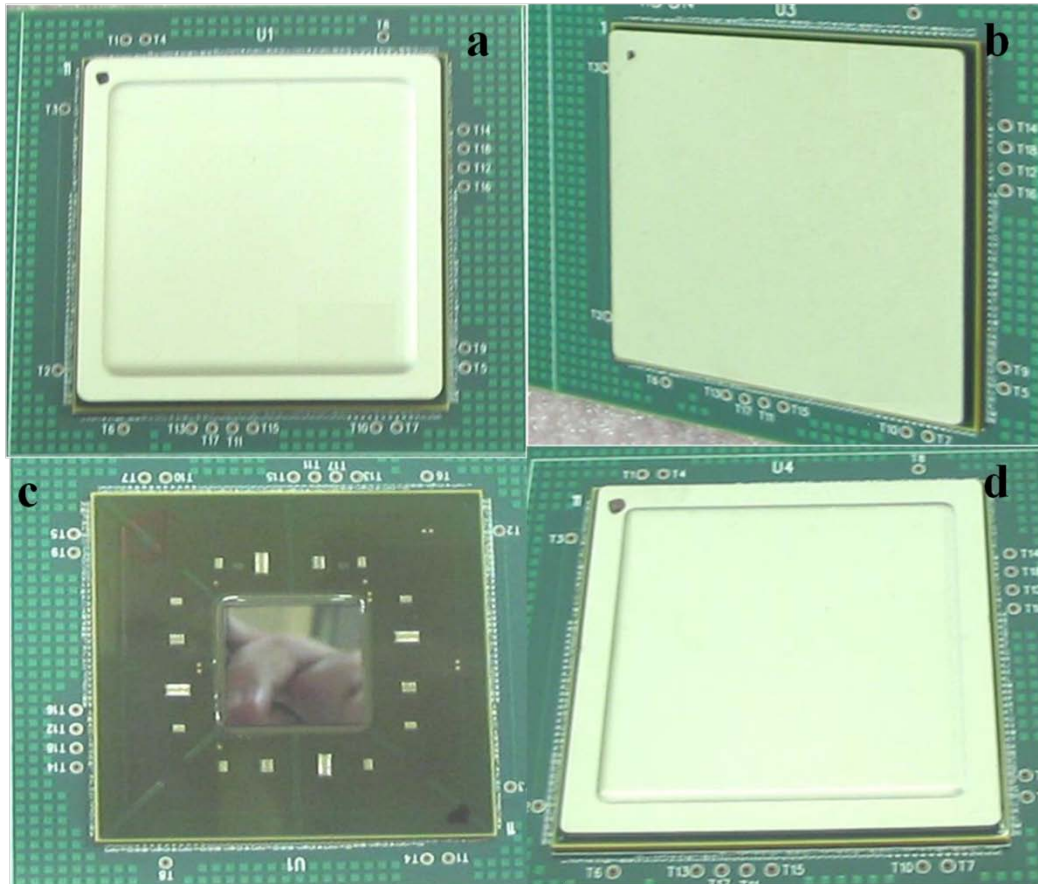


Figure 29 –Samples prepared for ATC Test with types presented in Table 11 as: a) Type A, b) Type B c) Type D and d) Type F.

The samples are being presented in Figure 29. As it is shown, the modules were built with different lid configurations, where type A and type F have one piece lid with different thicknesses; type B has two pieces lid configuration and type D is lidless. Modules configurations are presented in Figure 30 in more detail, showing the cross-sections. All the Lids are made of an identical base material.

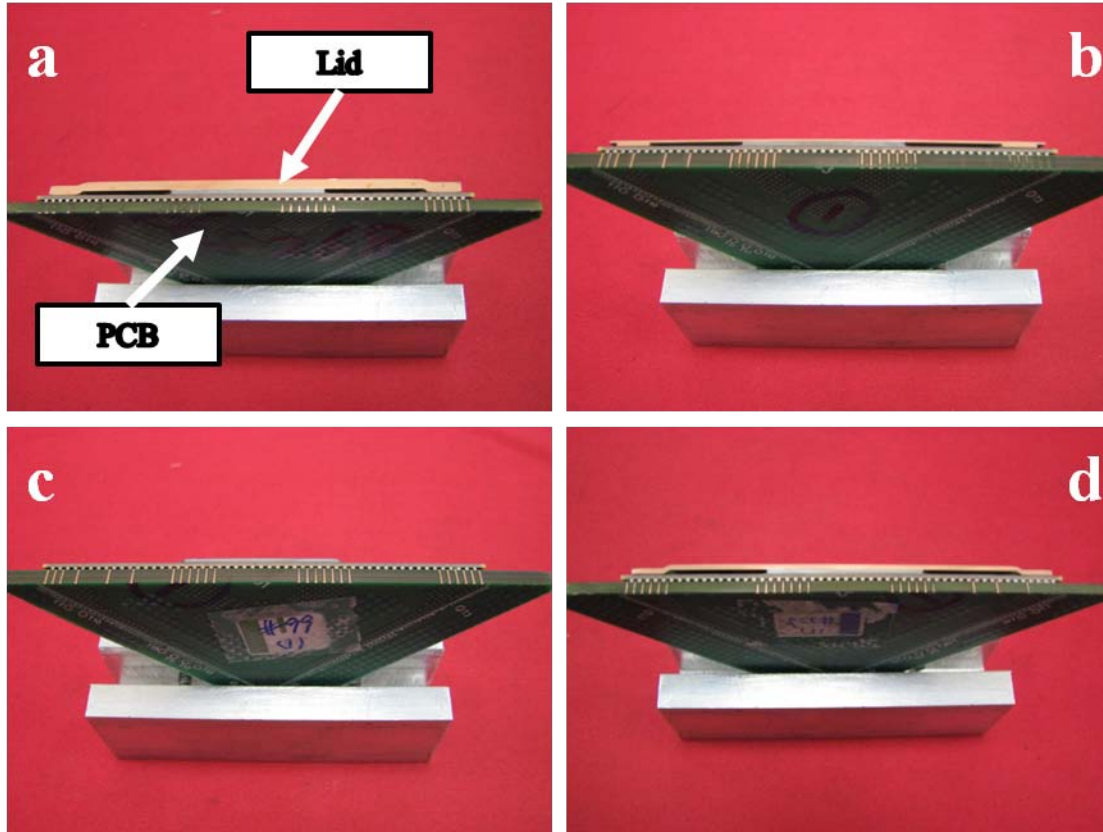


Figure 30 – Configurations of samples of: a) Type A, b) Type B, c) Type D and d) Type D [2] with cut along a BGA diagonal.

4.3.1.1 Accelerated thermal cycling test condition

The thermal cycling tests were performed on the completed assemblies [29]. The test followed the requirements of JEDEC JESD22-A104C [97]. The temperature profile cycled between 0°C and 100°C, with minimum dwell lengths of 5 minutes. All assemblies were in-situ monitored during the test using dataloggers. A failure was

defined as five consecutive readings that showed a 20% or greater resistance increase over the peak resistance measured during the hot dwell on the first cycle [29]. As failures reached, the oven was stopped to allow failures to be isolated before further damage to the sample could occur from additional thermal cycles. This verification of each failure and isolation of individual failings was performed to allow the first failure locations to be identified. The wirings around the solder joints form a daisy chain with a pattern described in Figure 31. The high stress areas are hence covered under the die periphery (the central squares); at PCB corners and periphery (the outer bound squares).

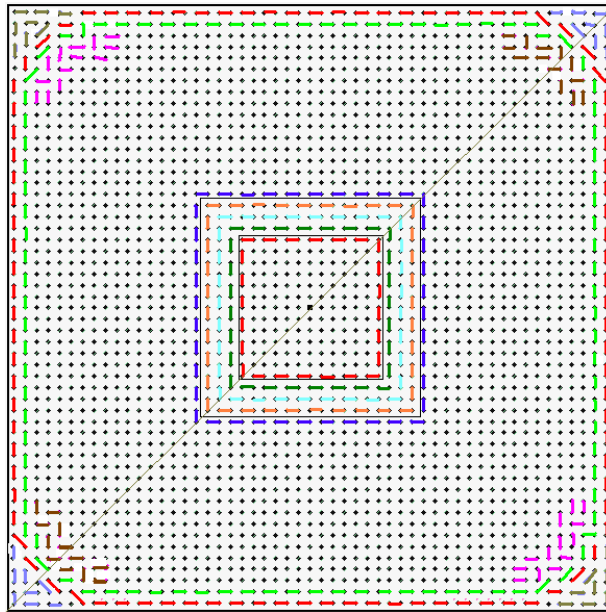


Figure 31- Design of daisy chain, shown from BGA side view [29].

4.3.2 Local testing method

In order to determine the fatigue life of the trilayer structure, the deformations of the critical joint of the dominant layer of the trilayer structure has been measured under thermal cycling condition. The next section explains the detail of the testing procedure and sample preparations.

4.3.2.1 Solder strain measurements under accelerated thermal cycling condition using DSC

Digital Speckle Correlation (DSC) is utilized to measure thermal-mechanical strains at selected solder joints in a diagonally cut cross-section of the assembly samples. The in-plane strain and displacement components in an area of a solder joint of a prepared sample are resolved simultaneously, based on evaluating the speckle correlation between surface images taken at different deformation (temperature) states. Detailed descriptions of the methodology and the measurement procedures can be found in section 4.1.5.2.

The test assemblies used for this measurement are cut along a BGA diagonal with a precision cutting machine. The exact diagonal cross section is reached by using a fine grit polishing method. The surface is further prepared by polishing and finally coating with white and black speckle paint. Sample preparation is a critical step to perform a precise analysis of the solder joint; the BGAs must be sampled at the maximum diameter while minimizing debris or sample preparation deformation.

Figure 32 shows the sample holder and micrographs of the cross-sectioned solder BGAs before and after speckle coating. The speckles are analyzed during temperature variations and translated into stress-strain levels. The DSC measurements were conducted on four different samples. The thermal cycling of the samples performed under two separate phases with the profiles close to the conditions the samples were subjected to during thermal cycling (ATC). The thermal profile and loading condition, presented in Figure 33 represents the Phase-I of cycling. In the second phase (Phase-II) the samples cycled under a similar profile and condition to measure the strain of the critical solder joint (Figure 34). The locations of the joints are presented in the Table 12 for each sample. The DSC measurement focused on a small area at the pad-solder joint interface on the PCB side where, by experience, crack propagation occurs during thermal cycling [29].

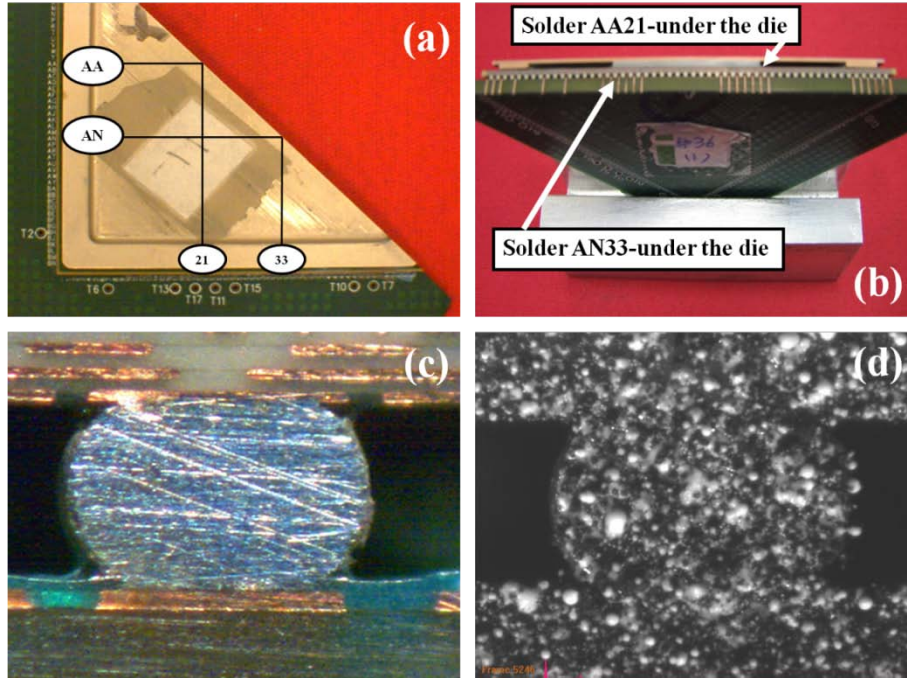


Figure 32 - DSC measurement steps presented at a) the diagonal cut of the sample, b) the location of critical corner joint, c) area of the measurement of critical joint in higher magnification and d) the solder joint after being speckled.

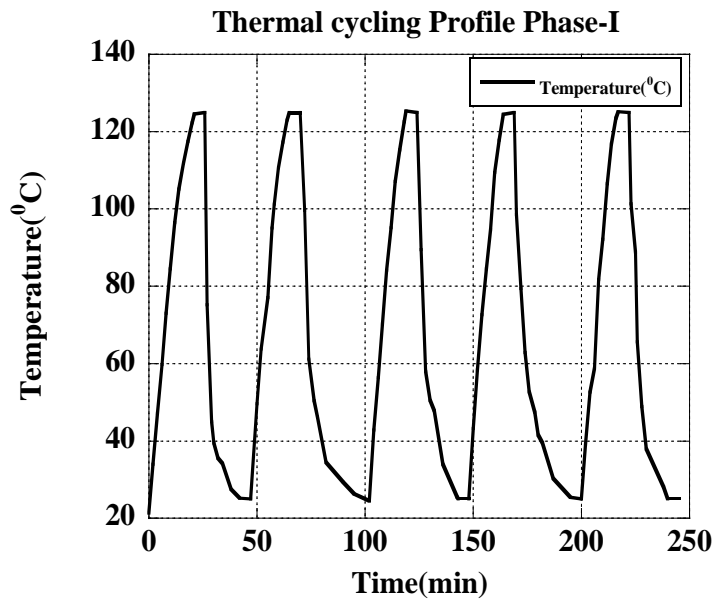


Figure 33 –Thermal profile of the pre-cycling condition of samples before DSC measurement.

Table 12 – Location of DSC measurement (critical joint) for each sample

Sample#	Critical Joint Location
1B	AA21
2A	AN33
4	AN33
6A	AN33

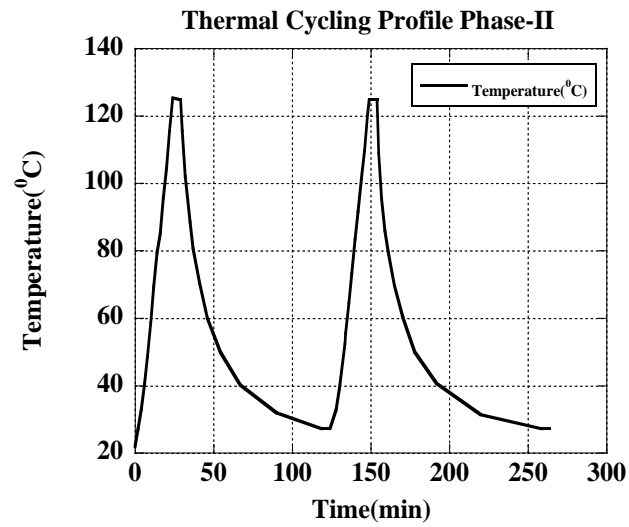


Figure 34 –Thermal profile of cycling condition of samples during DSC measurements.

CHAPTER FIVE

Experimental and Analytical Results and Discussions

This chapter presents the results of thermal cycling and creep tests carried out in this research. Results of each set of experiments are separately discussed. The analytical results, related to inverse method (HEAIM) and interfacial stress-strain of the trilayer samples at different temperatures are presented. The interfacial peel strains are evaluated against the experimental results. Parameters related to secondary creep stage of the solder alloy constitutive behaviour are examined and compared with the literature data. Microstructural behaviour of the as cast solder alloy has been compared with its counterpart from real application. Accelerated thermal cycling tests results of local level (single solder joint) and global level (array of joints) have been demonstrated, followed by the results of the life prediction method and its comparison with the experimental data.

5.1 Warpage of trilayer sample under thermal cycling

A matrix of trilayer samples was designed using available materials with different underfill thicknesses ranging from $0.13 \pm 0.03 \text{ mm}$ to $0.55 \pm 0.04 \text{ mm}$. All samples have been visually inspected using digitally driven high magnification/accuracy Buehler ViewMet Inverted Laboratory Metallograph (Mechanical and Industrial Department, Ryerson University) for their underfill layer integrity (void free) and uniform thickness across sides of the samples. Figure 35 exemplifies the images that were captured while measuring the underfill thickness of samples. Details of design of samples used in this study are presented in Table 13. Five randomly selected samples (Sample#3, 5, 11, 13 and 17) have been chosen for further analysis of the warpage.

Warpage measurements have been obtained from the substrate side of the warped trilayer; Figure 36 demonstrates the typical graphical representation of measured warpage at temperature. The results are representative of the absolute warpage of the package during a temperature profile. As the temperature increases, the warping direction changes from convex to concave. This is explained by the fact that, as the structure is heated from room temperature to peak reflow temperature, the substrate and the interfacial layer tend to expand more than the rigid top layer (Die) to exhibit an upward warpage of the package viewable from top to down (as the package is placed with the substrate facing downward).

The warpage direction change happens within a certain temperature range related to the T_g of underfill layer [6, 9, 13, 26, 74]. The temperature at which the warpage changes the direction is considered as the stress-free temperature of the package during thermal cycling test [13, 28] (Refer to Figure 36), which is usually close to the glass transition of the underfill material [6]. The above judgment is used in estimating T_g of the underfill materials. For the sample#17 (Refer to Figure 36) the range is found to be around 160°C. The rest of 3D contour plots of the absolute warpage of the samples are presented in Appendix 4.

5.1.1 Proposed inverse method and trilayer constitutive properties

Following HEIAM the material properties of the trilayer constituents (die, substrate and underfill) are characterized using warpage data along the centreline of the module though the data along diagonals can be used as well. In a normal case, the module relative warpage along the two diagonal lines (corner to corner) has been measured to show an average difference less than 10% as shown in Figure 36.

The bulk values of the material parameters including the elastic constants and CTE of the substrate and the die attachment materials vary from sample to sample and have been presented in the previous chapter (Chapter 4). The progressive correlation is made

between the shadow moiré measured module warpage obtained in different stages of heating and the warpage determined based on the warpage model solution.

Figure 37 presents typical both experimentally obtained relative warpage of the module along a centreline and that generated using HAEIM for (a) Sample#3 at $\Delta T=35^{\circ}\text{C}$ (20°C to 55°C) (correlation:94%), (b) Sample#5 at $\Delta T=57^{\circ}\text{C}$ (160°C to 217°C) (correlation (R^2): 97%), (c) Sample#11 at $\Delta T=35^{\circ}\text{C}$ (20°C to 55°C) (correlation:99.1%), (d) Sample#13 at $\Delta T=35^{\circ}\text{C}$ (20°C to 55°C) (correlation:80%), (e) Sample#17 at $\Delta T=30^{\circ}\text{C}$ (100°C to 130°C) (correlation:95.3%).

Due to the 2D nature of the warpage model, the material properties are inversely characterized using warpage data along the centreline of the module, though the data along diagonals can be used as well. The bilinear material properties of the trilayer structures so obtained are presented in Table 14. Also included in Table 14, are the estimated T_g of the underfill and substrate layers during cycling.

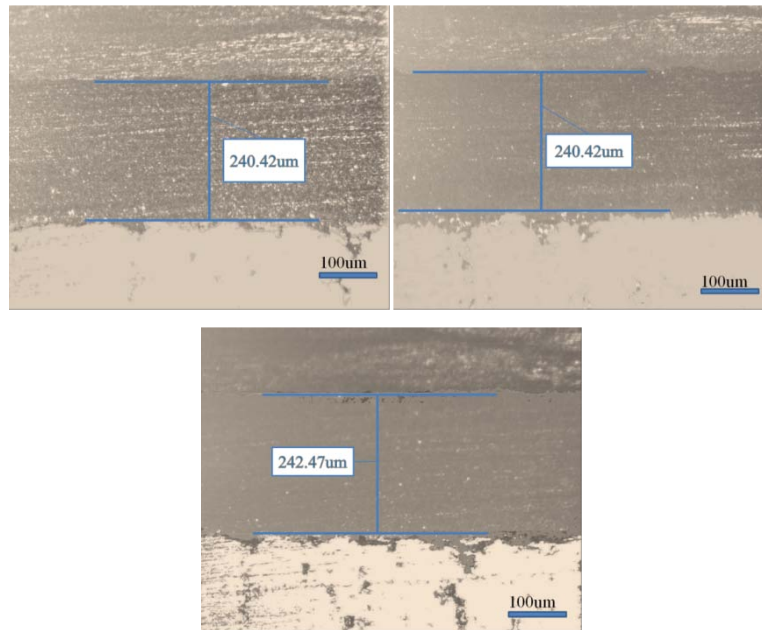


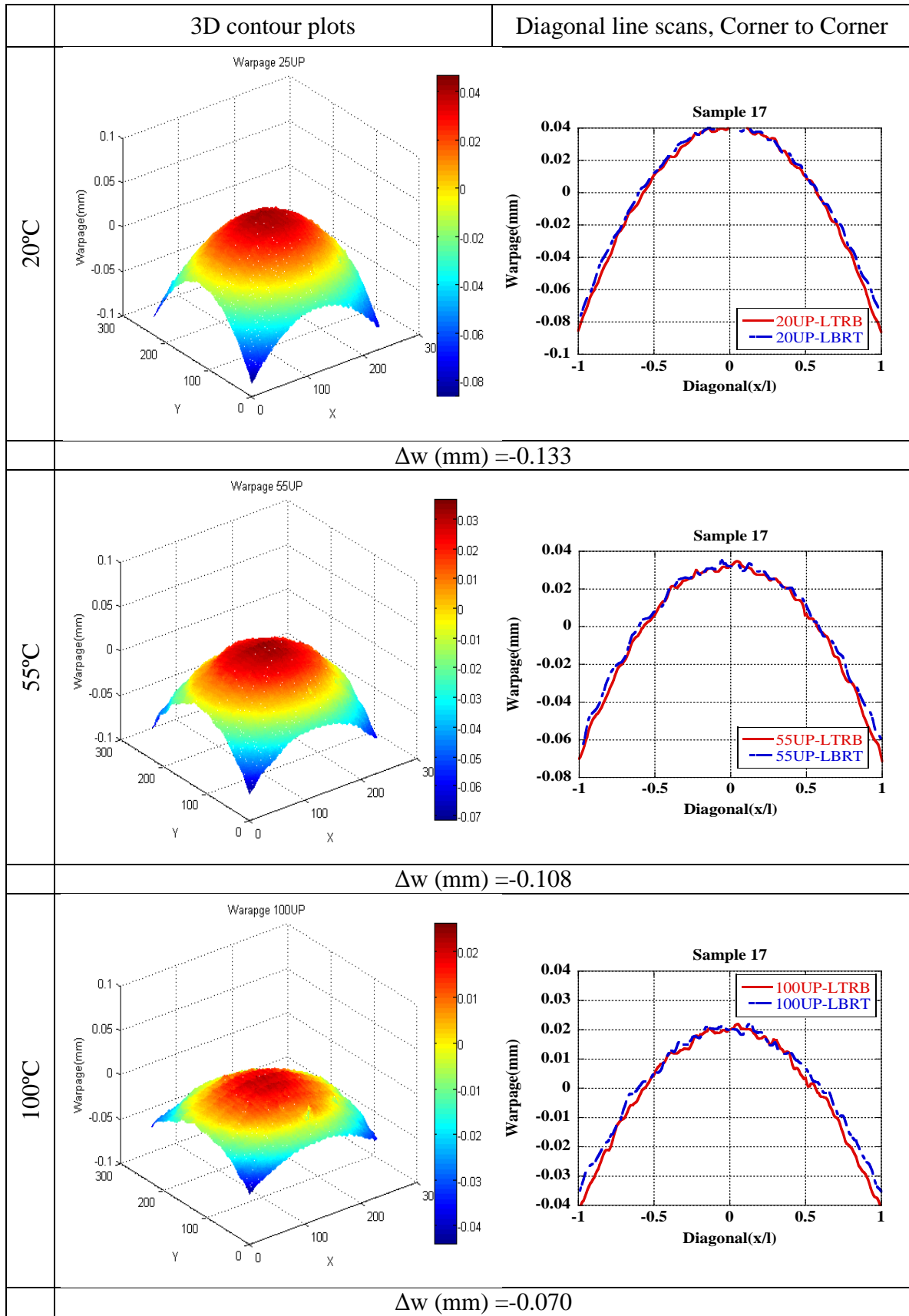
Figure 35: Typical image showing the thickness measurement of underfill layer using Buehler ViewMet Inverted Laboratory Metallograph

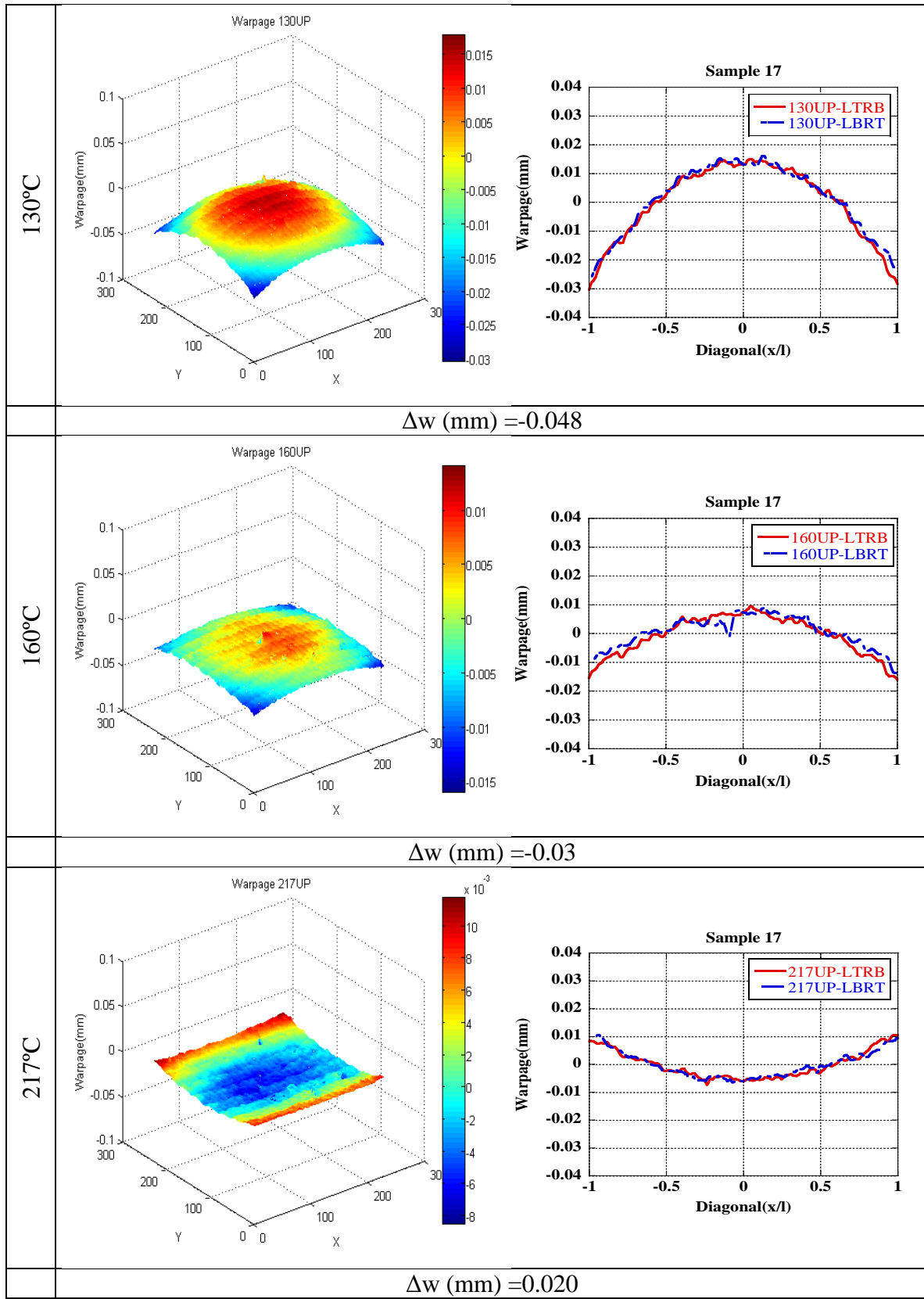
The turning points for the properties of underfill and substrate materials are indicated as a temperature representing a stress-free state [6,28]. The bilinear responses of underfill and substrate materials are further represented in Figures 38(a-c).

The thermally induced changes of material properties could substantially affect the warpage and the manufacturing induced interfacial residual stresses [5]. Due to insufficient data at multiple temperature points, no exact Z shaped variations are shown. However, the turning points around the respective T_g points are obvious. The full details of results of inverse modeling for different samples are presented in Appendix 5.

Table 13: Matrix of the trilayer samples design

Group	Sample #	Underfill Material	Substrate Type	Underfill Thickness (mm)
A	1	LOCTITE 3536	VT-47	0.31±0.03
	2	LOCTITE 3536	VT-47	0.46±0.04
	3	LOCTITE 3536	VT-47	0.33±0.04
	4	LOCTITE 3536	VT-47	0.50±0.05
B	5	LOCTITE 3536	GETEK	0.52±0.05
	6	LOCTITE 3536	GETEK	0.51±0.05
	7	LOCTITE 3536	GETEK	0.46±0.04
	8	LOCTITE 3536	GETEK	0.50±0.04
C	9	LOCTITE 3593	VT-47	0.50±0.05
	10	LOCTITE 3593	VT-47	0.55±0.05
	11	LOCTITE 3593	VT-47	0.51±0.05
	12	LOCTITE 3593	VT-47	0.52±0.05
D	13	LOCTITE 3593	GETEK	0.55±0.04
	14	LOCTITE 3593	GETEK	0.48±0.04
	15	LOCTITE 3593	GETEK	0.50±0.05
	16	LOCTITE 3593	GETEK	0.52±0.05
E	17	HYSOL P4531	VT-47	0.13±0.03
	18	HYSOL P4531	VT-47	0.36±0.03
	19	HYSOL P4531	VT-47	0.35±0.03
	20	HYSOL P4531	VT-47	0.25±0.02





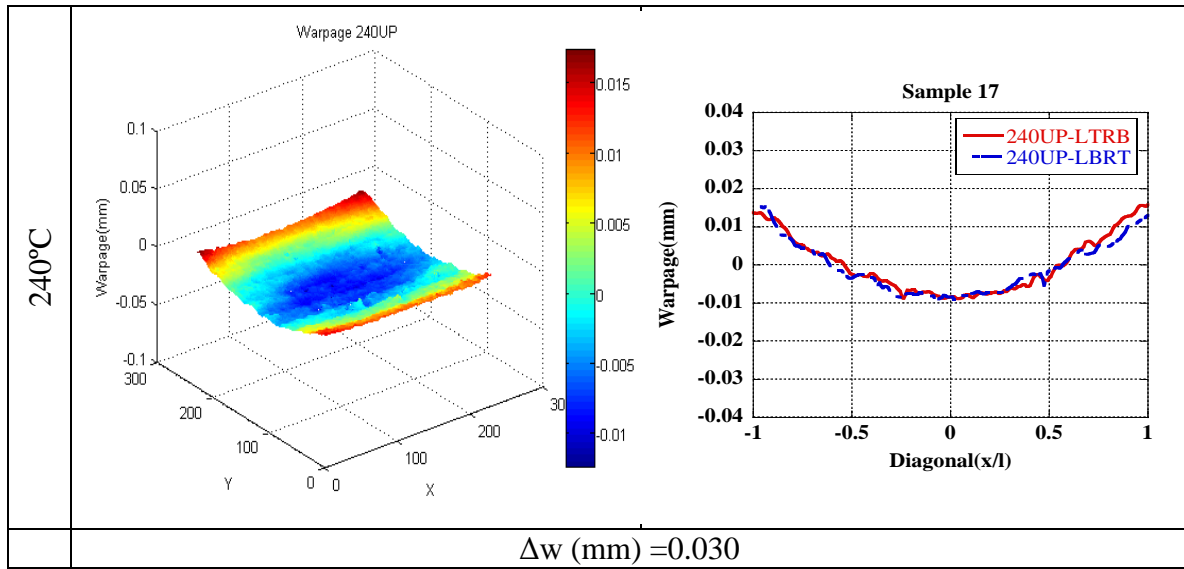
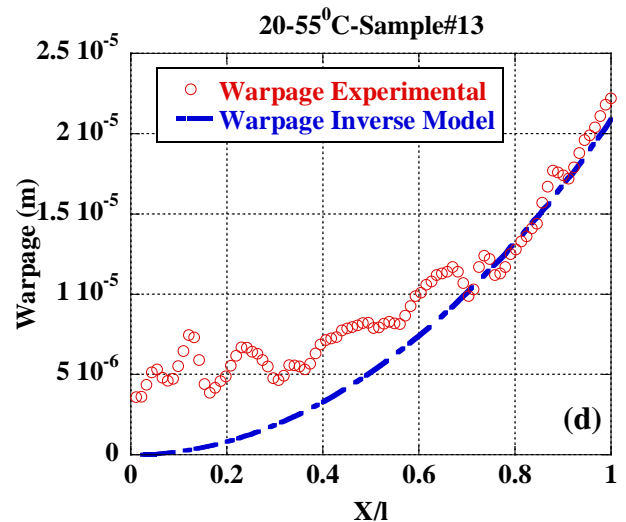
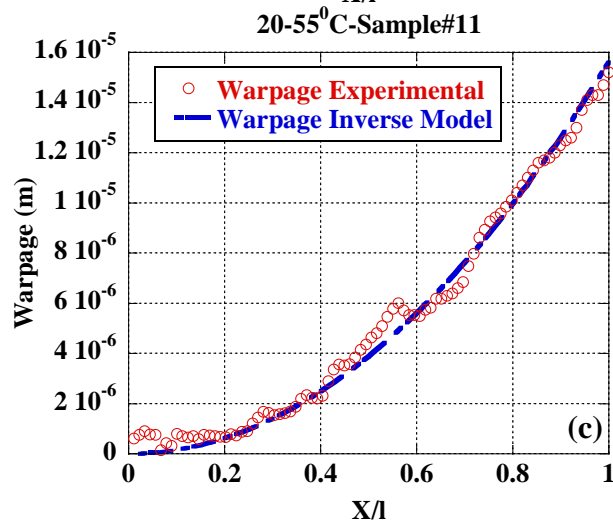
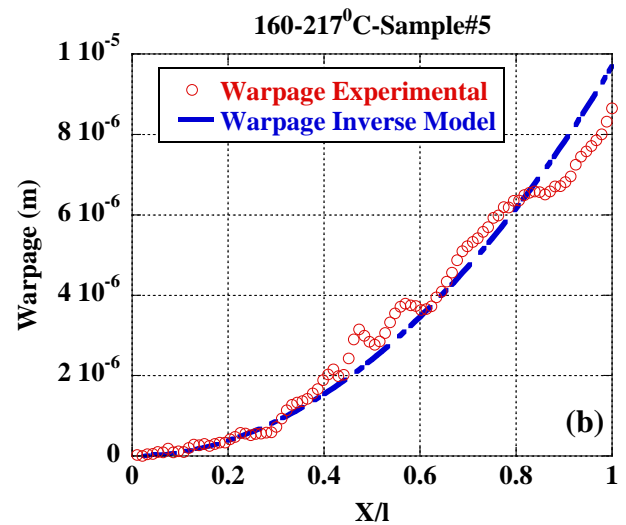
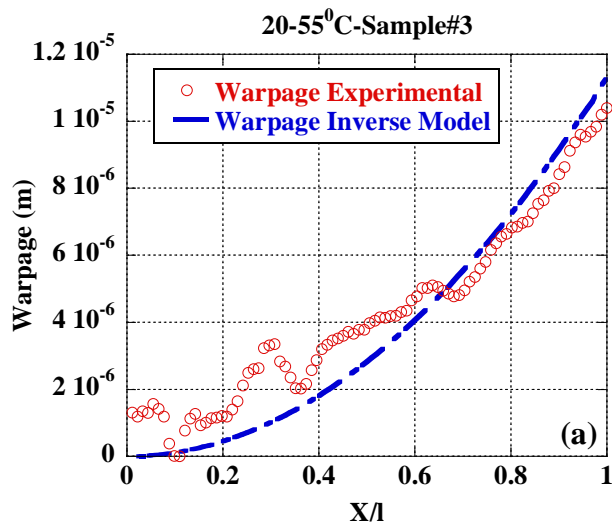


Figure 36: Typical 3-D graphical representation of measured warpage at temperature for sample#17 diagonal lines along LTRB (left-top to right-bottom) and LBRT (left-bottom to right-top).



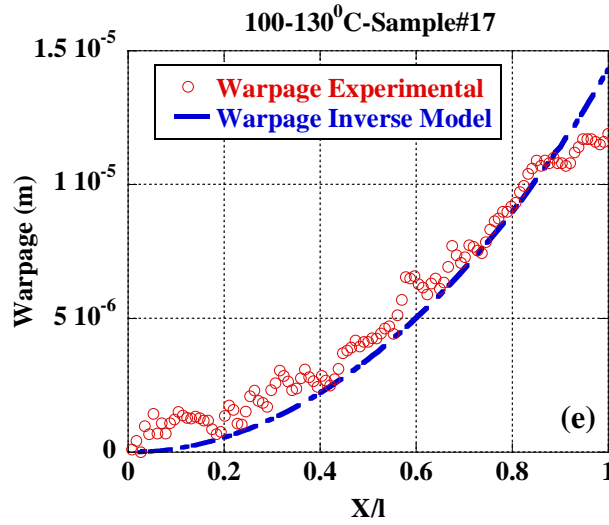


Figure 37: Typical results of predicted relative warpage over the length of the module using HAEIM compared with experimental measurements for (a) Sample#3 at $\Delta T=35^{\circ}\text{C}$ (20°C to 55°C), (b) Sample#5 at $\Delta T=57^{\circ}\text{C}$ (160°C to 217°C), (c) Sample#11 at $\Delta T=35^{\circ}\text{C}$ (20°C to 55°C), (d) Sample#13 at $\Delta T=35^{\circ}\text{C}$ (20°C to 55°C), (e) Sample#17 at $\Delta T=30^{\circ}\text{C}$ (100°C to 130°C)

Table 14: Bilinear material properties of the trilayer constituents determined using HAEIM

Materials Properties		Substrate Laminate		Underfill			Silicon Die
		VT-47	GETEK	LOCTITE 3593	LOCTITE 3536	HYSOL FP4531	
Elastic Modulus (GPa)	pre- T_g	23-24	18-19	0.8	0.19-0.3	1.9	98
	Post- T_g	15-17	15	0.01	0.011	0.08	
Coefficient of Linear expansion (ppm/ $^{\circ}\text{C}$)	pre- T_g	6-7	5-6	50	63	28	2.5
	Post- T_g	10.5-11.5	11.2	160	178	104	
Poison's ratio		0.23	0.24	0.35	0.34	0.31	0.22
Turning Point Temp. ($^{\circ}\text{C}$)		160	160	50-100	~50	~160	-

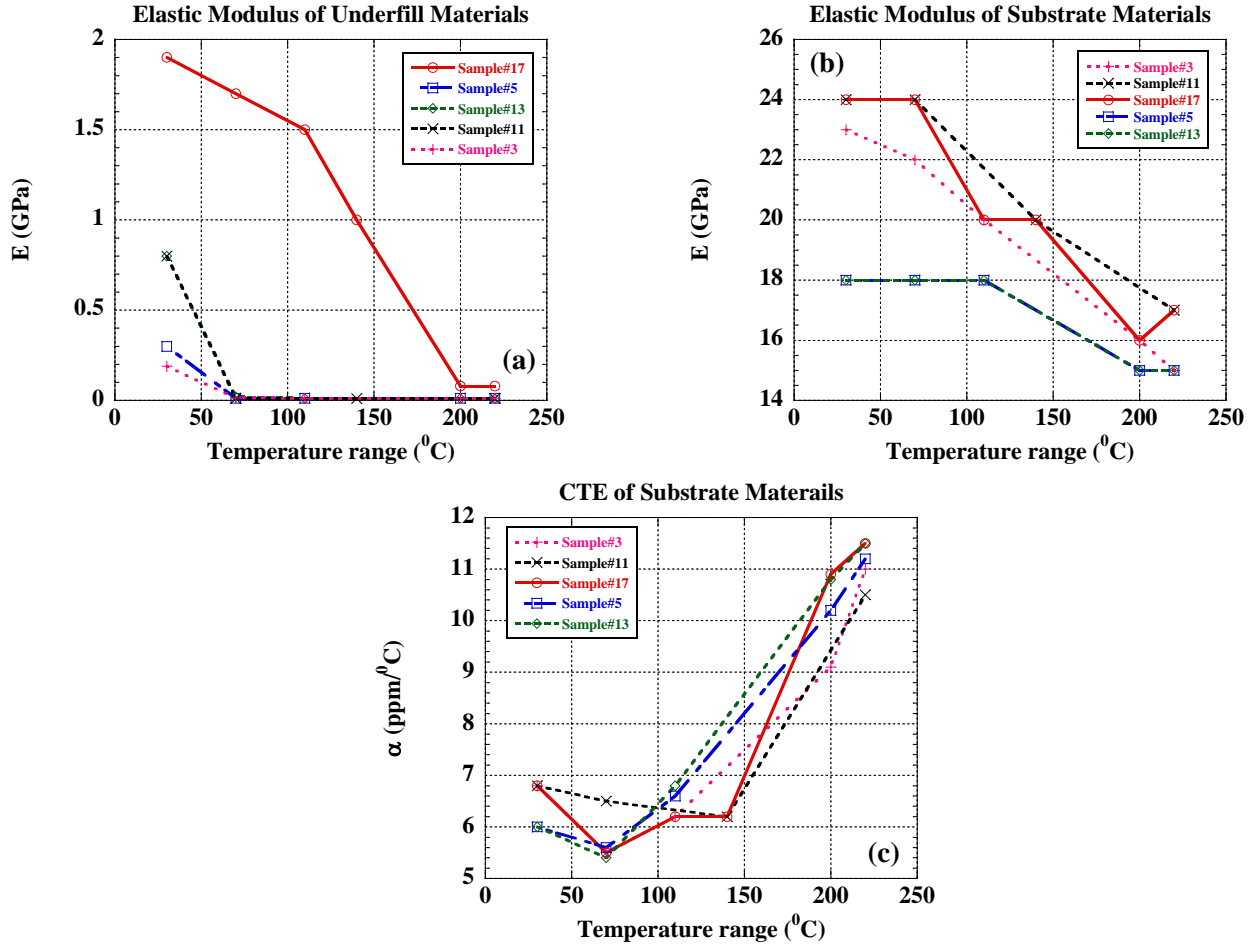


Figure 38: HAEIM predicted mechanical properties versus temperatures a) Underfill materials Elastic Modulus, b) Substrate Elastic Modulus c) Substrate CTE

5.1.2 Warpage models comparisons

Comparisons have been made between the results of the warpage predictions employing the proposed model, Suhir models [4,98] and experimental measurements, using the same material properties. Figure 39 represents these comparisons for different samples at different temperature ranges. Results indicate a good correlation between the proposed model and the experimental data. A large deviation is being observed between the experimental data and the Suhir presented models. The consideration of the non-local foundation method in present study leads to a more accurate estimation of interfacial shear behaviour of trilayer structure which consequently results in more accurate warpage predictions.

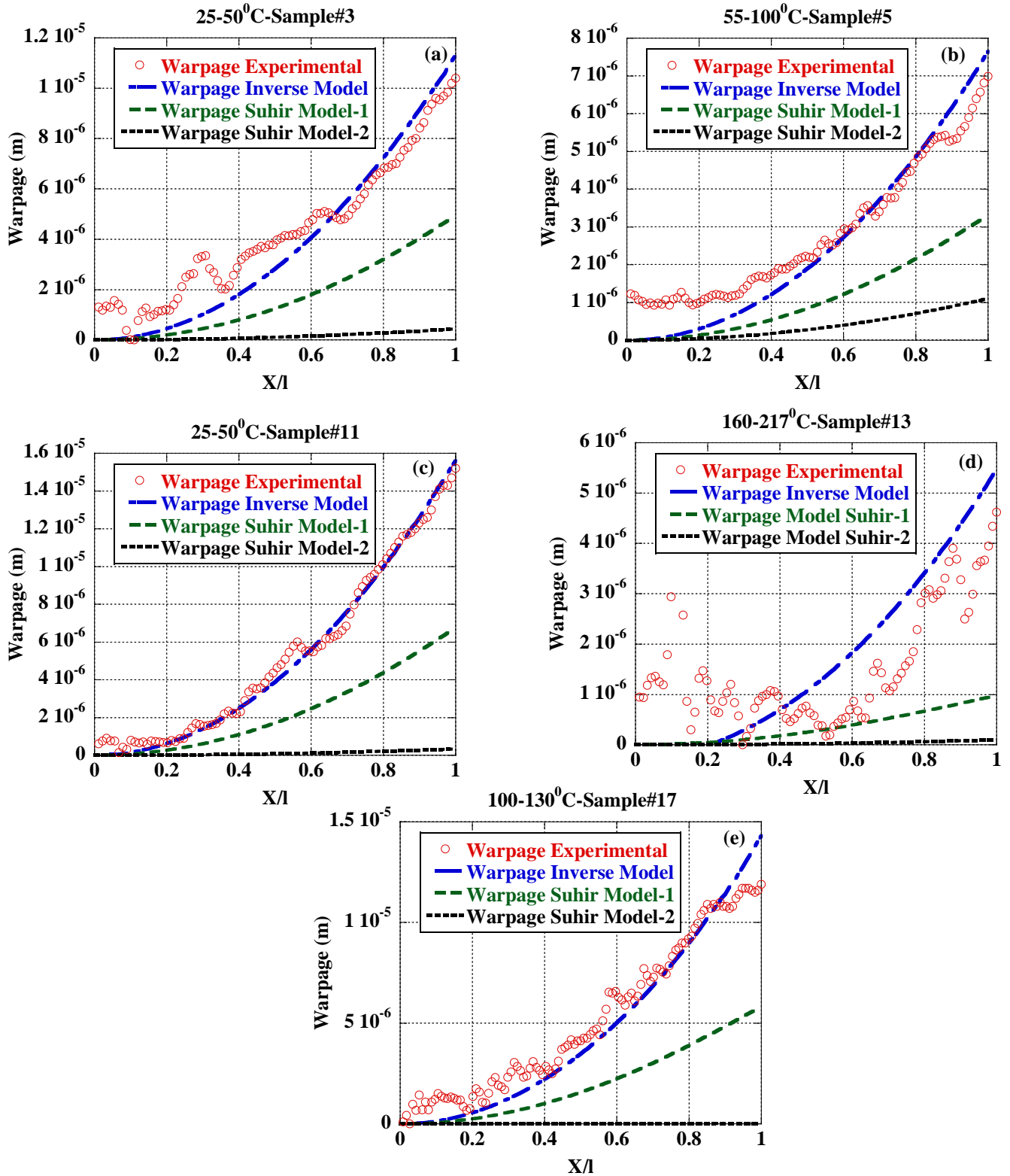


Figure 39: Typical results of comparison between the warpage obtained from experiments and analysis using present model and Suhir models a) Sample#3, b) Sample#5, c) Sample#11, d) Sample#13 and e) Sample#17.

5.1.3 Interfacial stresses and strains

The results for the analytical modeling of interfacial stress-strain, as well as the experimental measurements for the peel strain, are presented in this section. The interfacial peel strains are later evaluated against in-plane measurements of peel strain. Results of interfacial stresses obtained through the proposed models are also compared with the Suhir [5] model.

5.1.3.1 In-plane strain measurements results of side-section of trilayer

The results of the in-plane strain measurements under thermal cycle at the interfacial layer are presented. The peel stress and moment are at the edge to maintain the interfacial compatibility. This action provides a tensile stress at the free edge [75]. Figure 40 represents the highest magnitudes at the centre of the interfacial layer and are in tensile condition (Refer to section 4.1.5 for more detail of the location of measurements).

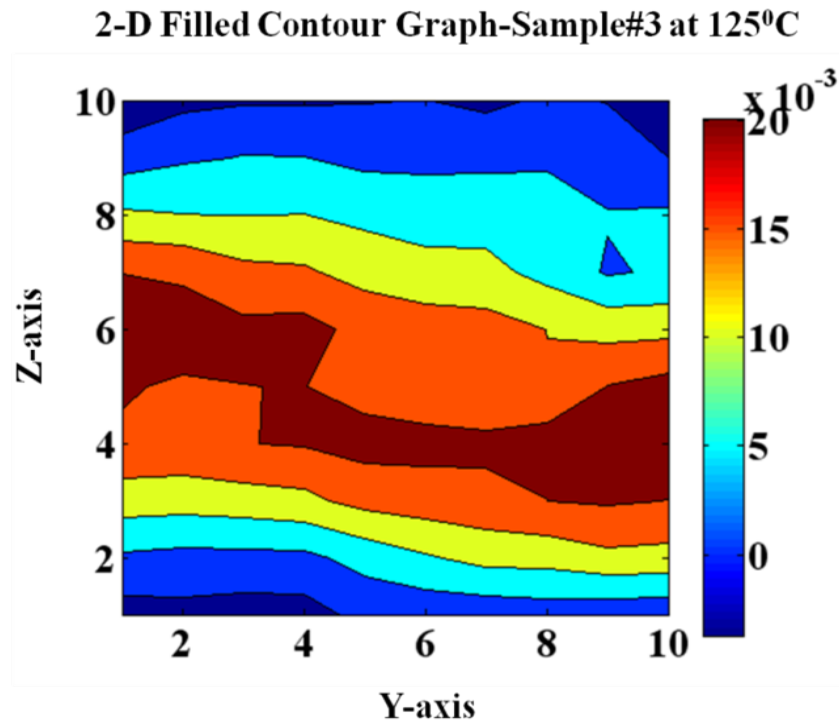


Figure 40: Typical contour pattern of strain measurements at T=125°C.

5.1.3.2 Interfacial stresses results based on analytical modeling

The results of the two-dimensional closed-form solutions of interfacial stresses are being presented in this section. The models represent the peel and shear interfacial stresses that are developed along the interface of the die attachment layer under thermal loading under the plane-strain condition (Figures 41 and 42).

The results for the interfacial shear stress satisfy the zero stress condition at the free edges. The results of peel stress follow the self-equilibrating nature of this stress. Present peel and shear stress comparisons show that the magnitude of shear stress is greater than that of peel stress. Table 15 shows the maximum peel stresses determined using present analytical model for different samples. It indicates that both stresses are higher under room temperature conditions. Stresses decrease as temperature increases while reaches the T_g of the underfill. Above T_g , the stresses continue to decline with a slower rate.

In the cases of sample#3 and sample#11 once the temperature reaches the T_g of the underfill the cylindrical bending of the substrate layer around the Y-axis causes the peel stress to increase (Refer to Figure 36). This can be observed more in the case of these types of samples that have substrate with higher expansions in comparison with the sample #5 and sample#13 (Refer to Table14). Away from the free edge the peel stress becomes compressive (negative). The peeling stress takes place from the action of one layer on the other layer, normal to their interface.

The integrations of the peel stress over the zones in which the stresses are tensile and compressive give equivalent tensile and compressive forces acting through a point located respectively in the tensile and compressive zones. These equivalent forces are necessarily equal and opposite to maintain equilibrium of forces in the normal direction [32]. Hence, the integration of the peeling stress over the half of the length of the trilayer structure (Figure 41) indicates the equilibrium of forces in the normal direction.

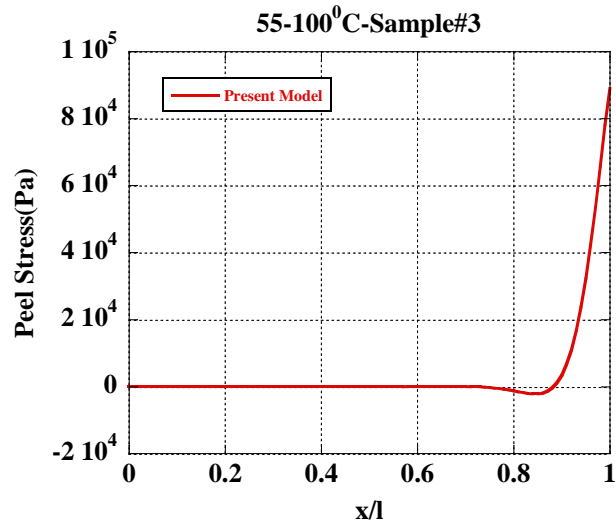


Figure 41: Typical plot of modeled peel stress along the mid-cross section of trilayer structure

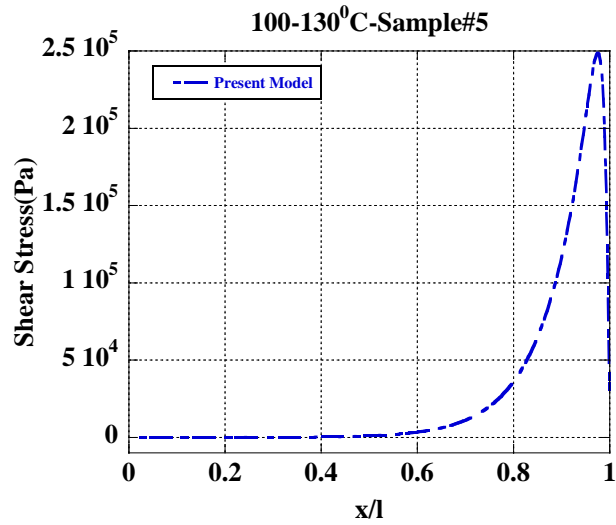


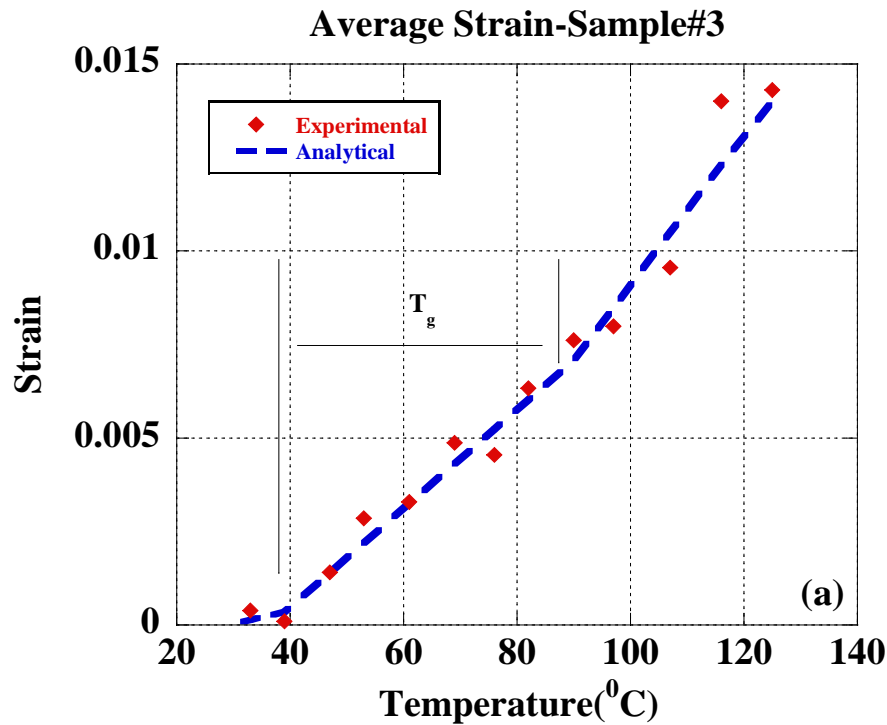
Figure 42: Typical plot of modeled shear stress along the mid-cross section of trilayer structure

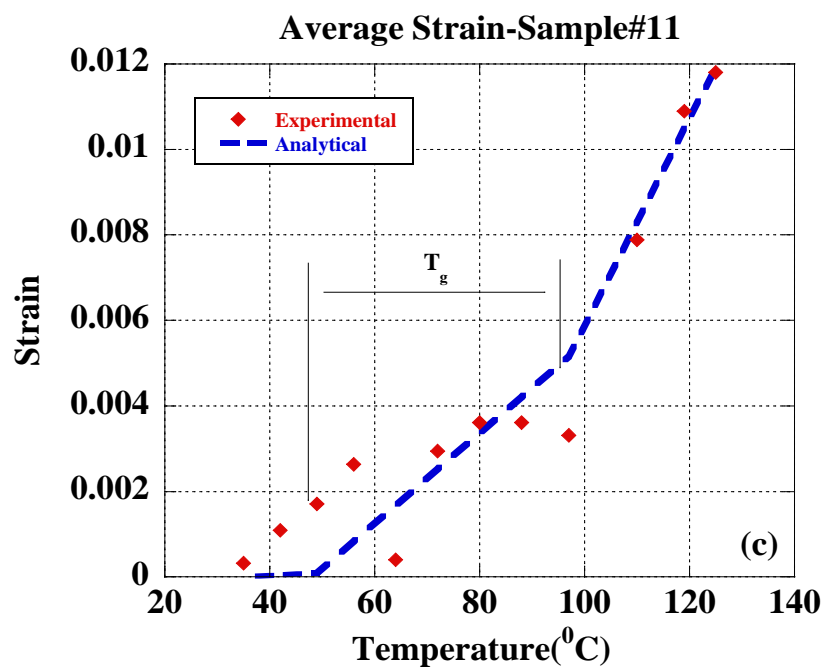
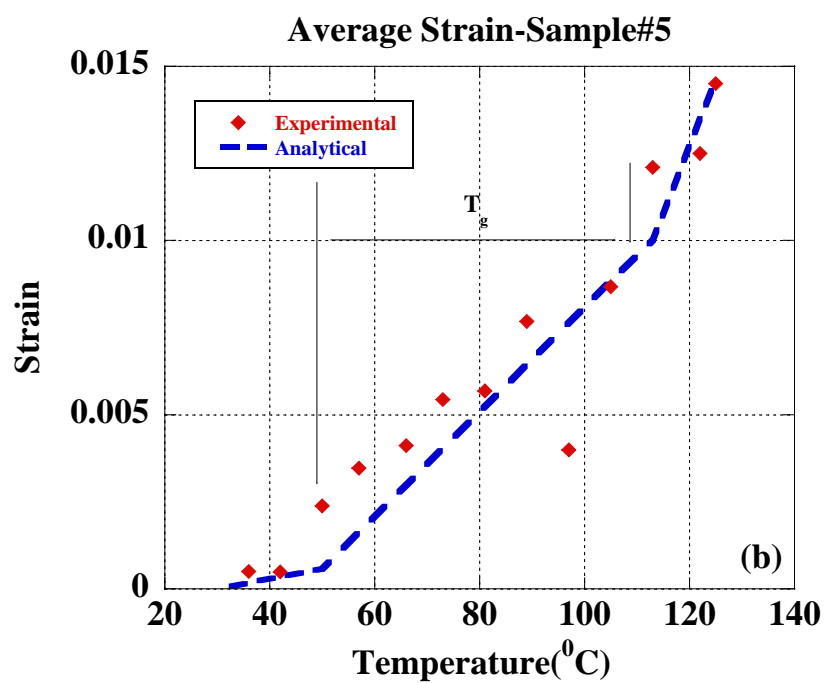
Table 15: Maximum peel stresses determined using present analytical model for different samples

Temp. Range (°C)	Max. Peel Stress (MPa)			
	Sample#3	Sample#5	Sample#11	Sample#13
25-55	0.217	0.165	0.174	0.114
55-100	0.0778	0.089	0.057	0.0625
100-130	0.126	0.0728	0.0581	0.00733

5.1.3.3 Results of comparisons between analytical and experimental peel strains

To further verify the results of the stresses along the interfaces, maximum peel strains have been measured from room temperature (25°C) up to 125°C and later compared with the results of predicted ones. The bilinear behaviour of the underfill materials is observed through the change of slopes, as the strain increases versus temperature. An average strain within the area of measurement (Refer to Chapter 4) has been compared with results from analytical modeling for peel strain along the interface. The results of comparisons are represented in Figure 43 and demonstrate a good agreement between the model and the experiments.





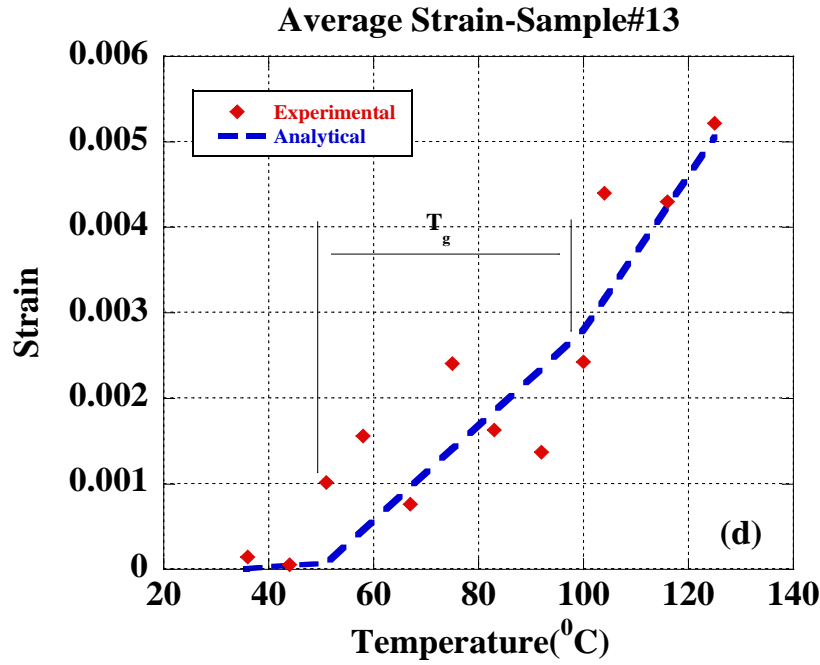


Figure 43: Plots of average measured strain versus temperature for a) sample#3, b) sample#5, c) sample#11 and d) sample#13

5.1.3.4 Interfacial peel stress-models comparisons

Comparisons have also been made between the results of the peel stress predictions employing the proposed model and the Suhir model [5] using the mechanical properties determined through HEAIM. Figure 44 represents these comparisons for different samples in different temperature ranges. Results of comparisons indicate that the peel stresses predicted by Suhir model [5] are not self-equilibrated through the zone and the maximum peel stress predicted by Suhir model [5] at the edge are lower than those predicted by the present model. Further comparisons indicate that away from the free edge the peel stress becomes compressive (negative) which is found that Suhir model [5] lacks to predict this phenomenon. The sensitivity of peel stress to the temperature range and the samples constituents' thermomechanical properties are presented in these figures. More results are also available for different temperature range and different samples in Appendix 6.

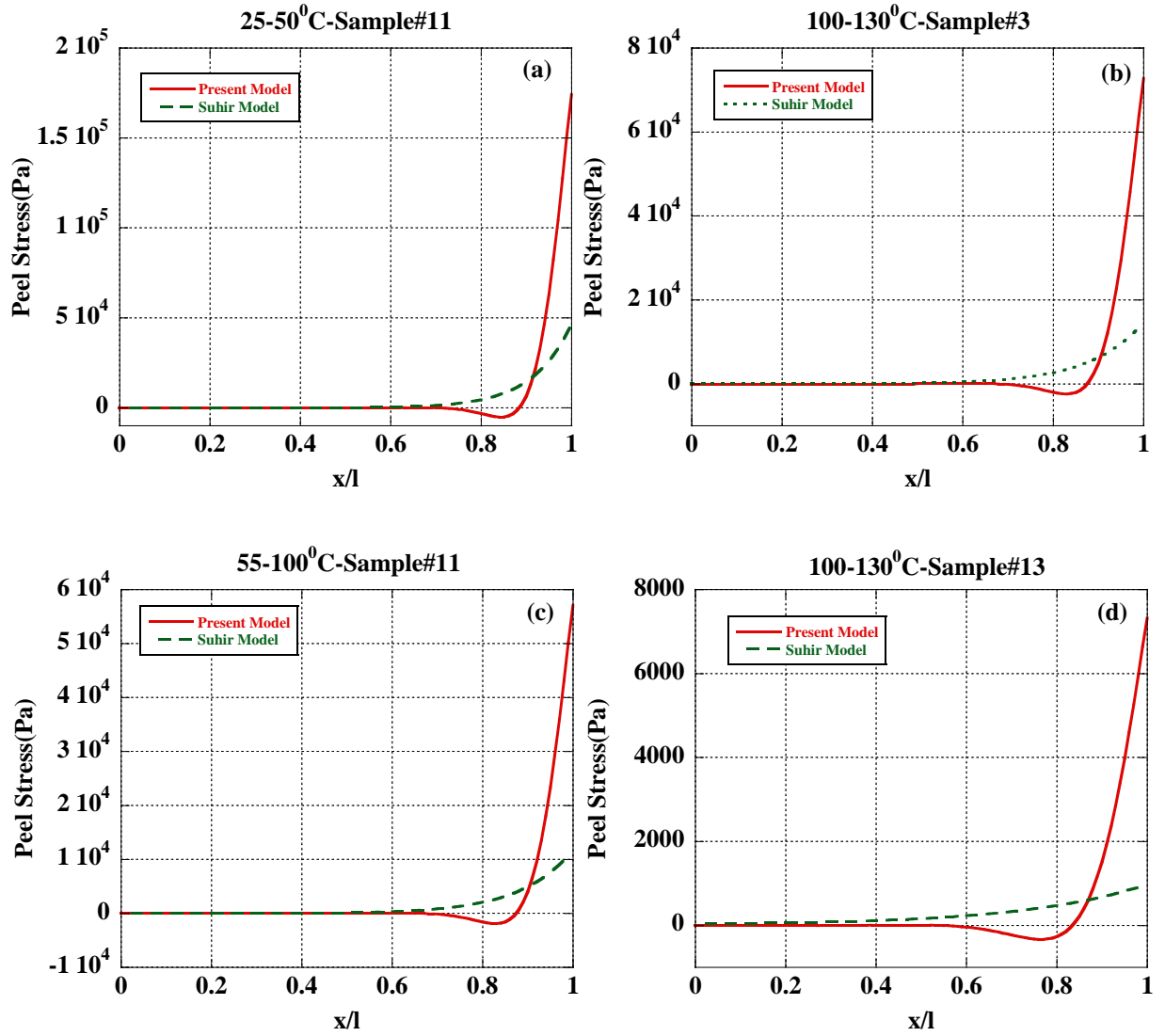


Figure 44: Typical results of comparison between the peel stresses obtained from analysis using present model and Suhir model a) Sample#3, b) Sample#5, c) Sample#11 and d) Sample#13

5.2 Viscoelastoplastic behaviour of SAC305 interfacial alloy

This section presents the results of the microstructures of cast samples as well as the comparison carried out between the microstructures of cast samples and real solders joints. Parameters related to elastic, plastic and steady state creep behaviour of the SAC305 interfacial solder alloy are also presented.

5.2.1 Microstructural assessment of samples

The microstructural behaviour of Sn3.0Ag0.5Cu (SAC305 with 3.0% silver (Ag), 0.5% copper (Cu) and 96.5% of Tin (Sn)) alloy, as-cast and real joints are compared in this section. The results of microstructural behaviour assessment are presented as follows.

Ternary alloy system of Sn3.0Ag0.5Cu with Tin (Sn)-rich and binary eutectics of Sn-Cu (Cu_6Sn_5) and Sn-Ag (Ag_3Sn) are widely used in solder joint layer of trilayer structures within microelectronics industry, as the primary cases studied in this study. The ternary alloy system has a eutectic composition of 3.5 wt.% Ag, 0.9 wt.% Cu at a temperature of $217.2 \pm 0.2^\circ\text{C}$ [99].

Figure 45 shows Sn3.5Ag0.5Cu solder views indicating examples of various regions of Sn, Ag_3Sn , Cu_6Sn_5 and $\text{Sn} + \text{Ag}_3\text{Sn} + \text{Cu}_6\text{Sn}_5$ using secondary electron image (SEI) and back scattered electron composition (BEC) for as cast solder and real solder joint. The as-cast specimens had very similar microstructure to that found in real solder joints. The smaller grains in real joints presented in Figure 45b in comparison with those of the as-cast alloy presented in Figure 45d are possibly the consequence of a faster cooling rate after soldering in real applications.

Energy dispersive spectroscopy (EDS) was employed in order to perform the composition analysis on large intermetallics of the Cu_6Sn_5 and Ag_3Sn and a Sn dendrite arm to determine the composition of the various phases in as-cast and real solder joint samples. The results of these analyses in Figure 34 indicate the low solubility of Ag in Cu_6Sn_5 and the low solubility Cu in Ag_3Sn as well as for Cu and Ag in Sn. This phenomenon has been repeatedly addressed in various studies [99].

Various evaluations of the experimental data between as-cast and real solder joint samples conform to the results from other studies [99, 100, 101]. Microstructural analysis of the SnAgCu solder consisted of essentially pure Sn matrix with elongated intermetallic Ag_3Sn and tiny round intermetallic Cu_6Sn_5 particles dispersed within the Sn matrix with

Ag_3Sn (with around 30 wt.% of tin) and Cu_6Sn_5 particles (with around 60 wt.% of tin) as shown in Figure 46.

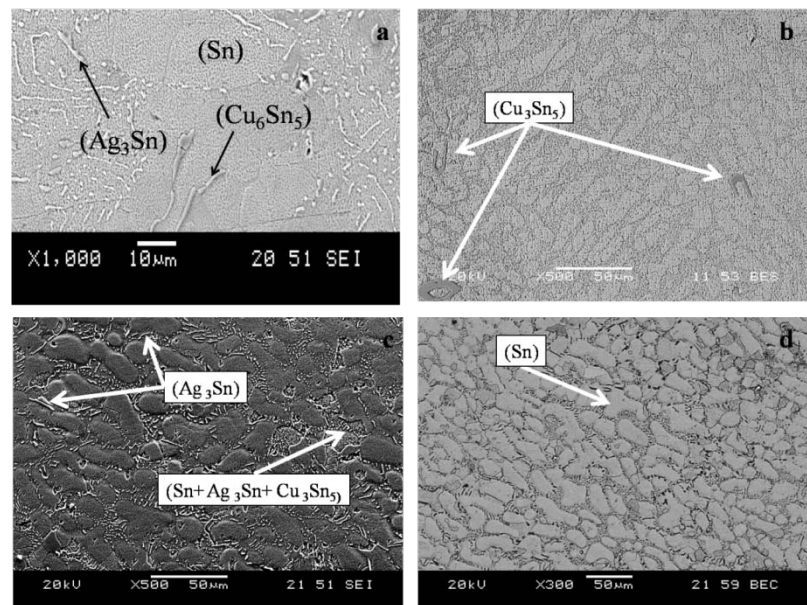
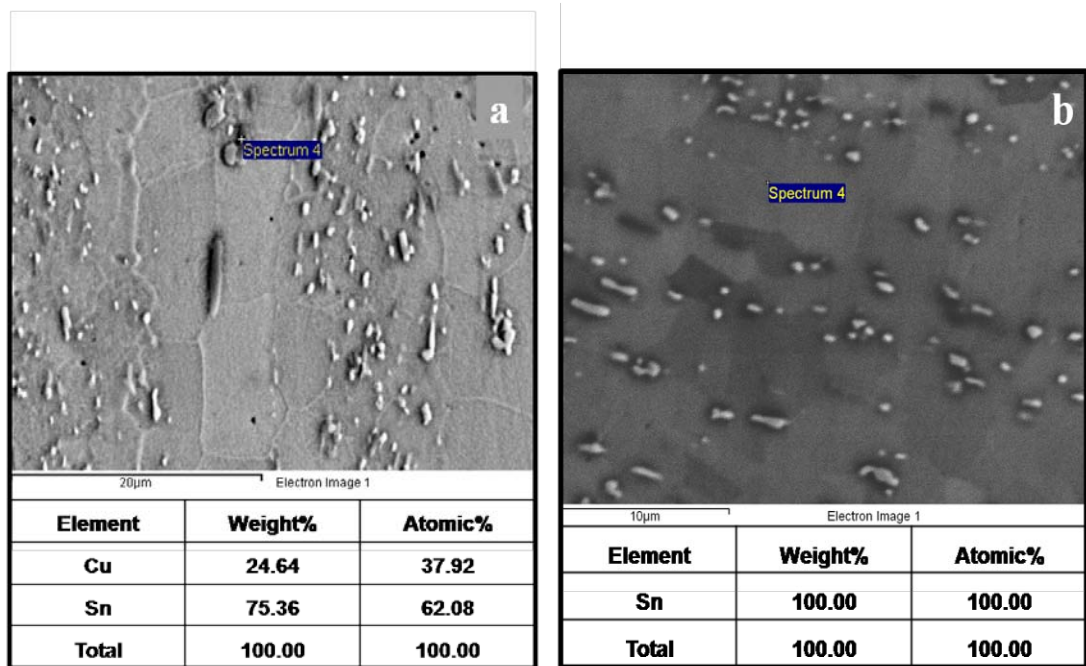


Figure 45: Microstructures of Sn3.5Ag0.5Cu solder view indicating examples of various regions of Sn, Ag_3Sn , Cu_6Sn_5 and Sn + Ag_3Sn + Cu_6Sn_5 using: a) secondary electron image (SEI) for real solder joint, b) back scattered electron composition (BEC) for real solder joint, c) SEI for as cast solder and d) BEC for as cast solder.



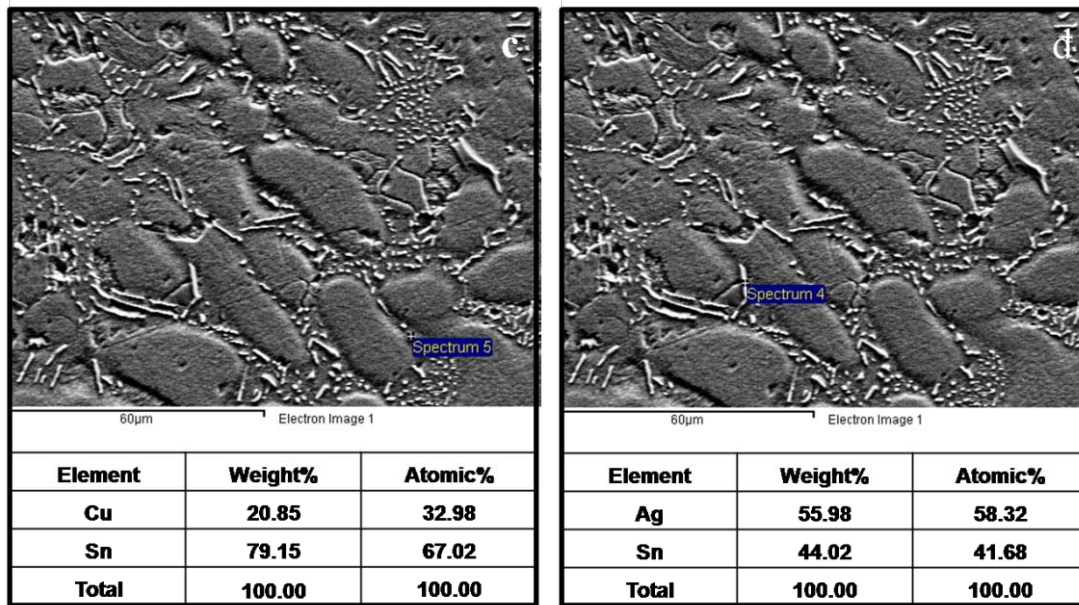


Figure 46: Summary of weights and atomic percent of elemental composition of the analyzed volume of phases of Sn, Ag₃Sn and Cu₆Sn₅ of SAC305 using EDS in: a) real solder joint, b) as casted solder alloy, c) as casted solder alloy and d) as casted solder alloy.

5.2.2 Test Matrix

In order to obtain creep constitutive properties of SAC305 interfacial alloy, a number of isothermal constant load tests were conducted. Table 16 summarizes the test matrix for these tests. Creep tests were designed in a way to embrace the conditions that real electronic packages are usually assessed based on, for their durability and reliability [36]. Details of creep tests at 0°C, 25°C, 70°C, 100°C and 165 °C and constant loads from 14.9 to 87.7MPa are presented in Appendix 9, including the samples geometries, nominal stresses, stress concentration factors and local stresses. Stress concentration factors of 60° V-shaped notches under tension are also tabulated for different thickness to width and radius of notch to width ratios.

Table 16: Test matrix for monotonic loading creep tests.

Solder Alloy	Test Type	Test Conditions				
SAC305	Creep(Load Control)	0°C	20°C	70°C	100°C	165°C
	Number of Samples	4	4	6	4	3

5.2.3 Steady-state creep constitutive behaviour

Tests were conducted using the Micro-tester with the thermal chamber attached. All data was experimentally determined at 0°C, 25°C, 70°C, 100°C and 165 °C. A typical strain versus time behaviour for SAC305 solder alloy during creep test under constant temperature and load, hence constant engineering stress is plotted in Figure 47. The three regions of creep and early stage of elastic-plastic are recognized (Refer to Figure 48). The steady-state of creep raw data of SAC305 versus tensile local stresses and isothermal lines of the hyperbolic sine model are plotted in Figure 49.

It was realized from Figure 49, that the creep deformation increases with increasing stress levels. Higher stresses will accelerate the movement of dislocations, which includes dislocation gliding and climb [36, 57]. Higher stresses will also induce greater grain boundary gliding. Figure 49 also indicates that higher temperatures induce more severe creep deformation in solder alloy. Creep deformation is diffusion controlled [36, 57], so a higher temperature will lead to a higher diffusion rate and a higher creep rate. It was found that dislocation gliding and grain boundary sliding accompanied with thermal diffusion are the major creep mechanisms for creep deformation.

Over 21 datasets were used in regression analysis and development of the creep model. Most of the data fall within or close to the correlation lines. A regression method has been utilized to determine the best fit for the steady-state constants (Refer to appendix 9). The model lines show that the steady state creep strain rates are strongly stress and

temperature-dependent. For convenience, this relationship is repeated in Equation (100) below:

$$\dot{\varepsilon} = C \left[\sinh(\alpha\sigma) \right]^n \exp\left(\frac{-Q}{kT}\right) \quad (100)$$

where k is the universal gas constant, T is the temperature in Kelvin, σ is the local stress, α and C are material dependent constants, n is the stress exponent, and Q is the activity energy. The normalized tensile strain rate is plotted versus tensile stress in Figure 50. Figure 50 suggest that the presented SAC305 creep model provides a reasonable fit of the data.

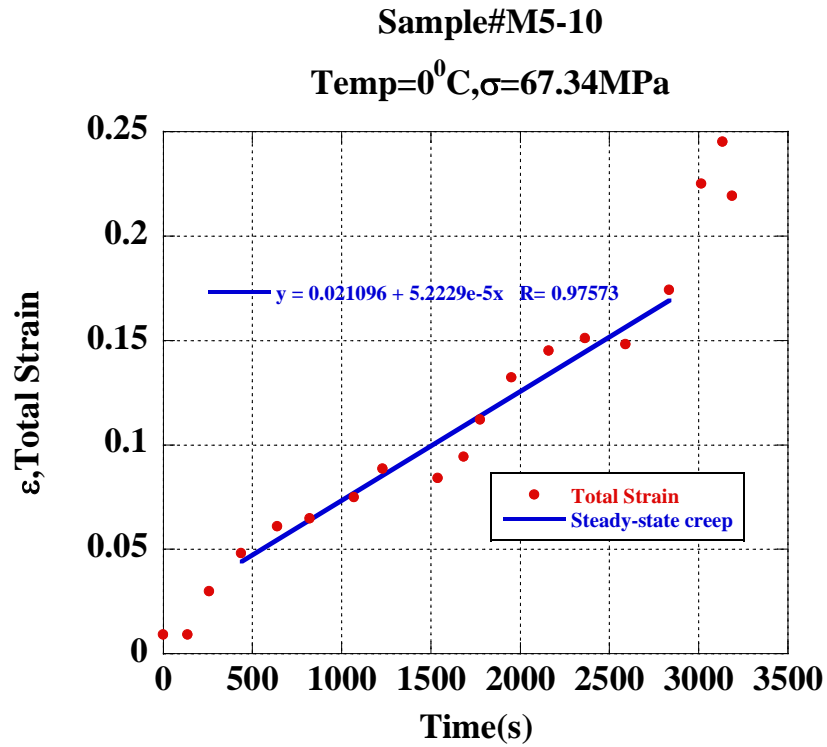


Figure 47: Typical strain vs. time behaviour during creep under constant temperature of 0°C and constant load, hence constant engineering stress, and the steady-state of creep.

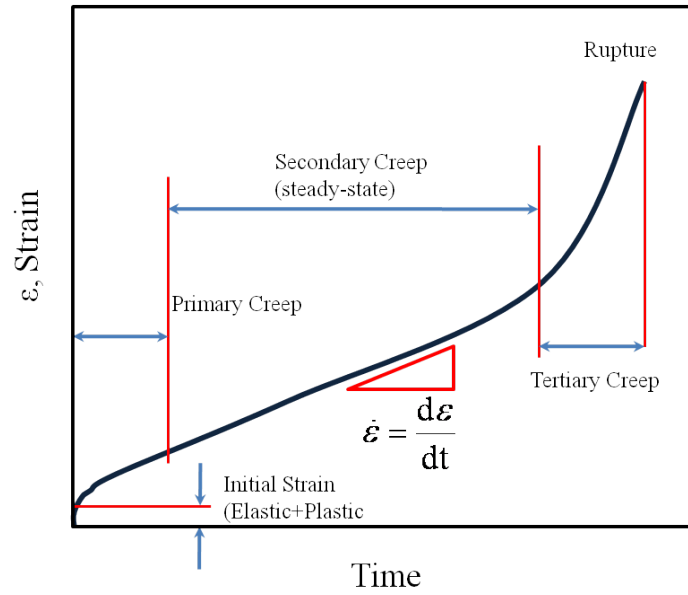


Figure 48: Typical elastic-plastic-creep curve for SAC305 solder alloy under constant stress and temperature.

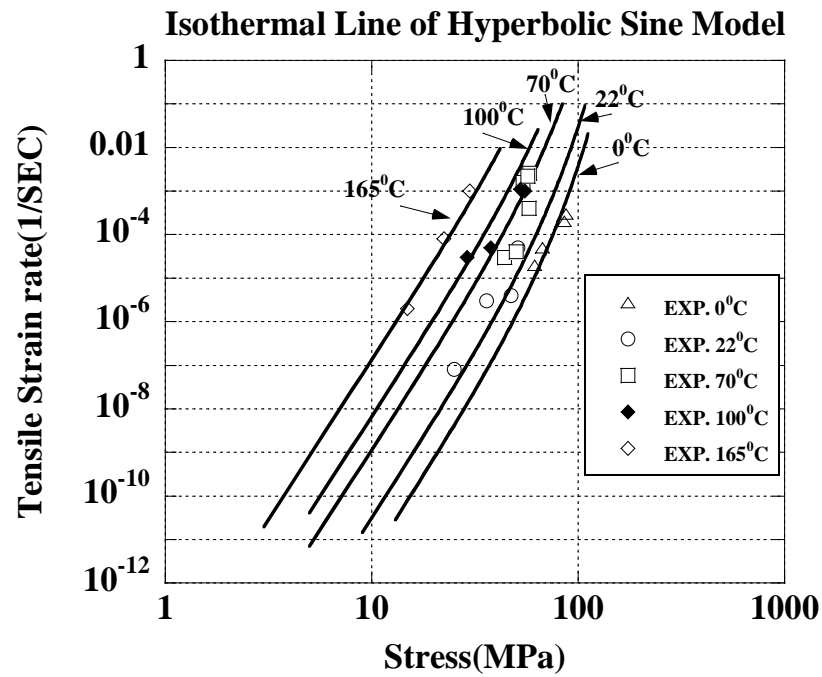


Figure 49: Steady-state behaviour of Sn3Ag0.5Cu (SAC305) solder alloy.

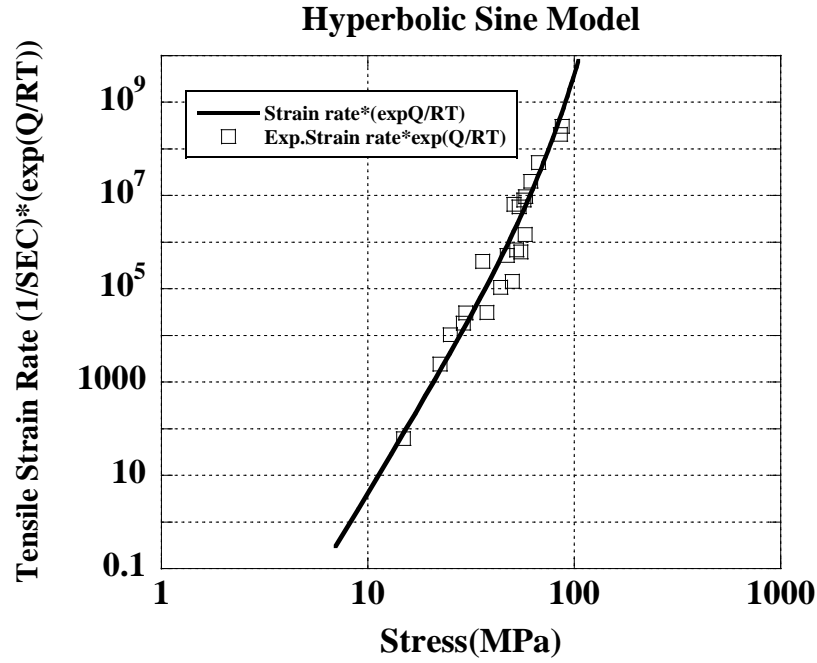


Figure 50: Normalized steady-state behaviour of Sn3Ag0.5Cu solder alloy.

Table 17 provides details of the proposed constants of SAC305 solder alloy following Garofalo hyperbolic sine law constitutive model. The power-law breakdown model gives an activation energy $Q = 62.8 \text{ kJ/mole}$ ($=0.65 \text{ eV}$) which is compared to values presented in previous studies for SAC solder alloys and is about the expected values for dislocation pipe diffusion [48,58]. The exponent of the hyperbolic sine function is $n = 7.3$, which also indicates that the dominant creep mechanism is the dislocation climb assisted by the dislocation pipe diffusion (thermal dislocation detachment) [48, 102, 103].

Table 17: SAC305 solder alloy Garofalo hyperbolic sine law constitutive model constants

	Q (kJ/mol)	n	C	α (MPa^{-1})
Creep Model Constants	62.8	7.3	7.806×10^5	0.0188

5.2.4 Elastic-plastic behaviour

In order to obtain the elastic-plastic model for this solder (SAC305), the following approach is used. An initial, instantaneous strain that develops at the start of a creep test includes both the elastic strain and the inelastic strain presenting the time independent plastic flow (Refer to Figure 48) [104]. An incremental analytical model is used to simulate the elastic-plastic behaviour of solder alloy under different temperatures. Finally, the model constants are determined by a least squares fit to the data at each temperature. The temperature dependent Young's modulus of the SAC305 alloy was determined as follows:

$$E(\text{MPa}) = 52126.2 - 55.35(T - 273) \quad (101)$$

where T is in Kelvin. Figure 51 demonstrates the temperature-dependent Young's modulus of different SAC lead-free solder alloys [104] along with the model presented in this study.

Figure 52 shows a comparison of measured strains with predicted elastic-plastic strains for the SAC305 solder alloy under various temperatures. The rate-independent plastic strain is formulated as follows:

$$\varepsilon_p = C_{pl} (\sigma)^m \quad (102)$$

where

$$C_{pl} = \left[\frac{1}{130 - 0.41(T - 273)} \right]^m \quad (103)$$

$$m = \frac{1}{0.22 - 0.00053(T - 273)} \quad (104)$$

where σ corresponds to local stress, C_{pl} and m are temperature-dependent constants. The elastic-plastic strain-stress curves at five temperatures are shown in Figure 53 for solder alloys. The experimental strains measured at the initial stage of the creep test are compared against curves for all temperatures.

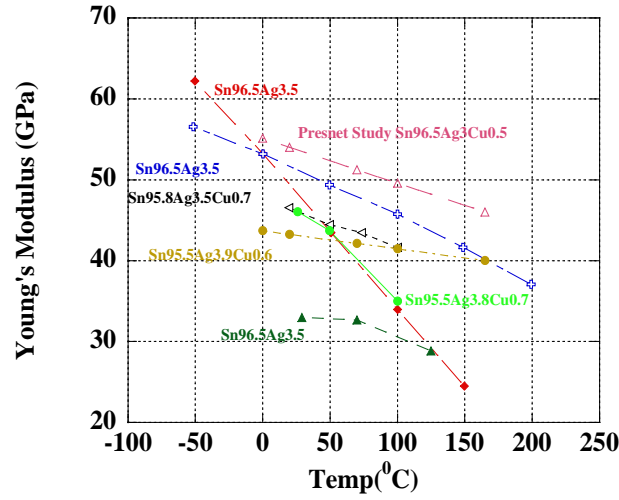


Figure 51: Comparison of Temperature dependent Young's modulus of SAC305 solder alloy measured in this study with the ones reported in literature [34] for SAC solder alloys.

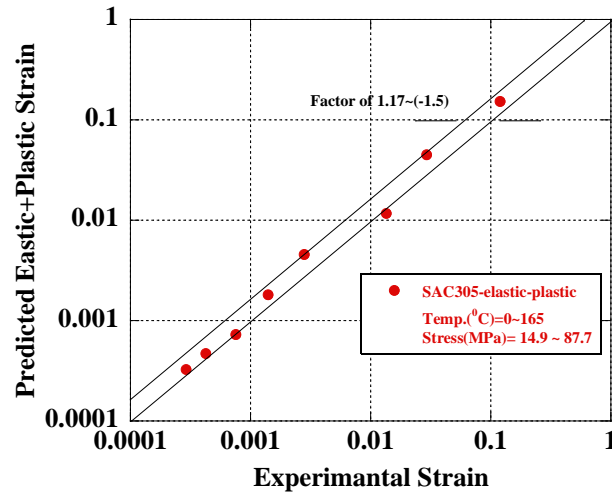


Figure 52: Comparison of measured strains with predicted elastic-plastic strains for SAC305 solder alloy under various temperatures.

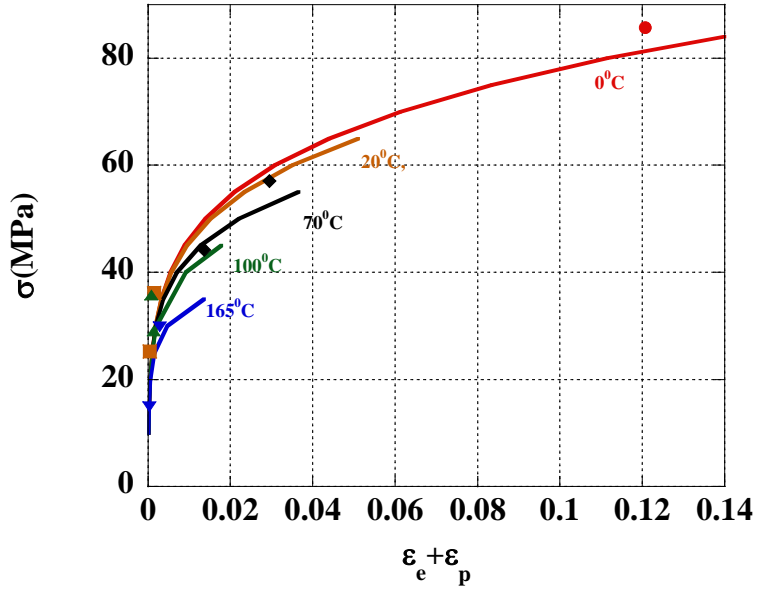


Figure 53: Comparison of temperature dependent elastic-plastic behaviour of SAC305 solder alloy with measured strains.

5.3 Fatigue life prediction of trilayer structure under thermal cycling

The following section represents the results of the life prediction method proposed in this study for trilayer structures under an accelerated thermal cycling condition. The first section shows the results of the life of structures with a dominant layer under the thermal cycling test with the failure criteria defined in an earlier chapter (Refer to section 4.3). The second part presents the fatigue life of the dominant layer of the trilayer structure correlating the energy-based critical plane fatigue damage parameter with the Coffin-Manson equation.

5.3.1 Accelerated thermal cycling test and Weibull distributions

The results of the thermal cycling of structures with different designs are presented in Table 18. The corresponding life of 50% failures of these structures was determined following the Weibull probability plots. Figure 54 shows the plots of failures for each sample in the Weibull plot. Results showed that sample#212(1.0mm lid) outperformed the other structures [29] by having a higher N_{f50} . Further failure analysis performed on each structure type revealed a very similar rupture mechanism for the various types with very similar failure locations. Crack propagation was preferentially on joints located in the die shadow region of the modules at a corner joint namely joint (AA21) or (AN33) (Refer to Figure 32 for more details of joints locations (AA21) and (AN33)).

Table 18: Thermal Cycling Results of Accelerated Thermal Cycling Test

Samples#(type)	Number of tested samples	Thermal Loading Condition	Experimental life (N_f 50%)
309 (1B)	15	0-100°C 5 minutes dwell	3956
36 (2A)	10	0-100°C 5 minutes dwell	4050
344 (4)	20	0-100°C 5 minutes dwell	3913
212 (6A)	6	0-100°C 5 minutes dwell	4550

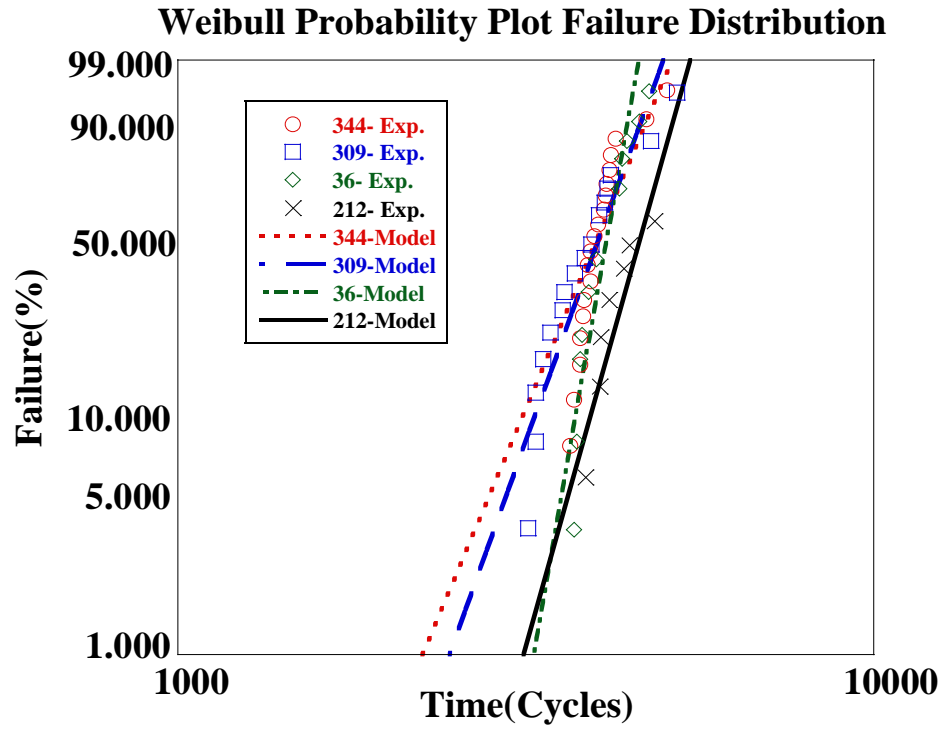


Figure 54: Weibull plots followed JEDEC ATC testing for four samples types [29].

5.3.2 The procedure of fatigue life assessment of trilayer structure

Fatigue lives of the structures with the dominant layer of SCA305 solder alloy have been compared with the results of the fatigue life prediction obtained using the energy-based critical plane damage approach. The procedure of the damage analysis and life prediction has been presented in detail in chapter 3. In following sections the results of each step of the procedure are explained in detail. The final results of life prediction for all the structures are compared with their counterparts from the experiments.

5.3.2.1 *Critical joint of discrete layer of joints*

The critical joint of discrete layer of joints of a trilayer structure was identified using the results from crack length measurements after failure under thermal cycling and the reported FEA studies on joints under a thermal load in literature [29]. Figure 55 demonstrates the location of the joints within the matrix of joints of a discrete layer. While the symmetrical design of the trilayer ensures identical loading on the corner joints, the results of the failure analysis after 4400 cycles indicate the failure occurs mostly under the die shadow region with highest crack length at the PCB side and at outermost diagonal corner solder joints (Refer to Figure 56).

The corner joints experience significantly higher magnitude of stress/strain than the inner joints. The primary failure mechanism of the solder joints in the structures of current study was confirmed to be solder fatigue failure. The premature brittle interfacial failure sometimes occurred in the package side, but nearly all of the failed packages under the studied thermal loading condition, showed the occurrence of the typical fatigue cracks of ductile materials along the plane of maximum shear strain (stress).

Figure 57 shows the 2-D FEA model simulating the trilayer structure under uniform temperature change. The Von Mises equivalent strains at the joints were obtained for diagonal joints under the die shadow region. Strain contours at the critical joints at the two end-extreme locations within the layer are presented in Figure 57. The contours indicate the largest strain/stress at the plane of maximum shear strain/stress along the diagonal with an angle of about 45°.

5.3.2.1.1 Critical corner of the critical joint

The critical joints were further analysed for the location of the critical corners within four corners of the joints, where the cracks initiates. As it has been indicated earlier, the results of the failure analysis on the critical joints after thermal cycles indicated that the cracks were mostly at the PCB side (Refer to Figure 56). Hence the investigation has

been narrowed to PCB side corners. Strains were measured experimentally using the DSC method at these corners. The Von Mises strains were further calculated at the critical corners for different samples. Figure 58 and 59 demonstrate results of the Von Mises strain contours for different samples. The Von Mises-strain contours indicate a diagonal direction where the microcracks during thermal loading within critical joints would initiate.

5.3.2.1.2 Critical plane of the critical corner

Figure 60 shows the strain mapping results for four structures under study. The mapping indicates the results of the ratio between the shear strain over tensile strain (γ/ϵ). For solder alloy ductile material under in-phase proportional fatigue loading of tension and shear, the critical plane of maximum shear stress acts on the free surface in a direction parallel to the length of the crack at an angle of 45° [105]. In this plane the ratio between the shear and tensile strains is expected is $\sqrt{3}$. By mapping this ratio within the surface of the critical corner, the critical planes are generated during loading and unloading. Figure 60 demonstrates the critical planes for the samples studied. The results show sample#309 has the critical joint at location AA-21 with the outer corner as the crack initiation corner, while sample#344, sample#36 and sample#212 have the critical joint at location AN-33 with the inner corner as the crack initiation corner.

5.3.2.2 Energy-critical plane damage parameter

This section demonstrates the results of fatigue analysis. Fatigue life analysis of the structures with fatigue failure of the discrete layer of joints requires measuring the strains at the stabilized cycle during the thermal cycling of the structures. The stabilized cycle has been reached in this study after seven consecutive cycles. The total shear and tensile engineering strains acting on the critical plane during the stabilized cycle of the selected joints for different structures were obtained using the DSC method.

Measured strains were further used in computing shear and tensile stresses acting on the critical plane. The strain partitioning law and SAC305 material viscoelastoplastic constitutive properties presented in Table 19 were used for later computation following an algorithm provided in Appendix 10.

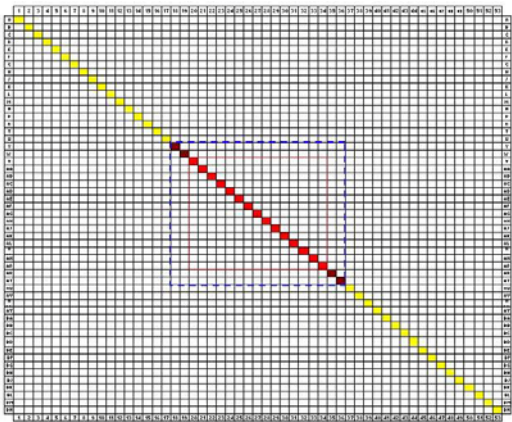


Figure 55: The location of solder joints along diagonal line under the die shadow region.

Figure 61 represents typical results of generated shear and tensile stress-strain points belonging to the stabilized cycle hysteresis loop. Figures 62 and 63 present amplitude and mean values of stresses and strains as well as the peak (P) and valley (Q) points within the cycle.

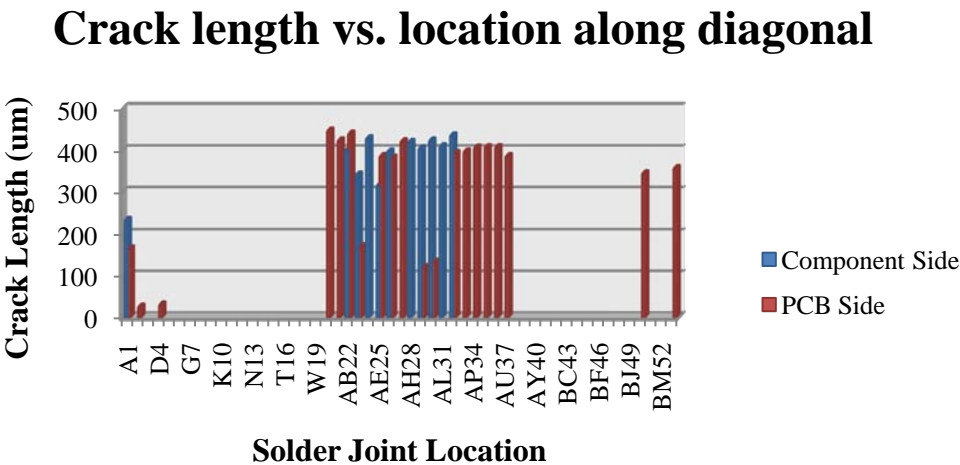


Figure 56: Typical results of crack length measurements of solder joints along the diagonal line, after 4400 cycles of ATC test, for sample#36.

Figure 64 and 65 bring the results of the Mohr's circles generated for shear and tensile stress-strain points of the shear and tensile hysteresis loops. It can be observed that the largest Mohr's circles during loading and unloading correspond to the strains and stresses located at P and Q points of related curves (Refer to Figures 62 and 63).

Once the largest stress and strain Mohr's circles during loading and unloading are separated from other circles, points P and Q can be found on their corresponding circles at an angle of about 45° (Refer to Figures 66 and 67).

The range of maximum shear strain $\Delta\left(\frac{\gamma}{2}\right)_{\max}$ and corresponding normal strain range $\Delta\epsilon_n$ on the largest stress and strain Mohr's circles during loading and unloading of the stabilized cycle were calculated next.

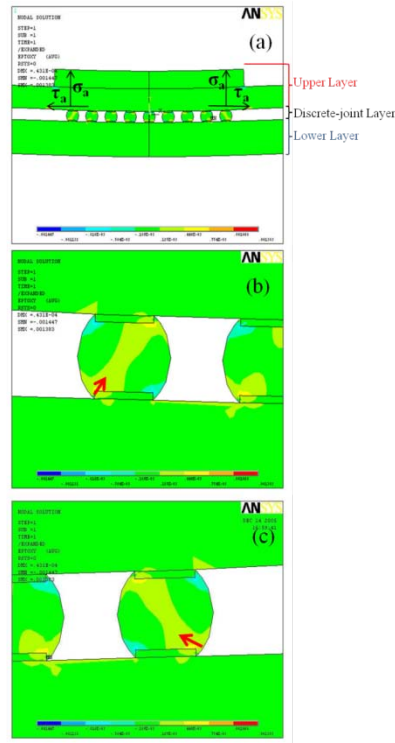


Figure 57: The reported FEM results in a) trilayer structure under multiaxial loading during thermal loading, b) Von Mises equivalent strain during thermal loading within critical joints (left-end joint under die shadow, c) Von Mises equivalent strain during thermal loading within critical joints (right-end joint under die shadow-joint), mapping the direction of the initiation of microcracks [29].

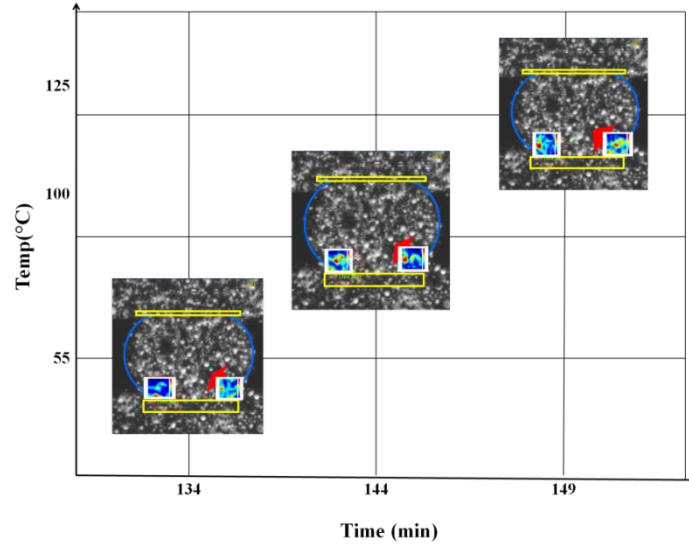


Figure 58: Von Mises-strain contour using DSC strain measurement system mapping the direction of the initiation of microcracks during thermal loading within critical joints (right-end joint under die shadow-joint with location of AA-21).

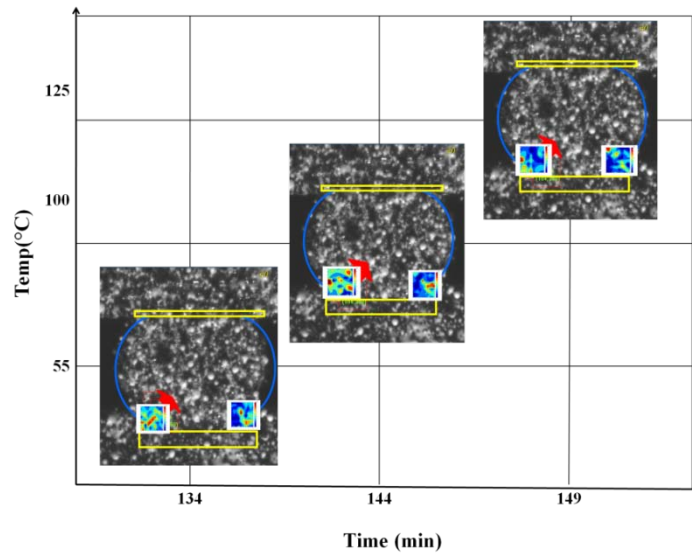


Figure 59: : Von Misses-strain contour using strain measurement results of DSC, mapping direction of the initiation of microcracks during thermal loading within critical joints (left-end joint under die shadow-joint with location of AN-33).

Similarly, the range of the maximum shear stress $\Delta\tau_{\max}$ and the corresponding normal stress range $\Delta\sigma_n$ were calculated from the largest stress Mohr's circles (Figures 67) during loading and unloading of the stabilized cycle. The maximum ranges on both strain

and stress Mohr's circles are defined after rotating the points P and Q to their extreme locations of P' and Q' anti-clockwise on the circles as is indicated in Figures 66 and 67.

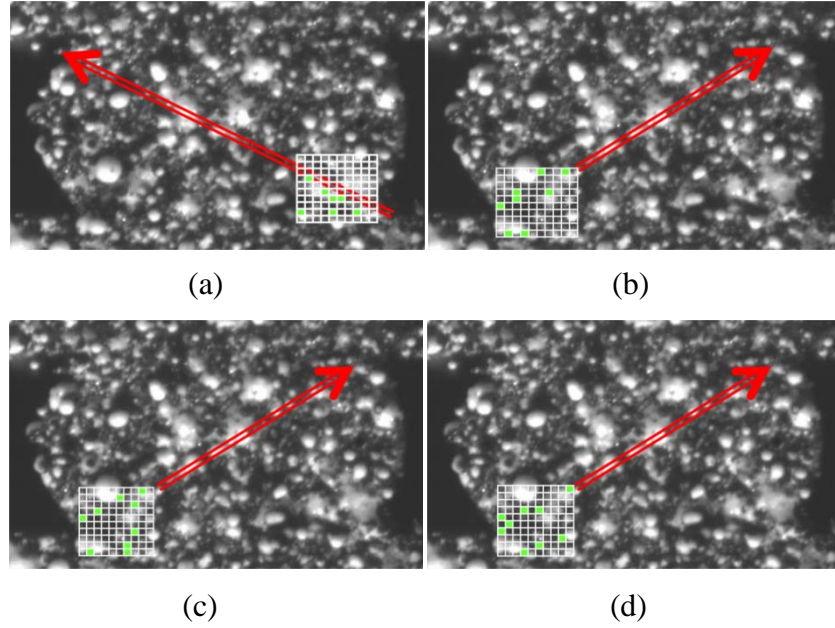


Figure 60: Mapping the ratio between the shear and tensile strains within the surface of the critical corner for a) sample#309 with critical joint at location of AA-21, b) sample#212 with critical joint at location of AN-33, c) sample#36 with critical joint at location of AN-33 and d) sample#344 with critical joint at location of AN-33.

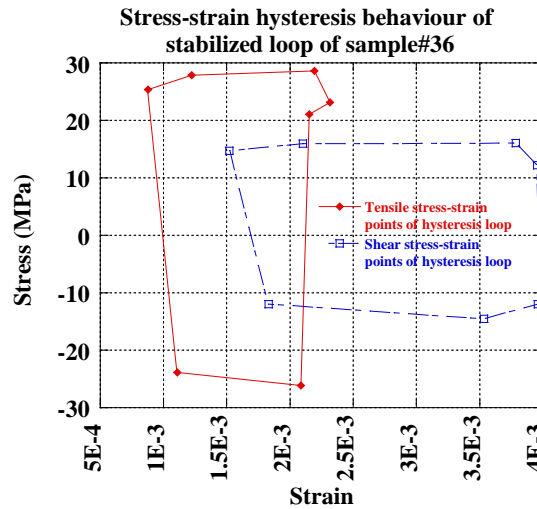


Figure 61: Typical stress-strain hysteresis behaviour of stabilized loop (seventh cycle) for tensile and shear condition.

Table 19: SAC305 solder alloy viscoelastoplastic constitutive properties

Steady-state creep model constants		
Tensile		Shear
$\dot{\varepsilon}_{scr} = C \left[\sinh(\alpha\sigma) \right]^n \exp\left(\frac{-Q}{kT}\right)$		$\dot{\gamma}_{scr} = C \left[\sinh(\alpha\tau) \right]^n \exp\left(\frac{-Q}{kT}\right)$
Q (kJ/mol)	62.8	62.8
n	7.3	7.3
C	7.806×10^5	1.352×10^6
α (MPa ⁻¹)	0.0188	0.0326
Rate-independent plastic model		
Tensile		Shear
$\varepsilon_{pl} = \left(\frac{1}{C_{pl}} \right)^m \sigma^m$		$\gamma_{pl} = \left(\frac{1}{C_{pl}} \right)^m \tau^m$
C _{pl}	$\left[\frac{1}{130 - 0.41(T - 273)} \right]^m$	$(3)^{\left(\frac{1+m}{2}\right)} \left[\frac{1}{130 - 0.41(T - 273)} \right]^m$
m	$\frac{1}{0.22 - 0.00053(T - 273)}$	$\frac{1}{0.22 - 0.00053(T - 273)}$
Elastic constants		
Tensile		Shear
$\varepsilon_e = \frac{\sigma}{E}$		$\gamma_e = \frac{\tau}{G}$
Modulus of Elasticity (MPa)	$52126.2 - 55.35(T - 273)$	$19306 - 20.5(T - 273)$

Note: T is in Kelvin.

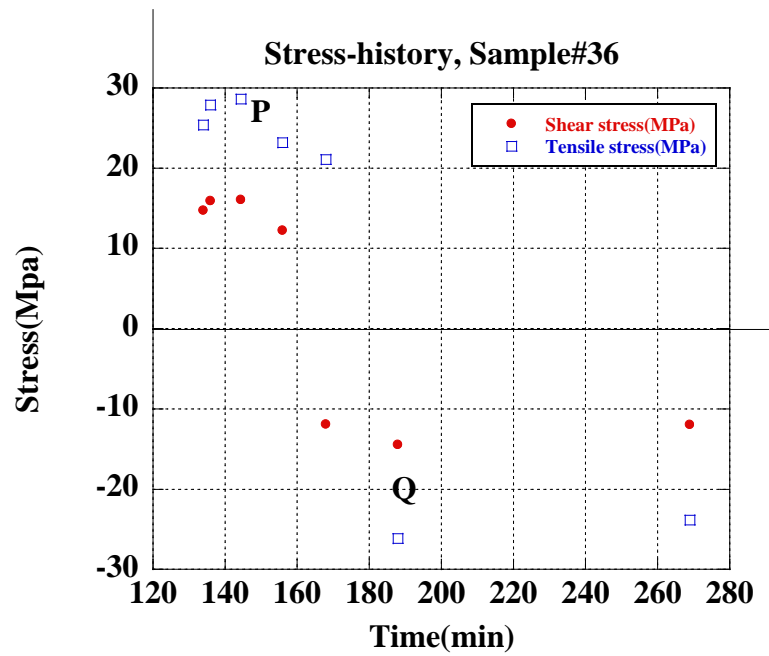


Figure 62: Typical results of proportional loading of tensile and shear with indication of peak point of loading (P) and unloading (Q).

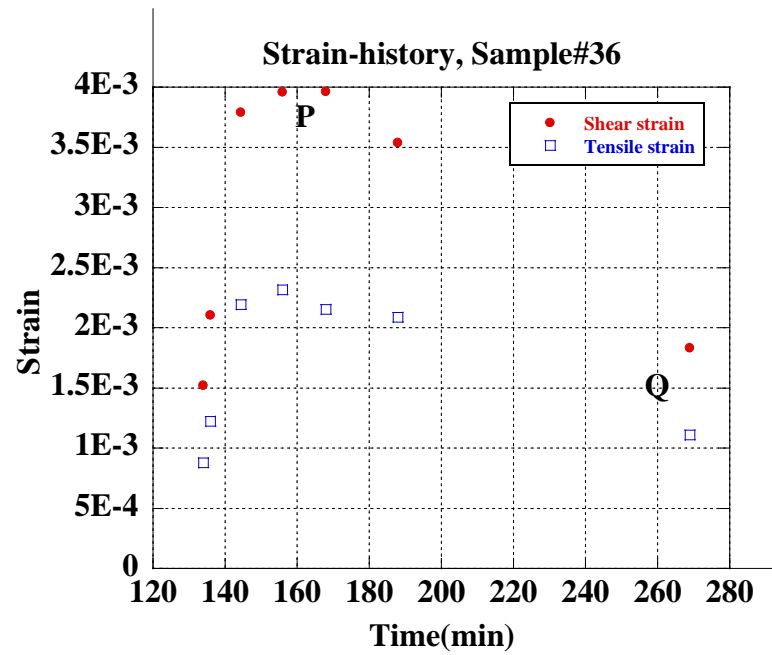


Figure 63: Typical results of shear and tensile strains with in-phase strain path with indication of peak point of loading (P) and unloading (Q).

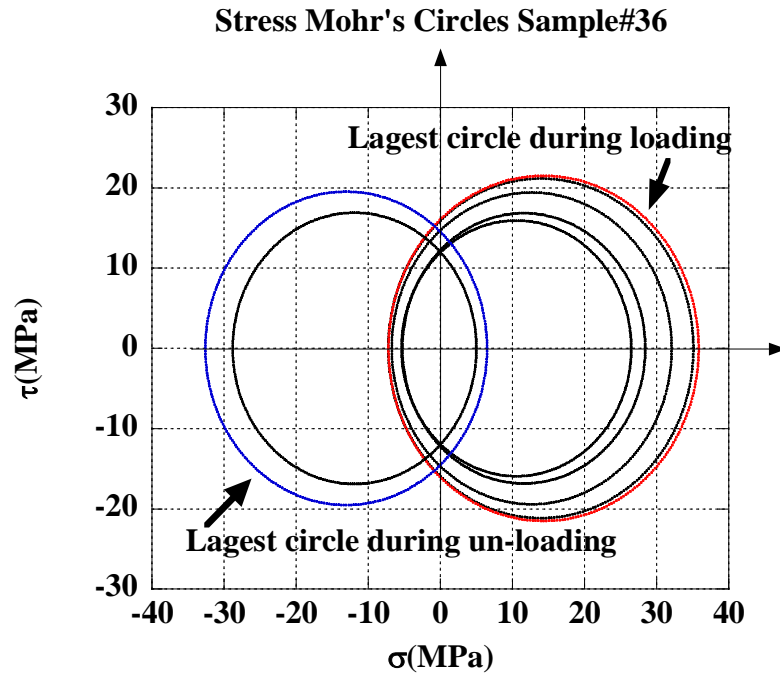


Figure 64: Typical stress Mohr's circle for in-phase path with mean-stress during loading and un-loading of stabilized loop.

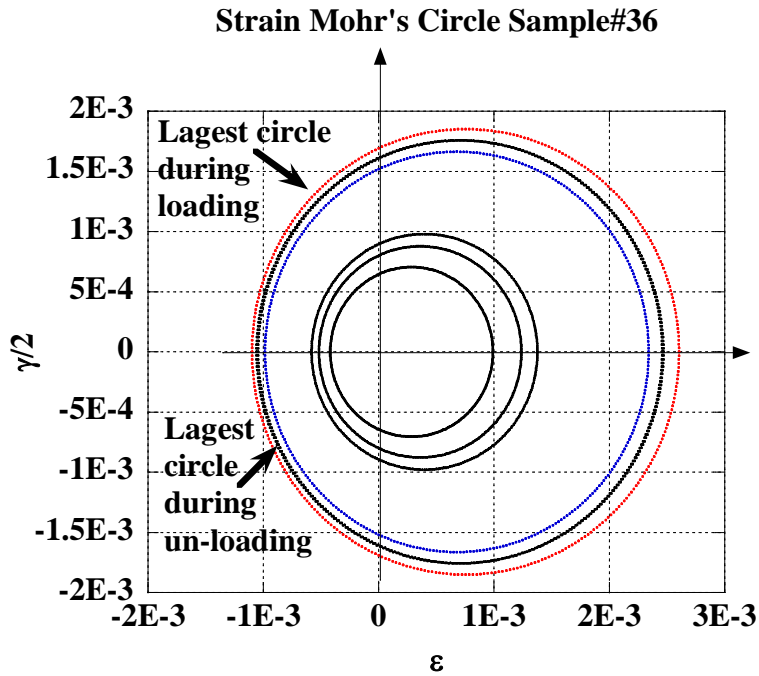


Figure 65: Typical strain Mohr's circle for in-phase path with mean-strain during loading and un-loading of stabilized loop.

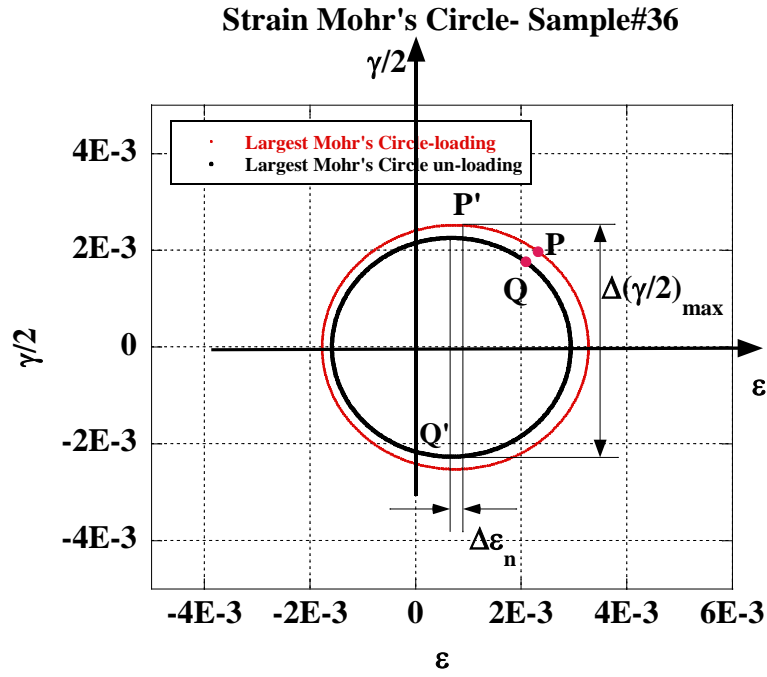


Figure 66: Strain Mohr's circle representing stress components of damage parameters for in-phase path for sample#36 during loading and un-loading of stabilized loop.

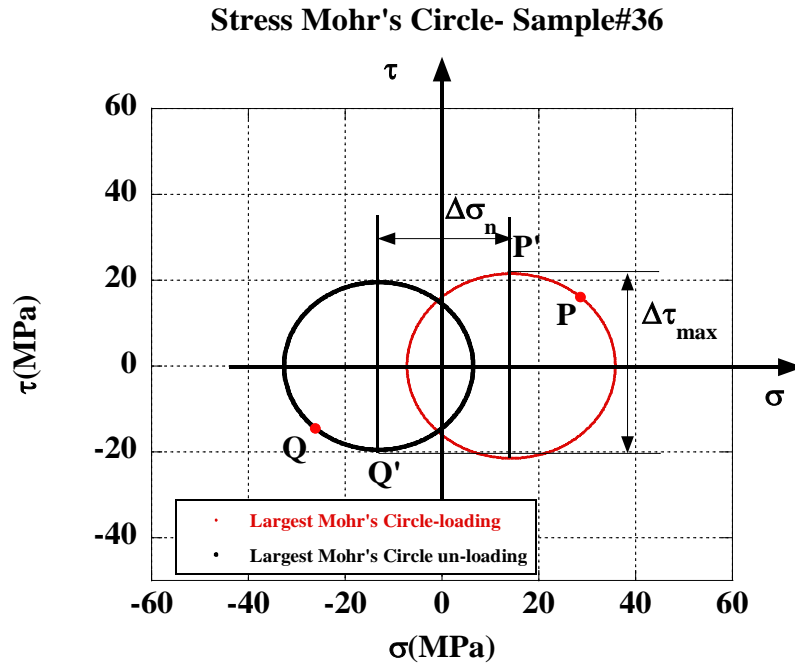


Figure 67: Stress Mohr's circle representing stress components of damage parameters for in-phase path for sample#36 during loading and un-loading of stabilized loop.

The largest range of maximum shear stress $\Delta\tau_{\max}$ and shear strain $\Delta\left(\frac{\gamma}{2}\right)_{\max}$ obtained from the largest stress and strain Mohr's circle during loading and unloading at points P' and Q' of the stabilized cycle and the corresponding normal stress range $\Delta\sigma_n$ and the normal strain range $\Delta\varepsilon_n$ on the critical plane are employed to generate the damage parameter.

To calculate the damage parameters (Equation(72)) the axial fatigue properties/coefficients of SAC305 (axial fatigue strength coefficient, σ'_f , axial fatigue ductility coefficient, ε'_f) have been determined based on the available strain range versus life experimental data for this material under two isothermal conditions with temperatures of 25°C and 125°C (Refer to Figure 68).

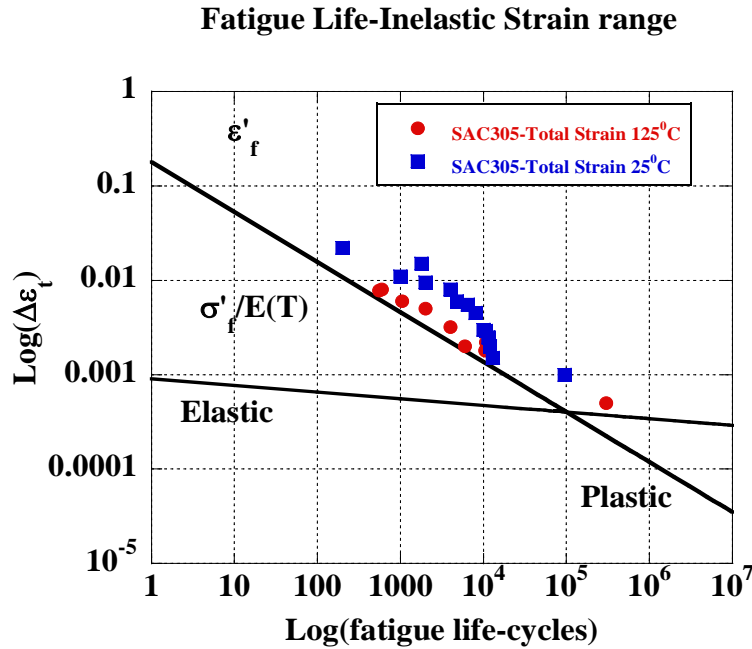


Figure 68: Durability curves and experiment data points for SAC305 solder joint tested under 25°C and 125°C temperatures [106].

Shear fatigue strength coefficient, τ'_f and shear fatigue ductility coefficient, γ'_f have been estimated using the axial fatigue coefficients. Table 20 provides the detail of the axial and shear fatigue properties/coefficients of SAC305. Shear and axial strength coefficients are determined as a function of temperature.

The calculated fatigue damage parameter for the samples of study, along with their experimental life ($N_{f50\%}$) under two different thermal conditions is presented in Table 21. The values of life in (0-100°C) condition and (25-125°C) with the same temperature ramp rate and dwell conditions are found to differ by a factor of 1.3 [107] where the structures tested under (0-100°C) condition show lower lives.

The present study further correlated the fatigue damage parameters with the Coffin-Manson type equation (LHS of Equation (80)) to calculate/predict the fatigue life of structures under (25-125°C) condition. The results of the N_{f50} fatigue life prediction and comparison with experimental cycles were presented in Table 22. The N_{f50} fatigue life predictions versus the experimental cycles show that the predicted lives of samples with SAC305 solder joints fall apart with a factor ranging from (1.24)~ (-1.45) (Refer to Figure 69).

A comparison of results of the life prediction based on fatigue damage parameter used in this study and other damage parameters presented in literature (Refer to section 2.3) shows the strain energy-based damage parameter may find as the preferred method in life prediction of trilayer structures with SnAgCu adhesive layer.

The advantage of the proposed method in comparison with the existing methods in life prediction of the trilayer structure with solder alloy [66, 69, 72, 73] is that there are no empirical parameters involved in energy-critical plane damage parameter in life prediction of the trilayer structure. Parameters within the proposed approach purely involves mechanical and fatigue properties of the midlayer alloy.

Table 20: Durability model fitting results for SAC305 board-level solder joint under thermal cycling and mechanical bending conditions

Properties	SAC305
σ'_f (MPa)	$0.001025(52126 - 55.35(T - 273))$
b_{tensile}	-0.07
ε'_f	0.19
c_{tensile}	-0.5
τ'_f (MPa)	$0.00059(19306 - 20.5(T - 273))$
b_{shear}	-0.07
γ'_f	0.329
c_{shear}	-0.5

Note: T is in Kelvin.

Table 21: Predicted damage parameter for samples following critical plane damage modeling

Samples#(type)	Predicted Damage Parameter	Experimental Life (N_{f50}) (0-100°C)	Experimental Life (N_{f50}) (25-125°C)
309 (1B)	0.0018	3964	5265
36 (2A)	0.0015	4050	5922
344 (4)	0.0066	3913	5153
212 (6A)	0.0011	4555	5087

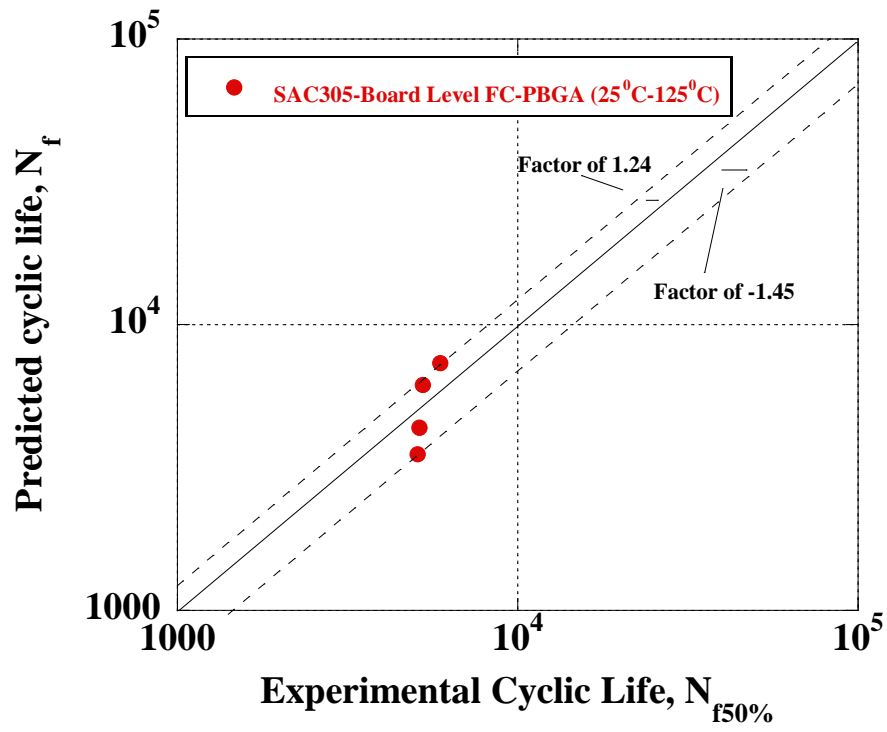


Figure 69: Assessment of critical plane damage parameter life prediction capability for SAC305 solder joint allot under thermal cycling of 25-125°C.

Table 22: Comparison between predicted and experimental fatigue life N_{f50} for samples

Samples#(type)	Predicted life (N_{f50})	Experimental Life (N_{f50})	Difference (%)
309 (1B)	6154	5265	16.8
36 (2A)	7343	5922	24
344 (4)	4374	5153	-17.8
212 (6A)	3517	5087	-44.6

CHAPTER SIX

Conclusions, Contributions and Suggestions for Future Work

6.1 Conclusions

This study has successfully developed the non-local closed-form solutions for interfacial peel and shear stress as well as warpage deformation for a trilayer structure under thermal cycling. An experimental method has been proposed to verify the analytical method for interfacial peel strain and warpage. The proposed modeling and experimental approaches address the current need of such models and modeling approaches that can be generally applicable to a trilayer bonded structure with adhesive material, regardless its specific structure design and materials constitutive behavior.

Furthermore, an inverse method based on the warpage deformations of the trilayer structures has been proposed to characterize the constitutive behaviour of the trilayer constituents under temperature changes. The proposed method allows the thermomechanical behaviour of trilayer constituents to be determined at the real scale, avoiding the controversy involving the use of bulk material properties. Applications of an optimization method in the characterization of several trilayer structures with different designs have reached the correlation of over 85% between the measured and the predicted thermal warpage of these trilayer structures.

A hybrid analytical and experimental method for characterizing the viscoelastoplastic joint alloy, which is vital to the analysis of the trilayer structures, was further proposed. The experimental approach includes a novel casting method for making double notched tensile samples of this alloy, as well as an experimental system, which together allows the viscoelastoplastic strain-stress behaviour of alloy to be determined at the local level. This

method replaces the conventional methods which use the non-local (distant) load data versus cross-head non-local strain measurements. The result of the viscoelastoplastic model of the joint alloy has been employed in fatigue life prediction of the trilayer structures with a layer consisting of the same joint material, where the adhesive layer is found to be the failure dominant layer under thermal cycling. The thermal fatigue life of the joint layer is further investigated using a method involving the critical plane-energy fatigue damage parameter in combination with a modified Coffin-Manson life model. The superiority of the fatigue life model is that it does not use any empirical parameters and all the parameters are a function of mechanical properties of the materials.

Custom-made as well as real microelectronics trilayer structures were used to evaluate the proposed models and approaches for characterization and thermal fatigue life prediction of these structures. Tangible results have been obtained in predicting the peel stress and strain at the interfacial level of trilayer structures. A good agreement has been found in predicting the warpage of the trilayer structure using the results for thermomechanical properties of the trilayer structure constituents from the inverse method. A well correlated constitutive model for predicting the creep behaviour of the joint alloy has been reached.

The proposed method for fatigue life prediction of a trilayer structure also has shown promising results using the critical plane-energy fatigue damage parameter. Unlike FEA, the proposed analytical-experimental method is straightforward and makes it much easier for engineers and researchers to perform design optimization. Moreover, it provides a clearer understanding of the mechanics governing the thermal fatigue process of trilayer structures.

6.2 Contributions

The current study contributes to the development of analytical and experimental methods to allow the characterization of interfacial behaviour and life assessment of trilayer

structures with compliant midlayer, when subjected to thermal loading. The main contributions are as follows:

- Developed an easy and novel approach to reach a closed-form solution for the prediction of warpage of trilayer structure. The proposed approach differs from the existing ones for closed-form solutions since it uses non-local models of thin elastic foundations. The new approach reaches not only the solutions for the interfacial stress and strain, but also, for the first time, the thermal warpage of the trilayer structure with compliant midlayer. The accuracy of the warpage solution is experimental verified for the first time using some advanced optical methods.
- Improved the existing interfacial peel and shear stress closed-form solutions for trilayer structure under temperature changes based on midlayer displacement continuity in both longitudinal and vertical directions. The new models satisfy the edge conditions of the trilayer structures using the non-local models of thin elastic foundations. Different from the previous studies, the accuracy of the maximum peel stress/strain are experimentally verified using advanced non-contact strain measurement methods.
- Proposed a novel inverse method to determine the material properties of trilayer constituents, based on optimization of the materials parameters, to allow the best correlation between the proposed model and the experimental results of warpage under thermal cycle.
- Improved the existing methods in characterization of the viscoelastoplastic behaviour of bulk midlayer joint alloy using a hybrid analytical and experimental method on a double notched tensile sample using a micro-testing rig and a non-contact micro strain measurement system, which together allow the viscoelastoplastic strain-stress behaviour of alloy to be determined at the notch root local area with high accuracy.

- Proposed a new method in prediction of life of joint layer using the critical plane-energy fatigue damage parameter in combination with the Coffin-Manson modified equation. This method improves the existing strain-energy based approaches in life prediction of solder alloy by using both axial and shear fatigue components that are purely function of mechanical properties of the materials.

6.3 Suggestions for future work

This research provided the foundation for continuation of research into the characterization and life prediction of trilayer structures under thermal loading. As this research was focused only on the fundamental aspects of the thermomechanical deformation of the trilayer structure and its constituents, several additional factors should be considered in interfacial stress-strain modeling and life prediction of the trilayer structure. For example:

1. Implement creep and plastic behaviour in the proposed analytical model to obtain stress and strain at the interface of viscoelastoplastic adhesive layer.
2. Use the inverse method with the improved viscoelastoplastic analytical model of warpage to predict the constitutive behaviour of the adhesive layer/joint.
3. Use the method to try to predict the life of the trilayer structure using the warpage deformation data of a trilayer structure under a stabilized thermal cycle.

REFERENCES

1. Timoshenko, S. P., 1925, Analysis of Bi-Metal Thermostats, Issue:11, J. Opt. Soc. Am., pp. 233–255.
2. Chen, W. T. and Nelson, C., 1979, Thermal Stresses in Bounded Joints, IBM J. Res. Develop, Vol. 23, pp. 179-188.
3. Suhir, E., 1986, Stresses in bi-metal thermostats, Vol. 53, ASME J. Appl. Mech., pp. 657-660.
4. Suhir, E., 2001, Analysis of interfacial thermal stresses in a trimaterial assembly, J Appl Phys, Vol. 89, pp. 3685–3694.
5. Suhir, E. Structural Analysis in Microelectronic and Fiber Optic Systems.: Van Nostrand Reinhold, New York, 1991.
6. Shirazi, A., Lu, H. and Varvani-Farahani, A., 2010, A hybrid inverse method for evaluating FC-PBGA material response to thermal cycles, Journal of Materials Science: Materials in Electronics Vol. 21/7, pp. 737-749.
7. Ghorbani, H. R. and Spelt, J. K., 2006, Interfacial thermal stresses in solder joints of leadless chip resistors, Microelectron. Reliab. Vol. 46, pp. 873-884 .
8. Tsai, M.Y., Jeter Hsu, C. H. and Otto Wang, C. T., 2004, Investigation of Thermomechanical Behaviors of Flip Chip BGA Packages During Manufacturing Process and Thermal Cycling, IEEE Transactions On Components And Packaging Technologies, Vol. 27, pp. 569-576.
9. Shirazi, A., Lu, H. and Varvani-Farahani, A., 2010, Mechanistic-based reliability evaluation of micro-BGA module and substrates under thermal cycle : SMTA International Conference on Soldering & Reliability, Toronto, May 18-20.
10. Shirazi, A., Lu, H. and Varvani-Farahani, A., 2010, Thermal Warpage in Micro-level Trilayer Structures: Experiment and Mathematical Modeling. Orlando, Florida : Surface Mount Technology Association (SMTA) International Conference, October 24 - 28.
11. Michaelides, S. and Sitaraman, S. K., 1999, Die Cracking and Reliable Die Design for Flip-Chip Assemblies. 4, IEEE Transactions on Advanced Packaging, Vol. 22, pp. 602-613.

12. Tsai, M.Y.; Lin, Y.C.; Huang, C.Y.; Wu, J.D., 2005, Thermal Deformations and Stresses of Flip-Chip BGA Packages With Low- and High-Tg Underfills, IEEE Transactions on Electronics Packaging Manufacturing, Vol. 28, pp. 328-337.
13. Shirazi, A., Varvani-Farahania, A. and Lua, H., An inverse analysis of warpage for trilayer thin-plate under thermal cycles, Vol. 31, 9, pp.4219-4228.
14. Vujosevic, M., 2008, Thermally induced deformations in die-substrate assembly. 1-3, Theoret Appl Mech, Vol. 35, pp. 305-322.
15. Valisetty, R. R., 1983, Bending of Beams, Plates and Laminates: Refined Theories and Comparative Studies. Ph.D. thesis, Georgia Institute of Technology, Atlanta.
16. Wen, Y. and Basaran, C., 2004, An Analytical Model for Thermal Stress Analysis of multi-layered Microelectronics Packaging. Proceedings of 54th Electronic Components and Technology Conference, Electronic Components and Technology Conference, Vol. 2, pp. 1592- 1601.
17. Ru, C.Q. , 2002, Interfacial thermal stresses in bimaterial elastic beams: modified beam models revisited. Trans ASME J Electron Pack, Vol. 124, pp. 141–146.
18. Kerr, A.D. ,1965, A study of a new foundation model. Acta Mech, 1965, pp. 135-147.
19. Ghorbani, H.R. and Spelt, Jan K., 2006, Analytical elasto-creep model of interfacial thermal stresses and strains in Trilayer assemblies, International Journal of Solids and Structures, Vol. 43, pp. 7424-7449.
20. Shirley, D. R., Ghorbani, H. R. and Spelt, J. K., 2008, Effect of primary creep and plasticity in the modeling of thermal fatigue of SnPb and SnAgCu solder joints, Microelectronics Reliability, Vol. 48, pp. 455-470 .
21. Basaran, C. and Zhao, Y., 2001, Mesh sensitivity and FEA for multilayered electronic packaging. Trans. ASME, J. Electron. Pack. 123(3), pp. 218–224.
22. Park, JH; Jang, KW; Paik, KW; Lee, SB., 2008, Reliability evaluation for flip-chip electronic packages under high temperature and moisture condition using moiré, 10th Electron Packag Technol Conf EPTC, pp. 633-638.

23. Zhang, F; Li, M; Chen, WT; Chian, KS.,2003, An investigation into the effects of flux residues on properties of underfill materials for flip chip packages, IEEE Trans. Compon. Packag. Technol., Vol. 26, pp. 233-244.
24. Wei, X, Marston, K and Sikka, K., 2008, Thermal modeling for warpage effects in organic packages. 11th IEEE Intersoc Conf Thermal Thermomec Phenom Electron Sys I-THERM, pp. 310-314.
25. Too, S.S.; Hayward, J.; Master, R.; Tan, TS.; Keok, KH., 2007, Effects of Organic Package Warpage on Microprocessor Thermal Performance, Proc Electron Compon Technol Conf, 2007, pp. 748-754.
26. Shirazi, A., Lu, H. and Varvani-Farahani, A., 2009, Evaluation of thermal stress in a flip chip package by hybrid experimental-analytical method, Proc. Int. Conf. Solder. Reliab. Tor.
27. Park, S.; Lee, HC.; Sammakia, B.; Raghunathan, K., 2007, Predictive Model for Optimized Design Parameters in Flip-Chip Packages and Assemblies, IEEE Trans Compon Packag Tech, Vol. 30, pp. 294-301.
28. Tsai, M.Y., Chang, H.Y. and Pecht, M., 2009, Warpage analysis of flip-chip PBGA packages subject to thermal loading,IEEE Transact Device Mat Reliab,Vol. 9, pp. 419-424.
29. DeSousa, I; McCormick, H; Lu, H; Martel, R.; Ouimet, S., 2008, Module Camber Effect on Card Assembly and Reliability for Large Flip Chip BGA Organic Packages, Proc Electron Compon Technol Conf, pp. 397- 405.
30. Okura, J.H.; Reinikainen, T.; Dasgupta, A.; Caers, J.F.J.M., 2000, Guidelines to Select Underfills for Flip Chip on Board Assemblies, Proc. 49th Electronic Components and Technology Conference, pp. 589-594.
31. Haswell, P., 2001, Advanced warpage characterization: location and type of displacement can be equally as important as magnitude,Proceedings of the Pan Pacific Microelectronics Symposium Conference.
32. Frear, D.R. and Vianco, P.T., 1994, Intermetallic Growth and Mechanical Behavior of Low and High Melting Temperature Solder Alloys, Metallurgical and Materials Transactions A, Vol. 25, pp. 1509-1523.

33. Schubert,A.; Dudek,R.; Doring, R.; Walter, H., 2002, Lead-free Solder Interconnects: Characterization, Testing, and Durability,3rd Int. Conf. On Benefiting from Thermal and Mechanica.
- 34.Wiese,S.; Schubert,A.; Walter,H.; Dukek,R.; Feustel,F.; Meusel,E.; Michel,B., 2001, Constitutive behavior of lead-free solders vs. lead-contained solders—experiments on bulk specimens and flip–chip joints, Proceedings of 51st Electronic Components and Technology Conference, pp. 890 – 902 .
35. Schubert, A.; Walter, H.; Dudek, R.; Michel, B.; Lefranc, G.; Otto, J.; Mitic, G., 2001, Thermo-Mechanical Properties and Creep Deformation of Lead-Contained and Lead-Free Solders, Proceedings of International Symposium of Advanced Packaging Materials: Processes, Properties and Interfaces, pp. 129 – 134.
36. Zhang, Q., A., Dasgupta and Haswell, P., 2005, Isothermal Mechanical Durability of Three Selected PB-Free Solders: Sn3.9Ag0.6Cu, Sn3.5Ag, and Sn0.7Cu, Journal of Electronic Packaging, Vol. 127, pp. 512-522.
37. Ma., H. and Suhling, J. C., 2009, A review of mechanical properties of lead-free solders for electronic packaging, J Mater Sci, 2009, Vol. 44, pp. 1141–1158.
38. Vianco, P.T., 2006, Fatigue and creep of lead-free solder alloys: fundamental properties. [book auth.] Shangguan D (ed). leadfree solder interconnect reliability, ASM International, Materials Park, OH, 3 , p. 67.
39. Vianco, P.T. and Rejent, J.A., 2002, Compression deformation response of 95.5Sn–3.9Ag–0.6Cu solder, UCLA Workshop on Pb-free Electronics.
40. Puttlitz, K.J. and Stalter, K.A., , 2004, Handbook of lead-free solder technology for microelectronic assemblies,Marcel Dekker,New York.
41. Fouassier, O.; Heintz, J-M.; , Chazelas, J.; Geffroy, P-M.; , Silvaina, J-F.,2006, J Appl Phys,Vol. 100.
42. Pang, J.H.L. and Xiong, BS., 2005, IEEE Trans Compon Pack Technol., Vol. 28, p. 830.
43. Wiese, S. and Walter, H.,2004, Microstructure and creep behaviour of eutectic SnAg and SnAgCu solders, Microelectronics Reliability, Vol.44, 12,pp. 1923-1931.
- 44.Lin,J.K.;De Silva,A. ;Frear,D.; Guo,Y.; Hayes,S.; Jang,J.W.; Li,L.; Mitchell,D.; Yeung,B.; Zhang,C., 2002, IEEE Trans Electron Pack Manuf,Vol. 25, p. 300.

45. Kanchanomai, C., Miyashita, Y. and Mutoh, Y., 2002, J Electron Mater, Vol. 31, p. 456.
46. Zhu, F.; Wang, Z.; Guan, R.; Zhang, H., 2005, International Conference on Asian Green Electronics, pp. 107–112.
47. Yeh, C.L. and Lai, Y.S., 2006, Transient fracturing of solder joints subjected to displacement-controlled impact loads, Microelectronics Reliability, Vol. 46, pp. 885–895.
48. Darveaux, R. and Banerji, K., 1992, Constitutive Relations for Tin-Based Solder Joints, IEEE Transactions on Components, Hybrids, and Manufacturing Technology, Vol. 15, pp. 1013-1024 .
49. Lee, Y. and Han, B.T., 2003, Calibration of Virtual Qualification Model for Leaded Packages with Pb-free Solder, CALCE Internal Report.
50. Haswell, P. and Dasgupta, A., 1999, Viscoplastic Characterization of Constitutive Behavior of Two Solder Alloys. Nashville, Tennessee : ASME International Mechanical Engineering Congress and Exposition, November 14-19.
51. Dowling, N.E., 1999, Mechanical Behavior of Materials, Prentice-Hall Inc, NJ, USA.
52. Chen, Z., Shi, Y. and Xia, Z., 2004, Constitutive Relations on Creep for SnAgCuRE Lead-Free Solder Joints, Journal of Electronic Materials, Vol. 33, pp. 964 -971.
53. Syed, A., 2004, Accumulated Creep Strain and Energy Density Based Thermal Fatigue Life Prediction Models for SnAgCu Solder Joints, Proceedings of 54th Electronic Components and Technology Conference, Vol. 1, pp. 737 - 746.
54. Tribula, D. and Jr., Morris and J.W., 1990, Creep in Shear of Experimental Solder Joints, Journal of Electronic Packaging, 112, pp. :87 - 93.
55. Harada, M. and Satoh, R., 1990, Mechanical characteristics of 96.5Sn/3.5Ag solder in micro-bonding, Proceedings of 40th Electronic Components and Technology Conference, Vol. 1, pp. 510 -517.
56. Xiao, L.; Liu, J.; Lai, Z.; Ye, L.; A., Tholen, 2000, Characterization of Mechanical Properties of Bulk Lead Free Solders, Proceedings of International Symposium of Advanced Packaging Materials: Processes, Properties and Interfaces, pp. 145 - 151 .
57. Ma, H., 2009, Constitutive models of creep for lead-free solders, J Mater Sci, Vol. 44, pp. 3841–3851.
58. Clech, J.P. , 2007, Review and analysis of lead-free materials properties, NIST.

59. Xiao, Q. and Armstrong, W.D. 2005, J Elec Materi, Vol. 34, p. 196.
60. Lau, J., Dauksher, W. and Vianco, P., 2003, Acceleration models constitutive equations reliability of lead-free solders and joints, Proceeding of the 53rd electronic components and technology conference, pp. 229–236.
61. Zhang, G.Q., Tay, A. and Ernst, L.J., 2000, Virtual thermo-mechanical prototyping of electronic packaging - Bottlenecks and solutions of damaging modeling, 3rd Electronic Packaging Technology Conference (EPTC), Singapore.
62. Pang, J., 2007, Lead-Free Solder Materials: Design For Reliability. Micro- and Optoelectronics Materials and Structures: Physics, Mechanics, Design, Reliability, Packaging, 2, pp. 429-458.
63. Coffin, L.F., 1954, A study of the effects of cyclic thermal stresses on a ductile metal, Trans. ASME, Vol. 76, p. 931.
64. Manson, S.S., 1965, Fatigue a complex subject-some simple approximations, Experimental Mechanics.
65. Lee, W.W., Nguyen, L.T. and Selvaduray, G.S., 2000, Solder joint fatigue models: review and applicability to chip scale packages, Microelectronics Reliability, Vol. 40, pp. 231-244.
66. Qi.Y., 2005, Accelerated Thermal Fatigue Of SnPb and Pb-free Solder Joints: Effect of Temperature Range and Rate of Change.
67. Kilinski, T.J., Lesniak, J.R. and Sandor, B.I., 1991, Modern approaches to fatigue life prediction of SMT solder joints. [book auth.] J.H. Ed. Lau. Solder Joint Reliability Theory and Applications. New York.
68. Knecht, S. and Fox, L., 1991, Integrated matrix creep: application to accelerated testing and lifetime prediction. [book auth.] J.H. Ed. Lau. Solder Joint Reliability, Van Nostrand Reinhold. New York, 16.
69. Osterman, M. and Pecht, M., 2007, Strain range fatigue life assessment of lead-free solder interconnects subject to temperature cycle loading, Soldering & Surface Mount Technology, Vol. 19, pp. 12–17.
70. Engelmaier, W., 1991, Solder attachment reliability, accelerated testing, and result evaluation. [book auth.] J.H. Ed. Lau. Solder Joint Reliability, Van Nostrand Reinhold. New York, 17.

71. Darveaux, R., 2000, Effect of simulation methodology on solder joint crack growth correlation, Components and Technology Conference, IEEE, pp. 158–169.
72. Ernic, M.; Schreurs, P.J.G.; Zhang, G.Q.; Geers, M.G.D., 2005, Microstructural damage analysis of SnAgCu solder joints and an assessment on indentation procedures, Journal of Materials Science: Materials in Electronics, Vol. 16, pp. 693– 700.
73. Kuna, M. and Wippler, S., 2010, A cyclic viscoplastic and creep damage model for lead free solder alloys, Engineering Fracture Mechanics, Vol. 77, 18, pp. 3635-3647
74. Shirazi, A., Lu, H. and Varvani-Farahani, A., 2010, Thermal Warpage and Interfacial Stresses in Micro-level Trilayer Structures: Experiment and Mathematical Modeling. Orlando, Florida : Proceeding of Surface Mount Technology Association (SMTA) International Conference.
75. Moore, T. D. and Jarvis, J. L., 2003, A Simple and Fundamental Design Rule for Resisting Delamination in Bimaterial Structures, Microelectron. Reliability, Vol. 43, pp. 487–494.
76. Timoshenko, S.P. and Woinowsky-Krieger, S., 1967, 2nd. s.l. : McGraw-Hill, New York, pp. 4-6 .
77. Gray, A., 1997, Curvature of Curves in the Plane, Modern Differential Geometry of Curves and Surfaces with Mathematica. 2nd. Boca Raton, FL: CRC Press, pp. 14-17.
78. Zhao, R.; Lu, H.; Zhou, M.; Sun, C., 2006, Improved Shadow Moiré Method for Out-of-plane Displacement Measurement. Kananaskis, Alberta. : Proceedings of CSME Forum, 21-24.
79. Yeh, C. P.; Banejee, K.; Martin, T.; Umeagukwu, C.; Fulton, R., 1991, Experimental and Analytical Investigation of Thermally Induced Warpage for Printed Wiring Boards, IEEE Electronic Component Technology Conference, pp. 382-387.
80. Spiegel, M.R. Correlation Theory. [book auth.] Spiegel, MR; Schiller, J.J.; Srinivasan, R.A.[editors]. Theory and Problems of Probability and Statistics. New York : McGraw-Hill, 1992, pp. 294-323.
81. Guo, W., Wang, C. H. and Rose, L. R. F. Elastoplastic Analysis of Notch-Tip Fields in Strain Hardening Materials. August 1998. DSTO-RR-0137.

82. Davies, C. M.; O'Dowd, N. P.; Nikbin, K. M.; Webster, G.A.; Biglari, F., 2005, Comparison of methods for obtaining crack-tip stress distributions in an elastic-plastic material, *J. Strain Analysis*, Vol. 40, pp. 431-450.
83. Neuber, H., 1961, Theory of stress concentration for shear-strained prismatic bodies with arbitrary nonlinear stress-strain law, *J. Appl. Mech.*, Vol. 23, pp. 544-550.
84. Glinka, G., 1985, Calculation of Inelastic Notch-Tip strain-stress historie Under Cyclic Loading, *Engineering Fracture Mechanics*, Vol. 22, pp. 839-854.
85. Kubo, S. and Ohji, K. Prediction of creep relaxation stress at notch root based on concept of small scale creep. s.l. : Preprint of the 31st Symp., Sot. Material Sci., Japan, 1982. pp. 261-263.
86. Kuwabara, K., Nitta, A. and Kitamura, T., 1985, Crack Initiation Llife at Notch Root Under The Transition Of Creep Condition, *Engineering Fracture Mechanics*, Vol. 21, pp. 229-231.
87. Nisitani, H., 1986, Stress Concentrations of a Strip with Double Edge Notches Under Tension or In-Plane Bending, *Engineering Frocrure Mechanics*, 1986, Vol. 23, pp. 1051-1065 .
88. E 292 – 09:Standard Test Methods for Conducting Time-for-Rupture Notch Tension Tests of Materials.ASTM.
89. Varvani-Farahani, A., 2000, A new energy-critical plane parameter for fatigue life assessment of various metallic materials subjected to in-phase and out-of-phase multiaxial fatigue loading conditions, *International Journal of Fatigue*, Vol. 22, pp. 295–305.
90. Varvani-Farahani, A., Kodric, T. and Ghahramani, A., 2005, A method of fatigue life prediction in notched and un-notched components,J Mater Process Technol, Vol. 169, pp. 94–102.
91. Timoshenko, S. P. and Woinowsky-Krieger, S. *Theory of Plates and Shells*. s.l. : McGraw–Hill, New York, 1959.
92. Verma, K., Columbus, D. and Han, B., 1999, Development of Real Time/Variable Sensitivity Warpage Measurement Technique and its Application to Plastic Ball Grid Array Package, *IEEE Transactions on Electronics Packaging Manufacturing*, Vol. 22, pp. 63-70 .

93. Zhou, M. and Lu, H., 2007, BGA component thermal warpage and implication for interconnect reliability. Orlando : proceedings of SMTAI Conference, October 7-11, pp. 374-379.
94. Dirckx, J., Decraemer, W.F and Dielis, M.M.E., 1988, A phase shift method based on object translation for full field automatic three dimensional surface reconstruction from moiré topograms, *Applied optics*, Vols. 27,6, pp. 1164-1169.
95. Lu, H., 1988, Application of Digital Speckle Correlation to Microscopic Strain Measurement and Materials' Property Characterization, *Transaction of the ASME Journal of Electronic Packaging*, Vol. 120, pp. 275-279.
96. National Center for Manufacturing Sciences, Lead-Free Solder Project Final Report. August 1997.
97. JESD22-A104C, JEDEC STANDARD, Temperature Cycling. s.l. : JEDEC Solid State Technology Association, 2005.
98. Suhir, E. and Manzione, L.T., 1992, Predicted Bow of Plastic Packages Due to the Nonuniform Through-Thickness Distribution of Temperature, *Journal of Electronic Packaging*, Vol. 114, pp. 329-335.
99. Moon, K.W.; Boettinger, W.J.; Kattner, U.R.; Biancaniello, F.S.; Handwerker, C.A., 2000, Experimental and thermodynamic assessment of Sn–Ag–Cu solder alloys, *J. Electr. Mater.*, Vol. 29, pp. 1122–1136.
100. Pietrikova, A. and Ďurisin, J., 2010, Microstructure of Solder Joints and Isothermal Aging, *Acta Electrotechnica et Informatica*, Vol. 10, pp. 43–46.
101. Li, X. and Wang, Z., 2007, Thermofatigue Life Evaluation of SnAgCu/Cu Solder Joints in Flip Chip Assemblies, *J. Mater. Process. Tech.*, Vol. 183, pp. 6-12.
102. Cuddalorepatta, G., Williams, M. and Dasgupta, A., 2010, Viscoplastic Creep Response and Microstructure of As-Fabricated Microscale Sn-3.0Ag-0.5Cu Solder Interconnects, *Journal of Electronics Materials*, Vol. Vol.39, pp. 2292-2309.
103. Langdon, T. G., 1982, Deformation at high temperatures, *Strength of Metals and alloys: Proc. 6th Int. Conf.*, pp. 1105-1120.
104. Shirazi, A., Varvani-Farahani, A. and Lu, H., 2008, A comparative study on stress-strain hysteresis response of SAC solder joints thermal cycles, In *J Frac*, 2008, Vol. 151, pp. 135-150.

105. Brown, M.W. and Miller, K.J., 1973, A theory of fatigue failure under multiaxial stress-strain condition, *Proc. Inst. Mech. Eng.*, Vol. 187, pp. 745-755.
106. KARIYA, Y. and SUGA, T., 2007, Low-cycle fatigue properties of eutectic solders at high temperatures, *Fatigue Fract Engng Mater Struct*, pp. 413–419.
107. Ahmad, M.; Xie, W.; Liu, K.C.; Xue, J.; Towne, D., 2009, Parametric Acceleration Transforms for Lead-Free Solder Joint Reliability under Thermal Cycling Conditions, *Electronic Components and Technology Conference*, pp. 682-691.

APPENDIX1

Interfacial Shear Stress Model for Trilayer Structure

The equation for shear stress is given by:

$$\tau(x) - F\tau''(x) + B\tau'''(x) = 0 \quad (\text{A1.1})$$

where

$$F = \frac{\mu_1 - \mu_2 + \mu_3}{\left[(\lambda_1 + \lambda_3) + \frac{I}{(D_1 + D_3)} \left(\frac{h_1}{2} + \frac{h_3}{2} \right)^2 \right]} \quad (\text{A1.2})$$

$$B = \frac{\mu_1\beta_1 - \mu_2\beta_2 + \mu_3\beta_3}{\left[(\lambda_1 + \lambda_3) + \frac{I}{(D_1 + D_3)} \left(\frac{h_1}{2} + \frac{h_3}{2} \right)^2 \right]} \quad (\text{A1.3})$$

Equation (A1.1) is transformed to a new form by introducing a new parameter to replace for

$\tau(x) = e^{\Phi x}$ as:

$$1 + F\Phi^2 - B\Phi^4 = 0 \quad (\text{A1.4})$$

And

$$1 - F\Phi^2 + B\Phi^4 = 0 \quad (\text{A1.5})$$

Solving the polynomial of degree 4 leads to:

$$\Phi_{1,2}^2 = \frac{F \pm \sqrt{F^2 - 4B}}{2B} \quad (\text{A1.6})$$

where for the cases of trilayer structures such as those found in microelectronics, $F^2 - 4B < 0$. For other possible cases the $F^2 - 4B > 0$ separate solutions are developed.

Case I: $F^2 - 4B < 0$

Since F and $B > 0$ hence $F^2 - 4B < F^2$ therefore $F + i\sqrt{-F^2 + 4B} > 0$ and $F - i\sqrt{-F^2 + 4B} > 0$.

Consequently the positive roots to the equation are in the form of:

$$\begin{aligned}\Phi_{1,2}^2 &= \frac{F + i\sqrt{4B - F^2}}{2B} \\ \Phi_{3,4}^2 &= \frac{F - i\sqrt{4B - F^2}}{2B}\end{aligned}\tag{A1.7}$$

$$\begin{aligned}\Phi_{1,2} &= \frac{\pm 1}{\sqrt{2B}} \sqrt{F + i\sqrt{-F^2 + 4B}} \\ \Phi_{3,4} &= \frac{\pm 1}{\sqrt{2B}} \times \sqrt{F - i\sqrt{-F^2 + 4B}}\end{aligned}\tag{A1.8}$$

Hence:

$$\begin{aligned}\Phi_1 &= \frac{1}{\sqrt{2B}} \sqrt{F + i\sqrt{-F^2 + 4B}} = -\Phi_2 \\ \Phi_3 &= \frac{1}{\sqrt{2B}} \times \sqrt{F - i\sqrt{-F^2 + 4B}} = -\Phi_4\end{aligned}\tag{A1.9}$$

Following the fundamental theorem of algebra every polynomial with complex coefficients has a complex root. In such a complex number as $c = a + bi$ where a and b are real ($b \neq 0$) has an explicit representation for its square root as $p + qi$ where p and q are real:

$$(p + iq)^2 = a + ib\tag{A1.10}$$

Equating the real and imaginary parts gives the two equations as:

$$p^2 - q^2 = a \quad (\text{A1.11})$$

$$2pq = b \quad (\text{A1.12})$$

where $p \neq 0$ since $b \neq 0$. Solving equation (A1.12) for q gives:

$$q = \frac{b}{2p} \quad (\text{A1.13})$$

and substituting this value for q into Equation (A1.11) leads to:

$$p^2 - q^2 = p^2 - \left(\frac{b}{2p}\right)^2 = a \quad (\text{A1.14})$$

or

$$4p^4 - 4ap^2 - b^2 = 0 \quad (\text{A1.15})$$

This is a quadratic in p^2 , so by solving for p^2 using the quadratic formula and considering the positive solution, it results in:

$$p^2 = \frac{a + \sqrt{a^2 + b^2}}{2} \quad (\text{A1.16})$$

so:

$$p = \frac{1}{\sqrt{2}} \sqrt{a + \sqrt{a^2 + b^2}} \quad (\text{A1.17})$$

From Equation (A1.13) it is found:

$$q = \frac{b}{2p} = \frac{b}{\frac{2}{\sqrt{2}}\sqrt{a + \sqrt{a^2 + b^2}}} = \frac{\text{sgn}(b)}{\sqrt{2}}\sqrt{\sqrt{a^2 + b^2} - a} \quad (\text{A1.18})$$

The sign of b (defined to be +1 if $b > 0$ and -1 if $b < 0$).

In practice, square roots of complex numbers are more easily found by first converting to polar form and then using DeMoivre's Theorem. Any complex number $a + ib$ can be written as:

$$a + ib = r(\cos \theta + i \sin \theta) \quad (\text{A1.19})$$

where $r = \sqrt{a^2 + b^2}$, $\cos \theta = a/r$ and $\sin \theta = b/r$. DeMoivre's Theorem states that if n is any positive real number, then:

$$(a + bi)^n = r^n(\cos n\theta + i \sin n\theta) \quad (\text{A1.20})$$

In particular, if $n = 1/2$:

$$\sqrt{a + ib} = \sqrt{r\left(\cos \frac{\theta}{2} + i \sin \frac{\theta}{2}\right)} \quad (\text{A1.21})$$

This gives a straightforward way to calculate $\sqrt{a + ib}$. Applying the half-angle formula as:

$$\begin{aligned} \cos \frac{\theta}{2} &= \pm \sqrt{\frac{1 + \cos \theta}{2}} \\ \sin \frac{\theta}{2} &= \pm \sqrt{\frac{1 - \cos \theta}{2}} \end{aligned} \quad (\text{A1.22})$$

to Equation (A1.21) yields to:

$$\sqrt{a+ib} = \sqrt{r} \left(\sqrt{\frac{1+\cos\theta}{2}} \pm i \sqrt{\frac{1-\cos\theta}{2}} \right) \quad (\text{A1.23})$$

where the “+” sign has been chosen arbitrarily for the first radical. Using the value for $\cos\theta = a/r$ leads to:

$$\begin{aligned} \sqrt{a+ib} &= \sqrt{r} \left(\sqrt{\frac{1+\frac{a}{r}}{2}} \pm i \sqrt{\frac{1-\frac{a}{r}}{2}} \right) \\ &= \sqrt{\frac{r+a}{2}} \pm i \sqrt{\frac{r-a}{2}} \\ &= \sqrt{\frac{\sqrt{a^2+b^2}+a}{2}} \pm i \sqrt{\frac{\sqrt{a^2+b^2}-a}{2}} \end{aligned} \quad (\text{A1.23})$$

The \pm sign should be chosen to be the same as the sign of b . If a and b are real with $b > 0$, and $b = \sqrt{d}$ then:

$$\sqrt{a+ib} = \frac{1}{\sqrt{2}} \left(\sqrt{\sqrt{a^2+d}+a} + i \sqrt{\sqrt{a^2+d}-a} \right) \quad (\text{A1.24})$$

Hence for case I the roots are as follows:

$$\begin{aligned} \Phi_1 &= \frac{1}{\sqrt{2B}} \sqrt{F + i\sqrt{-F^2 + 4B}} = \frac{1}{2\sqrt{B}} \left(\sqrt{\sqrt{4B}+F} + i\sqrt{\sqrt{4B}-F} \right) = p + iq = -\Phi_2 \\ \Phi_3 &= \frac{1}{\sqrt{2B}} \times \sqrt{F - i\sqrt{-F^2 + 4B}} = \frac{1}{2\sqrt{B}} \left(\sqrt{\sqrt{4B}+F} - i\sqrt{\sqrt{4B}-F} \right) = p - iq = -\Phi_4 \end{aligned} \quad (\text{A1.25})$$

where

$$\begin{aligned} \frac{1}{2\sqrt{B}} \sqrt{\sqrt{4B}+F} &= p \\ \frac{1}{2\sqrt{B}} \sqrt{\sqrt{4B}-F} &= q \end{aligned} \quad (\text{A1.26})$$

Even the roots are complex, the solution should be real. Since the solutions are complex conjugate of each other the general solution is in the form of Equation (A1.27) which naturally splits to two parts as following:

$$\tau(x) = (e^{(px)}) (\cos(qx) + \sin(qx)) \quad (A1.27)$$

$$\begin{aligned} \tau(x) &= (e^{(px)}) (\cos(qx) + \sin(qx)) = (\cosh(px) + \sinh(px)) (\cos(qx) + \sin(qx)) = \\ &\cosh(px) \cos(qx) + \cosh(px) \sin(qx) + \sinh(px) \cos(qx) + \sinh(px) \sin(qx) \end{aligned} \quad (A1.28)$$

So the general solution will be of combination of:

$$\begin{aligned} \tau(x) &= C_{11} \cosh(px) \cos(qx) + C_{22} \cosh(px) \sin(qx) + \\ &C_{33} \sinh(px) \cos(qx) + C_{44} \sinh(px) \sin(qx) \end{aligned} \quad (A1.29)$$

Case II: $F^2 - 4B > 0$

Since F and B > 0 hence $F^2 - 4B < F^2$ therefore $F + \sqrt{F^2 - 4B} > 0$ and $F - \sqrt{F^2 - 4B} > 0$

.

Consequently the positive roots to the equation are in the form of:

$$\begin{aligned} \Phi_{1,2}^2 &= \frac{F + \sqrt{-4B + F^2}}{2B} \\ \Phi_{3,4}^2 &= \frac{F - \sqrt{-4B + F^2}}{2B} \end{aligned} \quad (A1.30)$$

$$\begin{aligned} \Phi_{1,2} &= \frac{\pm 1}{\sqrt{2B}} \sqrt{F + \sqrt{F^2 - 4B}} \\ \Phi_{3,4} &= \frac{\pm 1}{\sqrt{2B}} \times \sqrt{F - \sqrt{F^2 - 4B}} \end{aligned} \quad (A1.31)$$

Hence:

$$\begin{aligned}\Phi_1 &= \frac{1}{\sqrt{2B}} \sqrt{F + \sqrt{F^2 - 4B}} = \Gamma = -\Phi_2 \\ \Phi_3 &= \frac{1}{\sqrt{2B}} \times \sqrt{F - \sqrt{F^2 - 4B}} = \Omega = -\Phi_4\end{aligned}\tag{A1.32}$$

where

$$\begin{aligned}e^{\Phi_1(x)} &= \cosh(\Gamma x) + \sinh(\Gamma x) \\ e^{\Phi_2(x)} &= \cosh(\Gamma x) - \sinh(\Gamma x)\end{aligned}\tag{A1.33}$$

and

$$\begin{aligned}e^{\Phi_3(x)} &= \cosh(\Omega x) + \sinh(\Omega x) \\ e^{\Phi_4(x)} &= \cosh(\Omega x) - \sinh(\Omega x)\end{aligned}\tag{A1.34}$$

Now that we have the roots the solution is going to be found by replacing into the initial assumption has been made earlier in as $\tau(x) = e^{\Phi(x)}$. The linear combinations of the solutions are as follow:

$$\tau(x) = C_1 e^{\Phi_1(x)} + C_2 e^{\Phi_2(x)} + C_3 e^{\Phi_3(x)} + C_4 e^{\Phi_4(x)}\tag{A1.35}$$

After substituting for parameters, and considering the real part of the solution leads to:

$$\begin{aligned}\tau(x) &= (C_1)(\cosh \Gamma x + \sinh \Gamma x) + (C_2)(\cosh \Gamma x - \sinh \Gamma x) + \\ &C_3(\cosh \Omega x + \sinh \Omega x) + C_4(\cosh \Omega x - \sinh \Omega x) = (C_1 + C_2)\cosh \Gamma x + (C_1 - C_2)\sinh \Gamma x + \\ &(C_1 + C_2)\cosh \Omega x + (C_1 - C_2)\sinh \Omega x = C_{11}(\cosh \Gamma x) + C_{22}(\sinh \Gamma x) + C_{33}(\cosh \Omega x) + C_{44}(\sinh \Omega x)\end{aligned}\tag{A1.36}$$

Boundary conditions:

In order to find the coefficients in Case I and Case II there are two boundary conditions as follow:

$$(\alpha_3^* - \alpha_1^*)\Delta T + (\mu_1 + \mu_3 - \mu_2)\tau'(l) - (\mu_1\beta_1 + \mu_3\beta_3 - \mu_2\beta_2)\tau'''(l) = 0 \quad (\text{A1.37})$$

or

$$-\frac{(-\alpha_3^* + \alpha_1^*)}{\left[(\lambda_1 + \lambda_3) + \frac{I}{(D_1 + D_3)} \left(\frac{h_1}{2} + \frac{h_3}{2} \right)^2 \right]} \Delta T + F\tau'(l) - B\tau'''(l) = -\Delta\alpha\Delta T + F\tau'(l) - B\tau'''(l) = 0 \quad (\text{A1.38})$$

$$\tau(l) = 0 \quad (\text{A1.39})$$

Solution for Case I:

Since the shear stress is antisymmetric with respect to the mid-point, the antisymmetric solution of the equation is in the form of:

$$\tau(x) = C_{11} \sinh(px) \cos(qx) + C_{22} \cosh(px) \sin(qx) \quad (\text{A1.40})$$

$$\begin{aligned}
\tau'(x) &= pC_{11} \cosh(px) \cos(qx) + pC_{22} \sinh(px) \sin(qx) + \\
&- qC_{11} \sinh(px) \sin(qx) + qC_{22} \cosh(px) \cos(qx) = \\
&(pC_{11} + qC_{22}) \cosh(px) \cos(qx) + (pC_{22} - qC_{11}) \sinh(px) \sin(qx) \\
\\
\tau''(x) &= (p^2 C_{11} + pqC_{22}) \sinh(px) \cos(qx) + (p^2 C_{22} - pqC_{11}) \cosh(px) \sin(qx) + \\
&(-qpC_{11} - q^2 C_{22}) \cosh(px) \sin(qx) + (qpC_{22} - q^2 C_{11}) \sinh(px) \cos(qx) = \\
&\left((p^2 - q^2)C_{11} + 2pqC_{22}\right) \sinh(px) \cos(qx) + \left((p^2 - q^2)C_{22} - 2pqC_{11}\right) \cosh(px) \sin(qx) \\
\\
\tau'''(x) &= p\left((p^2 - q^2)C_{11} + 2pqC_{22}\right) \cosh(px) \cos(qx) + p\left((p^2 - q^2)C_{22} - 2pqC_{11}\right) \sinh(px) \sin(qx) \\
&- q\left((p^2 - q^2)C_{11} + 2pqC_{22}\right) \sinh(px) \sin(qx) + q\left((p^2 - q^2)C_{22} - 2pqC_{11}\right) \cosh(px) \cos(qx) = \\
&\left((p^3 - pq^2)C_{11} + 2p^2 qC_{22}\right) \cosh(px) \cos(qx) + \left((p^3 - pq^2)C_{22} - 2p^2 qC_{11}\right) \sinh(px) \sin(qx) \\
&+ \left((-qp^2 + q^3)C_{11} - 2pq^2 C_{22}\right) \sinh(px) \sin(qx) + \left((qp^2 - q^3)C_{22} - 2pq^2 C_{11}\right) \cosh(px) \cos(qx) = \\
&\left((p^3 - 3pq^2)C_{11} + (3qp^2 - q^3)C_{22}\right) \cosh(px) \cos(qx) + \left((p^3 - 3pq^2)C_{22} + (-3qp^2 + q^3)C_{11}\right) \sinh(px) \sin(qx)
\end{aligned} \tag{A1.41}$$

Considering the two boundary conditions yields to:

$$\begin{aligned}
\Delta\alpha\Delta T &= F\tau'(l) - B\tau'''(l) \\
\\
\Delta\alpha\Delta T &= \\
&((Fp \cosh(pl) \cos(ql)C_{11} + Fq \cosh(pl) \cos(ql)C_{22})) + \\
&((Fp \sinh(pl) \sin(ql)C_{22} - Fq \sinh(pl) \sin(ql)C_{11})) + \\
&(((-p^3 + 3pq^2)B \cosh(pl) \cos(ql)C_{11} + (-3qp^2 + q^3)B \cosh(pl) \cos(ql)C_{22})) + \\
&(((-p^3 + 3pq^2)B \sinh(pl) \sin(ql)C_{22} + (3qp^2 - q^3)B \sinh(pl) \sin(ql)C_{11})) \\
\\
\Delta\alpha\Delta T &= \\
&\left[p\{F - (p^2 - 3q^2)B\} \cosh(pl) \cos(ql) \right] C_{11} + \\
&\left[-q\{F + (q^2 - 3p^2)B\} \sinh(pl) \sin(ql) \right] C_{11} + \\
&\left[p\{F - (p^2 - 3q^2)B\} \sinh(pl) \sin(ql) \right] C_{22} \\
&+ \left[q\{F + (q^2 - 3p^2)B\} \cosh(pl) \cos(ql) \right] C_{22}
\end{aligned} \tag{A1.42}$$

and $\tau(l) = 0$ so:

$$\tau(l) = C_{22} \cosh(pl) \sin(ql) + C_{11} \sinh(pl) \cos(ql) = 0$$

$$\begin{bmatrix} \sinh(pl) \cos(ql) & \cosh(pl) \sin(ql) \end{bmatrix} \begin{pmatrix} C_{11} \\ C_{22} \end{pmatrix} = 0 \quad (\text{A1.43})$$

$$\begin{bmatrix} \Delta\alpha\Delta T \\ 0 \end{bmatrix} = \begin{bmatrix} \begin{bmatrix} p\{F - (p^2 - 3q^2)B\} \cosh(pl) \cos(ql) \\ -q\{F + (q^2 - 3p^2)B\} \sinh(pl) \sin(ql) \\ \sinh(pl) \cos(ql) \end{bmatrix} & \begin{bmatrix} p\{F - (p^2 - 3q^2)B\} \sinh(pl) \sin(ql) \\ +q\{F + (q^2 - 3p^2)B\} \cosh(pl) \cos(ql) \\ \cosh(pl) \sin(ql) \end{bmatrix} \end{bmatrix} \begin{pmatrix} C_{11} \\ C_{22} \end{pmatrix} \quad (\text{A1.44})$$

The solutions for the coefficients C_{11} and C_{22} are found to be in the form of:

$$C_{11} = \frac{\Delta\alpha\Delta T \cosh(pl) \sin(ql)}{\Sigma}$$

$$C_{22} = \frac{-\Delta\alpha\Delta T \sinh(pl) \cos(ql)}{\Sigma} \quad (\text{A1.45})$$

where

$$\begin{aligned}
\Sigma &= \cosh(pl) \sin(ql) \left[p \{ F - (p^2 - 3q^2)B \} \cosh(pl) \cos(ql) \right] - \\
&\sinh(pl) \cos(ql) \left[p \{ F - (p^2 - 3q^2)B \} \sinh(pl) \sin(ql) \right] + q \{ F + (q^2 - 3p^2)B \} \cosh(pl) \cos(ql) \Big] = \\
&\left[p \{ F - (p^2 - 3q^2)B \} \cosh^2(pl) \cos(ql) \sin(ql) \right] - \\
&\left[-q \{ F + (q^2 - 3p^2)B \} \cosh(pl) \sinh(pl) \sin^2(ql) \right] - \\
&\left[p \{ F - (p^2 - 3q^2)B \} \sinh^2(pl) \cos(ql) \sin(ql) \right] + \\
&\left[+q \{ F + (q^2 - 3p^2)B \} \sinh(pl) \cosh(pl) \cos^2(ql) \right] = \\
&\left[p \{ F - (p^2 - 3q^2)B \} \cos(ql) \sin(ql) \right] - \\
&\left[-q \{ F + (q^2 - 3p^2)B \} \cosh(pl) \sinh(pl) \right] = \\
&\frac{1}{2\sqrt{B}} \sqrt{\sqrt{4B} + F} \left\{ F - \left(\left(\frac{1}{2\sqrt{B}} \sqrt{\sqrt{4B} + F} \right)^2 - 3 \left(\frac{1}{2\sqrt{B}} \sqrt{\sqrt{4B} - F} \right)^2 \right) B \right\} \cos(ql) \sin(ql) \\
&- \frac{1}{2\sqrt{B}} \sqrt{\sqrt{4B} - F} \left\{ F + \left(\left(\frac{1}{2\sqrt{B}} \sqrt{\sqrt{4B} - F} \right)^2 - 3 \left(\frac{1}{2\sqrt{B}} \sqrt{\sqrt{4B} + F} \right)^2 \right) B \right\} \cosh(pl) \sinh(pl) = \\
&p\sqrt{B} \cos(ql) \sin(ql) + q\sqrt{B} \cosh(pl) \sinh(pl)
\end{aligned} \tag{A1.46}$$

Solution for Case II:

Since the shear stress is antisymmetric with respect to the mid-point, the antisymmetric solution of the equation is in the form of:

$$\tau(x) = C_{11}(\sinh \Gamma x) + C_{22}(\sinh \Omega x) \tag{A1.47}$$

$$\tau'(x) = C_{11}\Gamma(\cosh \Gamma x) + C_{22}\Omega(\cosh \Omega x)$$

$$\tau''(x) = C_{11}\Gamma^2(\sinh \Gamma x) + C_{22}\Omega^2(\sinh \Omega x) \tag{A1.48}$$

$$\tau'''(x) = C_{11}\Gamma^3(\cosh \Gamma x) + C_{22}\Omega^3(\cosh \Omega x)$$

Considering the two boundary conditions yields to:

$$\Delta\alpha\Delta T = F\tau'(l) - B\tau'''(l)$$

$$\begin{aligned} \Delta\alpha\Delta T = & (FC_{11}\Gamma(\cosh\Gamma) + FC_{22}\Omega(\cosh\Omega)) - (BC_{11}\Gamma^3(\cosh\Gamma) + BC_{22}\Omega^3(\cosh\Omega)) = \\ & [F\Gamma(\cosh\Gamma) - B\Gamma^3(\cosh\Gamma)]C_{11} + [F\Omega(\cosh\Omega) - B\Omega^3(\cosh\Omega)]C_{22} \end{aligned} \quad (\text{A1.49})$$

$$\tau(l) = 0 \quad (\text{A1.50})$$

$$\begin{aligned} \tau(l) = & C_{11}(\sinh\Gamma) + C_{22}(\sinh\Omega) = 0 \\ & [\sinh(\Gamma) \quad \sinh(\Omega)] \begin{pmatrix} C_{11} \\ C_{22} \end{pmatrix} = 0 \end{aligned} \quad (\text{A1.51})$$

$$\begin{bmatrix} \Delta\alpha\Delta T \\ 0 \end{bmatrix} = \begin{bmatrix} [F\Gamma(\cosh\Gamma) - B\Gamma^3(\cosh\Gamma)] & [F\Omega(\cosh\Omega) - B\Omega^3(\cosh\Omega)] \\ \sinh(\Gamma) & \sinh(\Omega) \end{bmatrix} \begin{pmatrix} C_{11} \\ C_{22} \end{pmatrix} \quad (\text{A1.52})$$

The solutions for the coefficients C_1 and C_2 are in the form:

$$\begin{aligned} C_{11} &= \frac{\Delta\alpha\Delta T \sinh(\Omega)}{\Sigma I} \\ C_{22} &= \frac{-\Delta\alpha\Delta T \sinh(\Gamma)}{\Sigma I} \end{aligned} \quad (\text{A1.53})$$

where

$$\begin{aligned} \Sigma I = & [F\Gamma(\cosh\Gamma \sinh(\Omega)) - B\Gamma^3(\sinh(\Omega)\cosh\Gamma)] - [F\Omega(\sinh(\Gamma)\cosh\Omega) - B\Omega^3(\sinh(\Gamma)\cosh\Omega)] = \\ & [(F\Gamma - B\Gamma^3)(\cosh\Gamma \sinh(\Omega))] - [(F\Omega - B\Omega^3)(\sinh(\Gamma)\cosh\Omega)] = \\ & \Gamma \left\{ \left(\frac{F}{2} \left(1 - \sqrt{1 - 4 \frac{B}{F^2}} \right) \right) \right\} (\cosh\Gamma \sinh(\Omega)) - \Omega \left\{ \left(\frac{F}{2} \left(1 + \sqrt{1 - 4 \frac{B}{F^2}} \right) \right) \right\} (\cosh\Gamma \sinh(\Omega)) \end{aligned} \quad (\text{A1.54})$$

APPENDIX2

Interfacial Peel Stress Model for Trilayer Structure

The Equation (A2.1) is a fourth-order nonhomogeneous linear differential equation of peel stress.

$$p(x) - Ep''(x) + Ap^{IV}(x) = G\tau'(x) \quad (\text{A2.1})$$

This equation leads to a solution for peel stress considering the general solution of the shear stress. The variables in the Equation (A2.1) are defined as follow:

$$\begin{aligned} E &= \frac{(\gamma_3 - \gamma_1)}{\left[\frac{1}{D_3} + \frac{1}{D_I} \right]} \\ A &= \frac{\eta}{\left[\frac{1}{D_3} + \frac{1}{D_I} \right]} \\ G &= \frac{\left[\frac{h_3}{2D_3} - \frac{h_I}{2D_I} \right]}{\left[\frac{1}{D_3} + \frac{1}{D_I} \right]} \end{aligned} \quad (\text{A2.2})$$

where for two cases of I and II ,shear stress ($\tau(x)$) is respectively presented as:

Case I of shear stress:

$$\tau(x) = \frac{\Delta\alpha\Delta T \cosh(pl)\sin(ql)}{\Sigma} \sinh(px)\cos(qx) + \frac{-\Delta\alpha\Delta T \sinh(pl)\cos(ql)}{\Sigma} \cosh(px)\sin(qx) \quad (\text{A2.3})$$

where

$$\Sigma = p\sqrt{B} \cos(ql)\sin(ql) + q\sqrt{B} \cosh(pl)\sinh(pl)$$

The longitudinal force (Equation (19)) is defined as:

$$T(x) = \int \tau(x) = \left(\frac{C_{11}}{2} \left(\left(\frac{e^{p(x)}}{p^2 + q^2} (q \sin(qx) + p \cos(qx)) \right) - \left(\frac{e^{-p(x)}}{p^2 + q^2} (q \sin(qx) - p \cos(qx)) \right) \right) + \frac{C_{22}}{2} \left(\left(\frac{e^{p(x)}}{p^2 + q^2} (p \sin(qx) - q \cos(qx)) \right) - \left(\frac{e^{-p(x)}}{p^2 + q^2} (p \sin(qx) + q \cos(qx)) \right) \right) \right) \quad (A2.4)$$

And for case II of shear stress:

$$\tau(x) = \frac{\Delta \alpha \Delta T \sinh(\Omega l)}{\Sigma l} (\sinh \Gamma x) - \frac{\Delta \alpha \Delta T \sinh(\Gamma l)}{\Sigma l} (\sinh \Omega x) \quad (A2.5)$$

where

$$\Sigma l = \Gamma \left\{ \left(\frac{F}{2} \left(1 - \sqrt{1 - 4 \frac{B}{F^2}} \right) \right) \right\} (\cosh \Pi \sinh(\Omega l)) - \Omega \left\{ \left(\frac{F}{2} \left(1 + \sqrt{1 - 4 \frac{B}{F^2}} \right) \right) \right\} (\cosh \Pi \sinh(\Omega l))$$

Similarly the longitudinal force is defined as:

$$T(x) = \int [C_{11} \sinh(\Gamma x) + C_{22} \sinh(\Omega x)] = \left[C_{11} \frac{\cosh(\Gamma x)}{\Gamma} + C_{22} \frac{\cosh(\Omega x)}{\Omega} \right] \quad (A2.6)$$

The final solution of the nonhomogeneous differential equation (A2.1) was written as there is a particular solution and a general solution. The general solution was found by replacing the $G\tau(x)$ with 0 in equation (A2.1) and solving for the homogeneous solution (Equation (A2.7)) as:

$$p(x) - Ep''(x) + Ap^{IV}(x) = 0 \quad (\text{A2.7})$$

Using superposition principle, the final solution will be the sum of the solutions to the complementary function (CF) (Equation (A2.7)), and the solution due to $G\tau(x)$ the particular integral (PI). In other words, the General Solution is “CF + PI”.

The solutions to the CF for two cases are in the form of followings:

Case I: $E^2 - 4A < 0$

$$p_c(x) = C_{11} \cosh(\Phi x) \cos(\Pi x) + C_{22} \cosh(\Phi x) \sin(\Pi x) + C_{33} \sinh(\Phi x) \cos(\Pi x) + C_{44} \sinh(\Phi x) \sin(\Pi x) \quad (\text{A2.8})$$

where

$$\begin{aligned} \Phi &= \frac{1}{2\sqrt{A}} \sqrt{\sqrt{4A} + E} \\ \Pi &= \frac{1}{2\sqrt{A}} \sqrt{\sqrt{4A} - E} \end{aligned} \quad (\text{A2.9})$$

case II: $E^2 - 4A > 0$

$$p_c(x) = C_{11}(\cosh \Theta x) + C_{22}(\sinh \Theta x) + C_{33}(\cosh \Psi x) + C_{44}(\sinh \Psi x) \quad (\text{A2.10})$$

where

$$\begin{aligned} \Theta &= \frac{1}{\sqrt{2A}} \sqrt{E + \sqrt{E^2 - 4A}} \\ \Psi &= \frac{1}{\sqrt{2A}} \times \sqrt{E - \sqrt{E^2 - 4A}} \end{aligned}$$

The general solution for the two cases can be respectively set up as follow:

Case I:

$$p(x) = C_I \cosh(\Phi x) \cos(\Pi x) + C_{II} \sinh(\Phi x) \sin(\Pi x) \quad (\text{A2.11})$$

and

Case II:

$$p(x) = C_I (\cosh \Theta x) + C_{II} (\cosh \Psi x) \quad (\text{A2.12})$$

The peel stress should be self equilibrated with respect to the internal bending moments and internal longitudinal and shear forces. The boundary conditions are as follow:

$$V(l) = - \int_{-l}^l P(\zeta) d\zeta = 0 \quad (\text{A2.13})$$

and

$$\int_{-l}^l \int_{-l}^x p(\zeta) d\zeta d\zeta = 0 \quad (\text{A2.14})$$

Implementing the Equation (A2.13) to Equation (45) leads to:

$$\gamma_1 p'(l) + \frac{h_1}{2D_1} \tau(l) - \frac{h_3}{2D_3} \tau(l) - \gamma_3 p'(l) - \eta p'''(l) = 0 \quad (\text{A2.15})$$

For the second boundary condition the Equation (44) results in:

$$\frac{(\gamma_1 - \gamma_3)}{\eta} p(l) = p''(l) \quad (A2.16)$$

Once the Equation (A2.15) was rearranged:

$$\frac{(\gamma_1 - \gamma_3)}{\eta} p'(l) + \frac{\left(\frac{h_1}{2D_1} - \frac{h_3}{2D_3} \right)}{\eta} \tau(l) - p'''(l) = 0 \quad (A2.17)$$

knowing the shear stress is zero at l leads to:

$$\gamma_1 p'(l) - \gamma_3 p'(l) = \eta p'''(l) \quad (A2.18)$$

Using the method of undetermined coefficients, substituting the particular solution into the given boundary condition equations yields to two cases of peel and shear stresses with total of four cases that are presented as follow:

CASE-I: PEEL STRESS AND CASE-I: SHEAR STRESS

Equation (A2.11) for the case-I of peel stress and Equation (A1.40) for the case-I of shear stress are considered. The first boundary condition must be met. This further allows determining the unknown coefficients of peel stress equation under different conditions. Necessary derivations of the peel and shear stress are later implemented into the boundary conditions equations.

For the first boundary condition is expresses as:

$$C_I \begin{bmatrix} \frac{(\gamma_1 - \gamma_3)}{\eta} \cosh(\Phi l) \cos(\Pi l) \\ -(\Phi^2 - \Pi^2) \cosh(\Phi l) \cos(\Pi l) \\ +2\Phi \Pi \sinh(\Phi l) \sin(\Pi l) \end{bmatrix} + C_{II} \begin{bmatrix} \frac{(\gamma_1 - \gamma_3)}{\eta} \sinh(\Phi l) \sin(\Pi l) \\ -(\Phi^2 - \Pi^2) \sinh(\Phi l) \sin(\Pi l) \\ -2\Phi \Pi \cosh(\Phi l) \cos(\Pi l) \end{bmatrix} = 0 \quad (\text{A2.19})$$

For the second boundary condition is reflected as:

$$C_I \begin{bmatrix} \frac{(\gamma_1 - \gamma_3)}{\eta} \begin{pmatrix} \Phi \sinh(\Phi l) \cos(\Pi l) \\ -\Pi \cosh(\Phi l) \sin(\Pi l) \end{pmatrix} \\ -(\Phi^2 - \Pi^2) \Phi \sinh(\Phi l) \cos(\Pi l) \\ +(\Phi^2 - \Pi^2) \Pi \cosh(\Phi l) \sin(\Pi l) \\ +2\Phi^2 \Pi \cosh(\Phi l) \sin(\Pi l) \\ +2\Phi \Pi^2 \sinh(\Phi l) \cos(\Pi l) \end{bmatrix} + C_{II} \begin{bmatrix} \frac{(\gamma_1 - \gamma_3)}{\eta} \begin{pmatrix} \Phi \cosh(\Phi l) \sin(\Pi l) \\ +\Pi \sinh(\Phi l) \cos(\Pi l) \end{pmatrix} \\ -(\Phi^2 - \Pi^2) \Phi \cosh(\Phi l) \sin(\Pi l) \\ -(\Phi^2 - \Pi^2) \Pi \sinh(\Phi l) \cos(\Pi l) \\ -2\Phi^2 \Pi \sinh(\Phi l) \cos(\Pi l) \\ +2\Phi \Pi^2 \cosh(\Phi l) \sin(\Pi l) \end{bmatrix} \\ + \frac{\left(\frac{h_1}{2D_1} - \frac{h_3}{2D_3} \right)}{\eta} \begin{bmatrix} \frac{\Delta \alpha \Delta T \cosh(pl) \sin(ql)}{\Sigma} \sinh(pl) \cos(ql) \\ -\frac{\Delta \alpha \Delta T \sinh(pl) \cos(ql)}{\Sigma} \cosh(pl) \sin(ql) \end{bmatrix} = 0 \quad (\text{A2.20})$$

Solving for C_I & C_{II} with first and second boundary condition yields to:

$$C_I = - \frac{\left(\frac{h_1}{2D_1} - \frac{h_3}{2D_3} \right) \left[\frac{\Delta\alpha\Delta T \cosh(pl) \sin(ql)}{\Sigma} \sinh(pl) \cos(ql) + \frac{-\Delta\alpha\Delta T \sinh(pl) \cos(ql)}{\Sigma} \cosh(pl) \sin(ql) \right]}{\eta \left[\begin{array}{c} \left(\frac{\gamma_1 - \gamma_3}{\eta} \right) \left(\Phi \sinh(\Phi l) \cos(\Pi l) \right) \\ - \Pi \cosh(\Phi l) \sin(\Pi l) \\ - (\Phi^2 - \Pi^2) \Phi \sinh(\Phi l) \cos(\Pi l) \\ + (\Phi^2 - \Pi^2) \Pi \cosh(\Phi l) \sin(\Pi l) \\ + 2\Phi^2 \Pi \cosh(\Phi l) \sin(\Pi l) \\ + 2\Phi \Pi^2 \sinh(\Phi l) \cos(\Pi l) \end{array} \right]} \left[\begin{array}{c} \left(\frac{\gamma_1 - \gamma_3}{\eta} \right) \cosh(\Phi l) \cos(\Pi l) \\ - (\Phi^2 - \Pi^2) \cosh(\Phi l) \cos(\Pi l) \\ + 2\Phi \Pi \sinh(\Phi l) \sin(\Pi l) \\ \left(\frac{\gamma_1 - \gamma_3}{\eta} \right) \sinh(\Phi l) \sin(\Pi l) \\ - (\Phi^2 - \Pi^2) \sinh(\Phi l) \sin(\Pi l) \\ - 2\Phi \Pi \cosh(\Phi l) \cos(\Pi l) \end{array} \right] \left[\begin{array}{c} \left(\frac{\gamma_1 - \gamma_3}{\eta} \right) \left(\Phi \cosh(\Phi l) \sin(\Pi l) + \right. \\ \left. \Pi \sinh(\Phi l) \cos(\Pi l) \right) \\ + (\Phi^2 - \Pi^2) \Phi \cosh(\Phi l) \sin(\Pi l) \\ + (\Phi^2 - \Pi^2) \Pi \sinh(\Phi l) \cos(\Pi l) \\ + 2\Phi^2 \Pi \sinh(\Phi l) \cos(\Pi l) \\ - 2\Phi \Pi^2 \cosh(\Phi l) \sin(\Pi l) \end{array} \right]$$

(A2.21)

$$C_{II} = - \frac{\left(\frac{h_1}{2D_1} - \frac{h_3}{2D_3} \right) \left[\frac{\Delta\alpha\Delta T \cosh(pl) \sin(ql)}{\Sigma} \sinh(pl) \cos(ql) + \frac{-\Delta\alpha\Delta T \sinh(pl) \cos(ql)}{\Sigma} \cosh(pl) \sin(ql) \right]}{\eta \left[\begin{array}{c} \left(\frac{\gamma_1 - \gamma_3}{\eta} \right) \cosh(\Phi l) \cos(\Pi l) \\ - (\Phi^2 - \Pi^2) \cosh(\Phi l) \cos(\Pi l) \\ + 2\Phi \Pi \sinh(\Phi l) \sin(\Pi l) \end{array} \right]} \left[\begin{array}{c} \left(\frac{\gamma_1 - \gamma_3}{\eta} \right) \left(\Phi \sinh(\Phi l) \cos(\Pi l) \right) \\ - \Pi \cosh(\Phi l) \sin(\Pi l) \\ - (\Phi^2 - \Pi^2) \Phi \sinh(\Phi l) \cos(\Pi l) \\ + (\Phi^2 - \Pi^2) \Pi \cosh(\Phi l) \sin(\Pi l) \\ + 2\Phi^2 \Pi \cosh(\Phi l) \sin(\Pi l) \\ + 2\Phi \Pi^2 \sinh(\Phi l) \cos(\Pi l) \end{array} \right] \left[\begin{array}{c} \left(\frac{\gamma_1 - \gamma_3}{\eta} \right) \cosh(\Phi l) \cos(\Pi l) \\ - (\Phi^2 - \Pi^2) \cosh(\Phi l) \cos(\Pi l) \\ + 2\Phi \Pi \sinh(\Phi l) \sin(\Pi l) \end{array} \right] \left[\begin{array}{c} \left(\frac{\gamma_1 - \gamma_3}{\eta} \right) \left(\Phi \cosh(\Phi l) \sin(\Pi l) + \right. \\ \left. \Pi \sinh(\Phi l) \cos(\Pi l) \right) \\ + (\Phi^2 - \Pi^2) \Phi \cosh(\Phi l) \sin(\Pi l) \\ + (\Phi^2 - \Pi^2) \Pi \sinh(\Phi l) \cos(\Pi l) \\ + 2\Phi^2 \Pi \sinh(\Phi l) \cos(\Pi l) \\ - 2\Phi \Pi^2 \cosh(\Phi l) \sin(\Pi l) \end{array} \right]$$

(A2.22)

The other cases are as follow:

CASE-I PEEL STRESS, CASE-II SHEAR STRESS:

Equation (A2.11) for the case-I of peel stress and Equation (A1.47) for the case-I of shear stress are considered. The first boundary condition leads to:

$$C_I \begin{bmatrix} \frac{(\gamma_1 - \gamma_3)}{\eta} \cosh(\Phi l) \cos(\Pi l) \\ -(\Phi^2 - \Pi^2) \cosh(\Phi l) \cos(\Pi l) \\ + 2\Phi \Pi \sinh(\Phi l) \sin(\Pi l) \end{bmatrix} + C_{II} \begin{bmatrix} \frac{(\gamma_1 - \gamma_3)}{\eta} \sinh(\Phi l) \sin(\Pi l) \\ -(\Phi^2 - \Pi^2) \sinh(\Phi l) \sin(\Pi l) \\ - 2\Phi \Pi \cosh(\Phi l) \cos(\Pi l) \end{bmatrix} = 0 \quad (\text{A2.23})$$

For the second boundary condition:

$$C_I \begin{bmatrix} \frac{(\gamma_1 - \gamma_3)}{\eta} \left(\Phi \sinh(\Phi l) \cos(\Pi l) \right) \\ -\Pi \cosh(\Phi l) \sin(\Pi l) \\ -(\Phi^2 - \Pi^2) \Phi \sinh(\Phi l) \cos(\Pi l) \\ +(\Phi^2 - \Pi^2) \Pi \cosh(\Phi l) \sin(\Pi l) \\ + 2\Phi^2 \Pi \cosh(\Phi l) \sin(\Pi l) \\ + 2\Phi \Pi^2 \sinh(\Phi l) \cos(\Pi l) \end{bmatrix} + C_{II} \begin{bmatrix} \frac{(\gamma_1 - \gamma_3)}{\eta} \left(\Phi \cosh(\Phi l) \sin(\Pi l) \right) \\ +\Pi \sinh(\Phi l) \cos(\Pi l) \\ -(\Phi^2 - \Pi^2) \Phi \cosh(\Phi l) \sin(\Pi l) \\ -(\Phi^2 - \Pi^2) \Pi \sinh(\Phi l) \cos(\Pi l) \\ - 2\Phi^2 \Pi \sinh(\Phi l) \cos(\Pi l) \\ + 2\Phi \Pi^2 \cosh(\Phi l) \sin(\Pi l) \end{bmatrix} \\ + \frac{\left(\frac{h_1}{2D_1} - \frac{h_3}{2D_3} \right)}{\eta} \left[\frac{\Delta \alpha \Delta T \sinh(\Omega l)}{\Sigma l} (\sinh \Gamma l) \right. \\ \left. - \frac{\Delta \alpha \Delta T \sinh(\Gamma l)}{\Sigma l} (\sinh \Omega l) \right] = 0 \quad (\text{A2.24})$$

Solving for C_I & C_{II} with first and second boundary condition:

$$C_I = - \frac{\left(\frac{h_1}{2D_1} - \frac{h_3}{2D_3} \right) \left[\frac{\Delta\alpha\Delta T \sinh(\Omega l)}{\Sigma l} (\sinh \Gamma l) \right]}{\eta \left[\frac{\Delta\alpha\Delta T \sinh(\Gamma l)}{\Sigma l} (\sinh \Omega l) \right]} \left[\begin{array}{c} \left[\frac{(\gamma_1 - \gamma_3)}{\eta} (\Phi \sinh(\Phi l) \cos(\Pi l) - \Pi \cosh(\Phi l) \sin(\Pi l)) \right. \\ - (\Phi^2 - \Pi^2) \Phi \sinh(\Phi l) \cos(\Pi l) \\ + (\Phi^2 - \Pi^2) \Pi \cosh(\Phi l) \sin(\Pi l) \\ + 2\Phi^2 \Pi \cosh(\Phi l) \sin(\Pi l) \\ + 2\Phi \Pi^2 \sinh(\Phi l) \cos(\Pi l) \end{array} \right] \left[\begin{array}{c} \frac{(\gamma_1 - \gamma_3)}{\eta} \cosh(\Phi l) \cos(\Pi l) \\ - (\Phi^2 - \Pi^2) \cosh(\Phi l) \cos(\Pi l) \\ + 2\Phi \Pi \sinh(\Phi l) \sin(\Pi l) \end{array} \right] \left[\begin{array}{c} \frac{(\gamma_1 - \gamma_3)}{\eta} (\Phi \cosh(\Phi l) \sin(\Pi l) + \Pi \sinh(\Phi l) \cos(\Pi l)) \\ - (\Phi^2 - \Pi^2) \Phi \cosh(\Phi l) \sin(\Pi l) \\ - (\Phi^2 - \Pi^2) \Pi \sinh(\Phi l) \cos(\Pi l) \\ - 2\Phi^2 \Pi \sinh(\Phi l) \cos(\Pi l) \\ + 2\Phi \Pi^2 \cosh(\Phi l) \sin(\Pi l) \end{array} \right] \right] \quad (A2.25)$$

$$C_{II} = - \frac{\left(\frac{h_1}{2D_1} - \frac{h_3}{2D_3} \right) \left[\frac{\Delta\alpha\Delta T \sinh(\Omega l)}{\Sigma l} (\sinh \Gamma l) \right]}{\eta \left[\frac{\Delta\alpha\Delta T \sinh(\Gamma l)}{\Sigma l} (\sinh \Omega l) \right]} \left[\begin{array}{c} \left[\frac{(\gamma_1 - \gamma_3)}{\eta} \sinh(\Phi l) \sin(\Pi l) \right. \\ - (\Phi^2 - \Pi^2) \sinh(\Phi l) \sin(\Pi l) \\ - 2\Phi \Pi \cosh(\Phi l) \cos(\Pi l) \end{array} \right] \left[\begin{array}{c} \frac{(\gamma_1 - \gamma_3)}{\eta} (\Phi \sinh(\Phi l) \cos(\Pi l) - \Pi \cosh(\Phi l) \sin(\Pi l)) \\ - (\Phi^2 - \Pi^2) \Phi \sinh(\Phi l) \cos(\Pi l) \\ + (\Phi^2 - \Pi^2) \Pi \cosh(\Phi l) \sin(\Pi l) \\ + 2\Phi^2 \Pi \cosh(\Phi l) \sin(\Pi l) \\ + 2\Phi \Pi^2 \sinh(\Phi l) \cos(\Pi l) \end{array} \right] \left[\begin{array}{c} \frac{(\gamma_1 - \gamma_3)}{\eta} \cosh(\Phi l) \cos(\Pi l) \\ - (\Phi^2 - \Pi^2) \cosh(\Phi l) \cos(\Pi l) \\ + 2\Phi \Pi \sinh(\Phi l) \sin(\Pi l) \end{array} \right] \left[\begin{array}{c} \frac{(\gamma_1 - \gamma_3)}{\eta} (\Phi \cosh(\Phi l) \sin(\Pi l) + \Pi \sinh(\Phi l) \cos(\Pi l)) \\ - (\Phi^2 - \Pi^2) \Phi \cosh(\Phi l) \sin(\Pi l) \\ - (\Phi^2 - \Pi^2) \Pi \sinh(\Phi l) \cos(\Pi l) \\ - 2\Phi^2 \Pi \sinh(\Phi l) \cos(\Pi l) \\ + 2\Phi \Pi^2 \cosh(\Phi l) \sin(\Pi l) \end{array} \right] \right] \quad (A2.26)$$

CASE-II PEEL STRESS AND CASE-I SHEAR STRESS:

Equation (A2.13) for the case-II of peel stress and Equation (A1.40) for the case-I of shear stress are considered. The first boundary condition leads to:

$$C_I \left[\frac{(\gamma_1 - \gamma_3)}{\eta} \cosh \Theta l - \Theta^2 \cosh \Theta l \right] + C_{II} \left[\frac{(\gamma_1 - \gamma_3)}{\eta} \cosh \Psi l - \Psi^2 \cosh \Psi l \right] = 0 \quad (\text{A2.27})$$

and for the second boundary condition:

$$\begin{aligned} & C_I \left[\frac{(\gamma_1 - \gamma_3)}{\eta} \Theta \sinh \Theta l \right] + C_{II} \left[\frac{(\gamma_1 - \gamma_3)}{\eta} \Psi (\sinh \Psi l) \right] \\ & + \frac{\left(\frac{h_1}{2D_1} - \frac{h_3}{2D_3} \right)}{\eta} \left[\frac{\Delta \alpha \Delta T \cosh(pl) \sin(ql)}{\Sigma} \sinh(pl) \cos(ql) \right. \\ & \left. + \frac{-\Delta \alpha \Delta T \sinh(pl) \cos(ql)}{\Sigma} \cosh(pl) \sin(ql) \right] = 0 \end{aligned} \quad (\text{A2.28})$$

Solving for C_I & C_{II} with first and second boundary condition:

$$\begin{aligned} C_I = - & \frac{\left(\frac{h_1}{2D_1} - \frac{h_3}{2D_3} \right) \left[\frac{\Delta \alpha \Delta T \cosh(pl) \sin(ql)}{\Sigma} \sinh(pl) \cos(ql) \right.}{\eta \left[\frac{-\Delta \alpha \Delta T \sinh(pl) \cos(ql)}{\Sigma} \cosh(pl) \sin(ql) \right]} \left[\frac{(\gamma_1 - \gamma_3)}{\eta} \cosh \Psi l - \Psi^2 \cosh \Psi l \right] \\ & \frac{\left[\frac{(\gamma_1 - \gamma_3)}{\eta} \Theta \sinh \Theta l \right] \left[\frac{(\gamma_1 - \gamma_3)}{\eta} \cosh \Psi l \right] - \left[\frac{(\gamma_1 - \gamma_3)}{\eta} \cosh \Theta l \right] \left[\frac{(\gamma_1 - \gamma_3)}{\eta} \Psi (\sinh \Psi l) \right]}{\left[\frac{(\gamma_1 - \gamma_3)}{\eta} \Theta \sinh \Theta l \right] \left[-\Psi^2 \cosh \Psi l \right] - \left[-\Theta^2 \cosh \Theta l \right] \left[-\Psi^3 (\sinh \Psi l) \right]} \end{aligned} \quad (\text{A2.29})$$

$$C_{II} = \frac{\left(\frac{h_1}{2D_1} - \frac{h_3}{2D_3} \right) \left[\frac{\Delta\alpha\Delta T \cosh(pl) \sin(ql)}{\Sigma} \sinh(pl) \cos(ql) + \frac{-\Delta\alpha\Delta T \sinh(pl) \cos(ql)}{\Sigma} \cosh(pl) \sin(ql) \right] \left[\frac{(\gamma_1 - \gamma_3)}{\eta} \cosh \Theta l - \Theta^2 \cosh \Theta l \right]}{\begin{bmatrix} \frac{(\gamma_1 - \gamma_3)}{\eta} \Theta \sinh \Theta l \\ -C_I \Theta^3 (\sinh \Theta l) \end{bmatrix} \begin{bmatrix} \frac{(\gamma_1 - \gamma_3)}{\eta} \cosh \Psi l \\ -\Psi^2 \cosh \Psi l \end{bmatrix} - \begin{bmatrix} \frac{(\gamma_1 - \gamma_3)}{\eta} \cosh \Theta l \\ -\Theta^2 \cosh \Theta l \end{bmatrix} \begin{bmatrix} \frac{(\gamma_1 - \gamma_3)}{\eta} \Psi (\sinh \Psi l) \\ -\Psi^3 (\sinh \Psi l) \end{bmatrix}}$$

(A2.30)

CASE-II PEEL STRESS AND CASE-II SHEAR STRESS:

Equation (A2.15) for the case-II of peel stress and Equation (A1.47) for the case-I of shear stress are considered. The first boundary condition leads to:

$$C_I \begin{bmatrix} \frac{(\gamma_1 - \gamma_3)}{\eta} (\cosh \Theta l) \\ -\Theta^2 (\cosh \Theta l) \end{bmatrix} + C_{II} \begin{bmatrix} \frac{(\gamma_1 - \gamma_3)}{\eta} (\cosh \Psi l) \\ -\Psi^2 (\cosh \Psi l) \end{bmatrix} = 0$$

(A2.31)

For the second boundary condition:

$$C_I \begin{bmatrix} \frac{(\gamma_1 - \gamma_3)}{\eta} \Theta (\sinh \Theta l) \\ -\Theta^3 (\sinh \Theta l) \end{bmatrix} + C_{II} \begin{bmatrix} \frac{(\gamma_1 - \gamma_3)}{\eta} \Psi (\sinh \Psi l) \\ -\Psi^3 (\sinh \Psi l) \end{bmatrix} + \frac{\left(\frac{h_1}{2D_1} - \frac{h_3}{2D_3} \right)}{\eta} \left[\frac{\Delta\alpha\Delta T \sinh(\Omega l)}{\Sigma l} (\sinh \Gamma l) - \frac{\Delta\alpha\Delta T \sinh(\Gamma l)}{\Sigma l} (\sinh \Omega l) \right] = 0$$

(A2.32)

Solving for C_I & C_{II} with first and second boundary condition:

$$C_I = - \frac{\left(\frac{h_1}{2D_1} - \frac{h_3}{2D_3} \right) \left[\frac{\Delta\alpha\Delta T \sinh(\Omega l)}{\Sigma l} (\sinh \Gamma l) \right] \left[\frac{(\gamma_1 - \gamma_3)}{\eta} (\cosh \Psi l) \right]}{\eta \left[- \frac{\Delta\alpha\Delta T \sinh(\Gamma l)}{\Sigma l} (\sinh \Omega l) \right] \left[- \Psi^2 (\cosh \Psi l) \right]} \left[\frac{(\gamma_1 - \gamma_3)}{\eta} \Theta(\sinh \Theta l) \right] \left[\frac{(\gamma_1 - \gamma_3)}{\eta} (\cosh \Psi l) \right] - \left[\frac{(\gamma_1 - \gamma_3)}{\eta} (\cosh \Theta l) \right] \left[\frac{(\gamma_1 - \gamma_3)}{\eta} \Psi(\sinh \Psi l) \right] \left[- \Theta^3 (\sinh \Theta l) \right] \left[- \Psi^2 (\cosh \Psi l) \right] - \left[- \Theta^2 (\cosh \Theta l) \right] \left[- \Psi^3 (\sinh \Psi l) \right] \right] \quad (\text{A2.33})$$

$$C_{II} = \frac{\left(\frac{h_1}{2D_1} - \frac{h_3}{2D_3} \right) \left[\frac{\Delta\alpha\Delta T \sinh(\Omega l)}{\Sigma l} (\sinh \Gamma l) \right] \left[\frac{(\gamma_1 - \gamma_3)}{\eta} (\cosh \Theta l) \right]}{\eta \left[- \frac{\Delta\alpha\Delta T \sinh(\Gamma l)}{\Sigma l} (\sinh \Omega l) \right] \left[- \Theta^2 (\cosh \Theta l) \right]} \left[\frac{(\gamma_1 - \gamma_3)}{\eta} (\cosh \Psi l) \right] \left[\frac{(\gamma_1 - \gamma_3)}{\eta} \Theta(\sinh \Theta l) \right] - \left[\frac{(\gamma_1 - \gamma_3)}{\eta} (\cosh \Theta l) \right] \left[\frac{(\gamma_1 - \gamma_3)}{\eta} \Psi(\sinh \Psi l) \right] \left[- \Psi^2 (\cosh \Psi l) \right] \left[- \Theta^3 (\sinh \Theta l) \right] - \left[- \Theta^2 (\cosh \Theta l) \right] \left[- \Psi^3 (\sinh \Psi l) \right] \right] \quad (\text{A2.34})$$

APPENDIX3

Program of Inverse method

```

type=input('Enter 1 for plane-strain/Enter 2 for plane-stress : ');

WWx=File name;                % Experimental warpage input

XX=Xdata;                      %X direction

n=length(XX);

l=Number;                      %Half of the die side size

b=1;
%DeltaT= number;              % Temperature Variance

E0=0.98E+11;    V0=2.3E-01; Alpha0=3E-06;    H0=5.50E-04;

E1=1.8E+08;      V1=3.1E-01; Alpha1=3E-05;    H1=3.30E-04;

E2=2.10E+10;    V2=2.3E-01; Alpha2=4.8E-06;    H2=7.50E-04;
rr=3;

M=[E0 Alpha0 V0 H0 E1 Alpha1 V1 H1 E2 Alpha2 V2 H2 l DeltaT rr];

for E1=M(1,1):1e9:98e9

E1=M(1,1);
    for E2=M(1,5):0.1e8:1.8e6
        for E3=M(1,9):1e9:22e9
            for v1=M(1,3):.01:.23
                for v2=M(1,7):.01:.32
                    for v3=M(1,11):.01:.25
                        for alpha1=M(1,2):0.1e-6:3e-6
                            for alpha2=M(1,6):.5e-5:5e-5
                                for alpha3=M(1,10):.2e-6:6e-6
                                    for rr=M(1,15):1:3

h1=M(1,4);
h2=M(1,8);
h3=M(1,12);

l=M(1,13);
DeltaT=M(1,14);

X=0;

G1=E1/(2*(1+v1));
G2=E2/(2*(1+v2));
G3=E3/(2*(1+v3));

beta1=h1^2/rr;
beta2=h2^2/rr;
beta3=h3^2/rr;

```

```

u1=h1/(3*G1);
u2=h2/(3*G2);
u3=h3/(3*G3);

Gama1=1/(G1*h1);
Gama3=1/(G3*h3);

if type==1 %Plane-strain
    D1=(E1*h1^3)/(12*(1-v1^2));
    %D2=(E2*h2^3)/(12*(1-v2^2));
    D3=(E3*h3^3)/(12*(1-v3^2));
    lemدا1=((1+v1)*(1-2*v1))/((1-v1)*E1*h1);
    lemدا3=((1+v3)*(1-2*v3))/((1-v3)*E3*h3);
    ALPHA1=alpha1*(1+v1);
    ALPHA3=alpha3*(1+v3);
    DeltaAlpha=(ALPHA3-
ALPHA1)/(lemدا1+lemدا3+((h1/2)+(h3/2))^2/(D1+D3));
    Eta=((1-2*v2)*(1+v2)*h2)/(3*(1-v2)*E2);

elseif type==2 %Plane-stress
    D1=(E1*h1^3)/12;
    %D2=(E2*h2^3)/12;
    D3=(E3*h3^3)/12;
    lemدا1=(1-v1^2)/(E1*h1);
    lemدا3=(1-v3^2)/(E3*h3);
    ALPHA1=alpha1;
    ALPHA3=alpha3;
    DeltaAlpha=(alpha3-
alpha1)/(lemدا1+lemدا3+((h1/2)+(h3/2))^2/(D1+D3));
    Eta=((1-v2^2)*h2)/(3*E2);
else
    error('Wrong Selection');
end

mxdff=0;

Mm(b,1)=E1;
Mm(b,3)=v1;
Mm(b,2)=alpha1;
Mm(b,4)=E2;
Mm(b,6)=v2;
Mm(b,5)=alpha2;
Mm(b,7)=E3;
Mm(b,9)=v3;
Mm(b,8)=alpha3;
Mm(b,10)=rr;

B=(u1*beta1-
u2*beta2+u3*beta3)/(lemدا1+lemدا3+((h1/2)+(h3/2))^2/(D1+D3));
B=abs(B);
F=(u1-
u2+u3)/(lemدا1+lemدا3+((h1/2)+(h3/2))^2/(D1+D3));
F=abs(F);

check1=F^(2)-(4*B);

```

```

if check1<0
    p=sqrt(sqrt(4*B)+F)/(2*sqrt(B));

    q=sqrt(sqrt(4*B)-F)/(2*sqrt(B));

Sigma=(p*sqrt(B)*cos(q*l)*sin(q*l))+(q*sqrt(B)*cosh(p*l)*sinh(p*l));

C11=DeltaAlpha*DeltaT*cosh(p*l)*sin(q*l)/Sigma;
C22=(-1)*DeltaAlpha*DeltaT*sinh(p*l)*cos(q*l)/Sigma;

    IntegrationConstant_1=((h1+h3)/(2*(D1+D3)))*((-
C11/(2*(p^2-q^2)))*(exp(p*l)*(p*cos(q*l)+q*sin(q*l))-exp(-p*l)*(-
p*cos(q*l)+q*sin(q*l)))+(-C22/(2*(p^2-q^2)))*(exp(p*l)*(p*sin(q*l)-
q*cos(q*l))+exp(-p*l)*(-p*sin(q*l)-q*cos(q*l))));
    %IntegrationConstant_2=0

IntegrationConstant_3=((h1+h3)/(2*(D1+D3)))*((3*p*q*(q*C11+p*C22))/(p^2
-q^2)^3);

    i=0;
    SSerr=0;
    Wsigma=0;
    for i=1:n
        x=XX(i)*l;
        AA=((h1+h3)/(2*(D1+D3)));
        Warpage(i)=-
IntegrationConstant_1*x^2+IntegrationConstant_3+(AA*((C11/(2*(p^2-
q^2)^3))*((p^3)-3*p*(q^2))*exp(p*x)*cos(q*x)+(-
q^3+3*(p^2)*q)*exp(p*x)*sin(q*x)+(-p^3-3*p*(q^2))*exp(-
p*x)*cos(q*x)+(q^3-3*(p^2)*q)*exp(-p*x)*sin(q*x))+(C22/(2*(p^2-
q^2)^3))*((p^3-3*p*(q^2))*exp(p*x)*sin(q*x)+(-
q^3+3*(p^2)*q)*exp(p*x)*cos(q*x)+(-p^3+3*p*q^2)*exp(-
p*x)*sin(q*x)+(q^3-3*(p^2)*q)*exp(-p*x)*cos(q*x))));
        Wxx=Warpage;
        dif(i)=(-Wxx(i)+WWx(i));
        SSerr=SSerr+(dif(i))^2;
        Wsigma=Wsigma+WWx(i);
    end

elseif check1>0
    gama_case2=sqrt(F+sqrt(F^2-(4*B)))/sqrt(2*B);

    ohm_case2=sqrt(F-sqrt(F^2-(4*B)))/sqrt(2*B);

    Sigma_1=gama_case2*((F/2)*(1-sqrt(1-
((4*B)/F^2))))*cosh(gama_case2*l)*sinh(ohm_case2*l)-
ohm_case2*((F/2)*(1+sqrt(1-
(4*B)/F^2))))*cosh(gama_case2*l)*sinh(ohm_case2*l);

```

```

C11=(DeltaAlpha*DeltaT*sinh(ohm_case2*1))/Sigma_1;

C22=((-
1)*DeltaAlpha*DeltaT*sinh(gama_case2*1))/Sigma_1;

IntegrationConstant_1=(-
1)*((h1+h3)/(2*(D1+D3)))*(C11*cosh(gama_case2*1))/gama_case2+(C22*cosh
(ohm_case2*1))/ohm_case2);
%IntegrationConstant_2=0
IntegrationConstant_3=(-
1)*((h1+h3)/(2*(D1+D3)))*(C11/gama_case2^3+C22/ohm_case2^3);

i=0;
SSerr=0;
Wsigma=0;
for i=1:n
    x=XX(i)*1;
    AA=((h1+h3)/(2*(D1+D3)));
    Warpage(i)=-
IntegrationConstant_1*x^2+IntegrationConstant_3+AA*((C11*sinh(gama_case
2*x))/gama_case2^3+C22*sinh(ohm_case2*x)/ohm_case2^3);
    Wxx=Warpage;
    dif(i)=(-Wxx(i)+WWx(i));
    SSerr=SSerr+((dif(i))^2);
    Wsigma=Wsigma+WWx(i);
end

end

Wmean=Wsigma/n;
SStot=0;
for j=1:n
    diff(j)=Wxx(j)-Wmean;
    SStot=((diff(j))^2)+SStot;
end
Rsquare=1-(SSerr/SStot);

if b==1
    mxR(b)=Rsquare;
    r=b;
else
    if mxR(r)<Rsquare
        r=b;
        mxR(r)=Rsquare;
    end
end
RS(b)=Rsquare;
b=b+1;
RS=RS.';

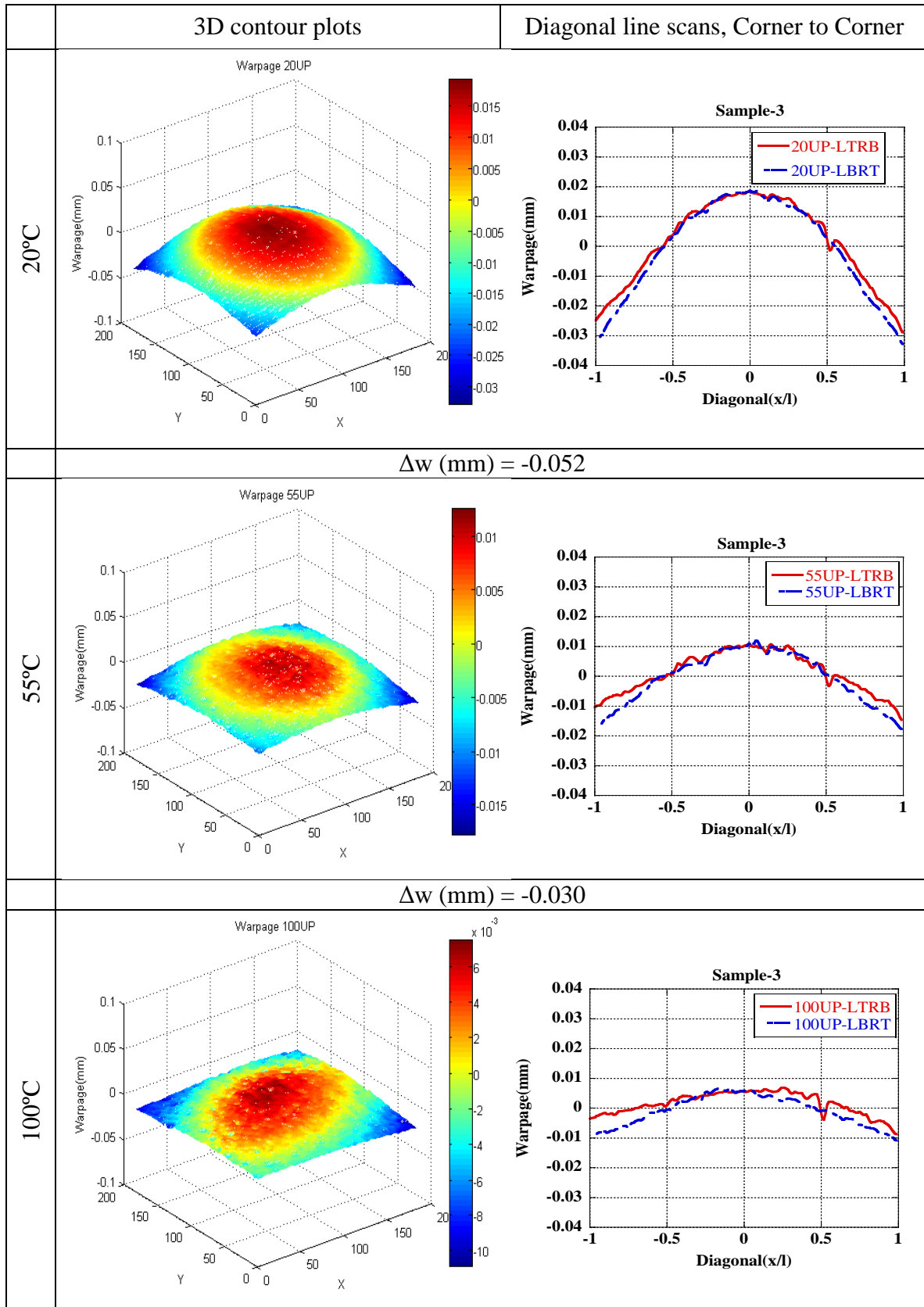
end
end
end
end
end

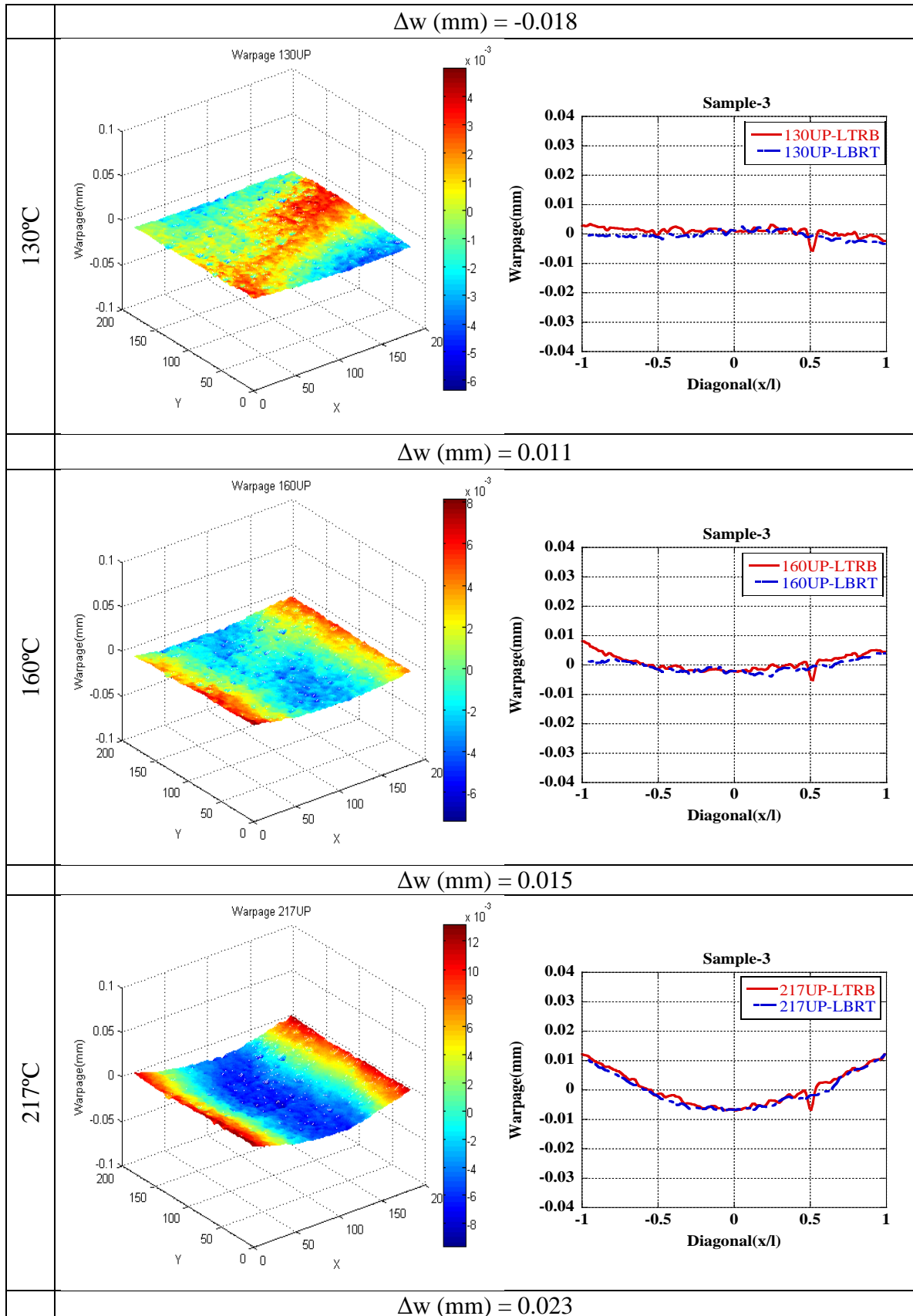
```


end
end
end
end

APPENDIX4

Warpage of Trilayer Structure- Experimental Results





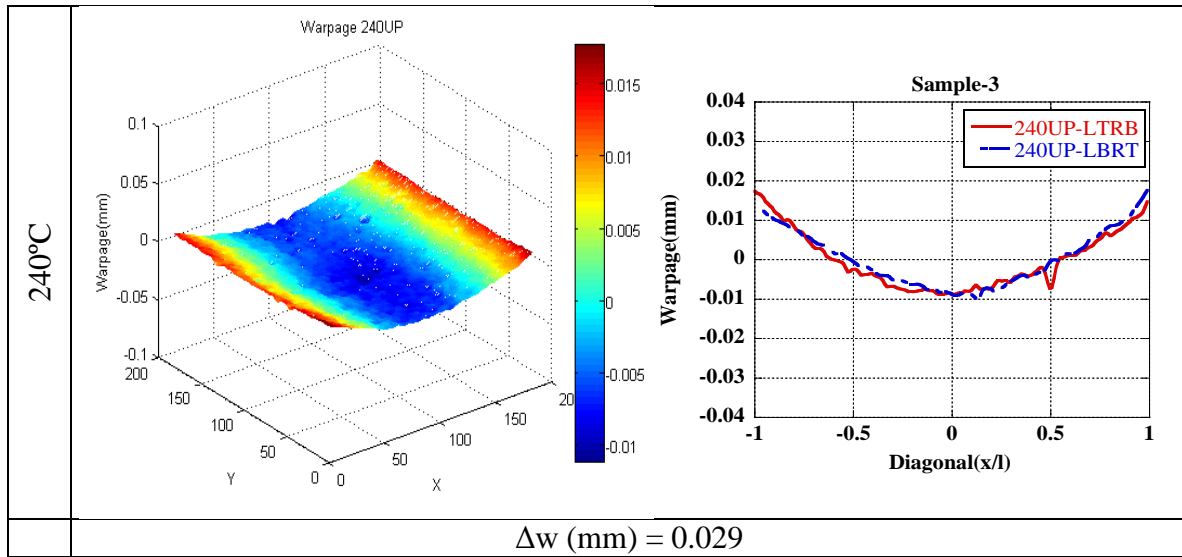
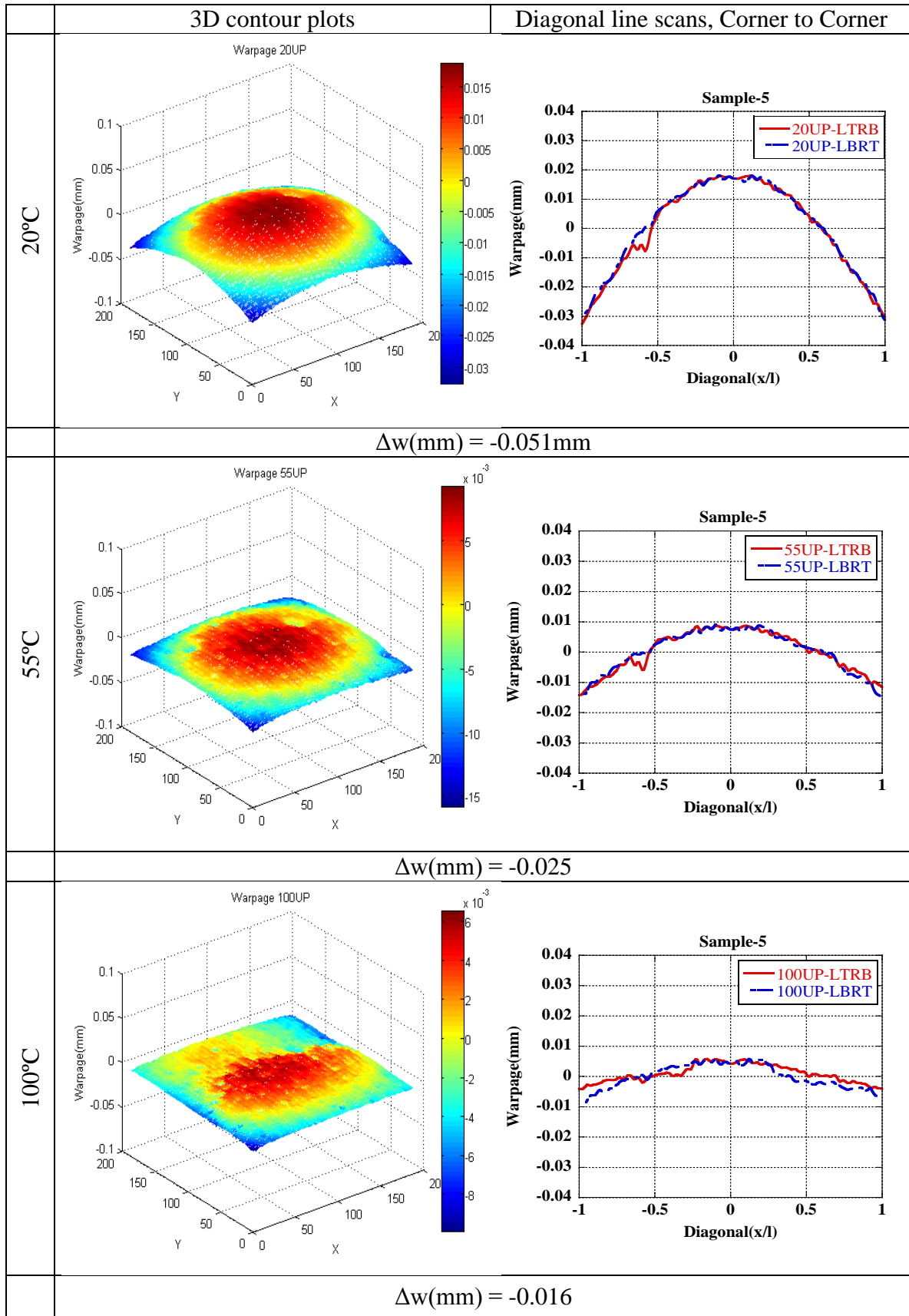
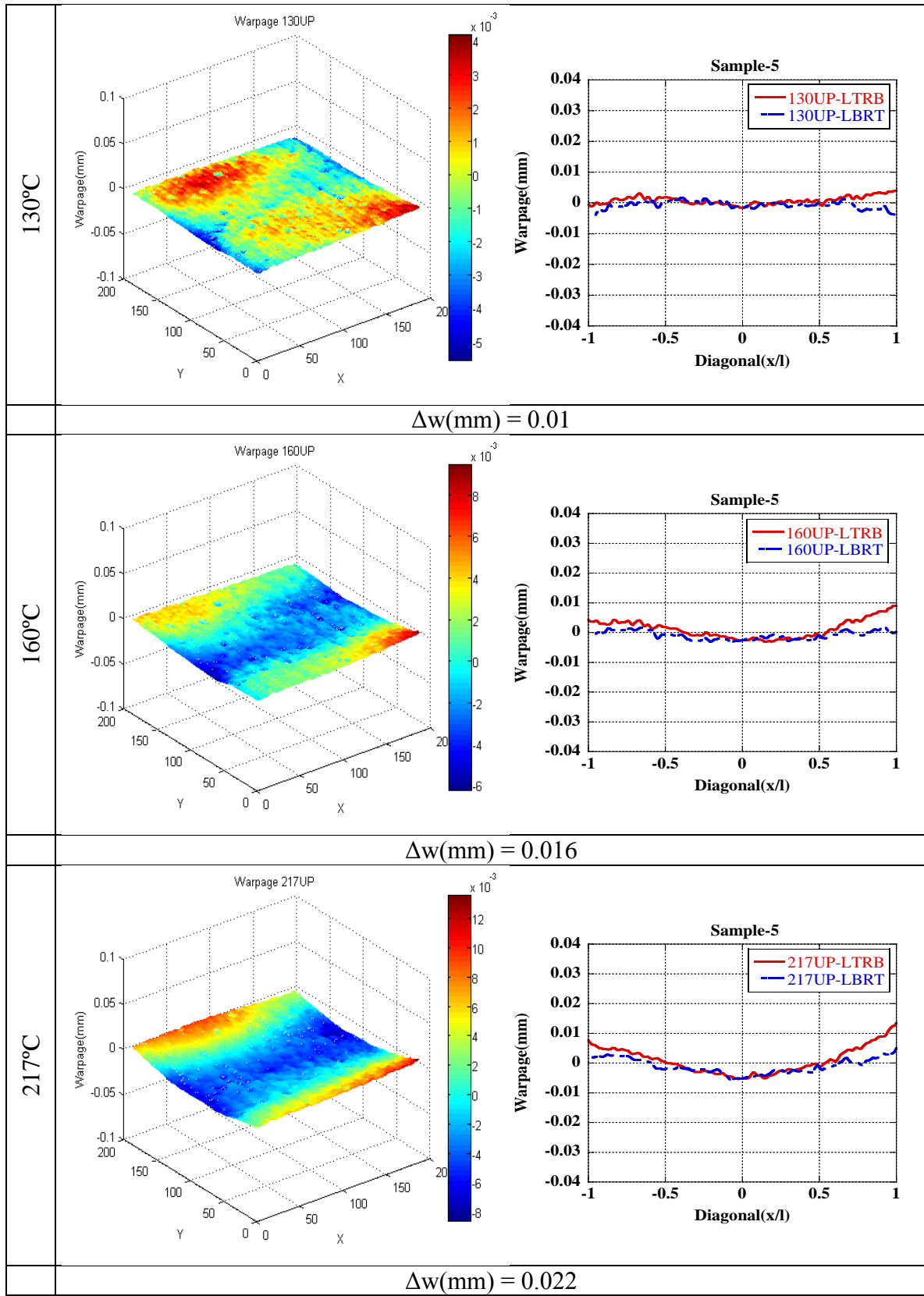


Figure A4.1: Typical 3-D graphical representation for measured warpage at temperature for sample#3.





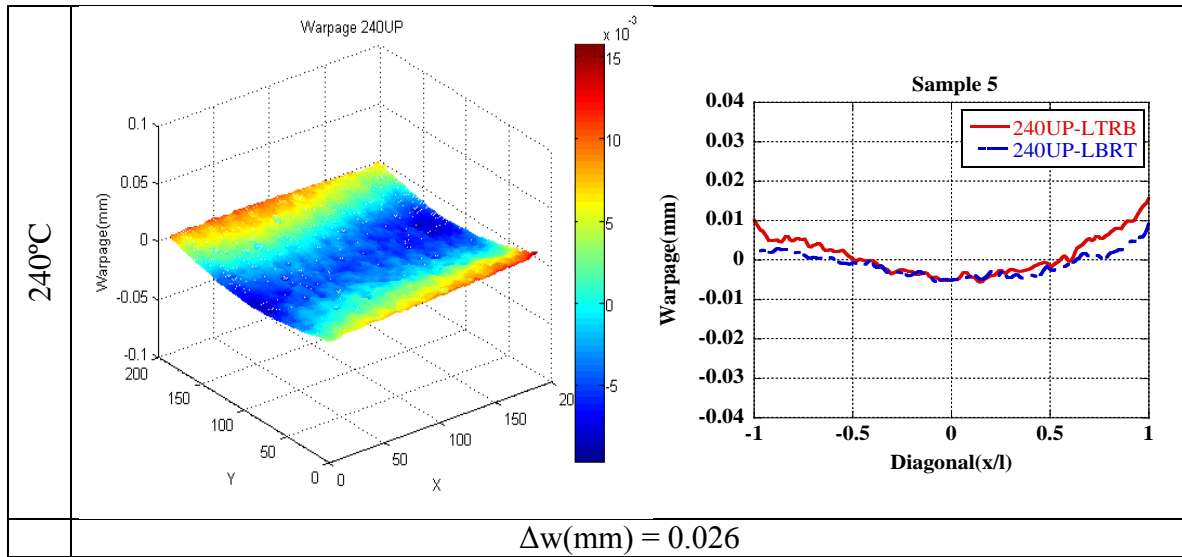
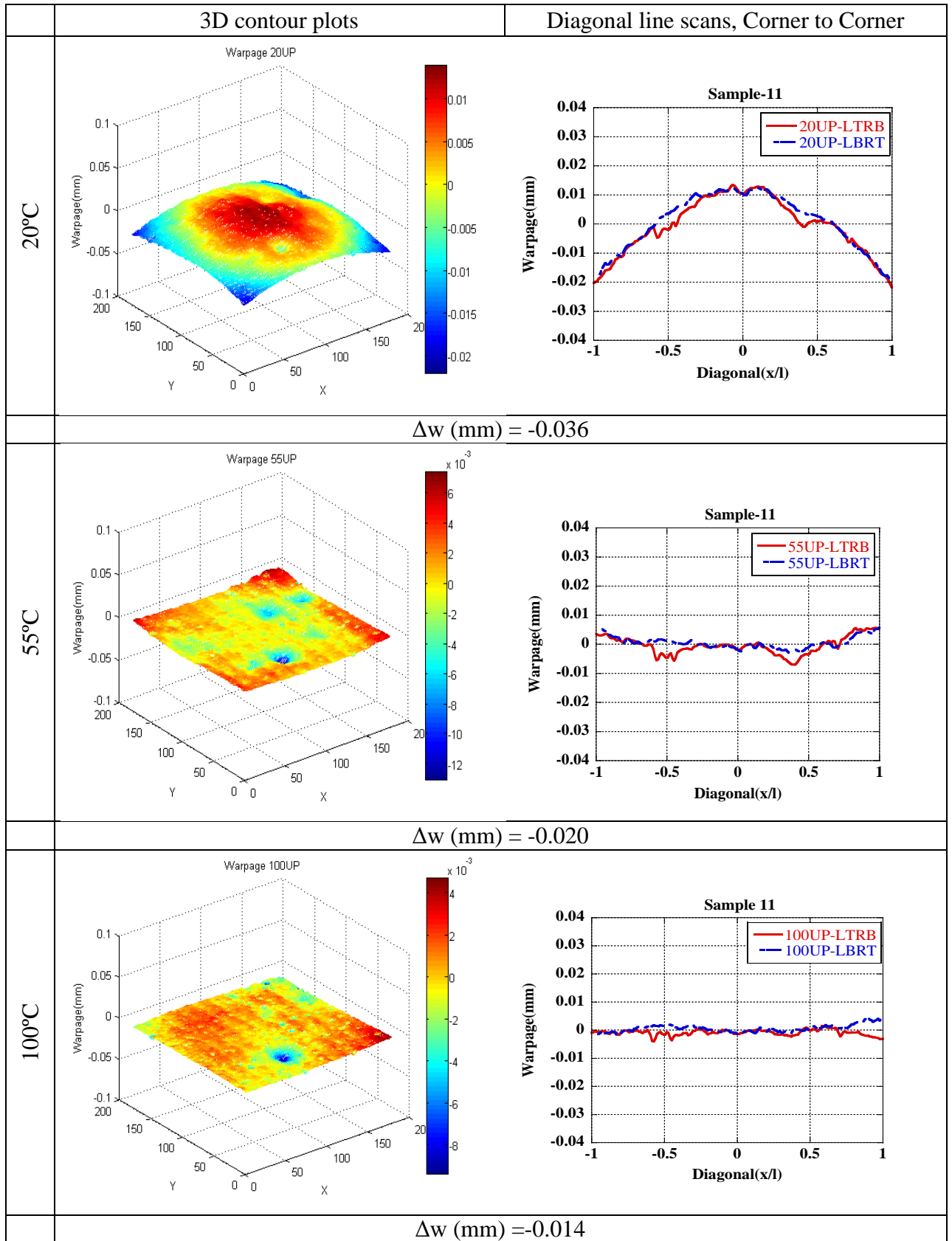


Figure A4.2: Typical 3-D graphical representation for measured warpage at temperature for sample#5.



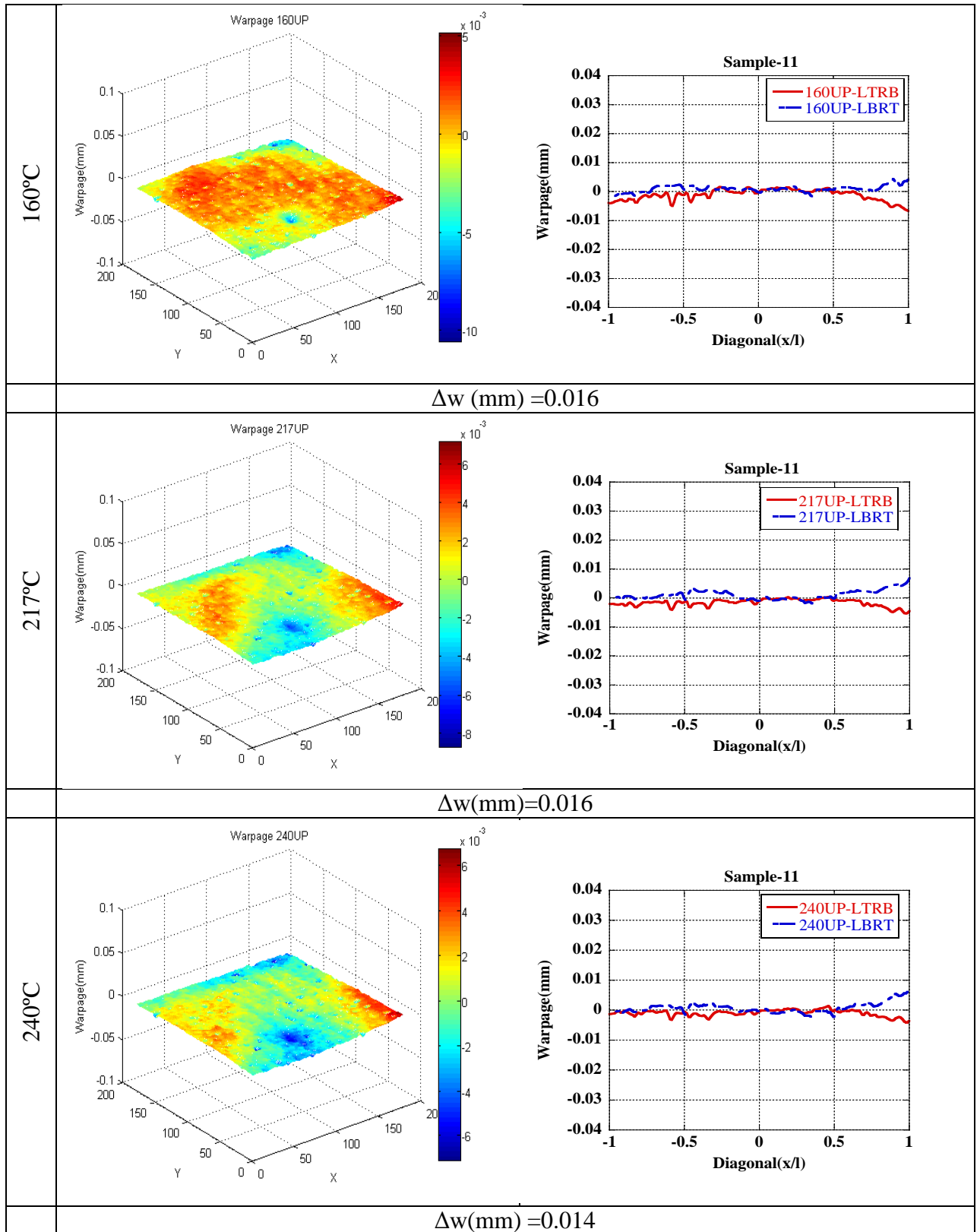
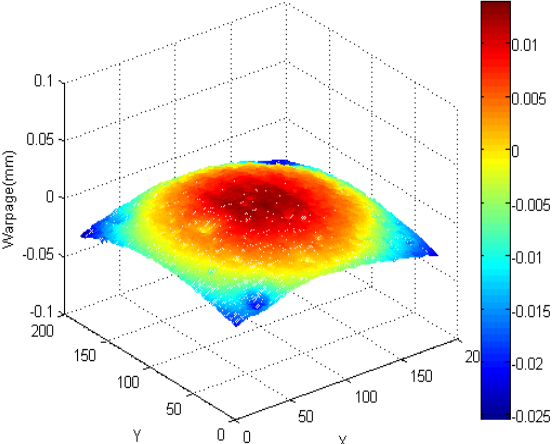
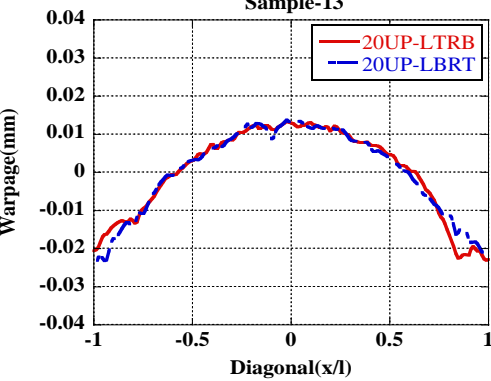
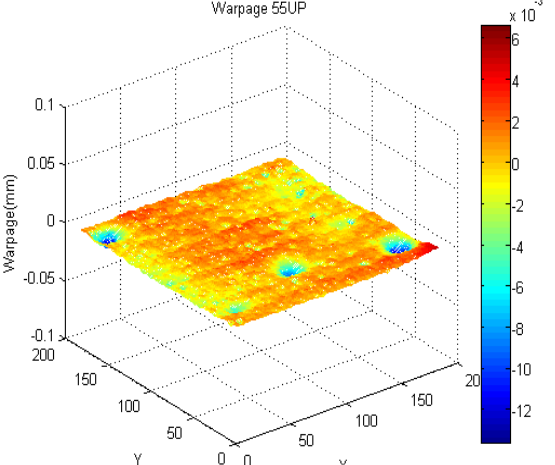
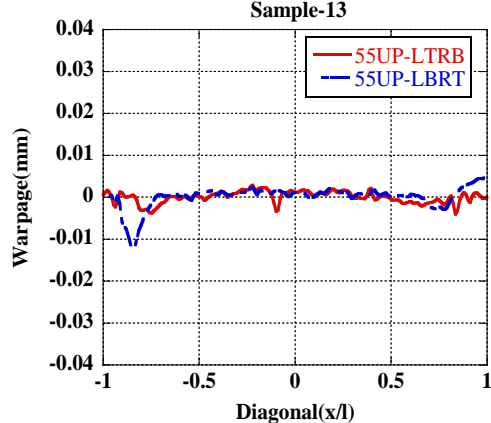
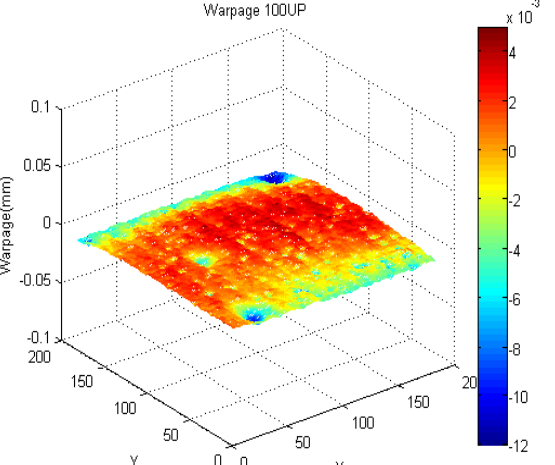
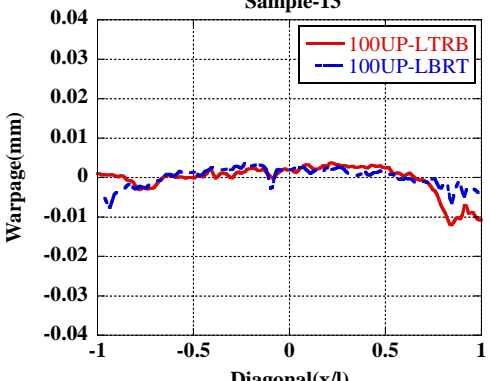
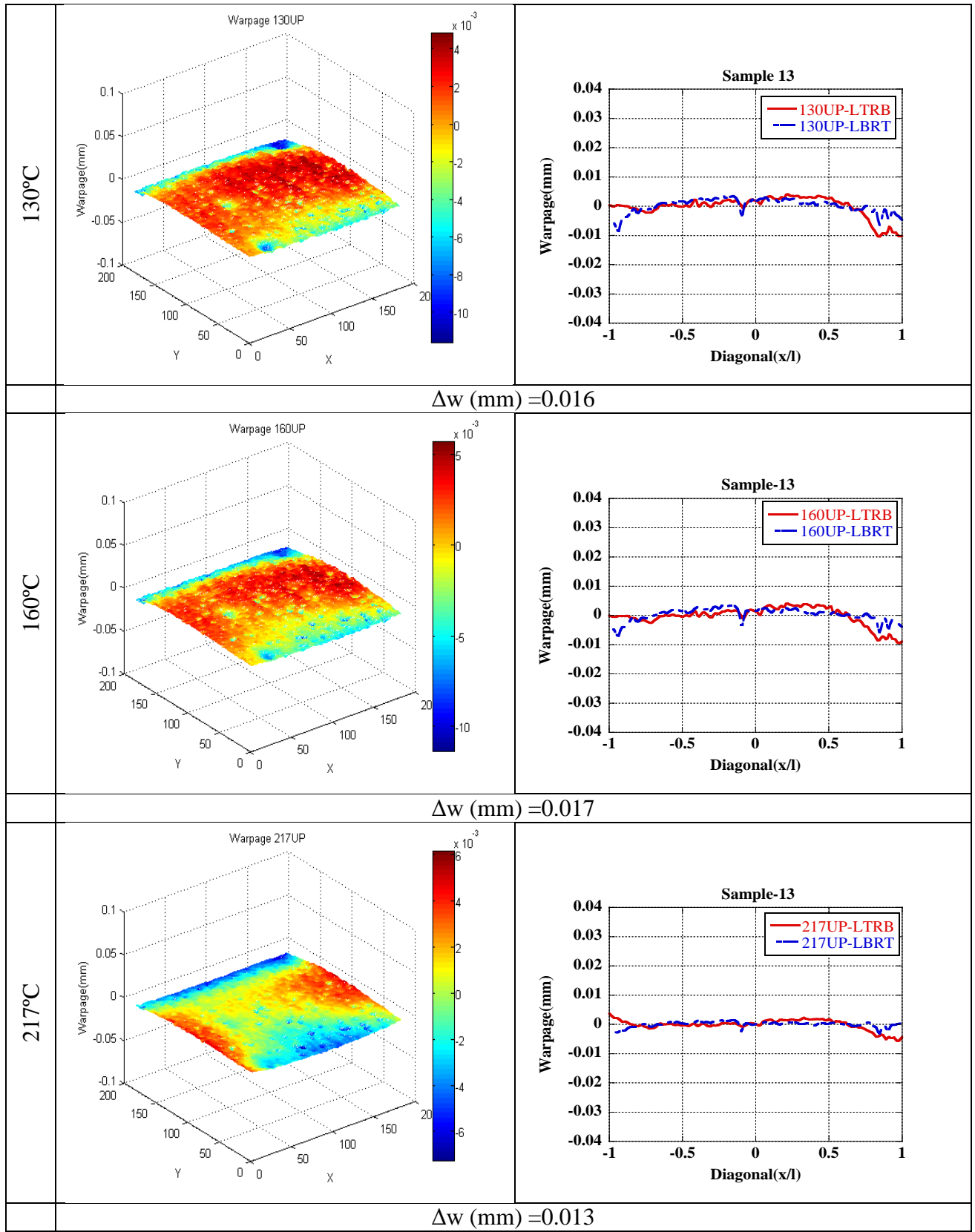


Figure A4.3: Typical 3-D graphical representation for measured warpage at temperature for sample#11.

	3D contour plots	Diagonal line scans, Corner to Corner
20°C	<p>Warpage 20UP</p> 	<p>Sample-13</p> 
$\Delta w \text{ (mm)} = -0.039$		
55°C	<p>Warpage 55UP</p> 	<p>Sample-13</p> 
$\Delta w \text{ (mm)} = -0.020$		
100°C	<p>Warpage 100UP</p> 	<p>Sample-13</p> 
$\Delta w \text{ (mm)} = -0.017$		



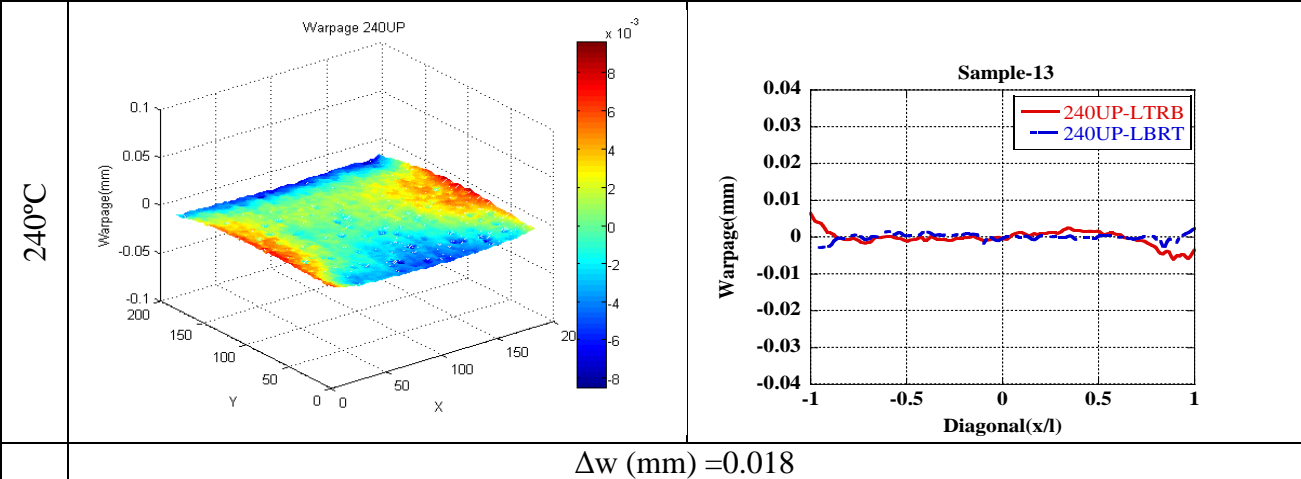


Figure A4.4: Typical 3-D graphical representation for measured warpage at temperature for sample#13.

APPENDIX5

Inverse Modeling Results and Warpage Prediction

A5.1 Trilayer constituents mechanical properties

Table A5.1: Bilinear material properties for sample#3 determined using HEAIM

Temperature range (°C)	Max. Correlation (%)	Die			Underfill		Substrate		
		E (GPa)	α (ppm/°C)	ν	E (GPa)	ν	E (GPa)	α (ppm/°C)	ν
20-55	94	98	2.5	0.22	0.19	0.30	23	6.8	0.24
55-100	70.8	98	2.5	0.22	0.014	0.30	22	5.5	0.24
100-130	94.2	98	2.5	0.22	0.012	0.30	20	6.2	0.24
160-217	80.7	98	2.5	0.22	0.011	0.31	16	9.10	0.24
217-240	48.3	98	2.5	0.22	0.011	0.31	15	11	0.24

Table A5.2: Bilinear material properties for sample#5 determined using HEAIM

Temperature range (°C)	Max. Correlation (%)	Die			Underfill		Substrate		
		E (GPa)	α (ppm/°C)	ν	E (GPa)	ν	E (GPa)	α (ppm/°C)	ν
20-55	99.6	98	2.5	0.22	0.3	0.30	19	6.0	0.24
55-100	92.8	98	2.5	0.22	0.012	0.30	18	5.6	0.24
100-130	89.9	98	2.5	0.22	0.011	0.30	17	6.6	0.24
160-217	97.0	98	2.5	0.22	0.011	0.31	15	10.2	0.25
217-240	30.5	98	2.5	0.22	0.011	0.31	15	11.2	0.25

Table A5.3: Bilinear material properties for Sample#11 determined using HEAIM

Temperature range (°C)	Max. Correlation (%)	Die			Underfill		Substrate		
		E (GPa)	α (ppm/°C)	ν	E (GPa)	ν	E (GPa)	α (ppm/°C)	ν
20-55	99.1	98	2.5	0.22	0.80	0.30	24	6.8	0.24
55-100	15.3	98	2.5	0.22	0.01	0.30	24	6.5	0.24
100-160	48.2	98	2.5	0.22	0.01	0.30	20	6.2	0.24
217-240	14.1	98	2.5	0.22	0.01	0.31	17	10.5	0.24

Table A5.4: Bilinear material properties for sample#13 determined using HEAIM

Temperature range (°C)	Max. Correlation (%)	Die			Underfill		Substrate		
		E (GPa)	α (ppm/°C)	ν	E (GPa)	ν	E (GPa)	α (ppm/°C)	ν
20-55	79.0	98	2.5	0.22	0.8	0.31	18	6.0	0.24
55-100	41.3	99	2.5	0.22	0.025	0.34	18	5.4	0.24
100-130	17.6	99	2.5	0.22	0.01	0.34	18	6.8	0.24
160-217	32	98	2.5	0.22	0.01	0.34	15	10.8	0.25
217-240	24.6	98	2.5	0.22	0.01	0.34	15	11.5	0.25

Table A5.5: Bilinear material properties for sample#17 determined using HEAIM

Temperature range (°C)	Max. Correlation (%)	Die			Underfill		Substrate		
		E (GPa)	α (ppm/°C)	ν	E (GPa)	ν	E (GPa)	α (ppm/°C)	ν
20-55	91.5	98	2.5	0.22	1.9	0.31	24	6	0.24
55-100	93.2	98	2.5	0.22	1.7	0.31	24	5.5	0.24
100-130	95.3	98	2.5	0.22	1.5	0.30	20	6.2	0.24
130-160	88.7	98	2.5	0.22	1	0.30	20	6.2	0.24
160-217	88.7	98	2.5	0.22	0.08	0.30	16	10.9	0.24
217-240	95.7	98	2.5	0.22	0.08	0.30	17	11.5	0.24

A5.2 Warpage prediction-Inverse modeling compared with experimental results

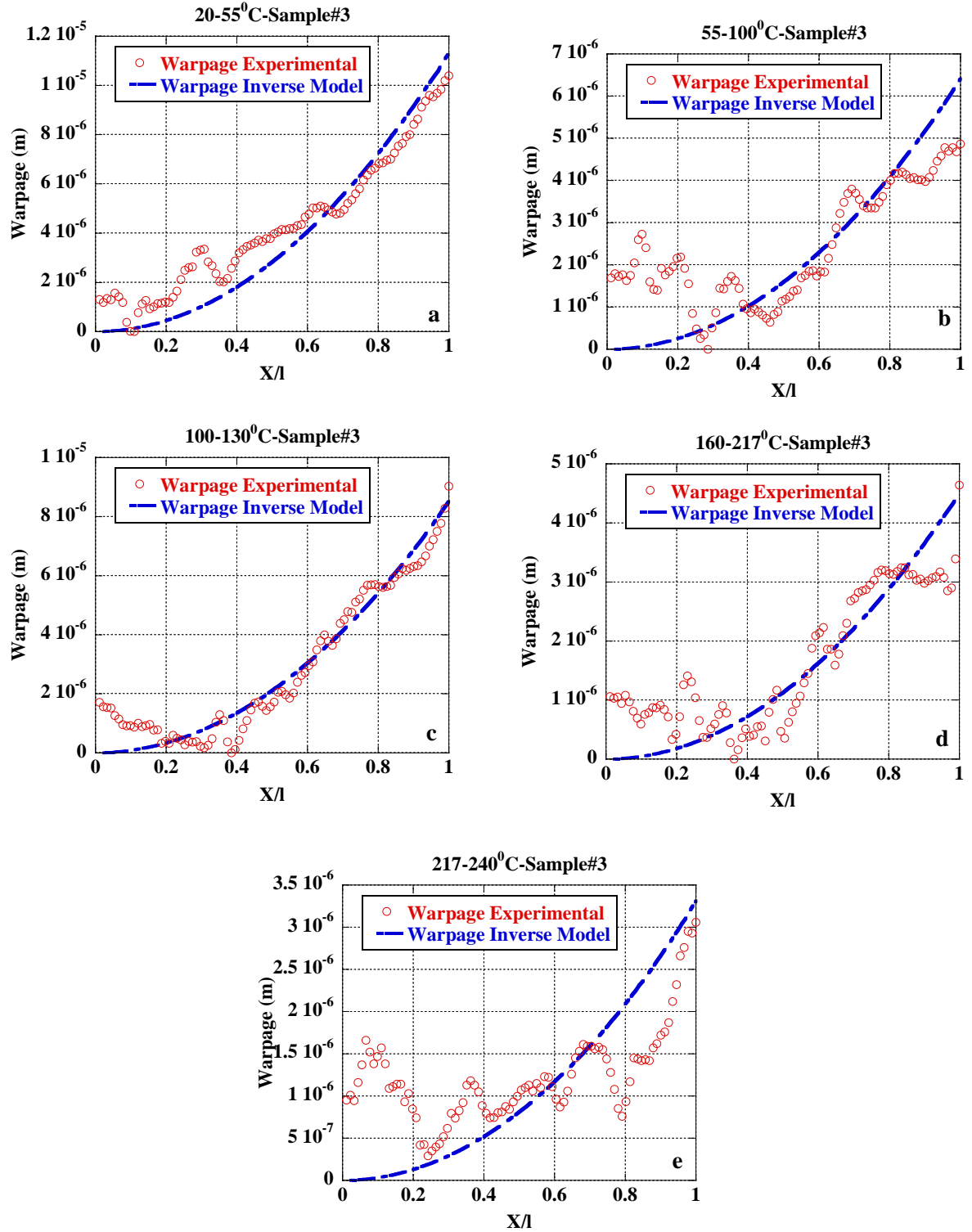


Figure A5.1: HAEIM predicted relative warpage over the length for sample#3 compared with experimental measurements at (a) $\Delta T=35^\circ\text{C}$ (25°C to 55°C), (b) $\Delta T=45^\circ\text{C}$ (55°C to 100°C), (c) $\Delta T=30^\circ\text{C}$ (100°C to 130°C), (d) $\Delta T=57^\circ\text{C}$ (160°C to 217°C), (e) $\Delta T=23^\circ\text{C}$ (217°C to 240°C)

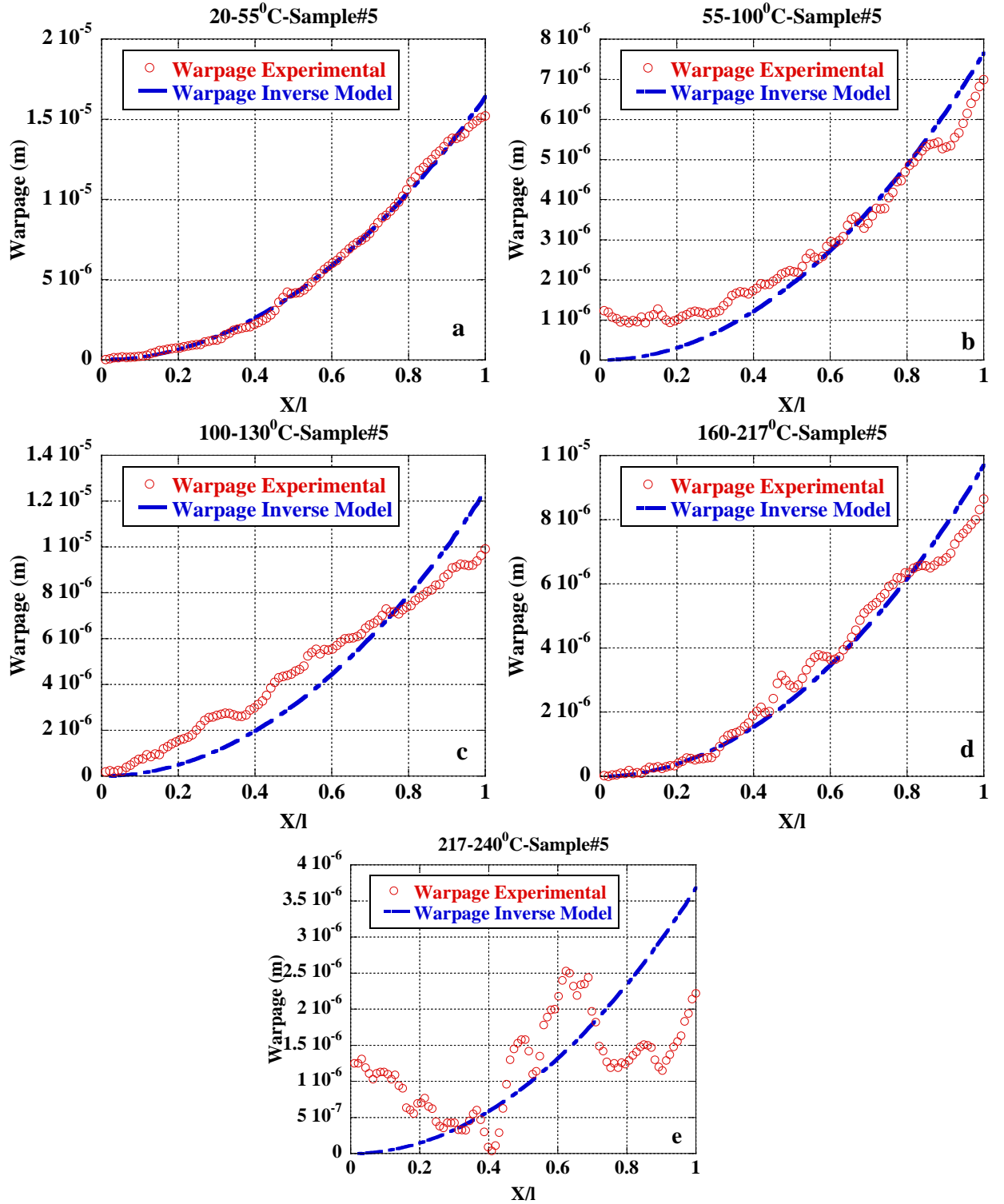


Figure A5.2: HAEIM predicted relative warpage over the length for sample#5 compared with experimental measurements at (a) $\Delta T=35^\circ\text{C}$ (25°C to 55°C), (b) $\Delta T=45^\circ\text{C}$ (55°C to 100°C), (c) $\Delta T=30^\circ\text{C}$ (100°C to 130°C), (d) $\Delta T=57^\circ\text{C}$ (160°C to 217°C), (e) $\Delta T=23^\circ\text{C}$ (217°C to 240°C)

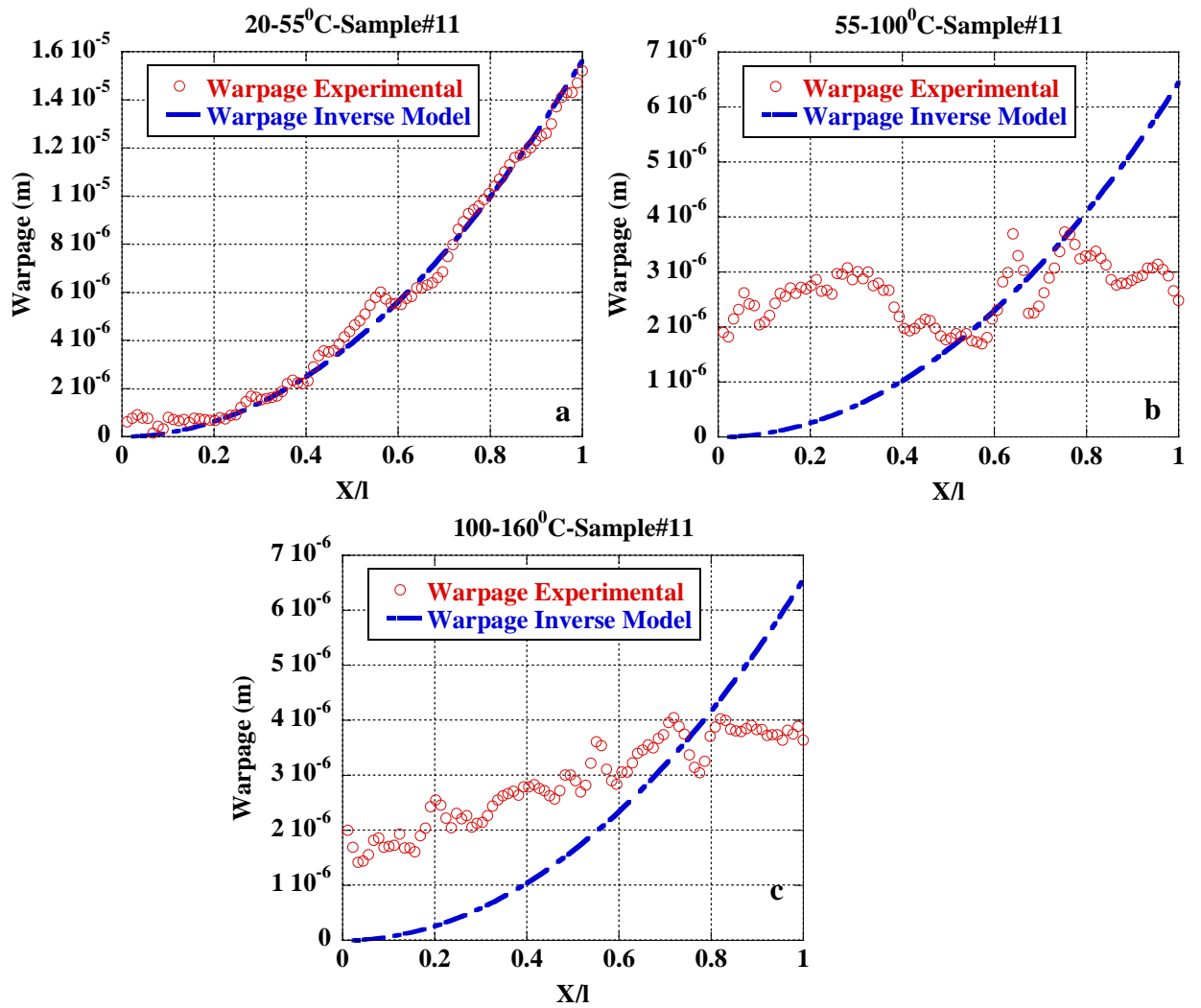


Figure A5.3: HAEIM predicted relative warpage over the length for sample#11 compared with experimental measurements at (a) $\Delta T=35^\circ\text{C}$ (25°C to 55°C), (b) $\Delta T=45^\circ\text{C}$ (55°C to 100°C), (c) $\Delta T=60^\circ\text{C}$ (100°C to 160°C)

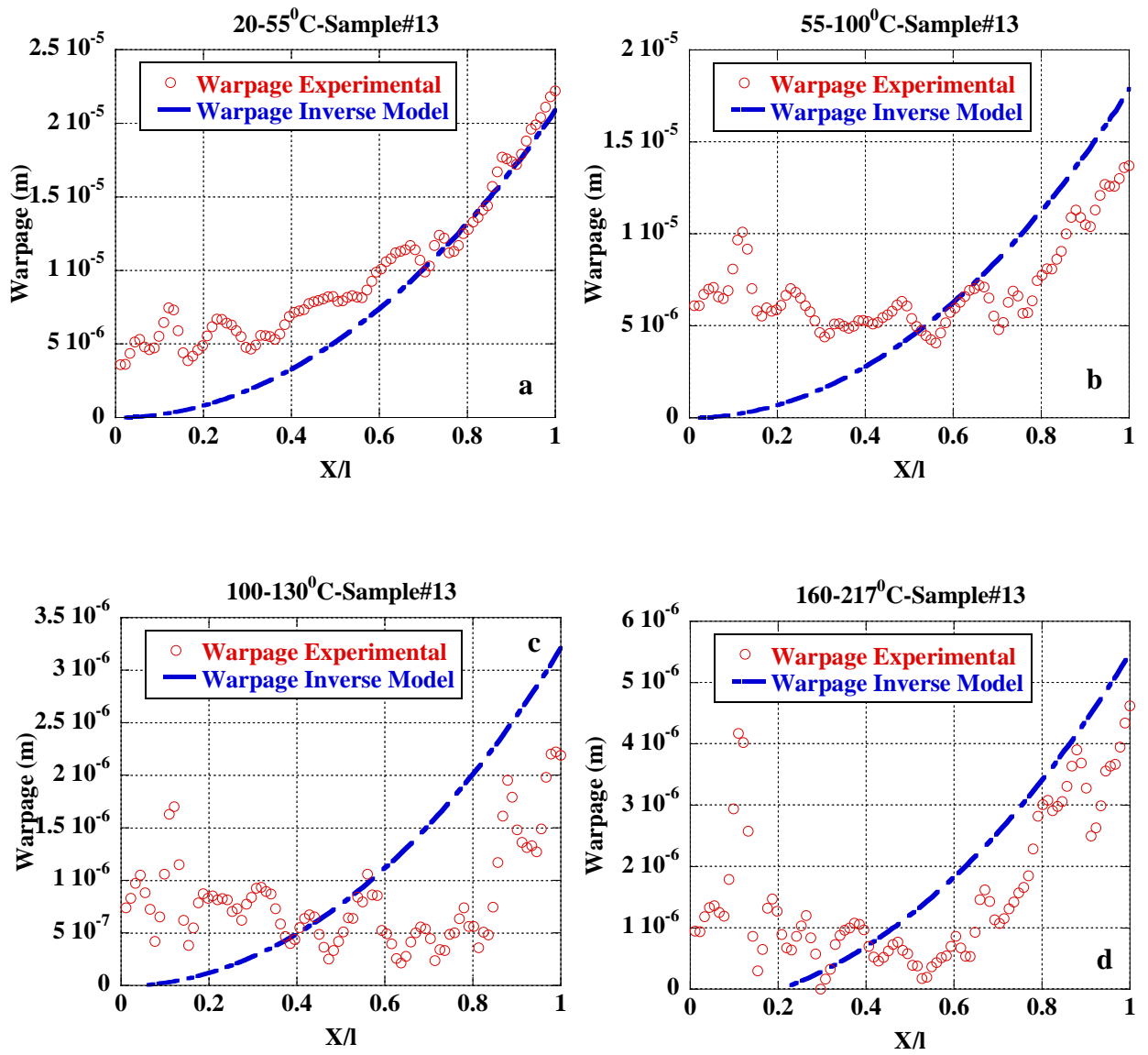


Figure A5.4: HAEIM predicted relative warpage over the length for sample#13 compared with experimental measurements at (a) $\Delta T=35^\circ\text{C}$ (25°C to 55°C), (b) $\Delta T=45^\circ\text{C}$ (55°C to 100°C), (c) $\Delta T=30^\circ\text{C}$ (100°C to 130°C), (d) $\Delta T=57^\circ\text{C}$ (160°C to 217°C)

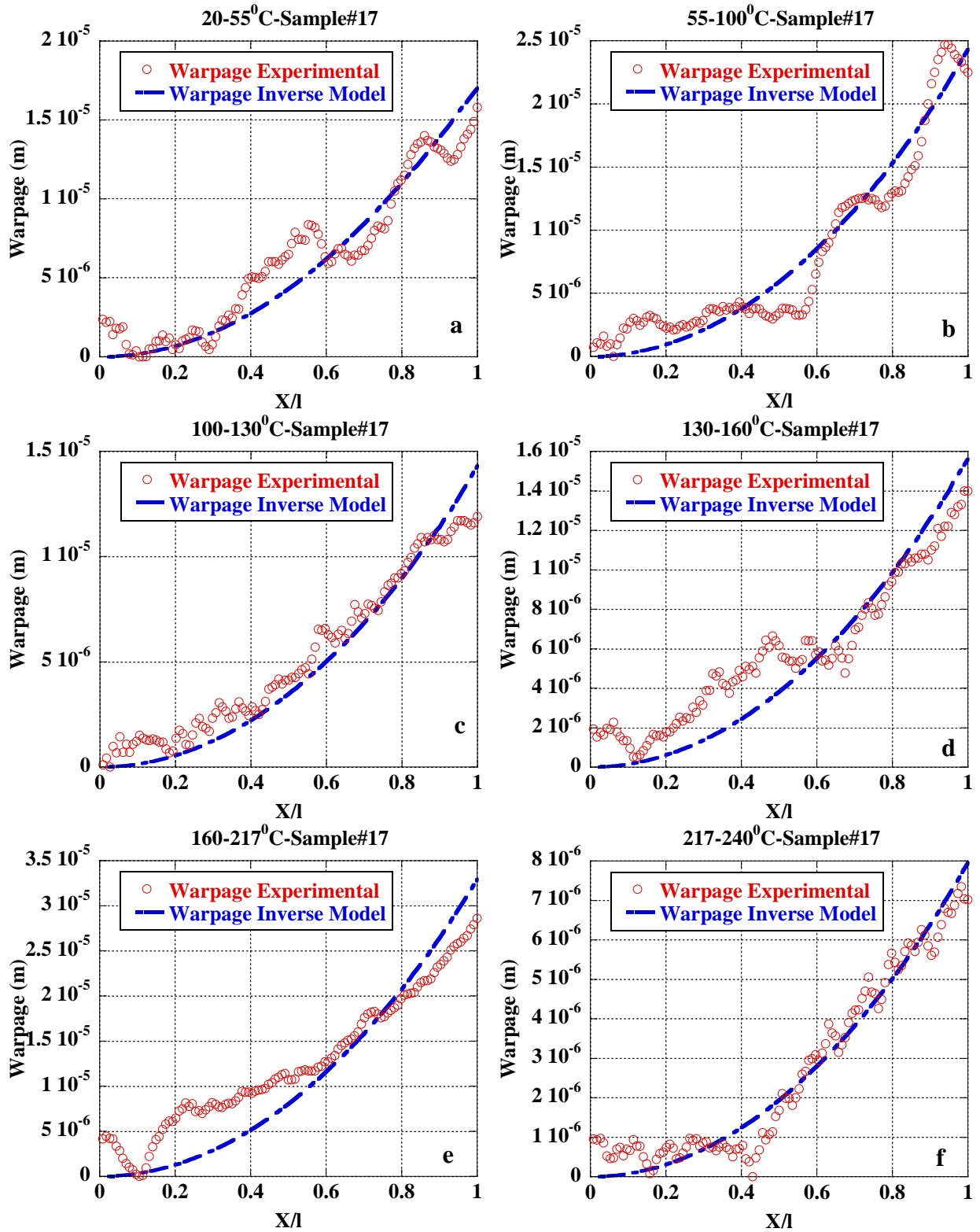


Figure A5.5: HAEIM predicted relative warpage over the length for sample#17 compared with experimental measurements at (a) $\Delta T=35^\circ\text{C}$ (20°C to 55°C), (b) $\Delta T=45^\circ\text{C}$ (55°C to 100°C), (c) $\Delta T=30^\circ\text{C}$ (100°C to 130°C), (d) $\Delta T=30^\circ\text{C}$ (130°C to 160°C), (e) $\Delta T=57^\circ\text{C}$ (160°C to 217°C), (f) $\Delta T=23^\circ\text{C}$ (217°C to 240°C)

APPENDIX6

Interfacial Stresses and Strains, Experimental and Analytical Results and Comparisons

A6.1 Results of analytical peel and shear stresses

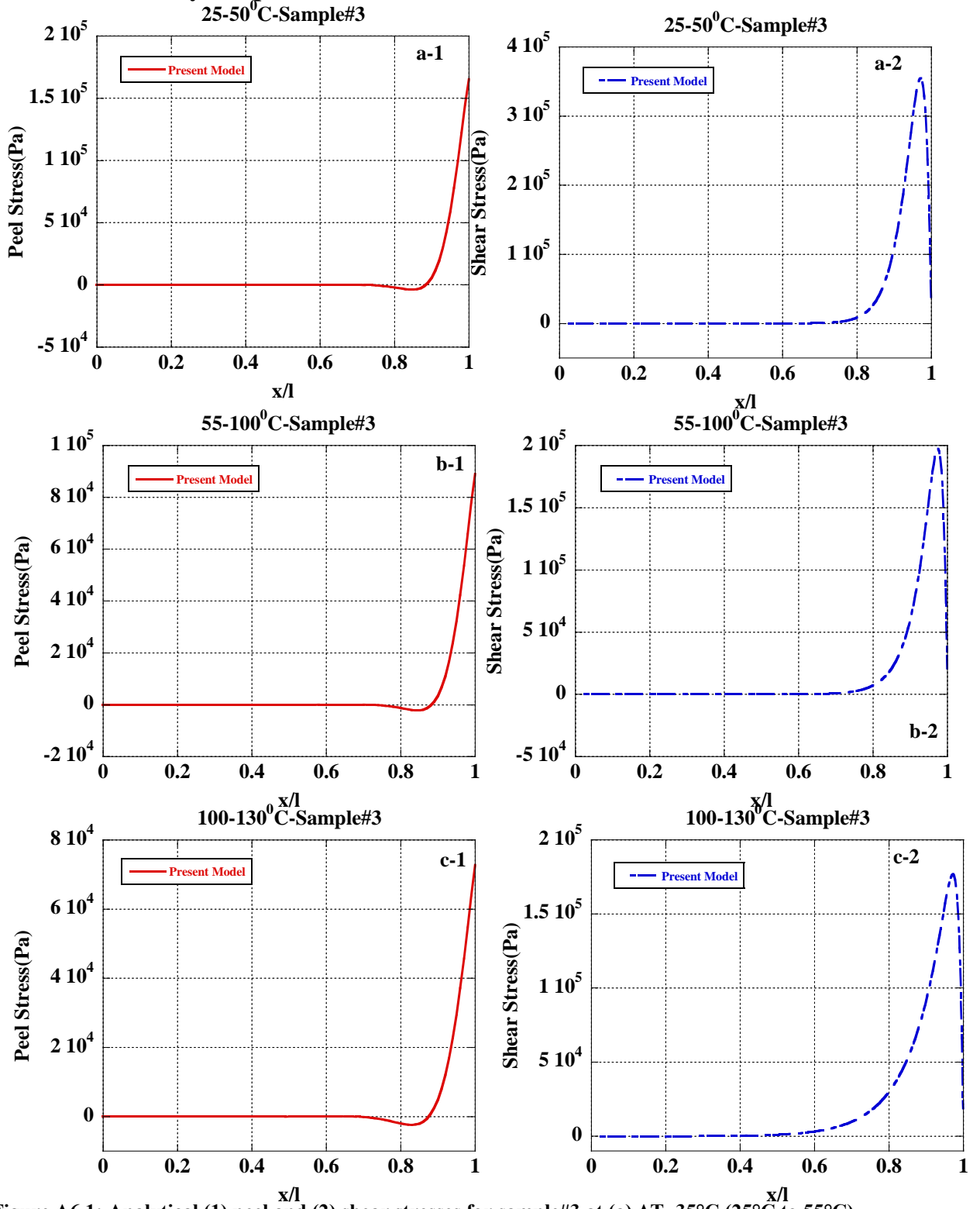


Figure A6.1: Analytical (1) peel and (2) shear stresses for sample#3 at (a) $\Delta T=35^\circ\text{C}$ (25°C to 55°C), (b) $\Delta T=45^\circ\text{C}$ (55°C to 100°C), (c) $\Delta T=30^\circ\text{C}$ (100°C to 130°C)

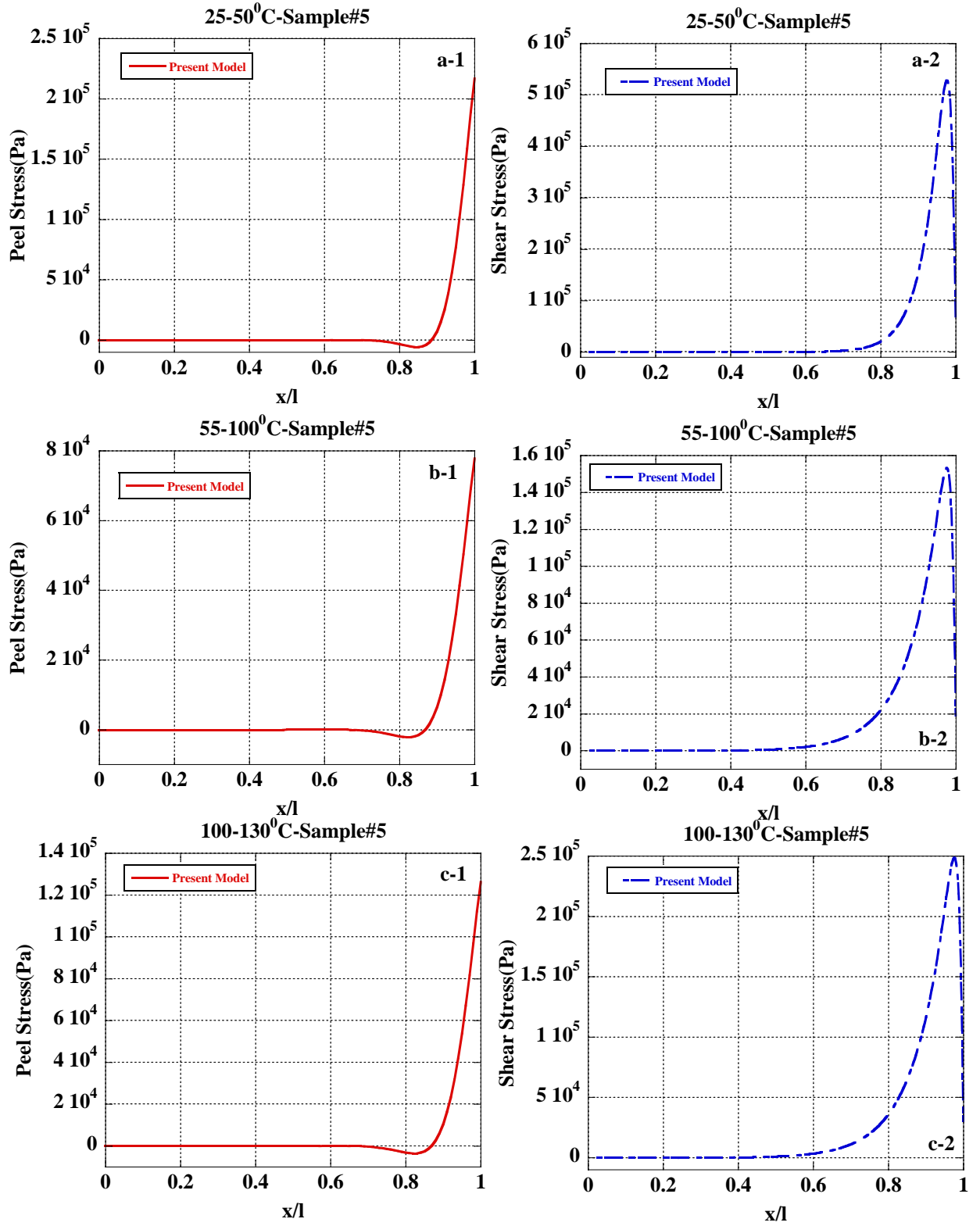


Figure A6.2: Analytical (1) peel and (2) shear stresses for sample#5 at (a) $\Delta T = 35^\circ\text{C}$ (25°C to 55°C), (b) $\Delta T = 45^\circ\text{C}$ (55°C to 100°C), (c) $\Delta T = 30^\circ\text{C}$ (100°C to 130°C)

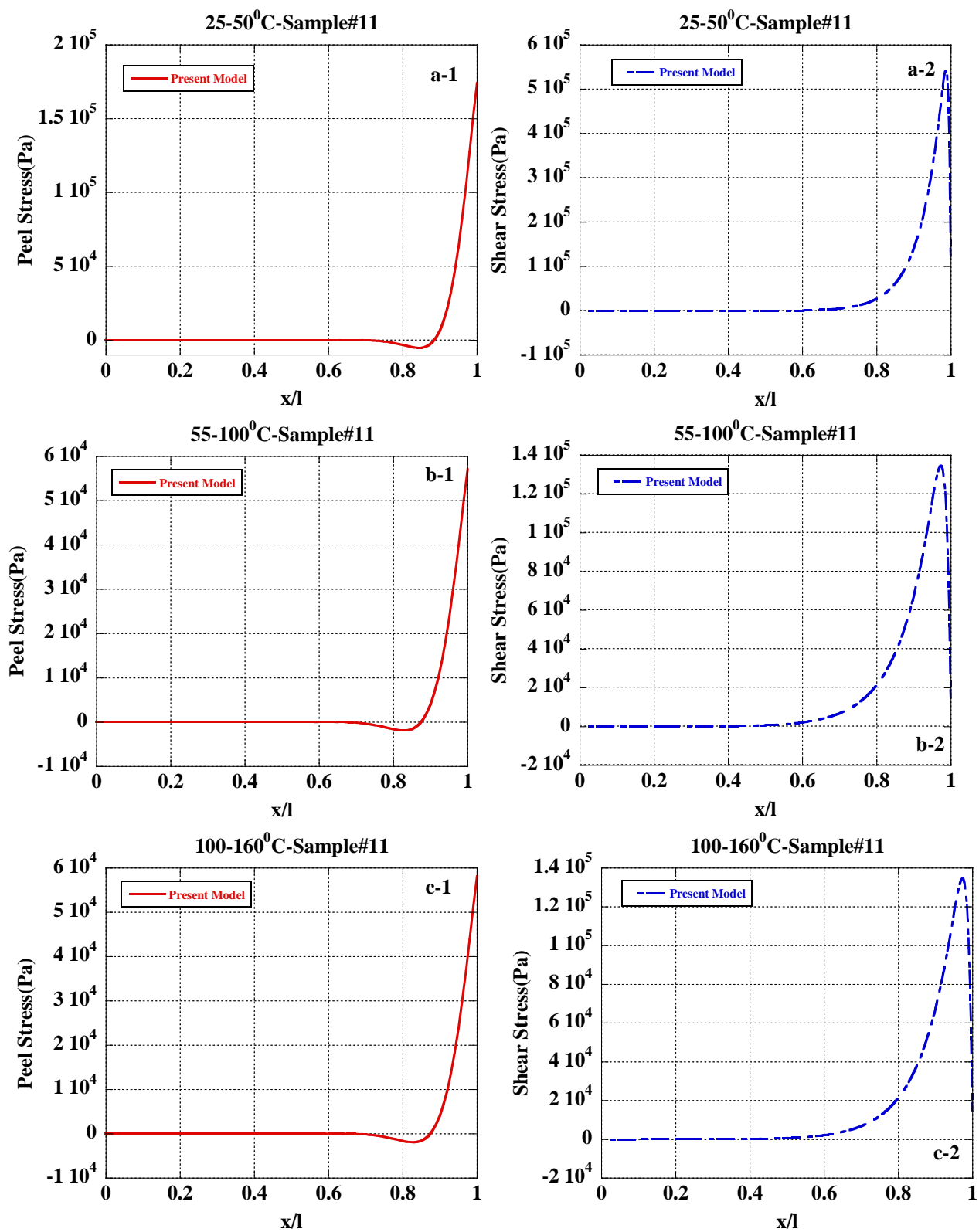


Figure A6.3: Analytical (1) peel and (2) shear stresses for sample#11 at (a) $\Delta T = 35^\circ\text{C}$ (25°C to 55°C), (b) $\Delta T = 45^\circ\text{C}$ (55°C to 100°C), (c) $\Delta T = 60^\circ\text{C}$ (100°C to 160°C)

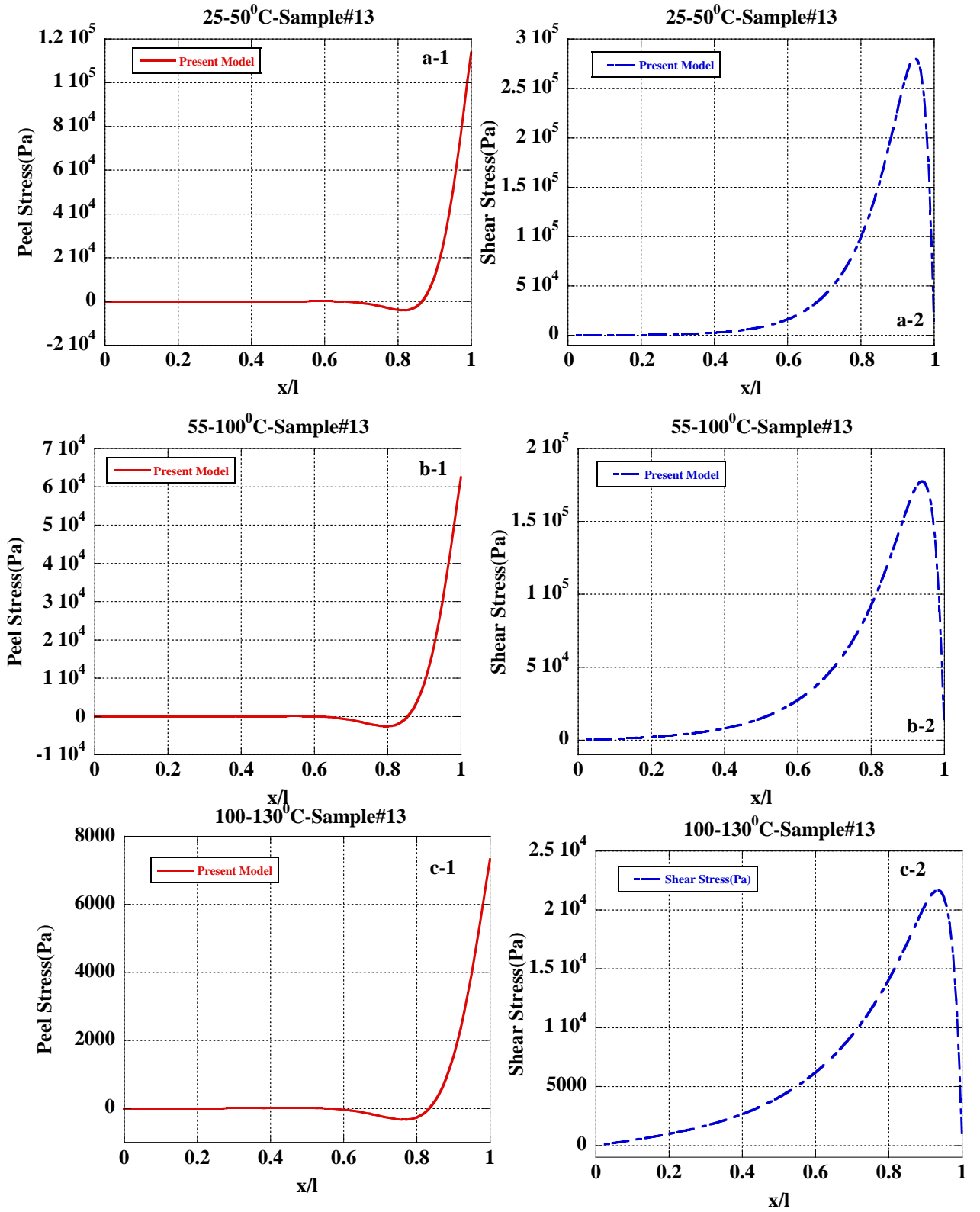
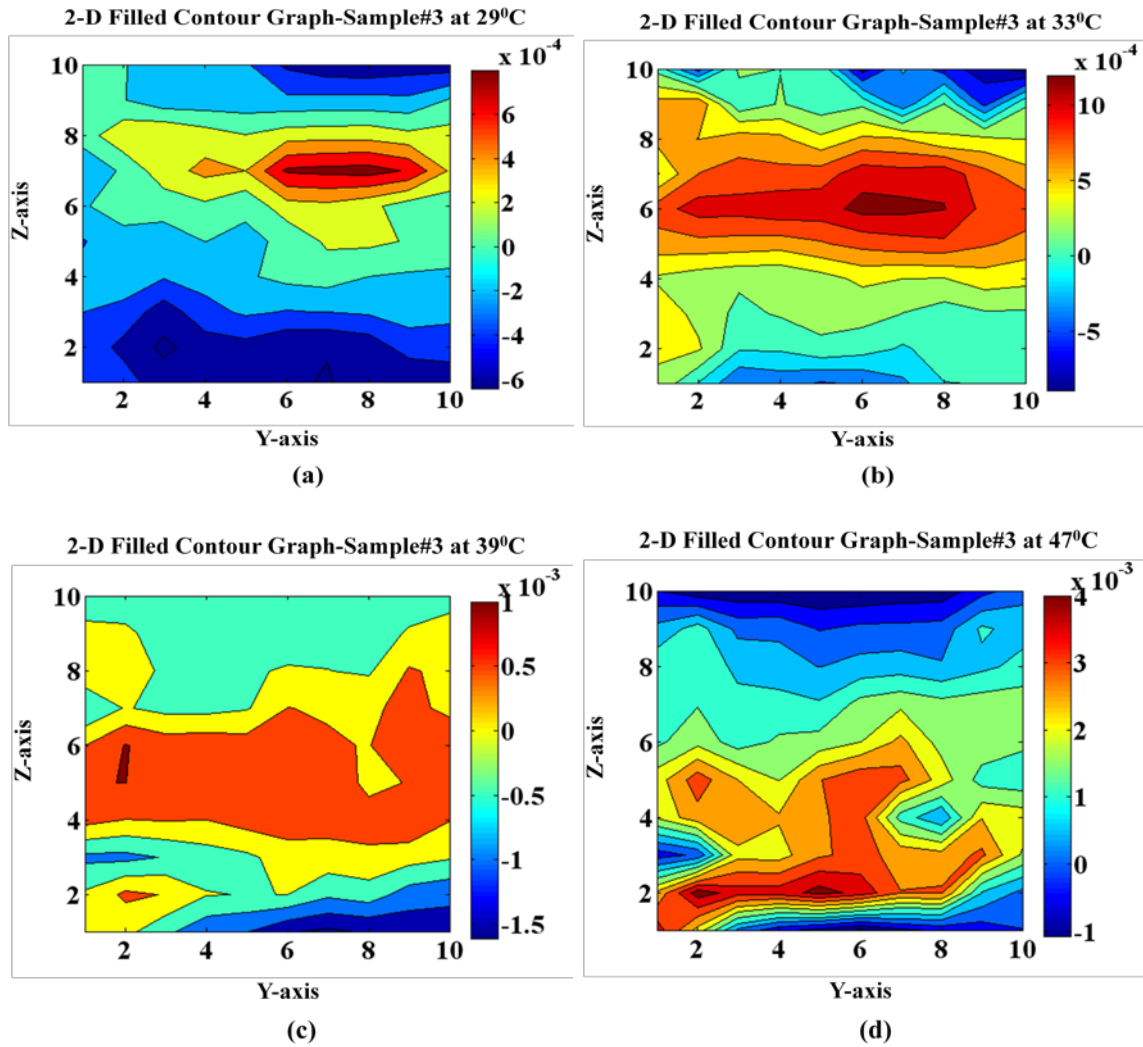


Figure A6.4: Analytical (1) peel and (2) shear stresses for sample#13 at (a) $\Delta T=35^\circ\text{C}$ (25°C to 55°C), (b) $\Delta T=45^\circ\text{C}$ (55°C to 100°C), (c) $\Delta T=30^\circ\text{C}$ (100°C to 130°C)

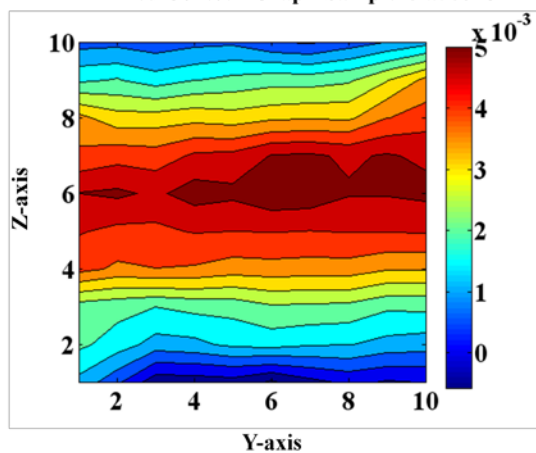
A6.2 Results of experimental strains

The interested location of measurement has been at the interfacial layer with the points along Y and Z- axis. Following graphs shows the 2-D filled contour graph of strains of samples 3,5,11 and 13.

A4.2.1 Contour pattern of strain measurement results

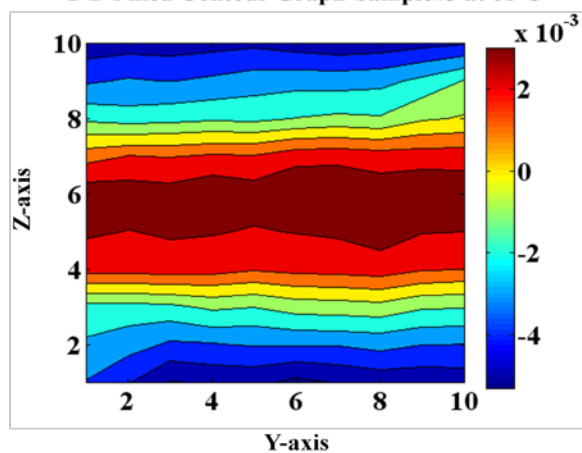


2-D Filled Contour Graph-Sample#3 at 53°C



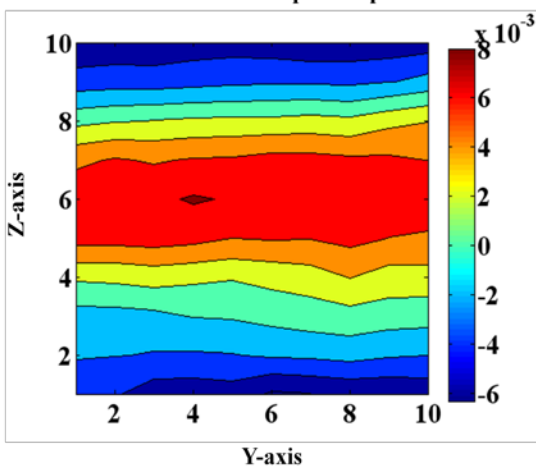
(e)

2-D Filled Contour Graph-Sample#3 at 61°C



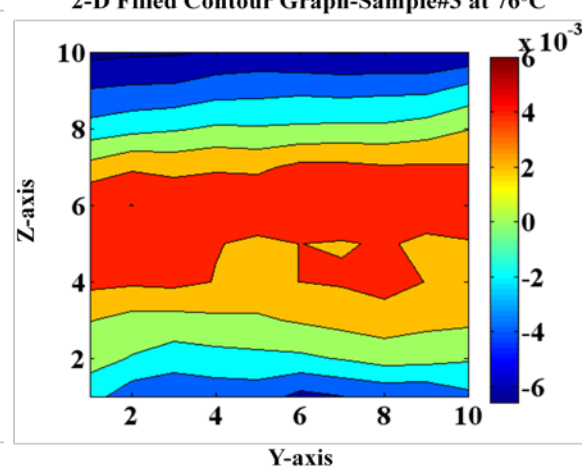
(f)

2-D Filled Contour Graph-Sample#3 at 69°C



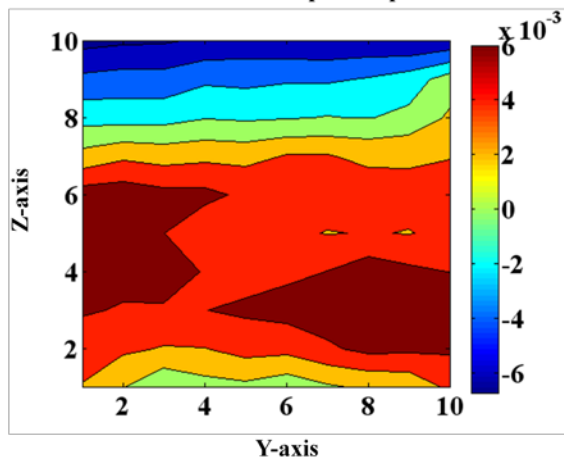
(g)

2-D Filled Contour Graph-Sample#3 at 76°C



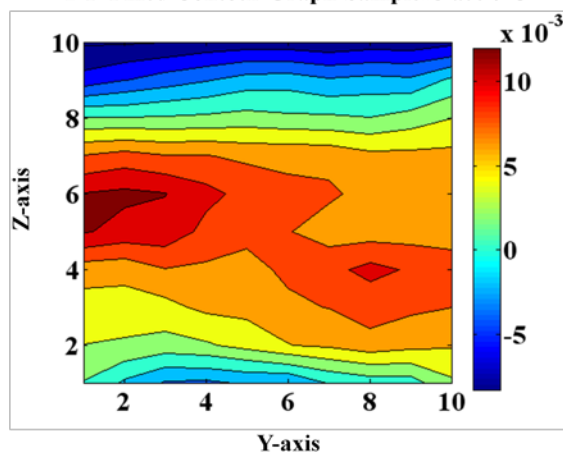
(h)

2-D Filled Contour Graph-Sample#3 at 82°C



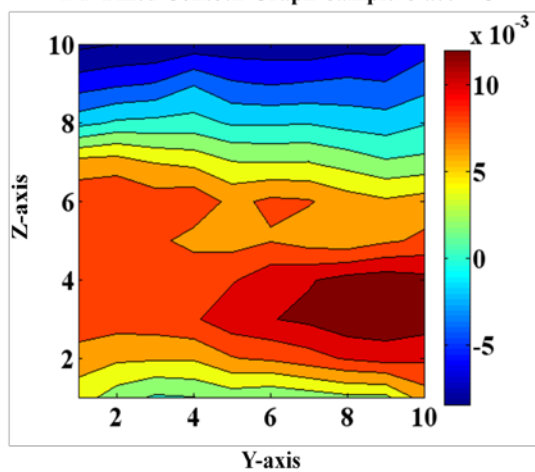
(i)

2-D Filled Contour Graph-Sample#3 at 90°C



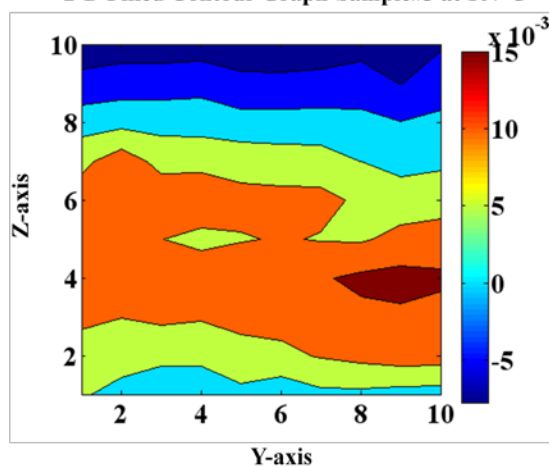
(j)

2-D Filled Contour Graph-Sample#3 at 97°C



(k)

2-D Filled Contour Graph-Sample#3 at 107°C



(l)

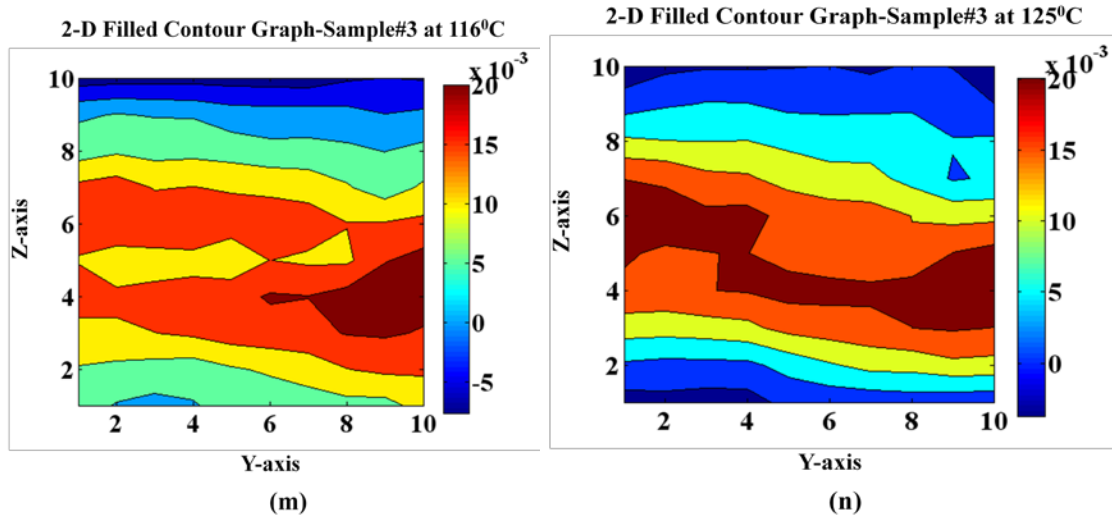
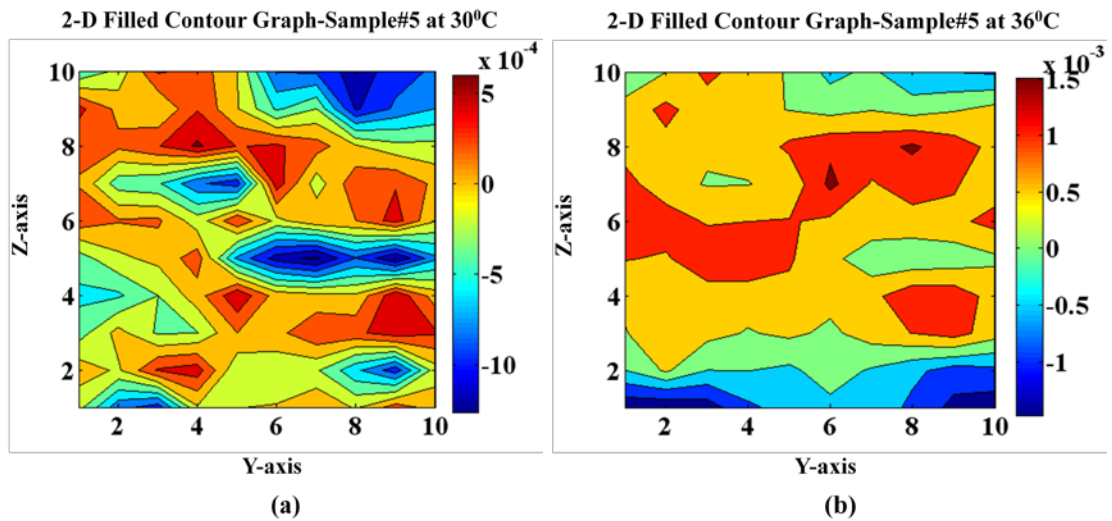
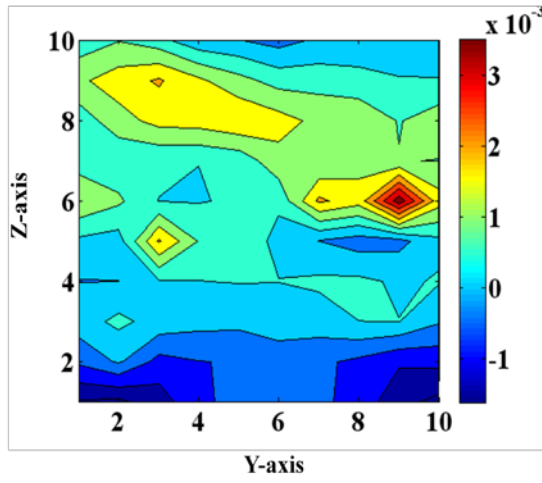


Figure A6.5: Contour pattern of strain measurement results for sample#3 at (a) $T=29^{\circ}\text{C}$, (b) $T=33^{\circ}\text{C}$, (c) $T=39^{\circ}\text{C}$, (d) $T=47^{\circ}\text{C}$, (e) $T=53^{\circ}\text{C}$, (f) $T=61^{\circ}\text{C}$, (g) $T=69^{\circ}\text{C}$, (h) $T=76^{\circ}\text{C}$, (i) $T=82^{\circ}\text{C}$, (j) $T=90^{\circ}\text{C}$, (k) $T=97^{\circ}\text{C}$, (l) $T=107^{\circ}\text{C}$, (m) $T=116^{\circ}\text{C}$, (n) $T=125^{\circ}\text{C}$

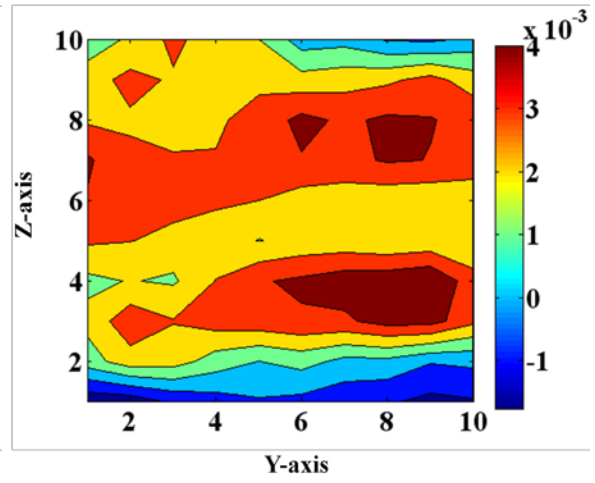


2-D Filled Contour Graph-Sample#5 at 42°C



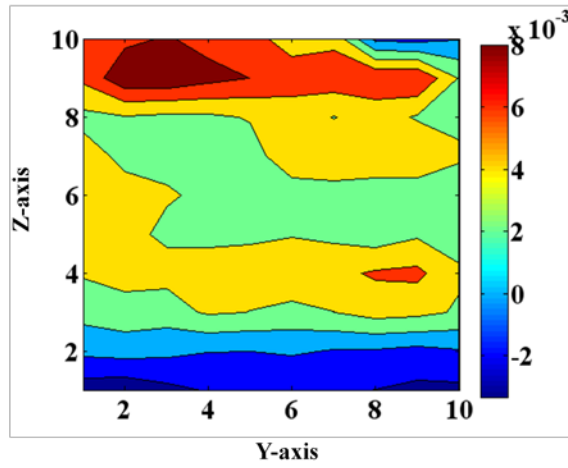
(c)

2-D Filled Contour Graph-Sample#5 at 50°C



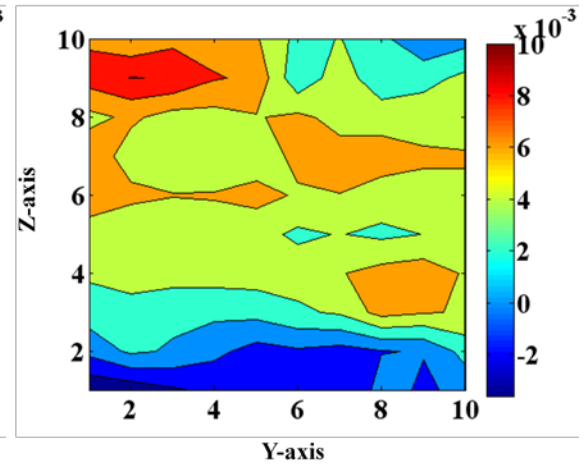
(d)

2-D Filled Contour Graph-Sample#5 at 57°C



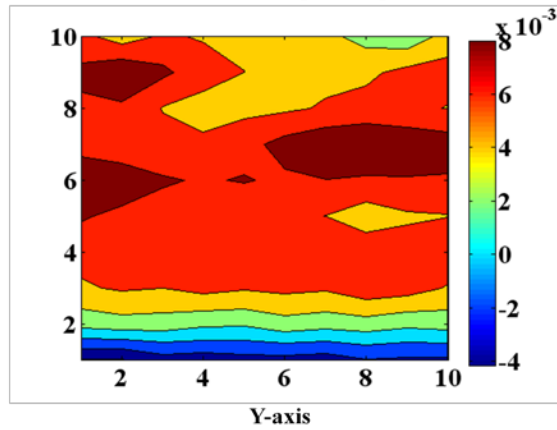
(e)

2-D Filled Contour Graph-Sample#5 at 66°C



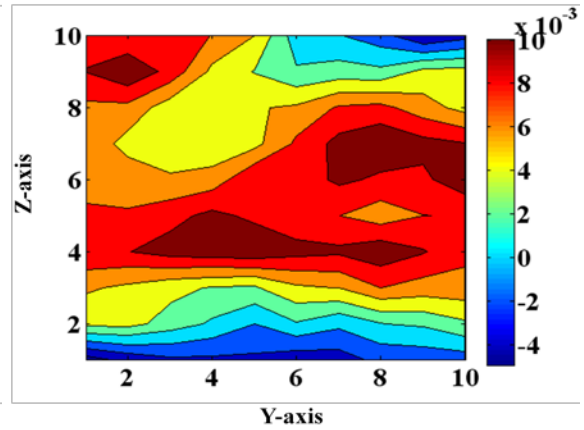
(f)

2-D Filled Contour Graph-Sample#5 at 73°C



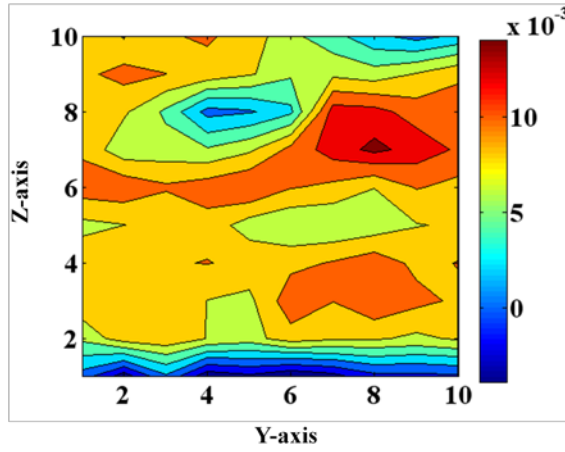
(g)

2-D Filled Contour Graph-Sample#5 at 81°C



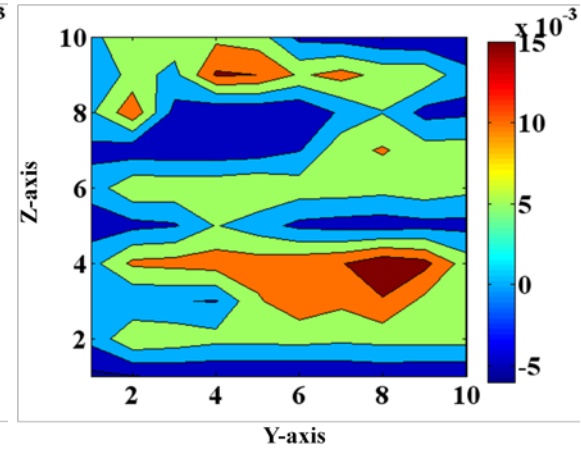
(h)

2-D Filled Contour Graph-Sample#5 at 89°C



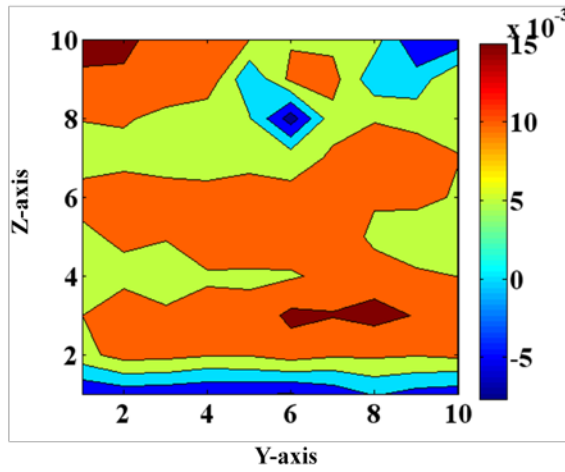
(i)

2-D Filled Contour Graph-Sample#5 at 97°C



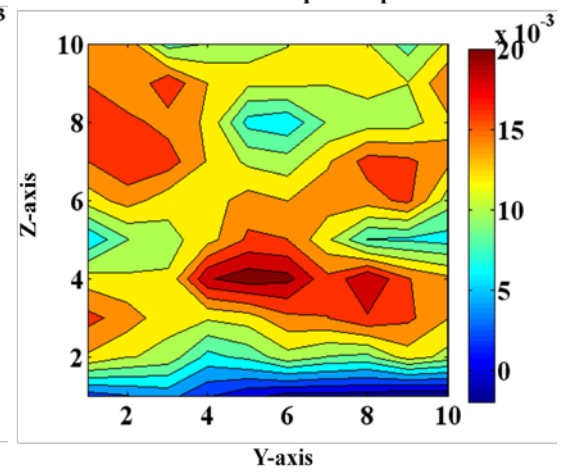
(j)

2-D Filled Contour Graph-Sample#5 at 105°C



(k)

2-D Filled Contour Graph-Sample#5 at 113°C



(l)

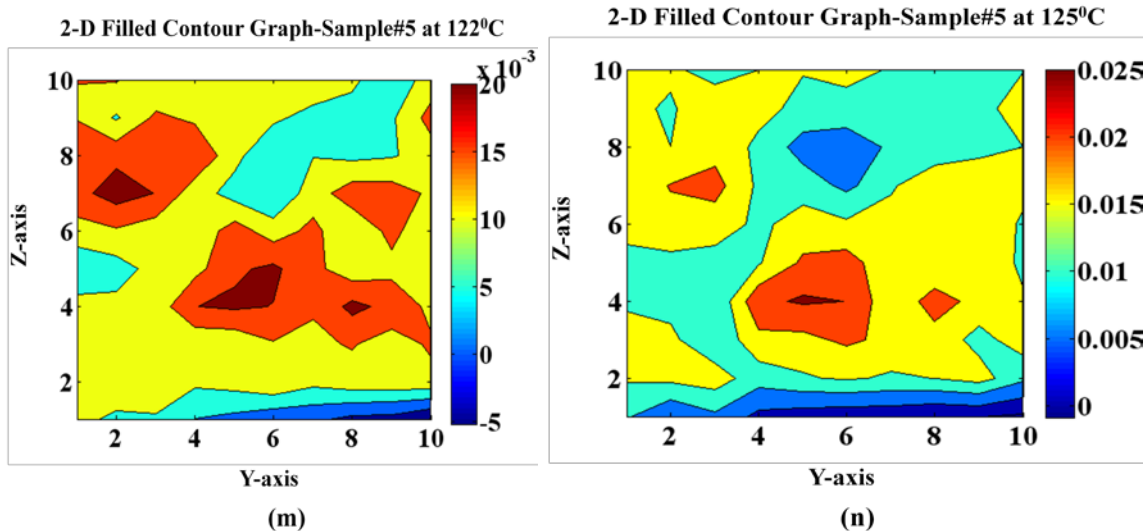
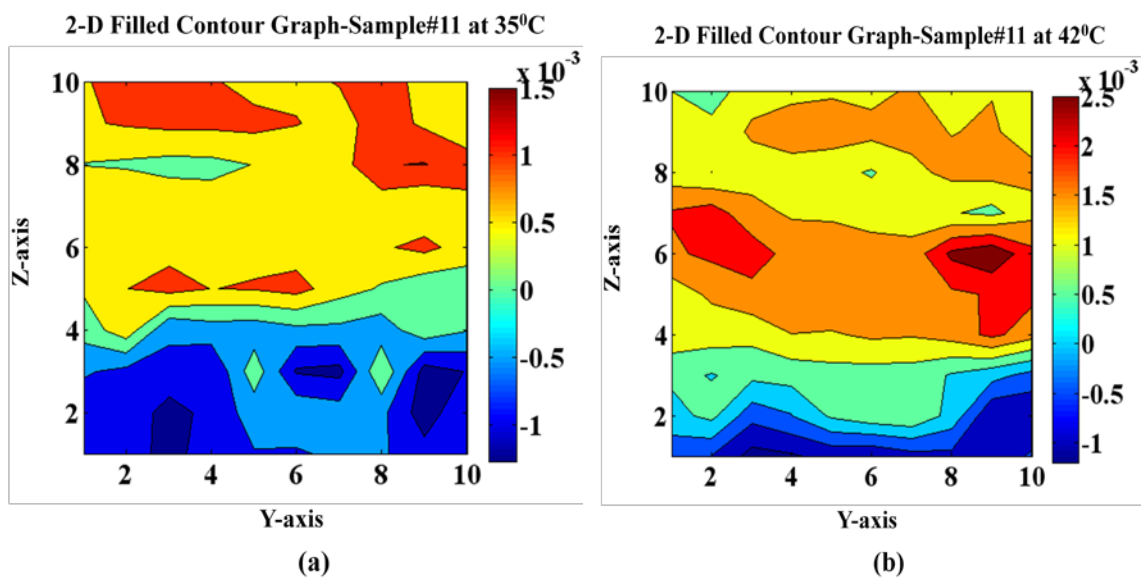
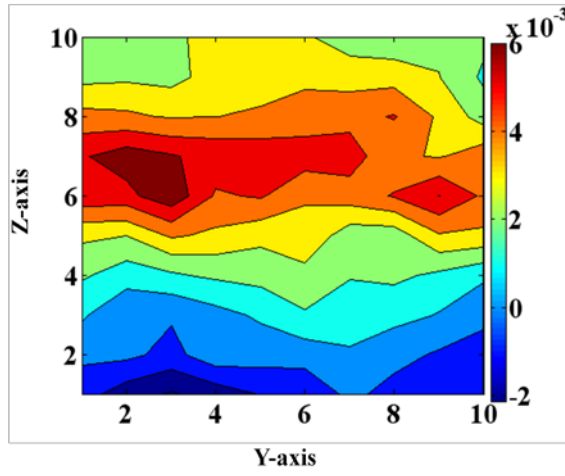


Figure A6.6: Contour pattern of strain measurement results for sample#5 at (a) T=30°C, (b) T=36°C, (c) T=42°C, (d) T=50°C, (e) T=57°C, (f) T=66°C, (g) T=73°C, (h) T=81°C, (i) T=89°C, (j) T=97°C, (k) T=105°C, (l) T=113°C, (m) T=122°C, (n) T=125°C

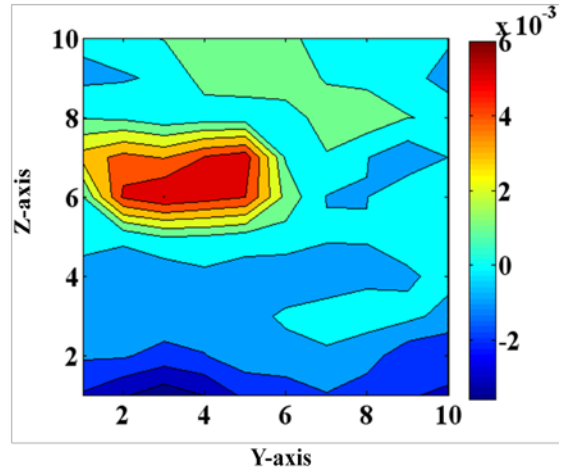


2-D Filled Contour Graph-Sample#11 at 56°C



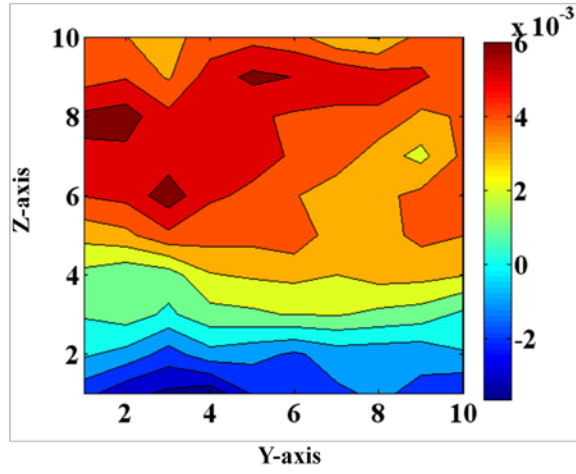
(c)

2-D Filled Contour Graph-Sample#11 at 64°C



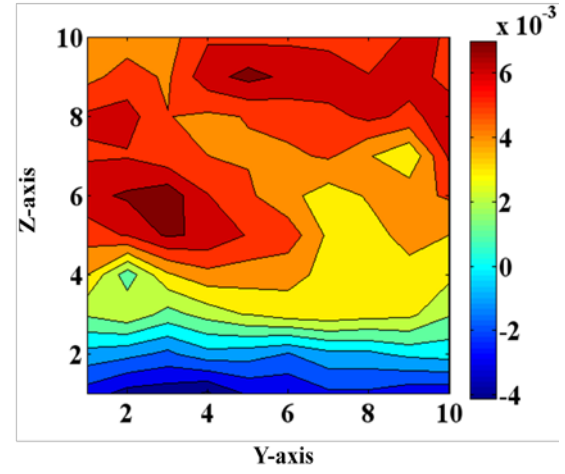
(d)

2-D Filled Contour Graph-Sample#11 at 72°C



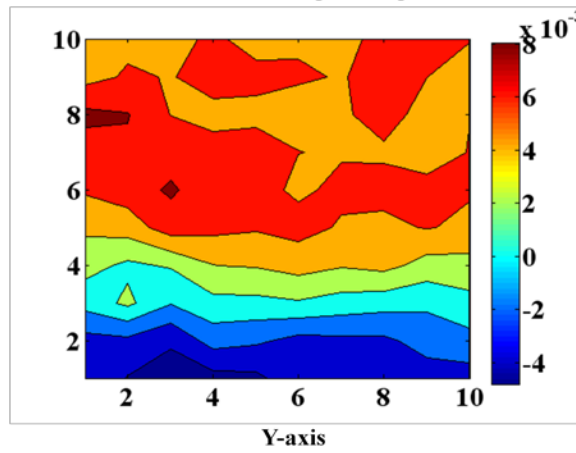
(e)

2-D Filled Contour Graph-Sample#11 at 80°C



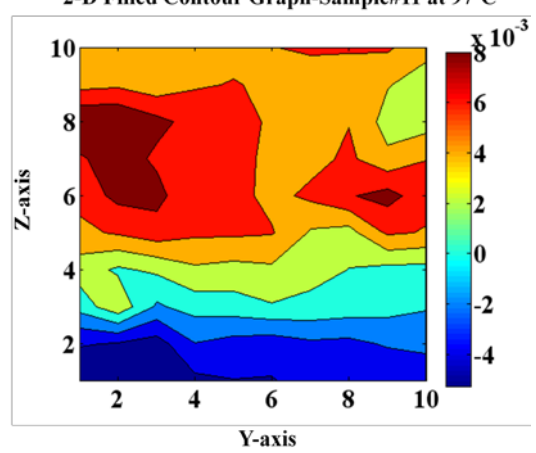
(f)

2-D Filled Contour Graph-Sample#11 at 88°C



(g)

2-D Filled Contour Graph-Sample#11 at 97°C



(h)

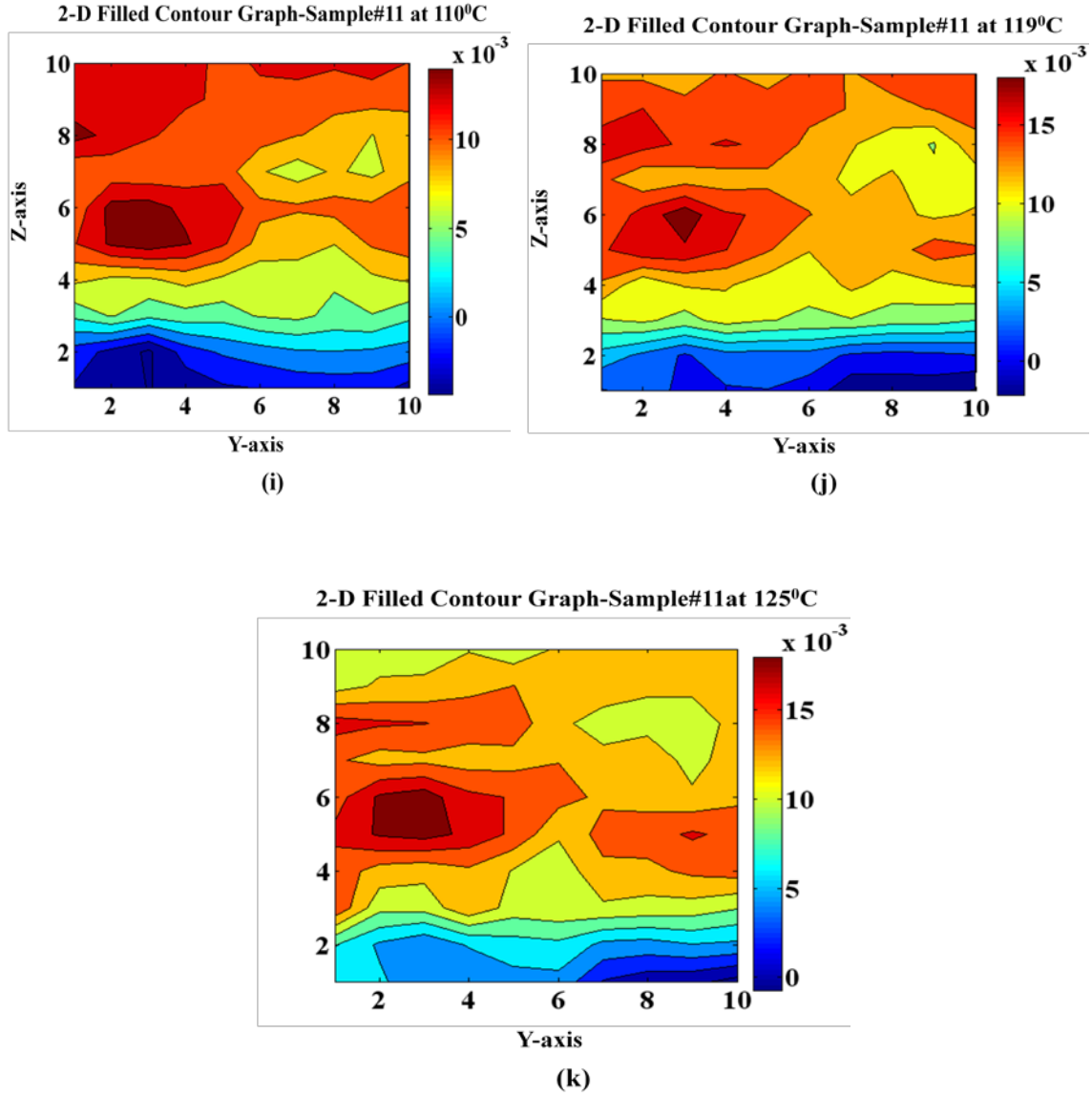
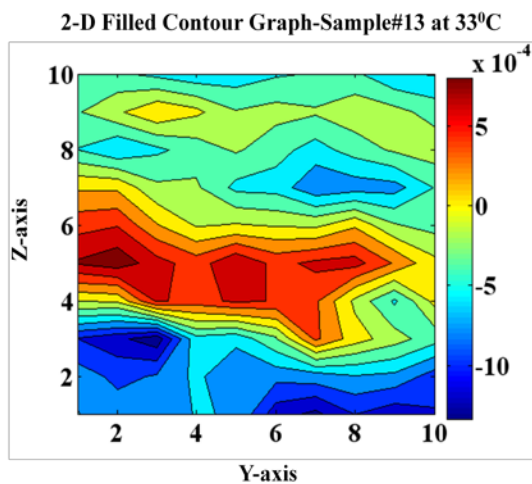
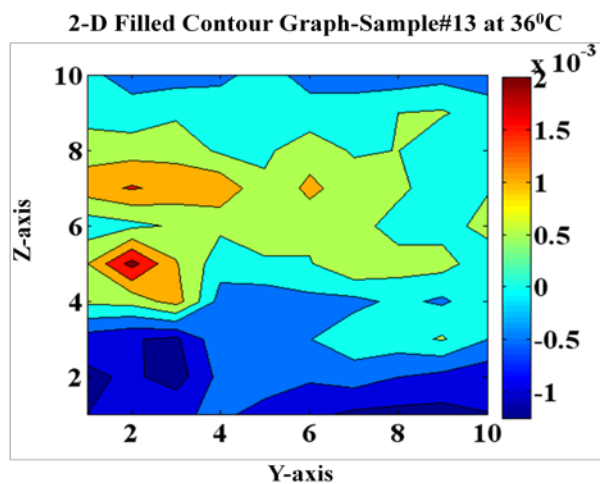


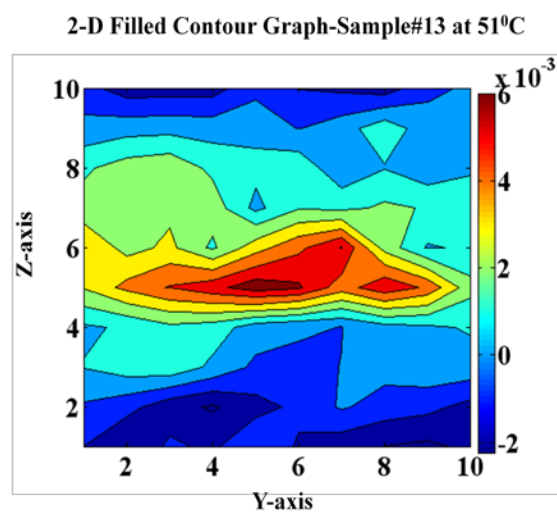
Figure A6.7: Contour pattern of strain measurement results for sample#11 at (a) $T=35^{\circ}\text{C}$, (b) $T=42^{\circ}\text{C}$, (c) $T=56^{\circ}\text{C}$, (d) $T=64^{\circ}\text{C}$, (e) $T=72^{\circ}\text{C}$, (f) $T=80^{\circ}\text{C}$, (g) $T=88^{\circ}\text{C}$, (h) $T=97^{\circ}\text{C}$, (i) $T=110^{\circ}\text{C}$, (j) $T=119^{\circ}\text{C}$, (k) $T=125^{\circ}\text{C}$



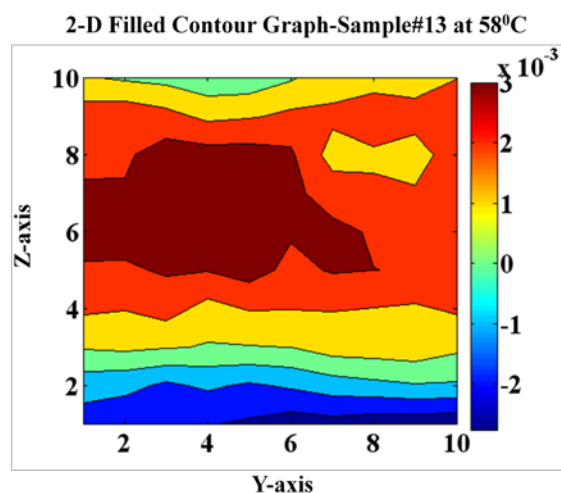
(a)



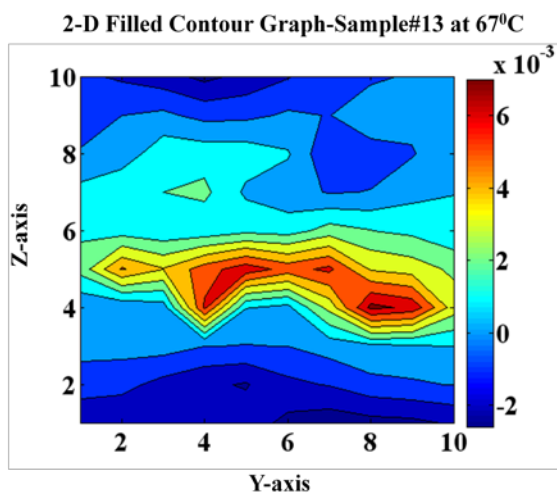
(b)



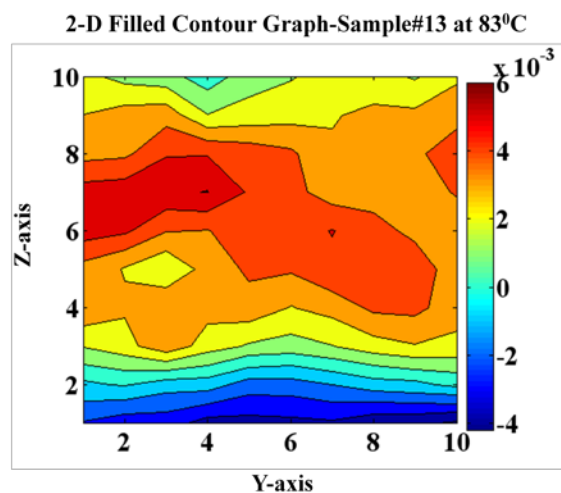
(c)



(d)



(e)



(f)

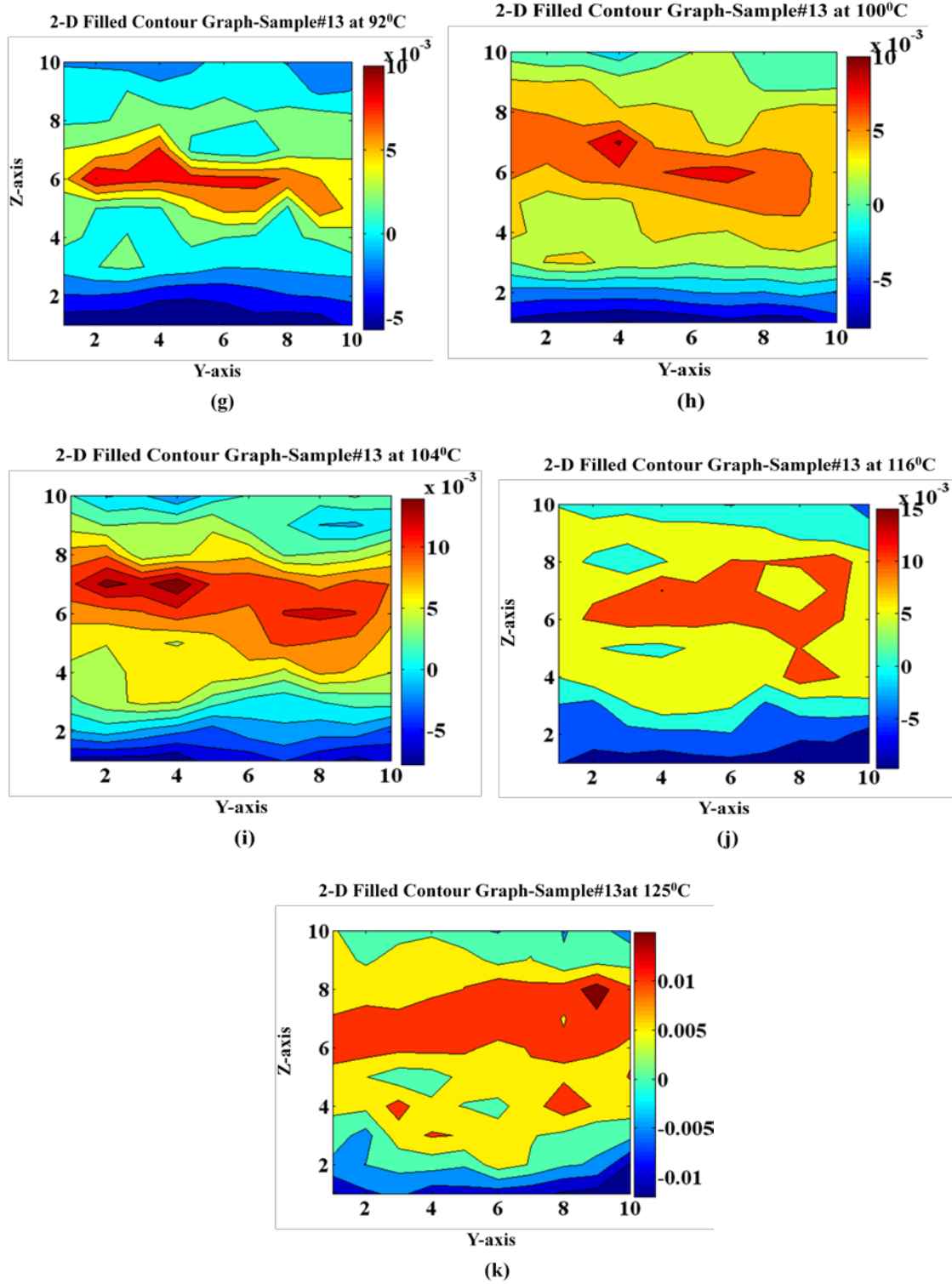


Figure A6.8: Contour pattern of strain measurement results for sample#13 at (a) $T=33^{\circ}\text{C}$, (b) $T=36^{\circ}\text{C}$, (c) $T=51^{\circ}\text{C}$, (d) $T=58^{\circ}\text{C}$, (e) $T=67^{\circ}\text{C}$, (f) $T=83^{\circ}\text{C}$, (g) $T=92^{\circ}\text{C}$, (h) $T=100^{\circ}\text{C}$, (i) $T=104^{\circ}\text{C}$, (j) $T=116^{\circ}\text{C}$, (k) $T=125^{\circ}\text{C}$

A6.2.2 Results of average measured strain for samples

Table A6.1: Average measured strain for sample#3

Temperature(°C)	Average Strain
29	-6.55E-05
33	3.84E-04
39	1.03E-04
47	1.41E-03
53	2.86E-03
61	3.29E-03
69	4.87E-03
76	4.55E-03
82	6.33E-03
90	7.61E-03
97	7.99E-03
107	9.56E-03
116	1.40E-02
125	1.43E-02

Table A6.2: Average measured strain for sample#5

Temperature(°C)	Average Strain
30	-9.01E-05
36	5.04E-04
42	4.81E-04
50	2.38E-03
57	3.47E-03
66	4.11E-03
73	5.44E-03
81	5.69E-03
89	7.67E-03
97	3.99E-03
105	8.67E-03
113	1.21E-02
122	1.25E-02
125	1.45E-02

Table A6.3: Average measured strain for sample#11

Temperature(°C)	Average Strain
35	3.16E-04
42	1.09E-03
49	1.70E-03
56	2.63E-03
64	4.04E-04
72	2.94E-03
80	3.61E-03
88	3.61E-03
97	3.31E-03
110	7.88E-03
119	1.09E-02
125	1.18E-02

Table A6.4: Average measured strain for sample#13

Temperature(°C)	Average Strain
33	-2.33E-04
36	1.46E-04
44	5.46E-05
51	1.02E-03
58	1.56E-03
67	7.63E-04
75	2.41E-03
83	1.63E-03
92	1.37E-03
100	2.43E-03
104	4.40E-03
116	4.30E-03
125	5.22E-03

A6.3 Comparisons between analytical and experimental results of peel strains

Table A6.5: Comparisons between analytical and experimental results of peel strains for sample#3

Temperature(°C)	Average Strain	
	Experimental	Analytical
29	-6.55E-05	0.00E+00
33	3.84E-04	1.39E-04
39	1.03E-04	3.47E-04
47	1.41E-03	1.40E-03
53	2.86E-03	2.20E-03
61	3.29E-03	3.25E-03
69	4.87E-03	4.31E-03
76	4.55E-03	5.23E-03
82	6.33E-03	6.02E-03
90	7.61E-03	7.08E-03
97	7.99E-03	8.47E-03
107	9.56E-03	1.05E-02
116	1.40E-02	1.23E-02
125	1.43E-02	1.40E-02

Table A6.6: Comparisons between analytical and experimental results of peel strains for sample#5

Temperature(°C)	Average Strain	
	Experimental	Analytical
30	-9.01E-05	0.00E+00
36	5.04E-04	1.74E-04
42	4.81E-04	3.47E-04
50	2.38E-03	5.79E-04
57	3.47E-03	1.63E-03
66	4.11E-03	2.98E-03
73	5.44E-03	4.04E-03
81	5.69E-03	5.24E-03
89	7.67E-03	6.44E-03
97	3.99E-03	7.64E-03
105	8.67E-03	8.85E-03
113	1.21E-02	1.00E-02
122	1.25E-02	1.35E-02
125	1.45E-02	1.46E-02

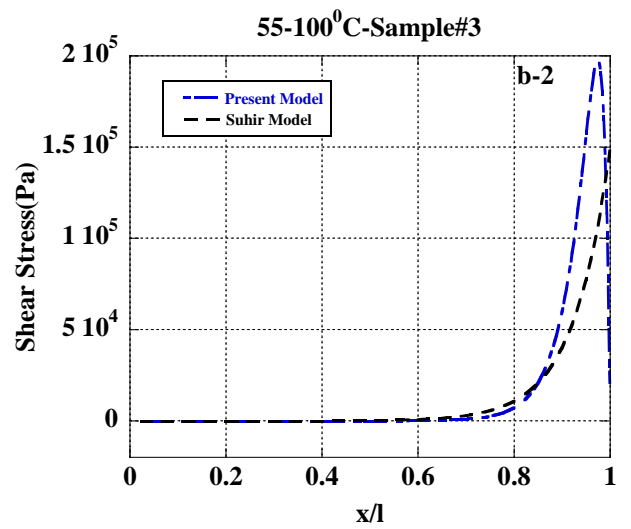
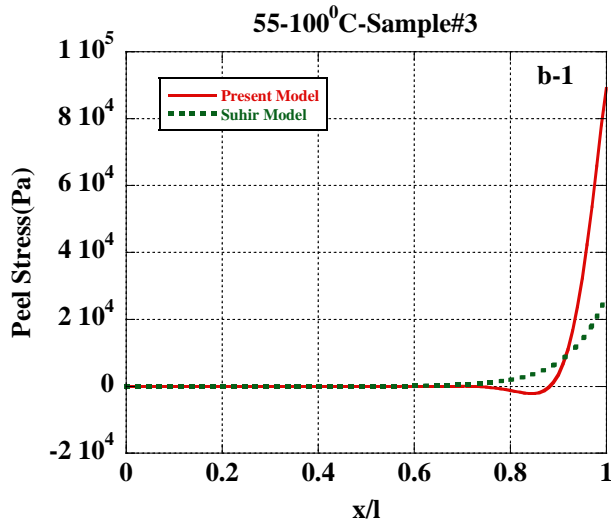
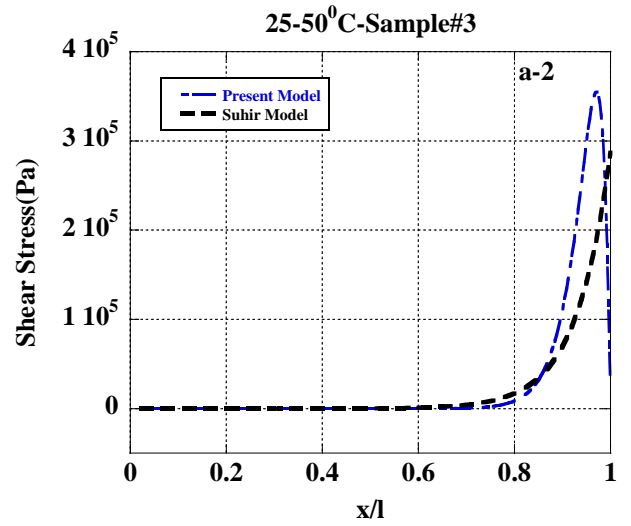
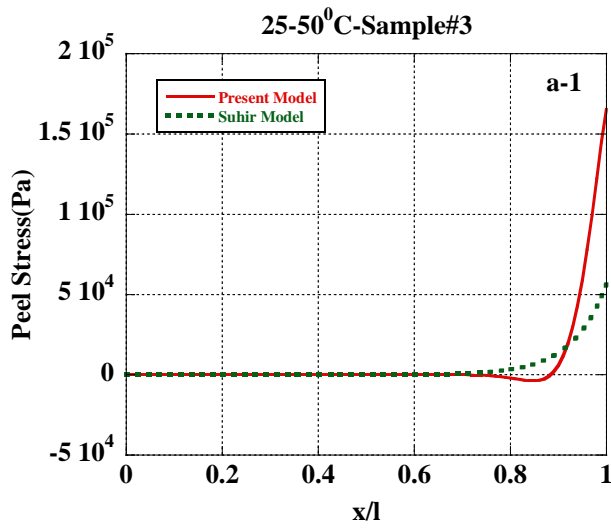
Table A6.7: Comparisons between analytical and experimental results of peel strains for sample#11

Temperature(°C)	Average Strain	
	Experimental	Analytical
35	3.16E-04	0.00E+00
42	1.09E-03	4.35E-05
49	1.70E-03	8.70E-05
56	2.63E-03	8.27E-04
64	4.04E-04	1.67E-03
72	2.94E-03	2.52E-03
80	3.61E-03	3.36E-03
88	3.61E-03	4.21E-03
97	3.31E-03	5.16E-03
110	7.88E-03	8.31E-03
119	1.09E-02	1.05E-02
125	1.18E-02	1.19E-02

Table A6.8: Comparisons between analytical and experimental results of peel strains for sample#13

Temperature(°C)	Average Strain	
	Experimental	Analytical
33	-2.33E-04	0.00E+00
36	1.46E-04	1.22E-05
44	5.46E-05	4.48E-05
51	1.02E-03	7.33E-05
58	1.56E-03	4.62E-04
67	7.63E-04	9.62E-04
75	2.41E-03	1.41E-03
83	1.63E-03	1.85E-03
92	1.37E-03	2.35E-03
100	2.43E-03	2.80E-03
104	4.40E-03	3.16E-03
116	4.30E-03	4.24E-03
125	5.22E-03	5.06E-03

A6.5 Results of comparison between peel and shear stresses obtained from analysis using present model and Suhir model



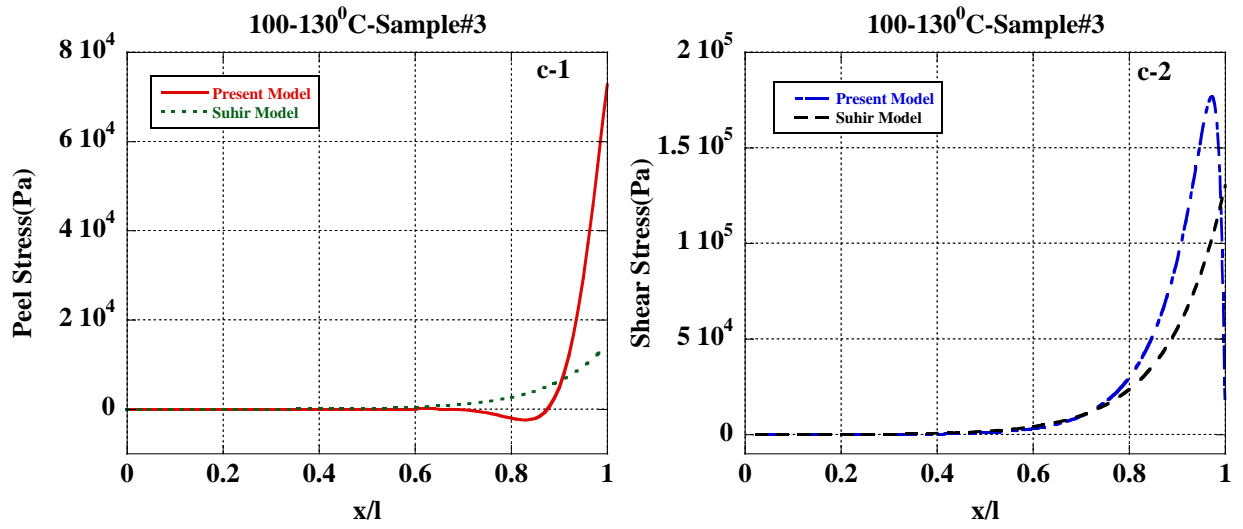
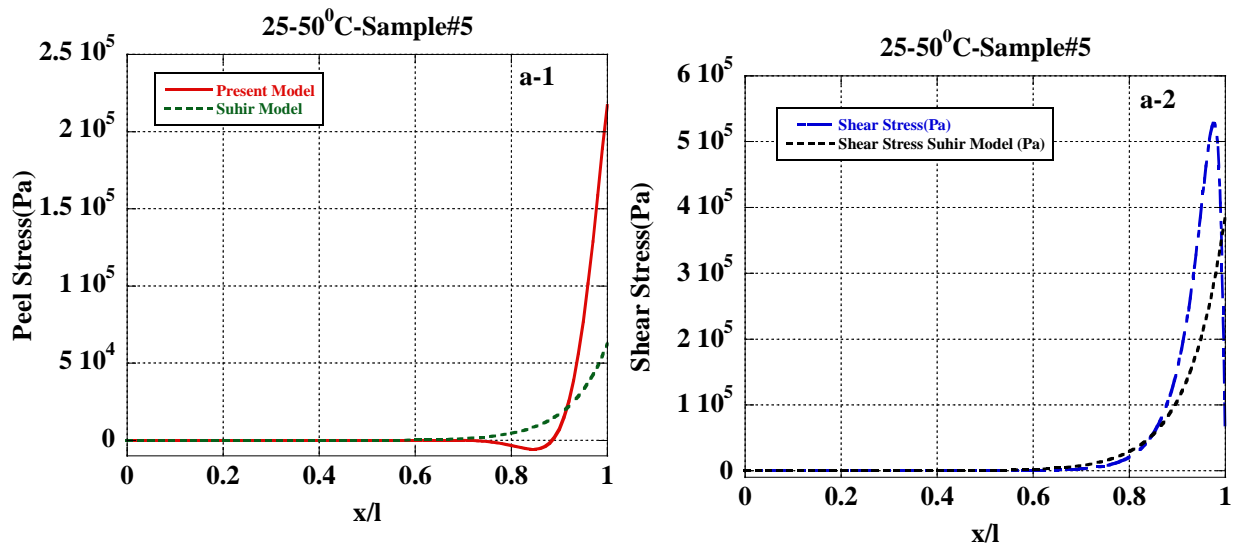


Figure A6.9: Comparison between (1) peel and (2) shear stresses obtained from analysis using present model and Suhir model for sample#3 at (a) $\Delta T = 35^\circ\text{C}$ (25°C to 55°C), (b) $\Delta T = 45^\circ\text{C}$ (55°C to 100°C), (c) $\Delta T = 30^\circ\text{C}$ (100°C to 130°C)



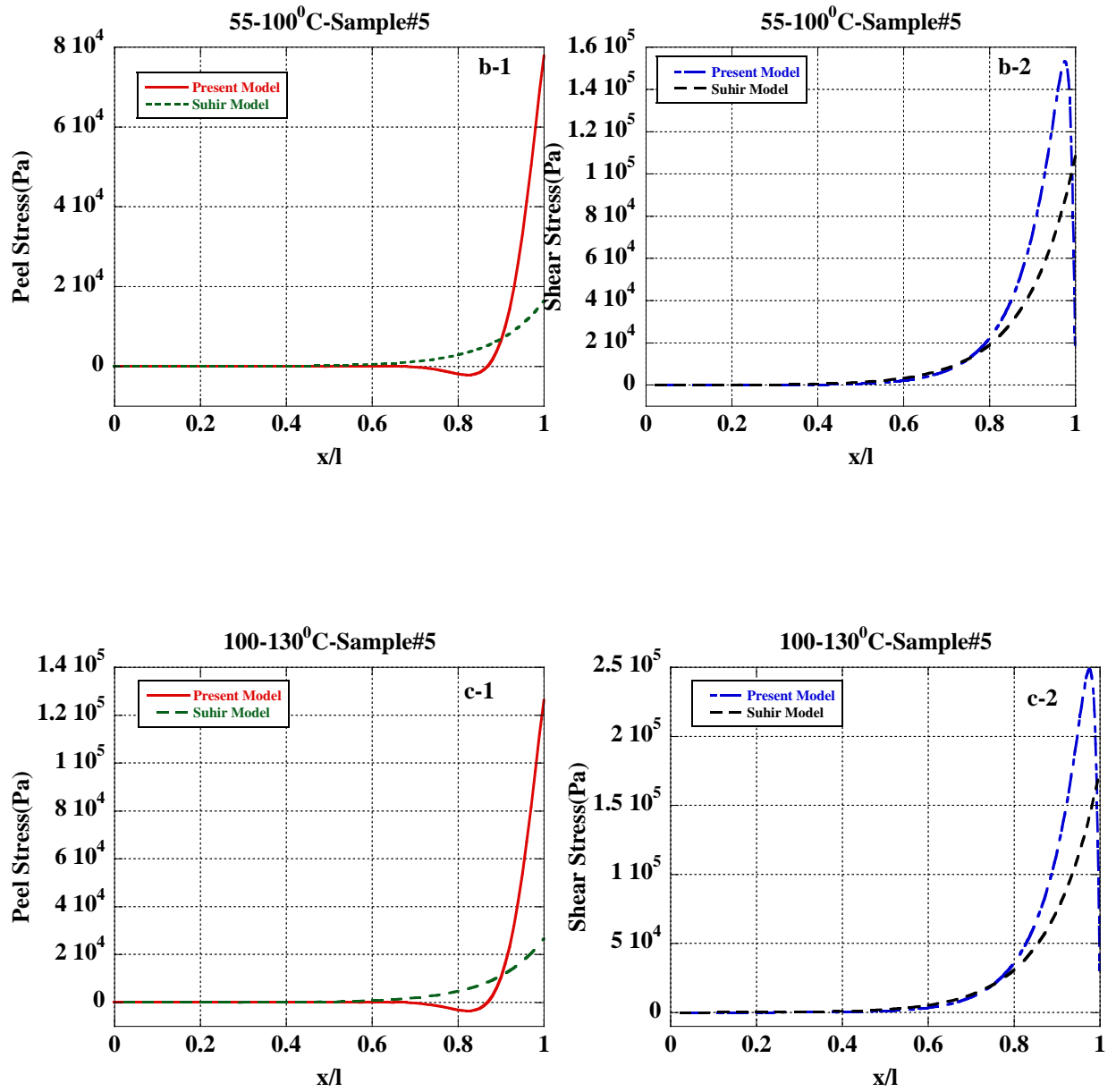


Figure A6.10: Comparison between (1) peel and (2) shear stresses obtained from analysis using present model and Suhir model for sample#5 at (a) $\Delta T=35^\circ\text{C}$ (25°C to 55°C), (b) $\Delta T=45^\circ\text{C}$ (55°C to 100°C), (c) $\Delta T=30^\circ\text{C}$ (100°C to 130°C)

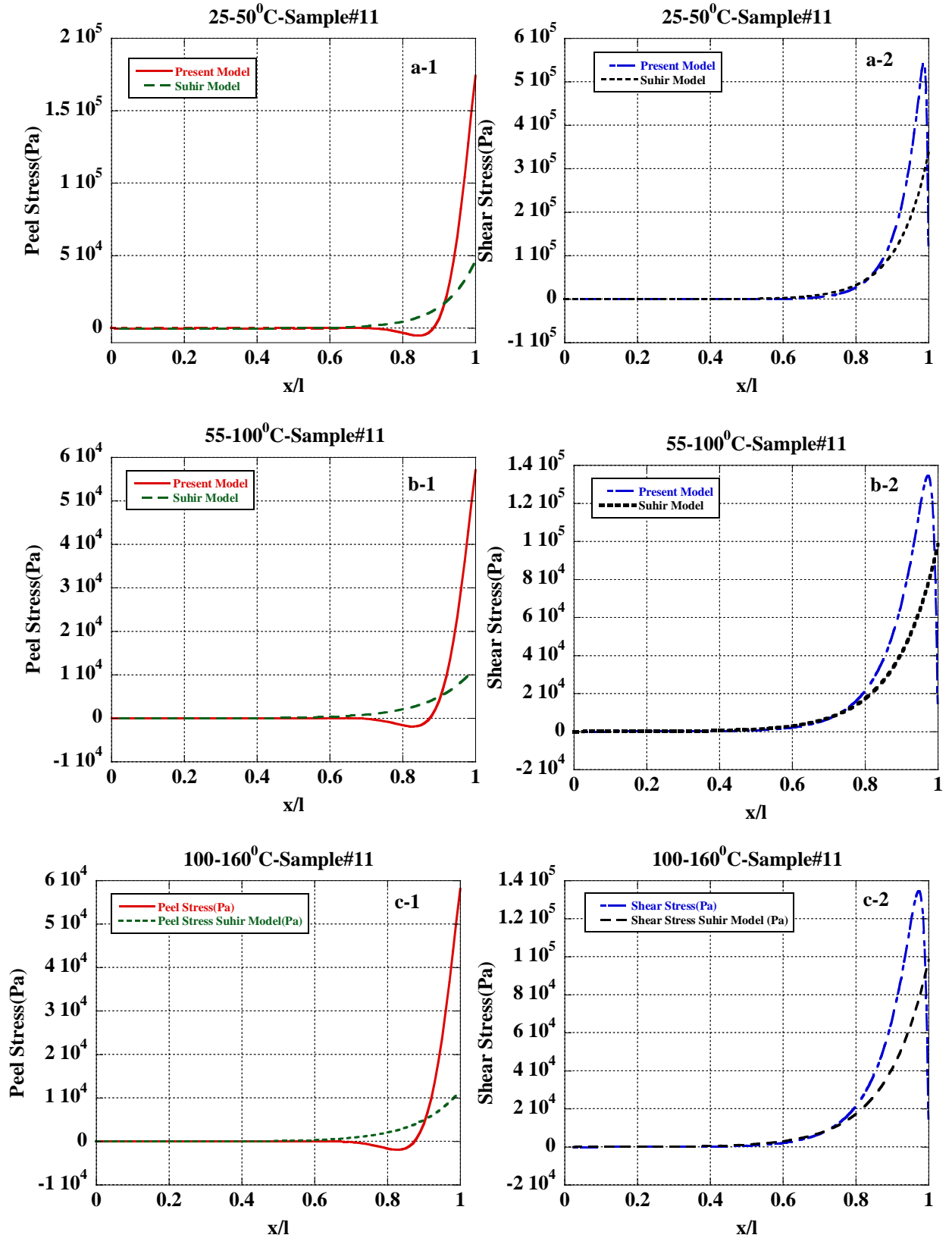
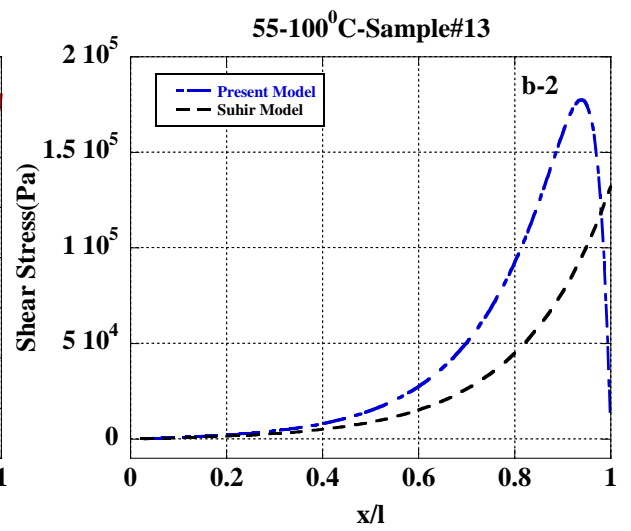
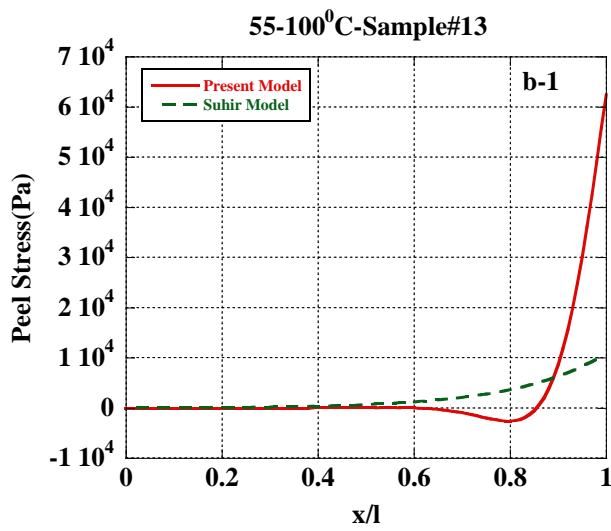
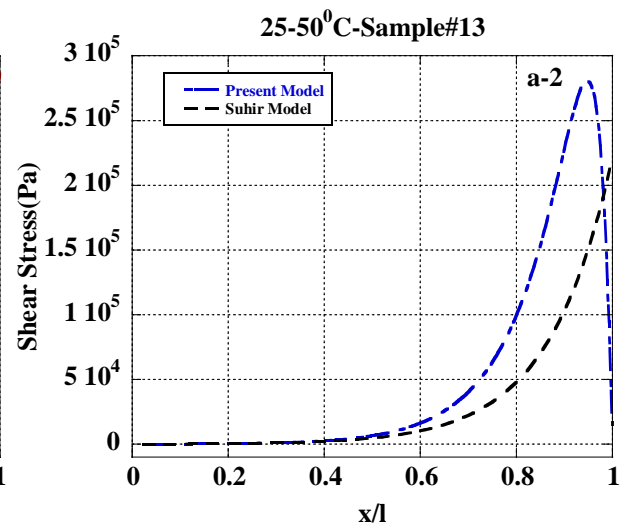
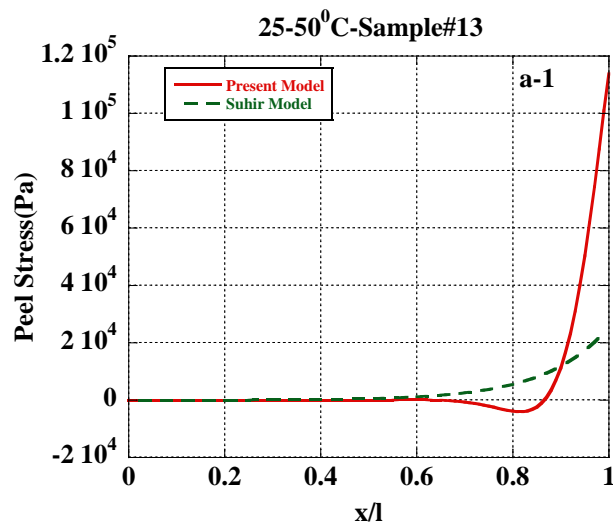


Figure A6.11: Comparison between (1) peel and (2) shear stresses obtained from analysis using present model and Suhir model for sample#11 at (a) $\Delta T = 35^\circ\text{C}$ (25°C to 55°C), (b) $\Delta T = 45^\circ\text{C}$ (55°C to 100°C), (c) $\Delta T = 30^\circ\text{C}$ (100°C to 130°C)



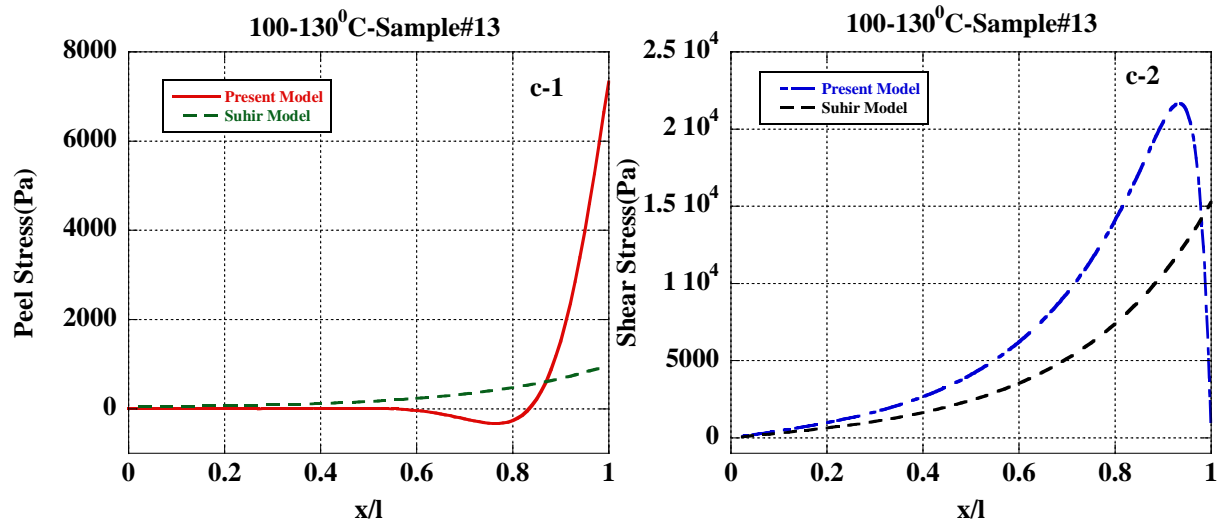
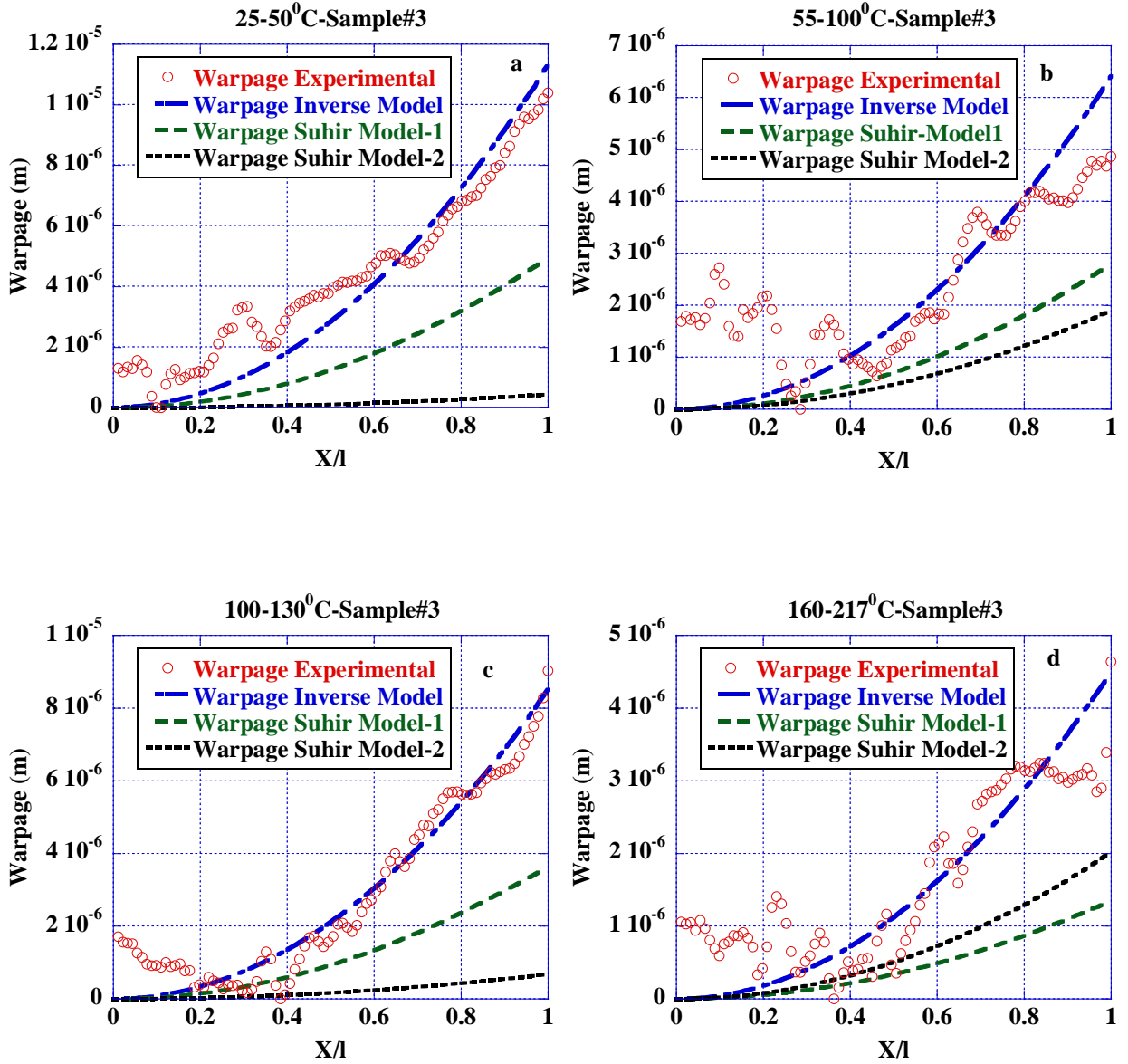


Figure A6.12: Comparison between (1) peel and (2) shear stresses obtained from analysis using present model and Suhir model for sample#13 at (a) $\Delta T = 35^\circ\text{C}$ (25°C to 55°C), (b) $\Delta T = 45^\circ\text{C}$ (55°C to 100°C), (c) $\Delta T = 30^\circ\text{C}$ (100°C to 130°C)

A6.6 Results of comparison between the warpage obtained from experiments and analysis using present model and Suhir models



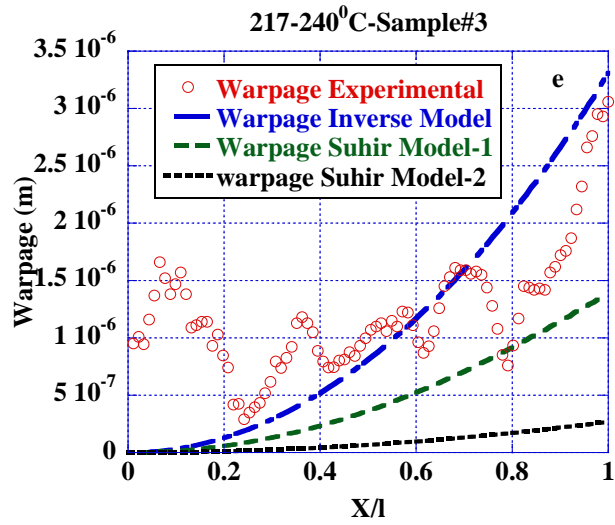
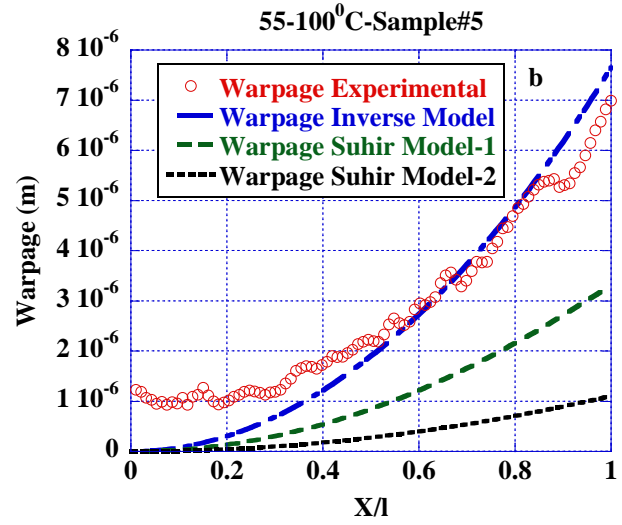
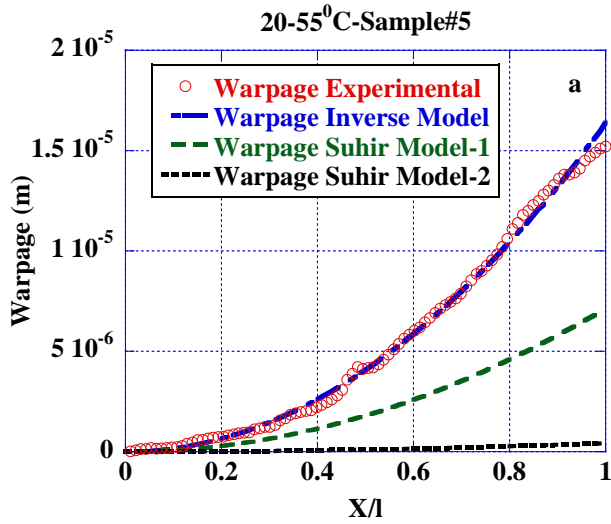


Figure A6.13: Comparison between the warpage obtained from analysis using present model and Suhir models sample#3 and experimental measurements at (a) $\Delta T=35^\circ\text{C}$ (25°C to 55°C), (b) $\Delta T=45^\circ\text{C}$ (55°C to 100°C), (c) $\Delta T=30^\circ\text{C}$ (100°C to 130°C), (d) $\Delta T=57^\circ\text{C}$ (160°C to 217°C), (e) $\Delta T=23^\circ\text{C}$ (217°C to 240°C)



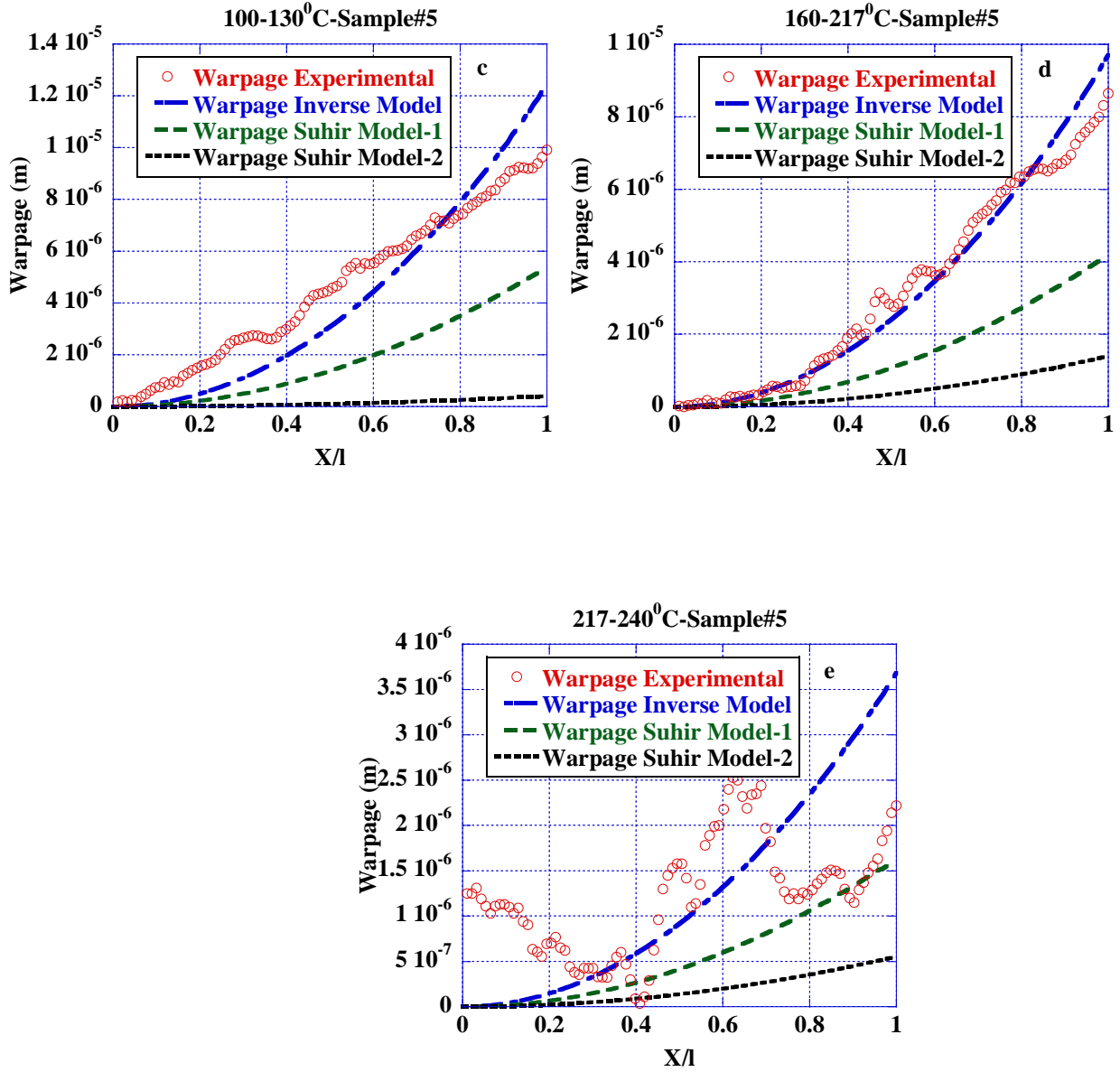


Figure A6.14: Comparison between the warpage obtained from analysis using present model and Suhir models for sample#5 and experimental measurements at (a) $\Delta T=35^\circ\text{C}$ (25°C to 55°C), (b) $\Delta T=45^\circ\text{C}$ (55°C to 100°C), (c) $\Delta T=30^\circ\text{C}$ (100°C to 130°C), (d) $\Delta T=57^\circ\text{C}$ (160°C to 217°C), (e) $\Delta T=23^\circ\text{C}$ (217°C to 240°C)

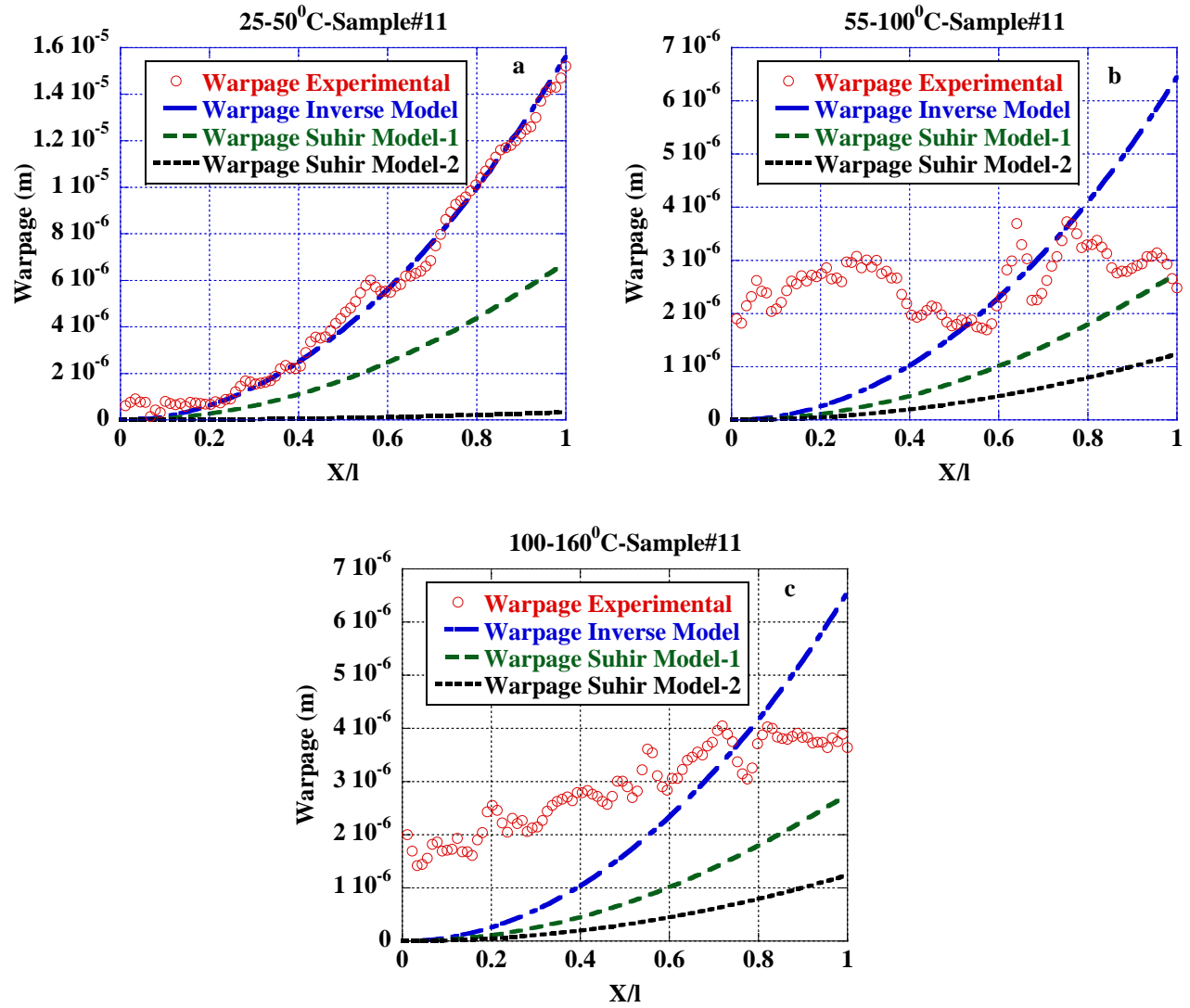


Figure A6.15: Comparison between the warpage obtained from analysis using present model and Suhir models for sample#11 and experimental measurements at (a) $\Delta T=35^\circ\text{C}$ (25°C to 55°C), (b) $\Delta T=45^\circ\text{C}$ (55°C to 100°C), (c) $\Delta T=60^\circ\text{C}$ (100°C to 160°C)

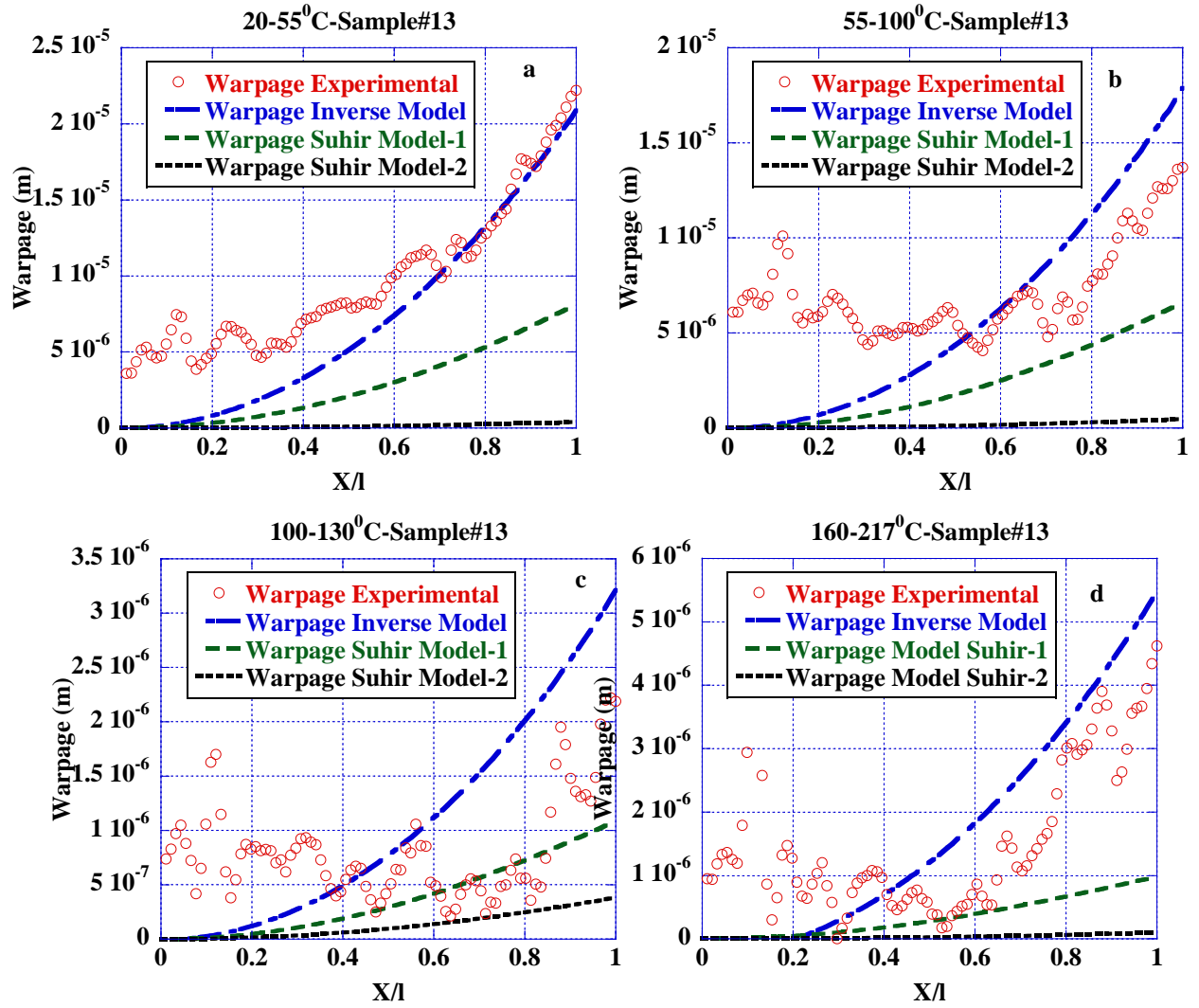
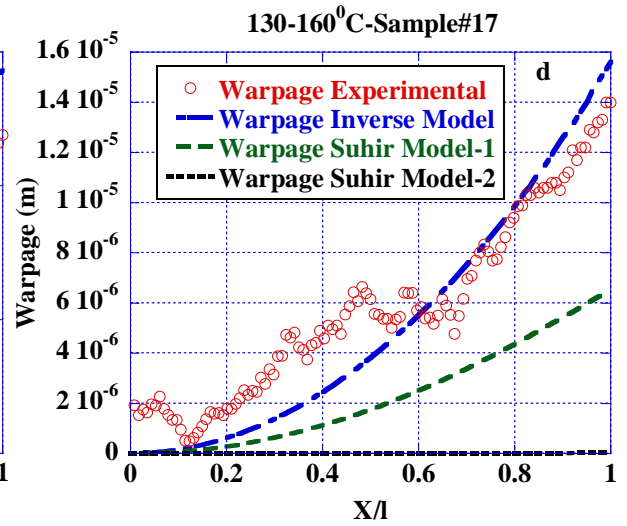
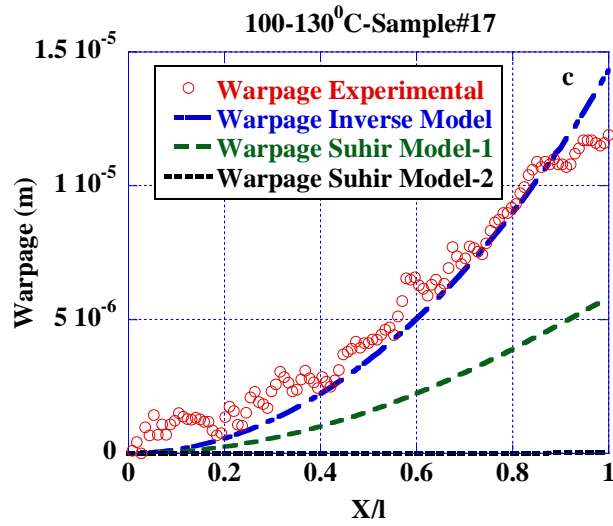
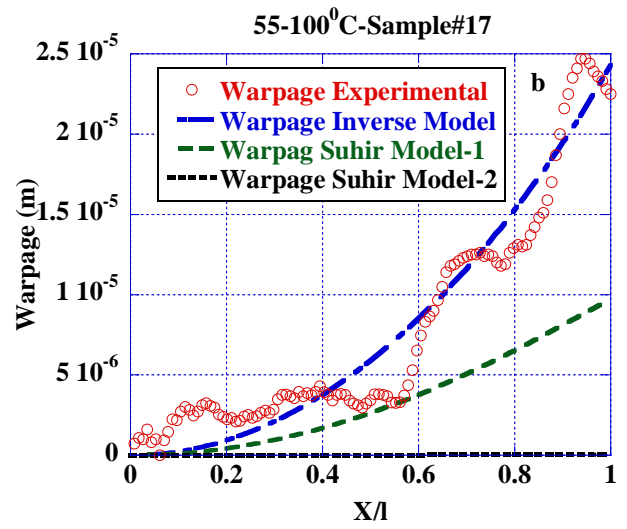
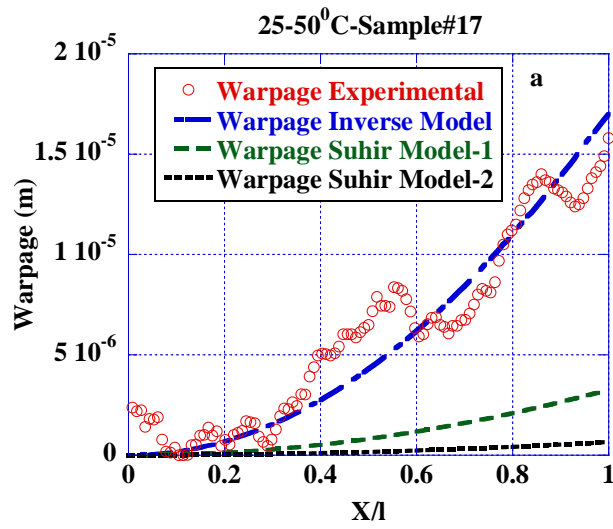


Figure A6.16: Comparison between the warpage obtained from analysis using present model and Suhir models for sample#13 and experimental measurements at (a) $\Delta T=35^\circ\text{C}$ (25°C to 55°C), (b) $\Delta T=45^\circ\text{C}$ (55°C to 100°C), (c) $\Delta T=30^\circ\text{C}$ (100°C to 130°C), (d) $\Delta T=57^\circ\text{C}$ (160°C to 217°C)



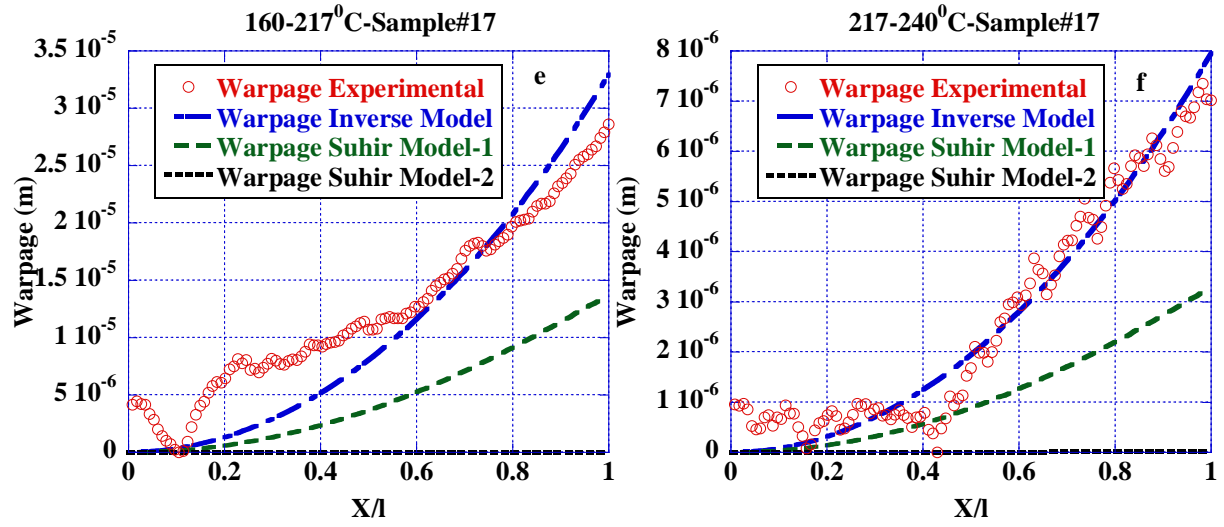


Figure A6.17: Comparison between the warpage obtained from analysis using present model and Suhir models for sample#17 and experimental measurements at (a) $\Delta T=35^\circ\text{C}$ (20°C to 55°C), (b) $\Delta T=45^\circ\text{C}$ (55°C to 100°C), (c) $\Delta T=30^\circ\text{C}$ (100°C to 130°C), (d) $\Delta T=30^\circ\text{C}$ (130°C to 160°C), (e) $\Delta T=57^\circ\text{C}$ (160°C to 217°C), (f) $\Delta T=23^\circ\text{C}$ (217°C to 240°C)

APPENDIX7

Cast Detailed Drawings

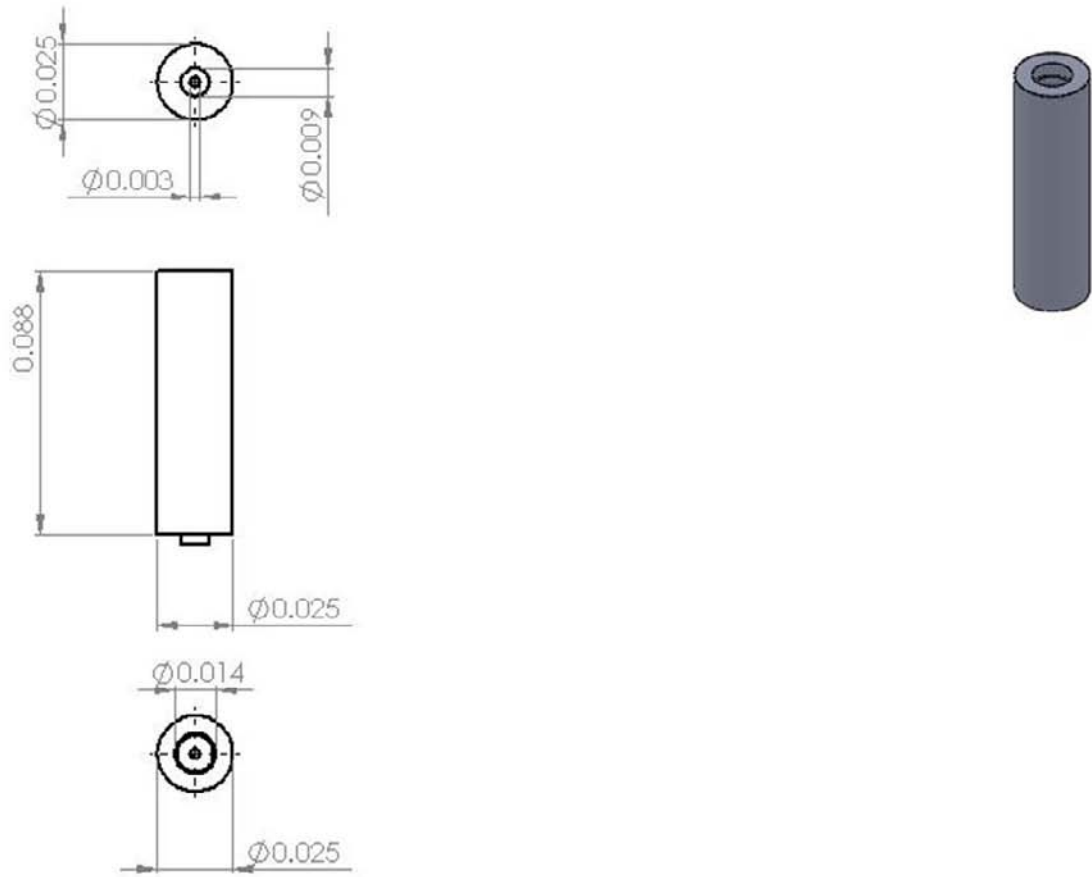


Figure A7.1: Isometric, top, bottom and front view of Feeder

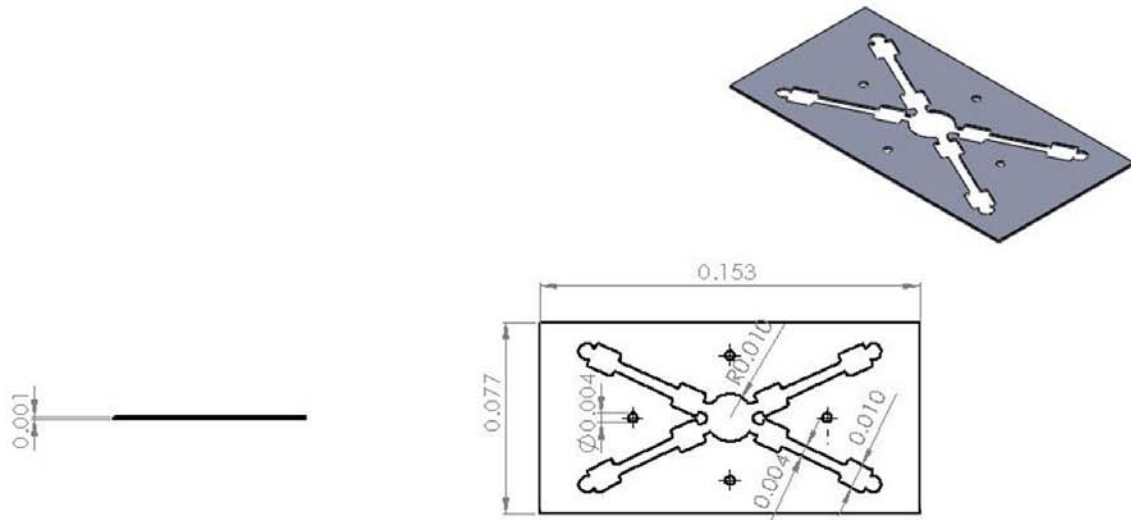


Figure A7.2: Isometric, top and front view of Mould

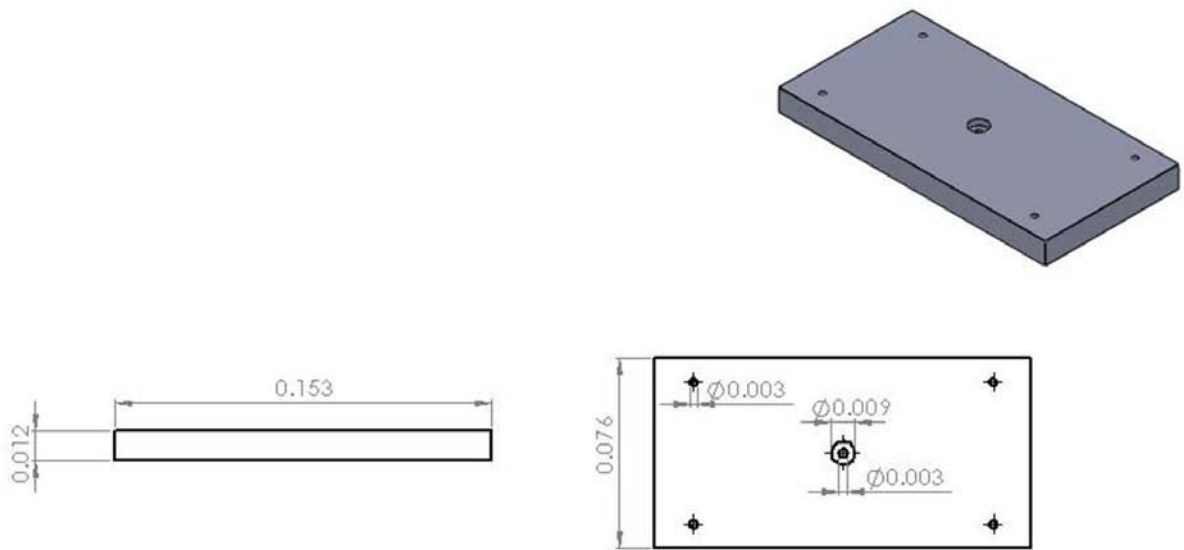


Figure A7.3: Isometric, top and front view of top piece of cast

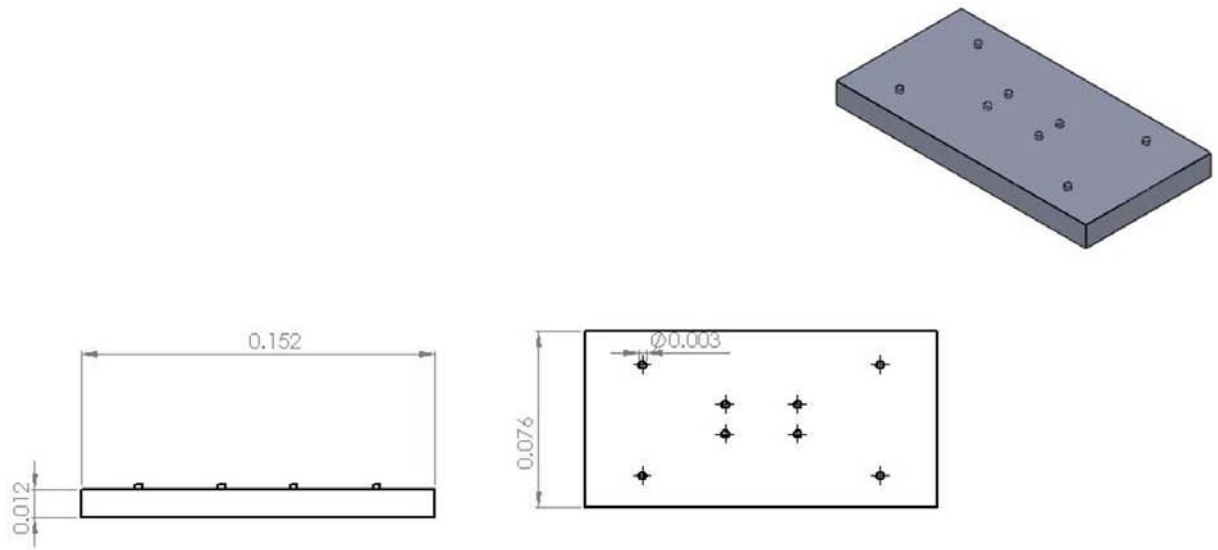


Figure A7.4: Isometric, top and front view of bottom piece of cast

APPENDIX8

Micro-tester Design Drawings

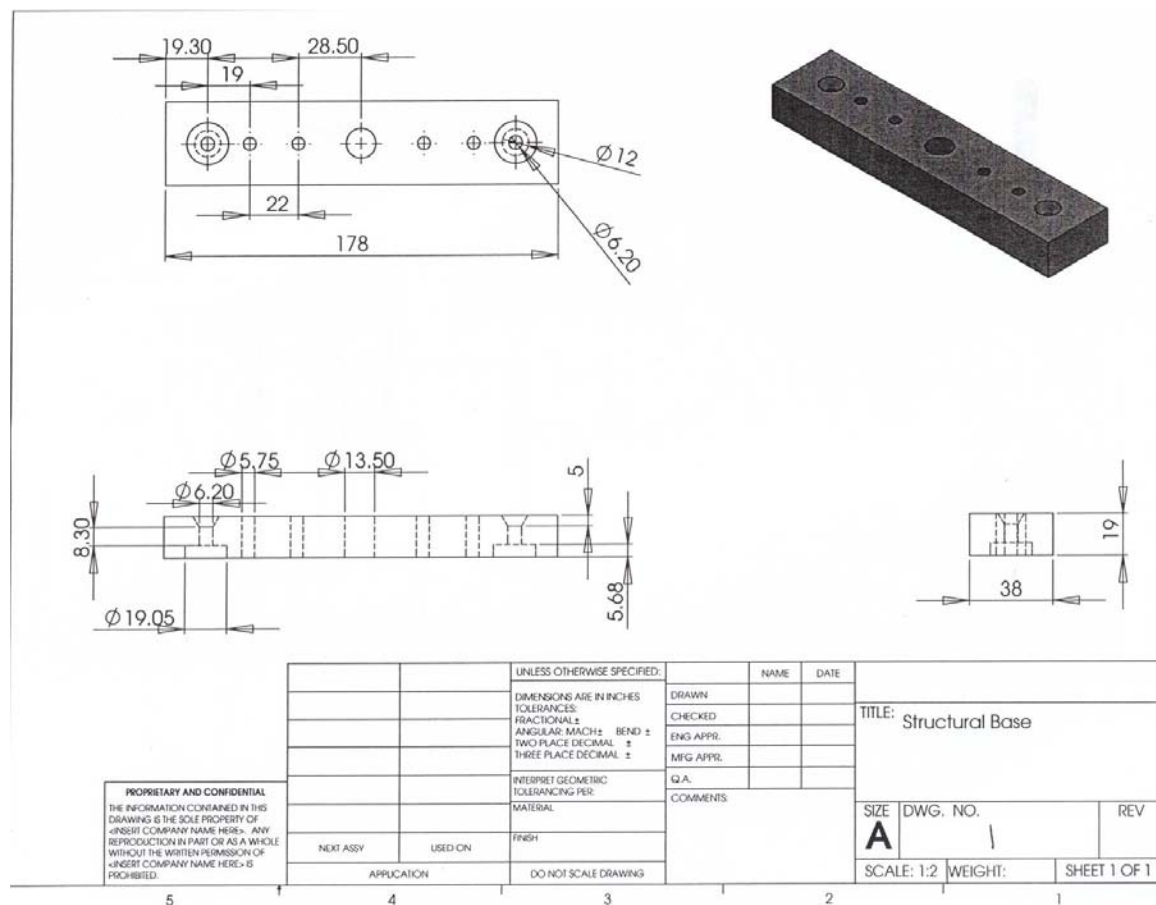


Figure A8.1: Isometric, top and front view

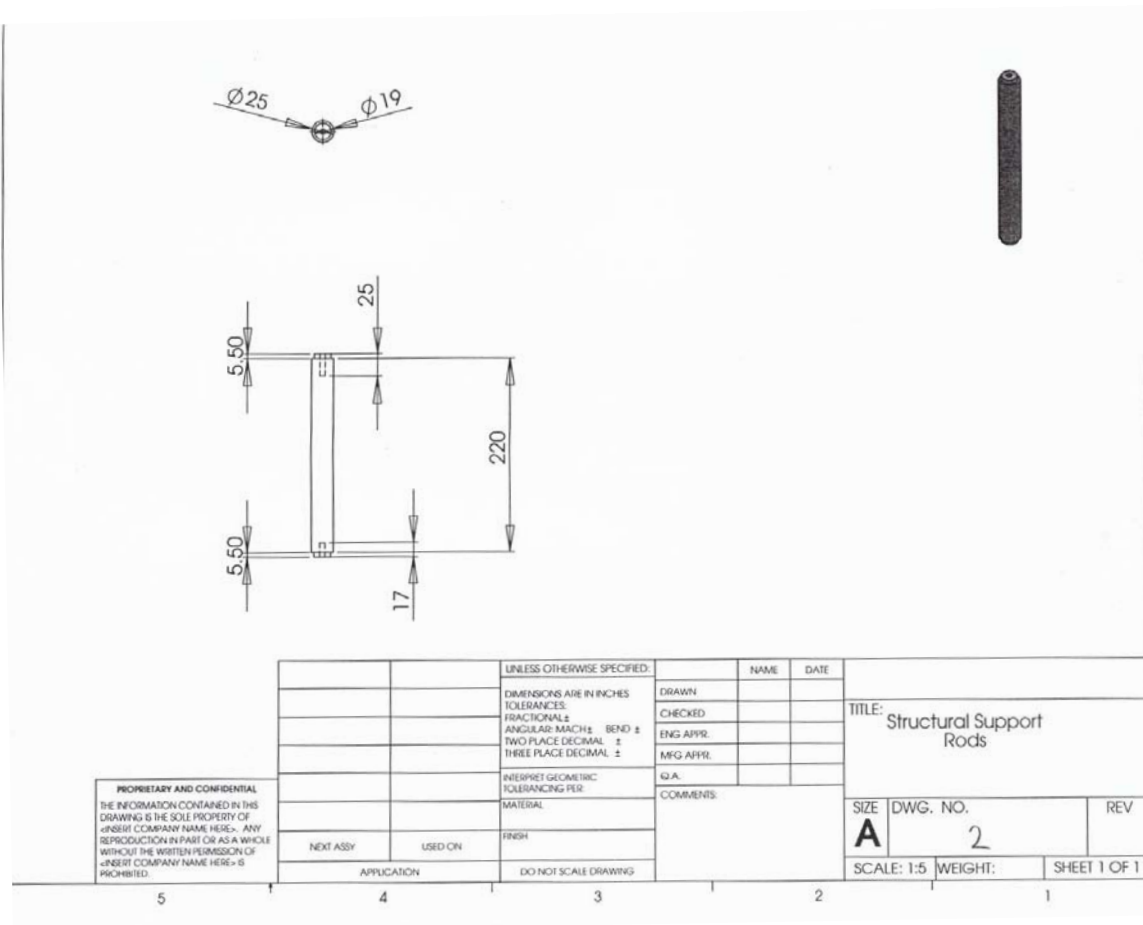


Figure A8.2: Isometric, top and front view

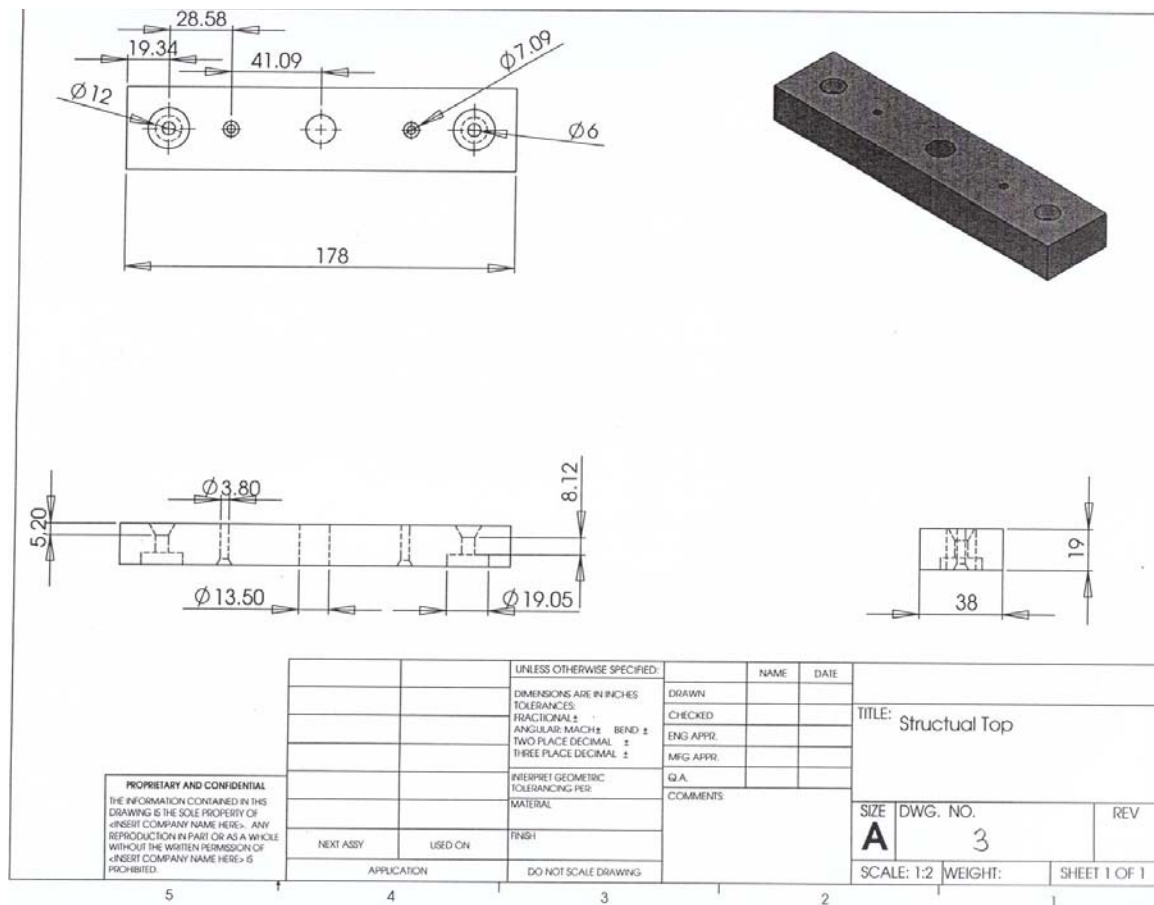


Figure A8.3: Isometric, top and front view

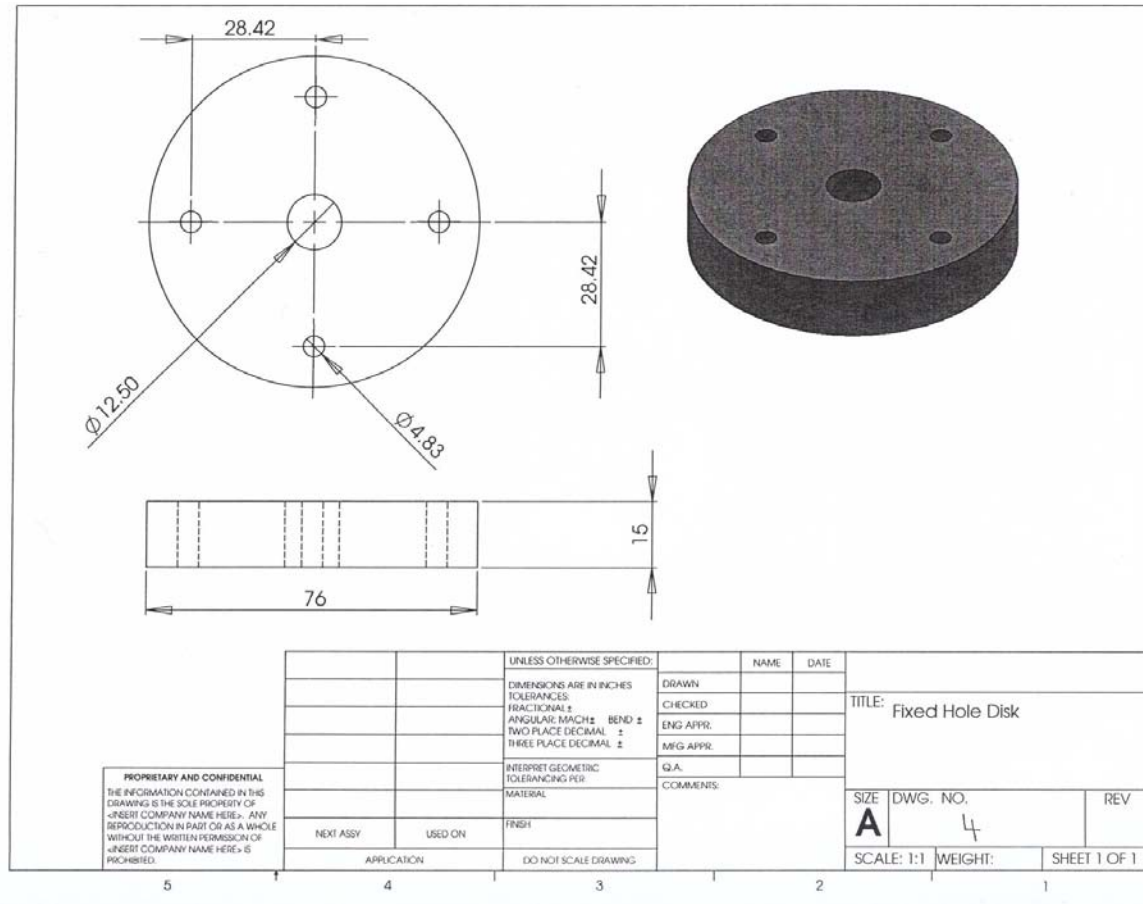


Figure A8.4: Isometric, top and front view

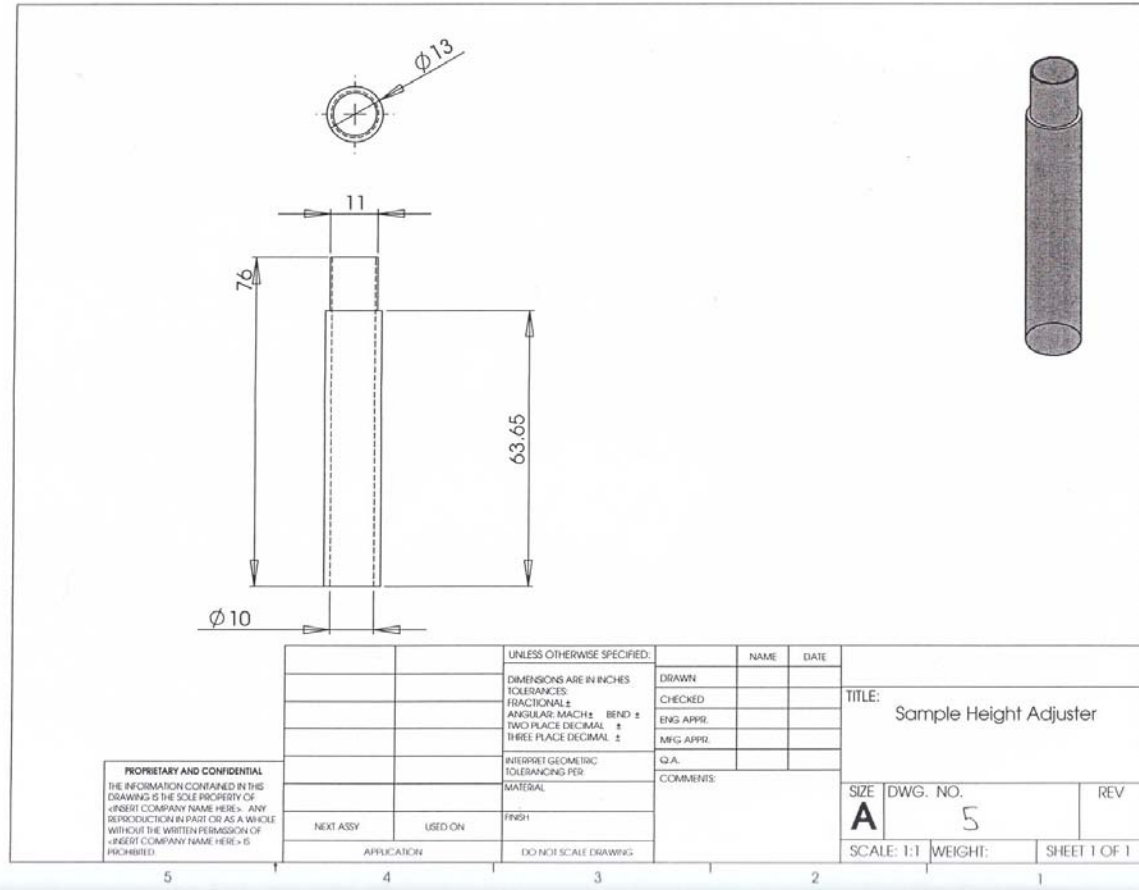


Figure A8.5: Isometric, top and front view

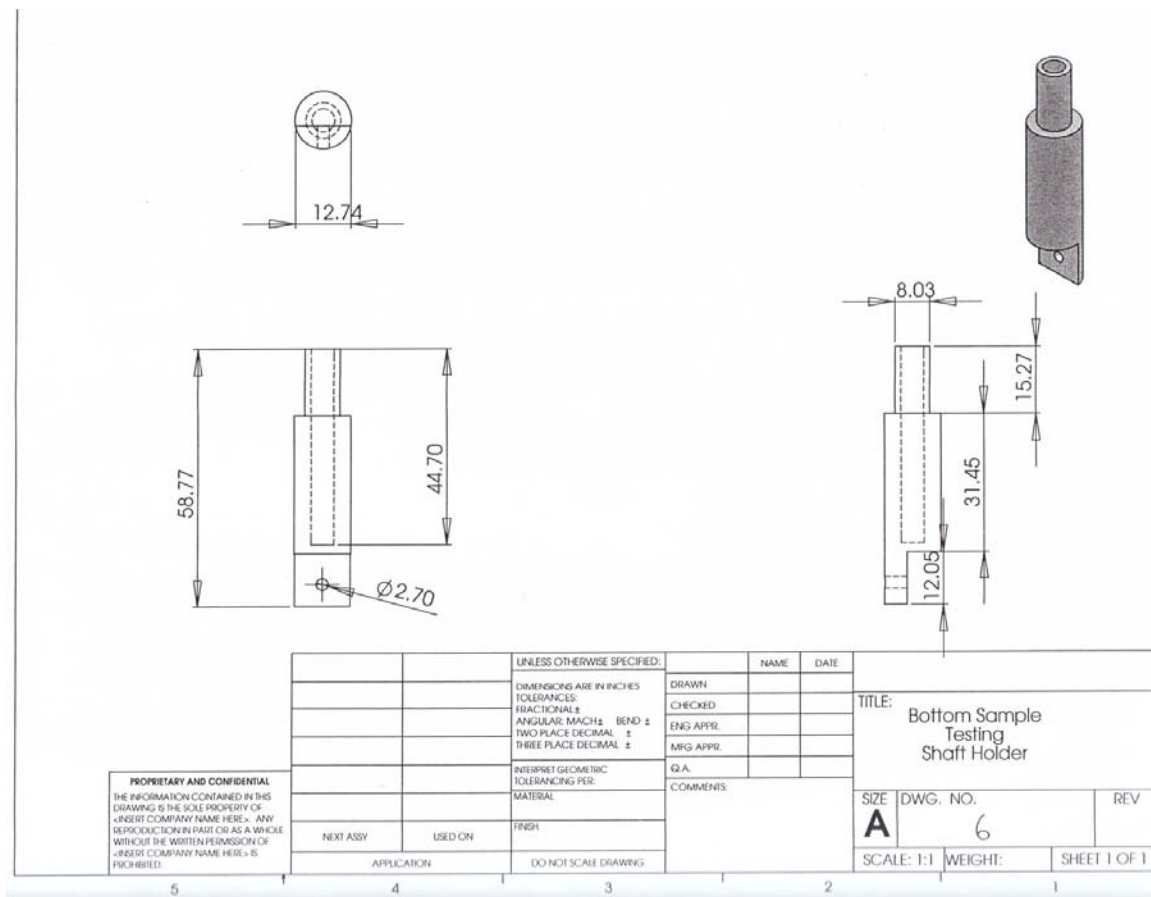


Figure A8.6: Isometric, top and front view

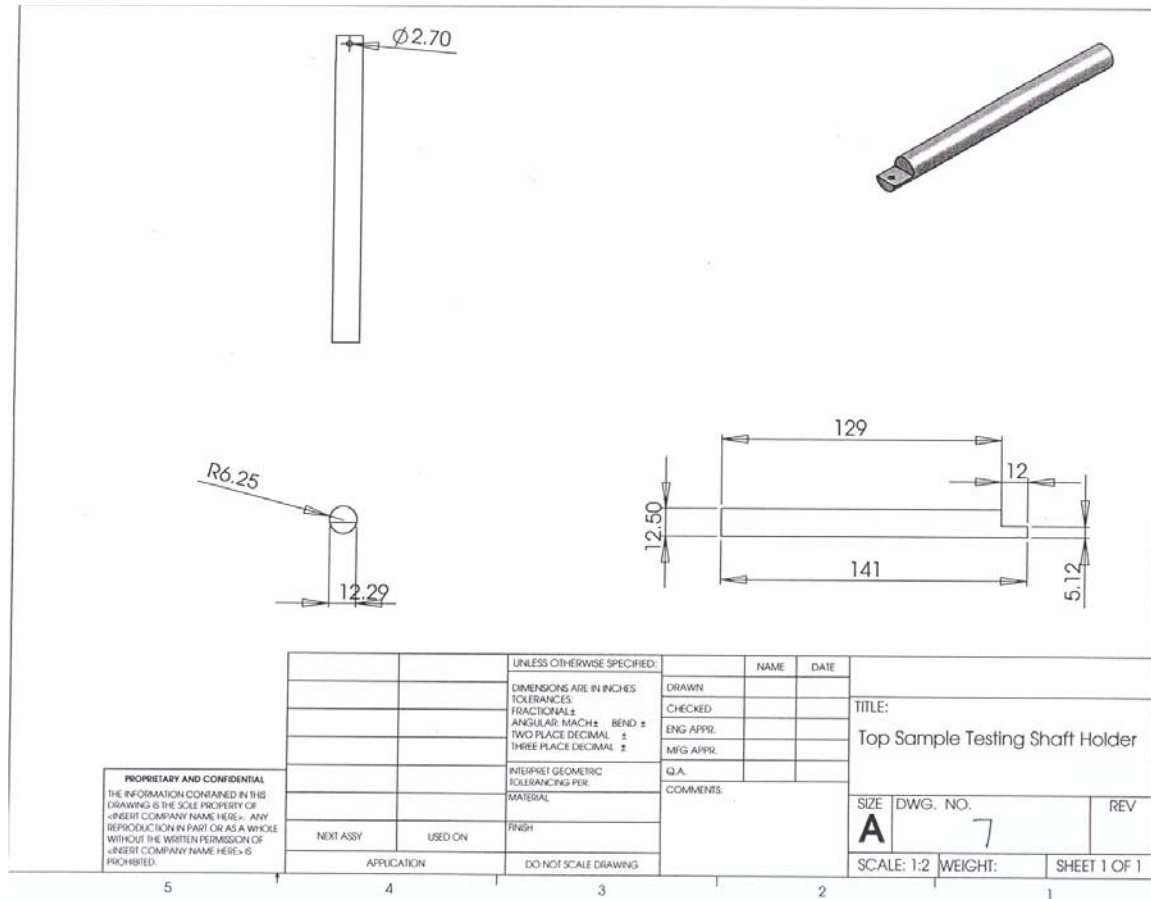


Figure A8.7: Isometric, top and front view

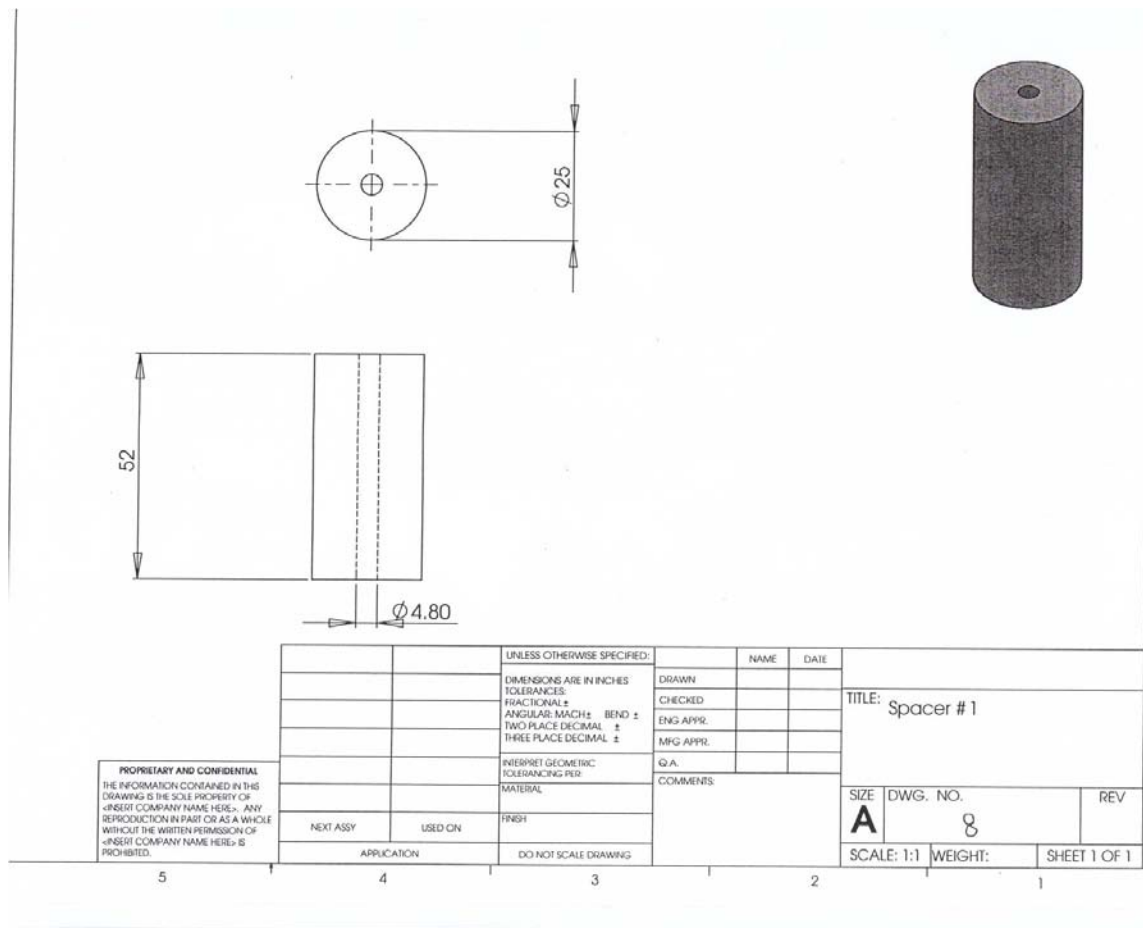


Figure A8.8: Isometric, top and front view

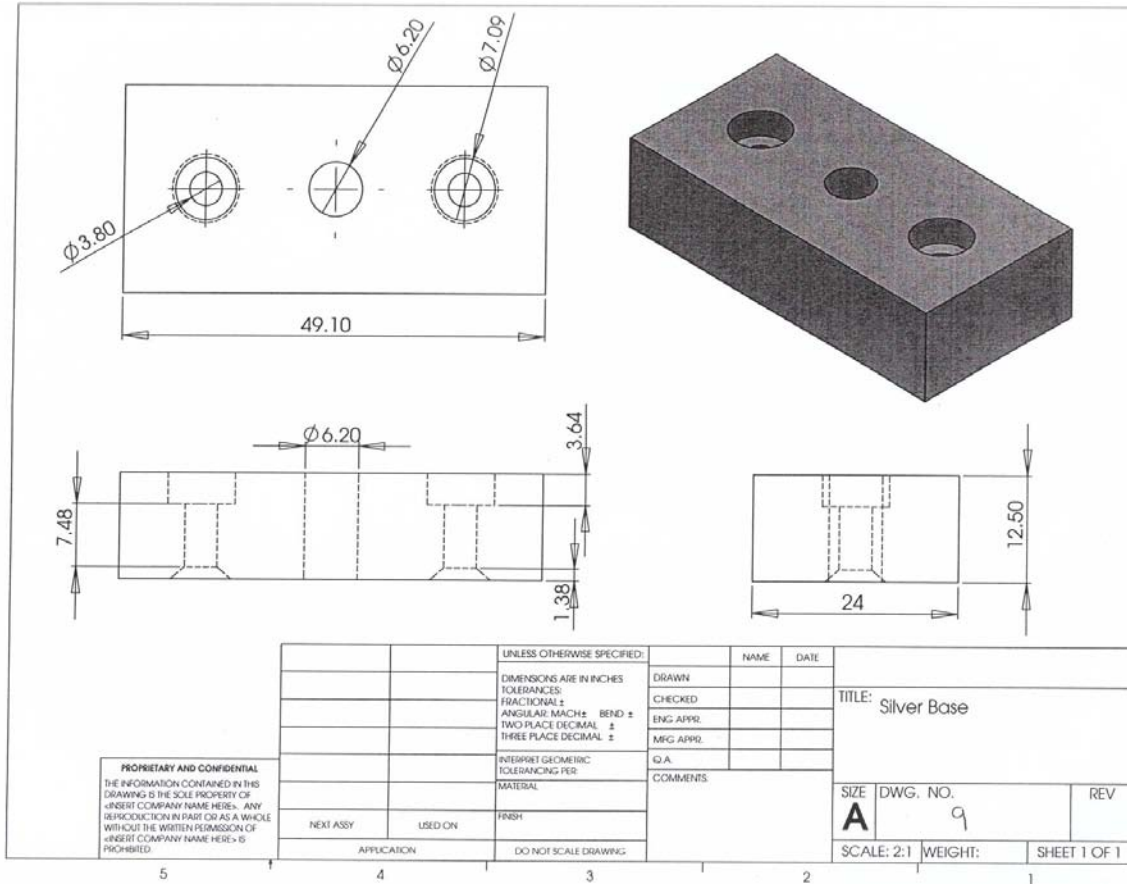


Figure A8.9: Isometric, top and front view

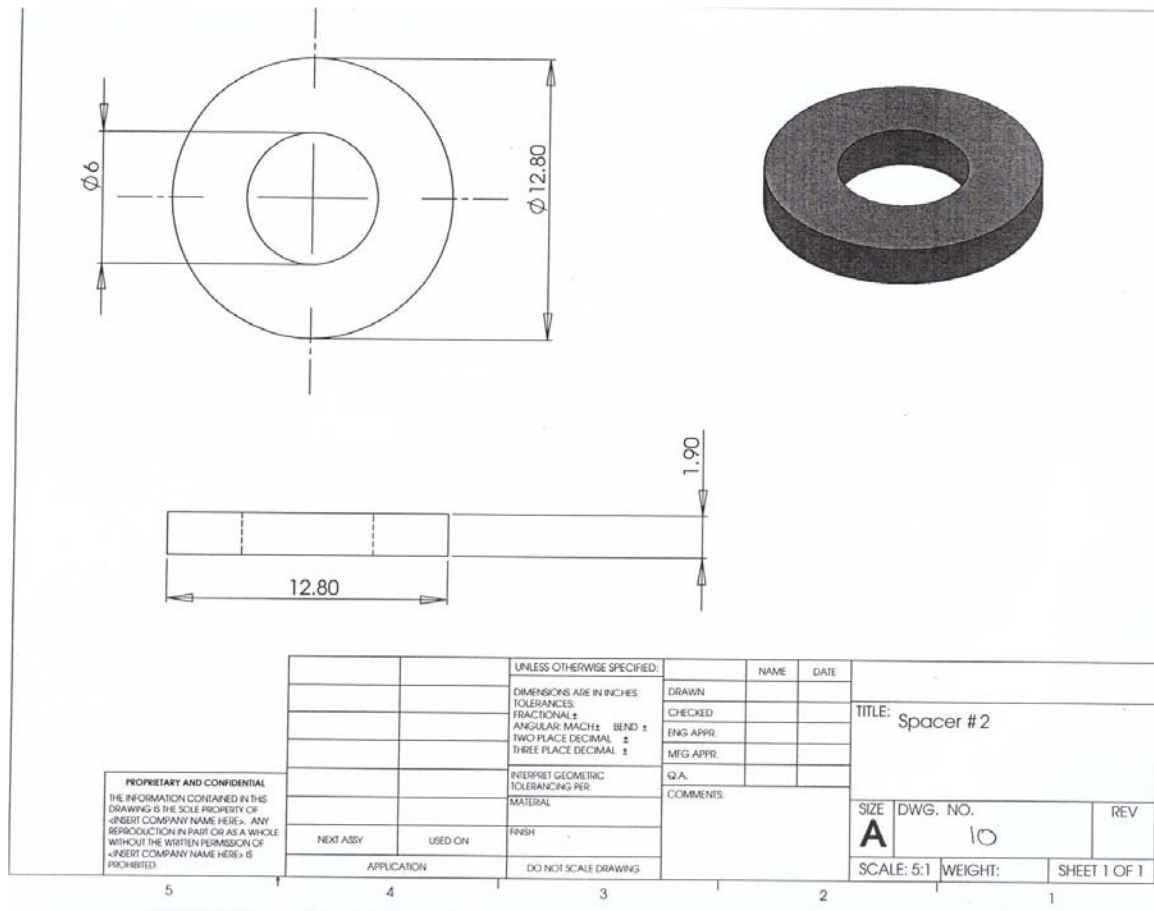


Figure A8.10: Isometric, top and front view

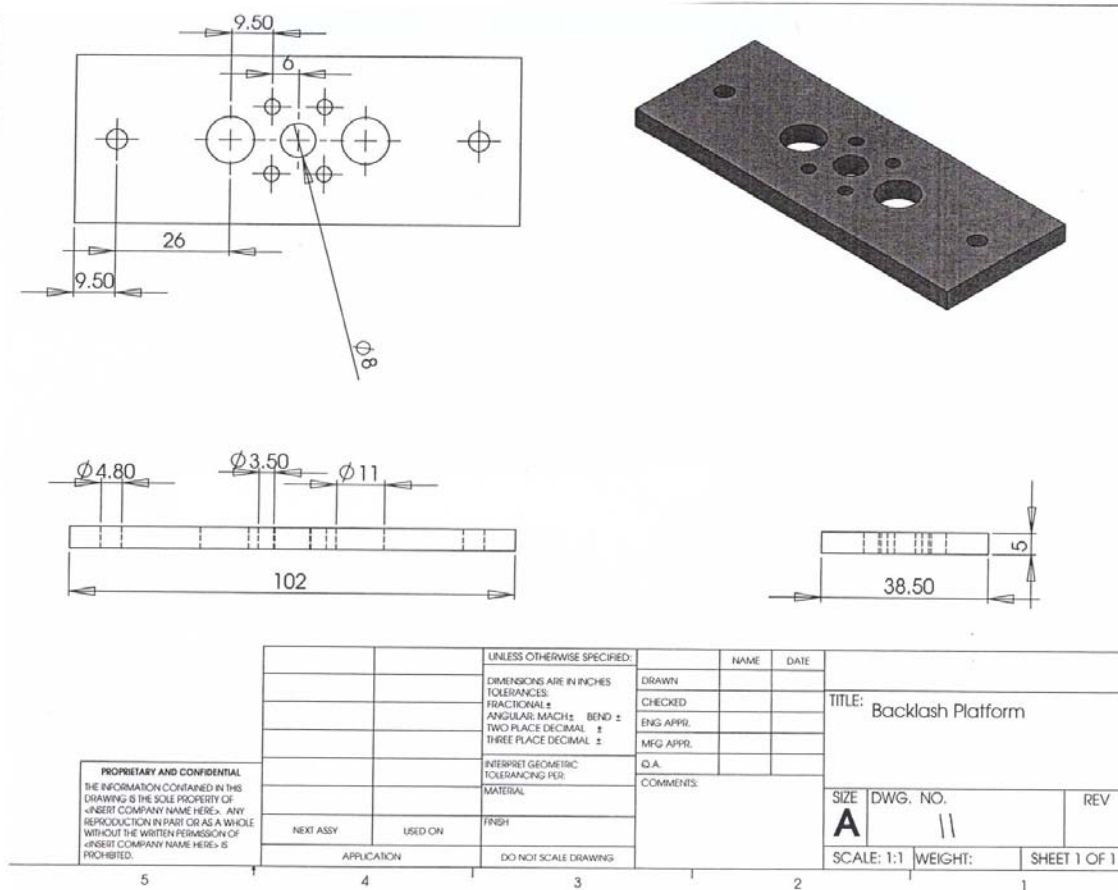


Figure A8.11: Isometric, top and front view

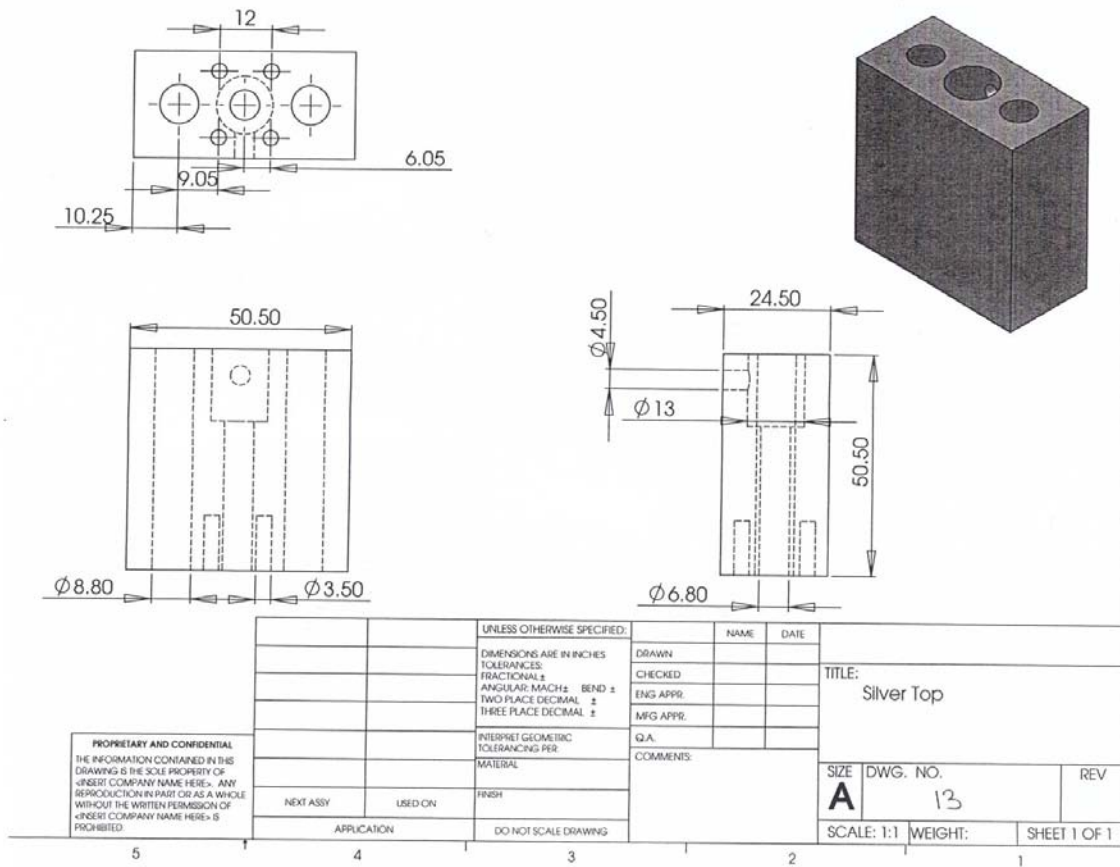


Figure A8.12: Isometric, top and front view

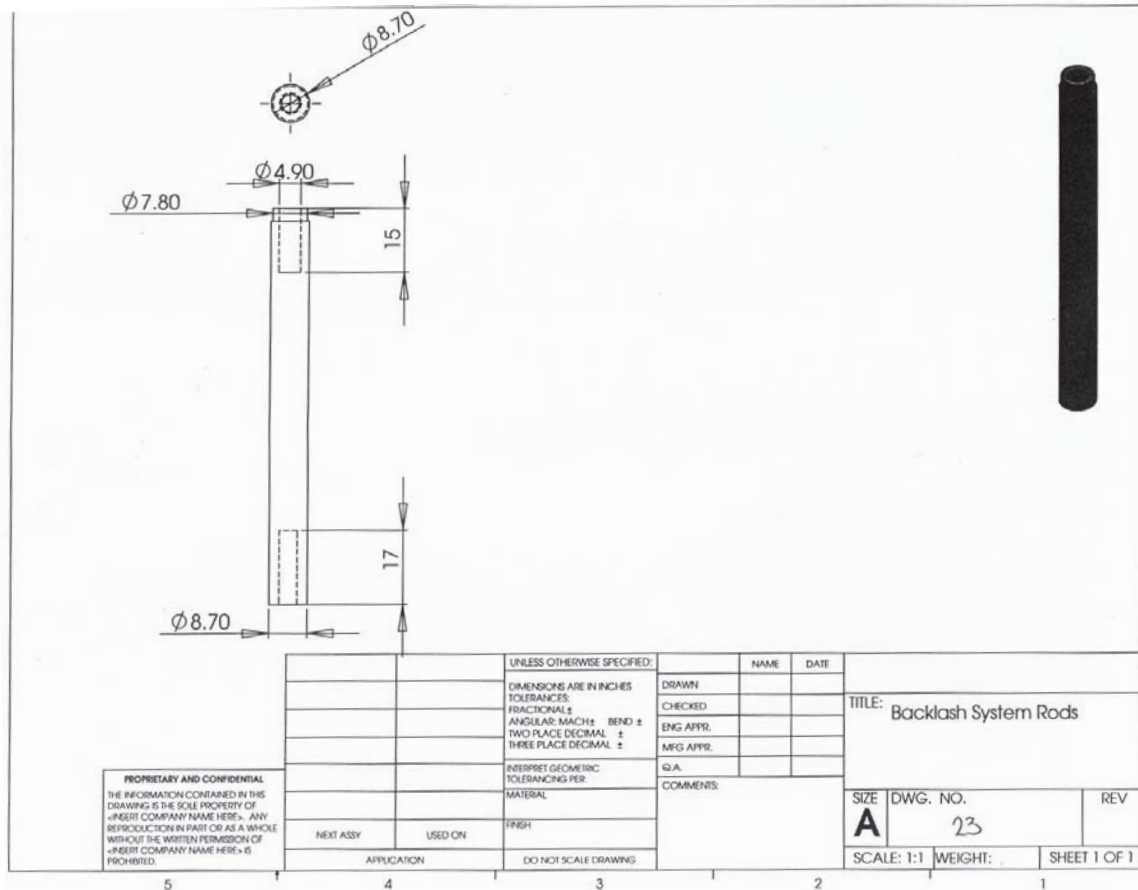


Figure A8.13: Isometric, top and front view

APPENDIX9

Creep Tensile Test Results

Table A9-1: Stress Concentration Factors of 60° V-shaped notches under tension

	2R/w = 0.05	2R/w = 0.075	2R/w = 0.1	2R/w = 0.125	2R/w = 0.15	2R/w = 0.175	2R/w = 0.2
2t/w	k_t	k_t	k_t	k_t	k_t	k_t	k_t
0.3	4.431	3.86	3.285	3.08	2.88	2.6815	2.483
0.32 5	4.42	3.85	3.28	3.075	2.87	2.66825	2.4665
0.35	4.41	3.83	3.26	3.06	2.86	2.655	2.45
0.37 5	4.4	3.82	3.25	3.045	2.84	2.6385	2.437
0.4	4.39	3.81	3.234	3.032	2.83	2.627	2.424
0.42 5	4.34	3.77	3.19	2.995	2.8	2.596	2.392
0.45	4.29	3.72	3.15	2.955	2.76	2.56	2.36
0.47 5	4.24	3.67	3.11	2.915	2.72	2.522	2.324
0.5	4.181	3.62	3.068	2.874	2.68	2.484	2.288

Table A9-2: Details of Creep-test under 0°C condition with different load

Sampl e	Loa d (kg)	Thicknes s (mm)	Widt h (w) (mm)	Crack length h (t) (mm)	Radiu s of Notch (R) (mm)	Area cross- section far from notch (mm ²)	Initial area at notch cross- section (mm ²)	2R/ w	2t/ w	Nomina l Stress (σ _n) (MPa)	Transient Stress Concentratio n Factor	Local Stress (σ _{max}) (MPa)	Strain Rate	Transien t Creep
M23- I	12	0.972	4.158	0.806	0.3	4.04	2.47	0.14	0.39	29.13	2.94	85.63	0.000 2	0.1215
M19- A	12	1.06	4.116	0.788	0.2	4.36	2.69	0.10	0.38	26.98	3.25	87.69	0.000 3	0.063
M5-10	10	1.13	3.86	0.83	0.23	4.36	2.49	0.12	0.43	22.49	2.994	67.34	5E-05	0.0212
M5-X	8	1.02	3.98	0.85	0.21	4.06	2.33	0.11	0.43	19.33	3.19	61.67	2E-05	0.017

Table A9-23: Details of Creep-test under 20°C condition with different load

Sample	Load (kg)	Thickness (mm)	Width (w) (mm)	Crack length (t) (mm)	Radius of Notch (R) (mm)	Area cross-section far from notch (mm ²)	Initial area at notch cross-section (mm ²)	2R/w	2t/w	Nominal Stress (σ_n) (MPa)	Transient Stress Concentration Factor	Local Stress (σ_{max}) (MPa)	Strain Rate	Transient Creep
2B	8	1.17	3.86	0.76	0.2	4.5162	2.7378	0.10	0.39	17.38	2.94	51.1	5E-05	0.02
3B	6	1.15	4.17	0.87	0.2	4.7955	2.7945	0.10	0.42	12.27	2.94	36.1	3E-06	0.018
M5-V	4	1.09	4.2	0.85	0.23	4.578	2.725	0.11	0.40	8.57	2.94	25.2	8E-08	0.0009
M5-III	6.4	0.96	4.06	0.82	0.21	3.8976	2.3232	0.10	0.40	16.11	2.94	47.4	4E-06	0.003

Table A9-4: Details of Creep-test under 70°C condition with different load

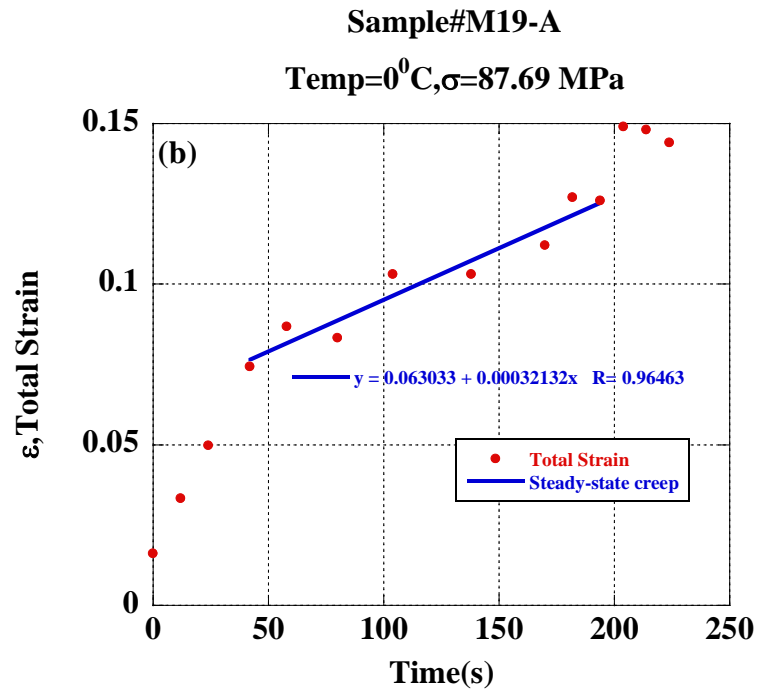
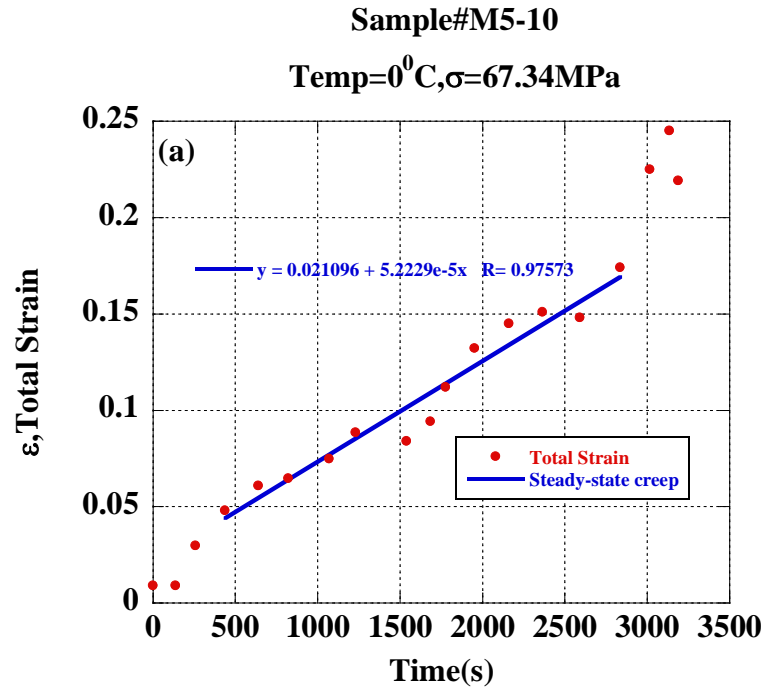
Sample	Load (kg)	Thickness (mm)	Width (w) (mm)	Crack length (t) (mm)	Radius of Notch (R) (mm)	Area cross-section far from notch (mm ²)	Initial area at notch cross-section (mm ²)	2R/w	2t/w	Nominal Stress (σ_n) (MPa)	Transient Stress Concentration Factor	Local Stress (σ_{max}) (MPa)	Strain Rate	Transient Creep
M 1	8	1.06	4.077	0.85	0.2	4.32162	2.51962	0.10	0.42	18.16	3.19	57.93	0.0004	0.0144
M 10-1	8	1.06	4.054	0.846	0.2	4.29724	2.50372	0.10	0.42	18.26	3.19	58.26	0.0026	0.02
M 10-3-I	8	1.063	4.085	0.865	0.23	4.342355	2.503365	0.11	0.42	18.07	3	54.22	0.0016	0.007
M 10-3-II	8	1.05	3.85	0.84	0.21	4.0425	2.2785	0.11	0.44	19.41	2.94	57.08	0.0022	0.06
M 10-3-III	6	1.055	4.0275	0.84	0.21	4.249013	2.476613	0.10	0.42	13.85	3.19	44.19	3E-05	0.024
M19-B	6	0.948	3.96	0.745	0.21	3.75408	2.34156	0.11	0.38	15.68	3.2	50.17	4E-05	0.072

Table A9-5: Details of Creep-test under 100°C condition with different load

Sample	Load (kg)	Thickness (mm)	Width (w) (mm)	Crack length (t) (mm)	Radius of Notch (R) (mm)	Area cross-section far from notch (mm ²)	Initial area at notch cross-section (mm ²)	2R/w	2t/w	Nominal Stress (σ_n) (MPa)	Transient Stress Concentration Factor	Local Stress (σ_{max}) (MPa)	Strain Rate	Transient Creep
APR-30-I	6	0.928	4.258	0.88	0.4	3.951424	2.318144	0.19	0.41	14.90	2.4	35.75	5E-05	0.0362
APR-30-V	4	1.036	4.22	0.82	0.2	4.37192	2.67288	0.09	0.39	8.98	3.23	28.99	3E-05	0.0043
APR-30-IV	8	1	4.22	0.84	0.3	4.22	2.54	0.14	0.40	18.60	2.83	52.63	0.0011	0.0077
M 10-2	8	1.013	3.93	0.846	0.3	3.98109	2.267094	0.15	0.43	19.71	2.8	55.20	0.001	0.0029

Table A9-6: Details of Creep-test under 165°C condition with different load

Sample	Load (kg)	Thickness (mm)	Width (w) (mm)	Crack length (t) (mm)	Radius of Notch (R) (mm)	Area cross-section far from notch (mm ²)	Initial area at notch cross-section (mm ²)	2R/w	2t/w	Nominal Stress (σ_n) (MPa)	Stress Concentration Factor	Local Stress (σ_{max}) (MPa)	Strain Rate	Transient Creep
M5-I	4	1.01	4.15	0.88	0.2	4.12	2.4139	0.10	0.42	9.36	3.19	29.86	0.001	0.0154
M5-IX	2.4	1.07	4.13	0.86	0.3	4.42	2.5787	0.15	0.42	5.33	2.8	14.92	2E-07	0.0003
M10-3	3	1.08	3.88	0.83	0.2	4.19	2.3976	0.10	0.43	7.02	3.19	22.40	8E-05	0.0206



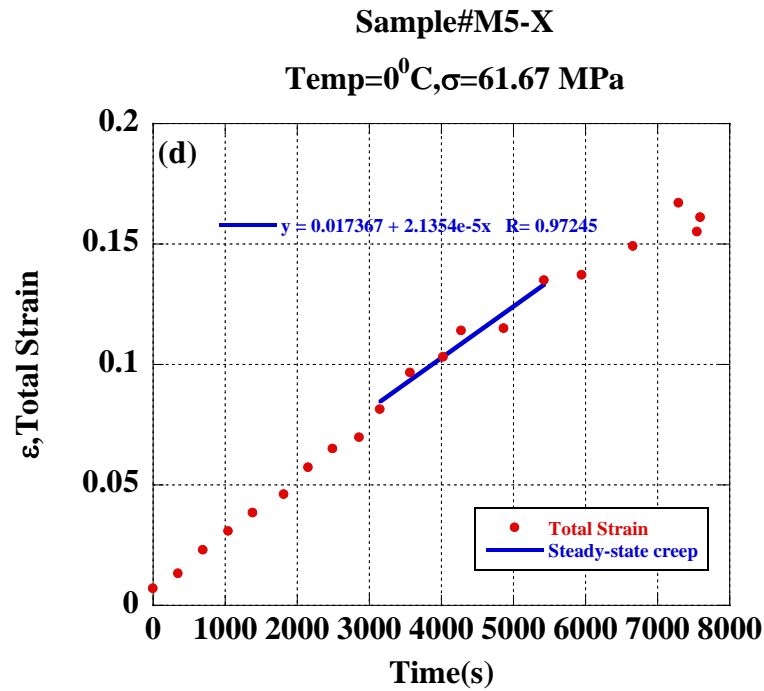
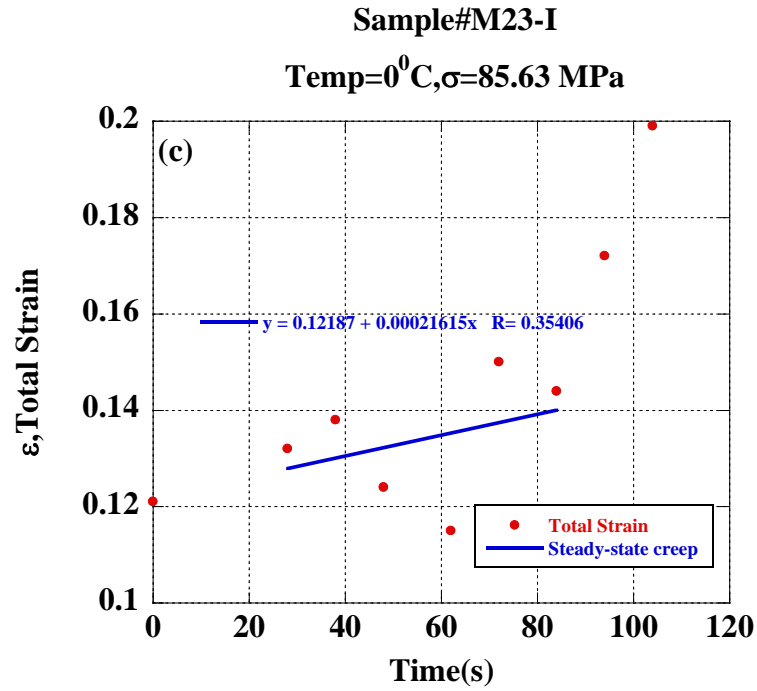
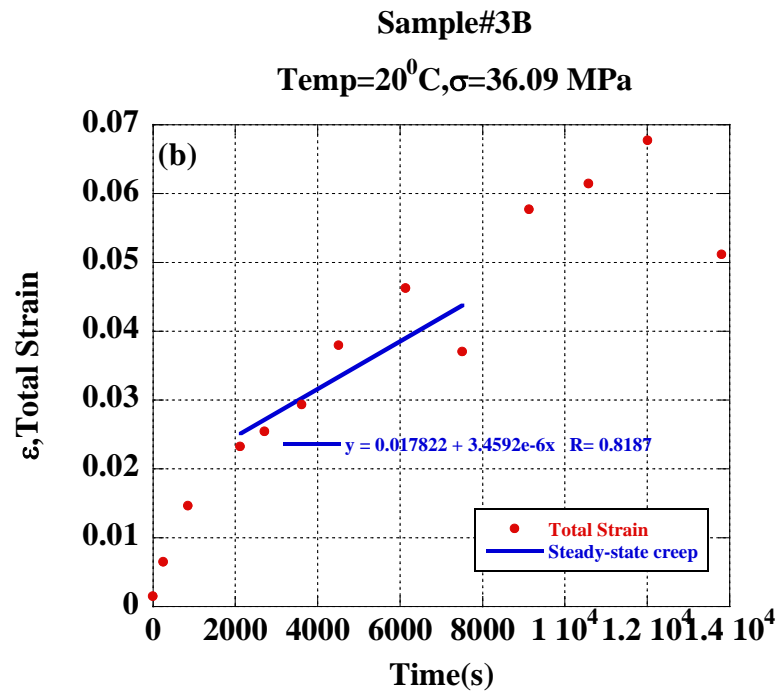
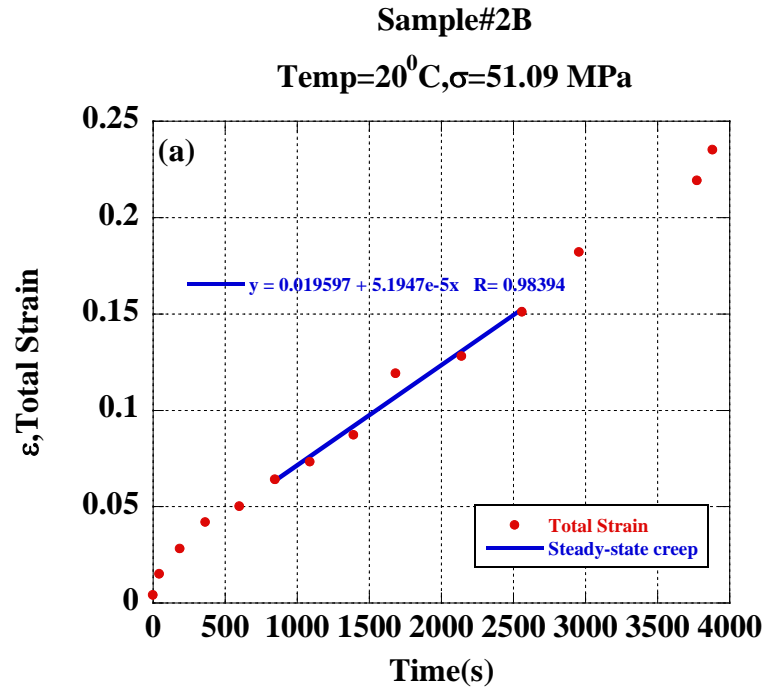


Figure A9-1 a-d: Strain vs. time behaviour during creep under constant temperature of 0°C and constant load, hence constant engineering stress, and the steady-state of creep.



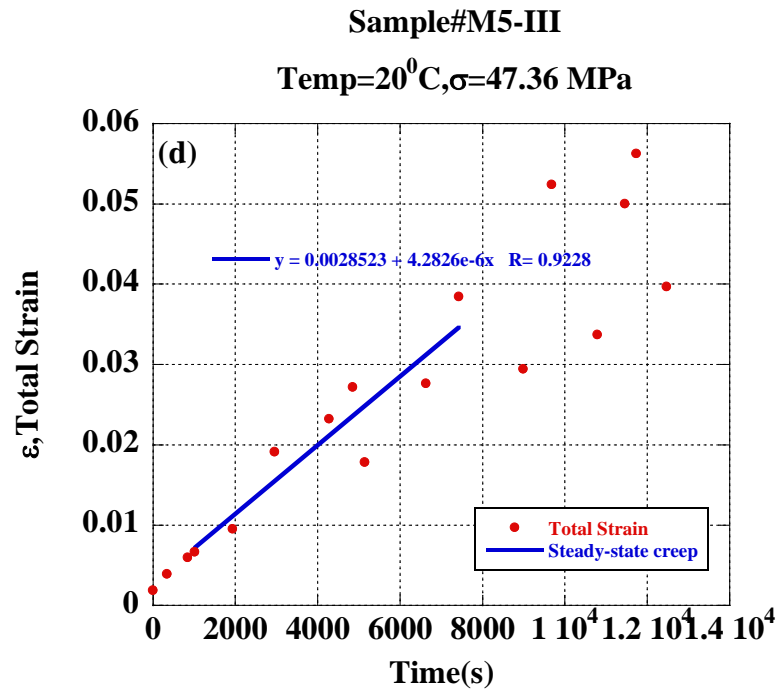
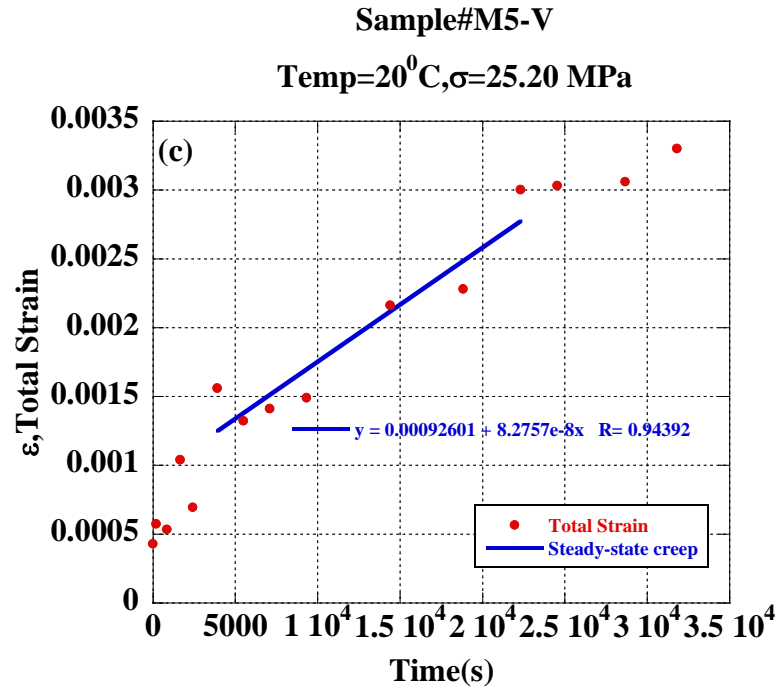
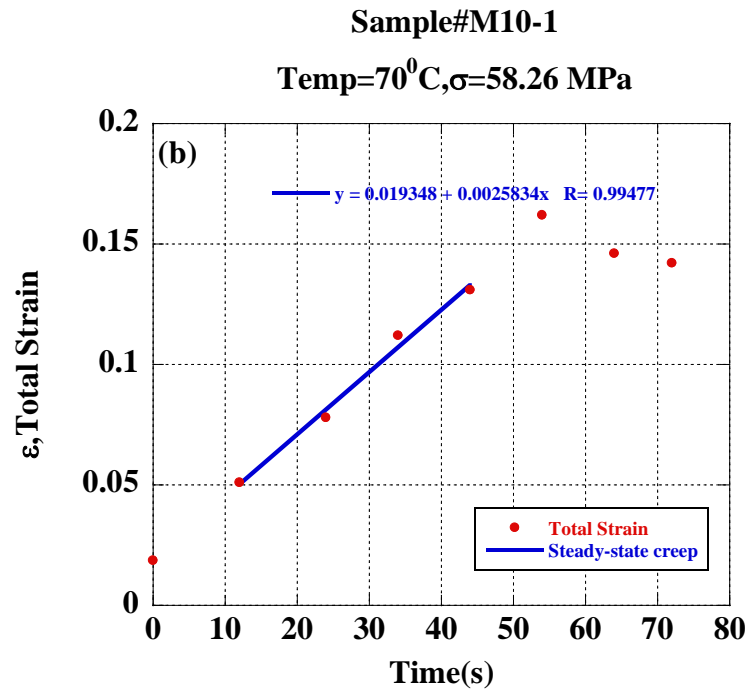
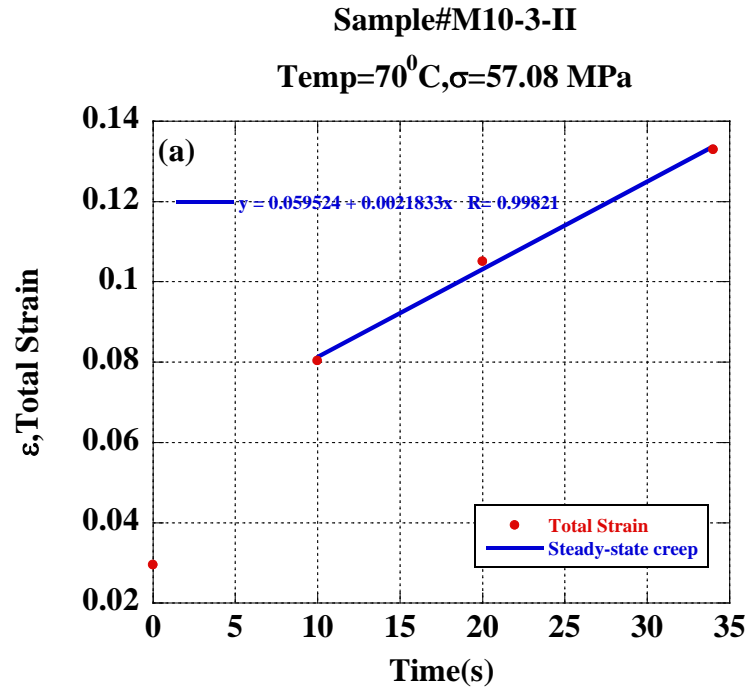
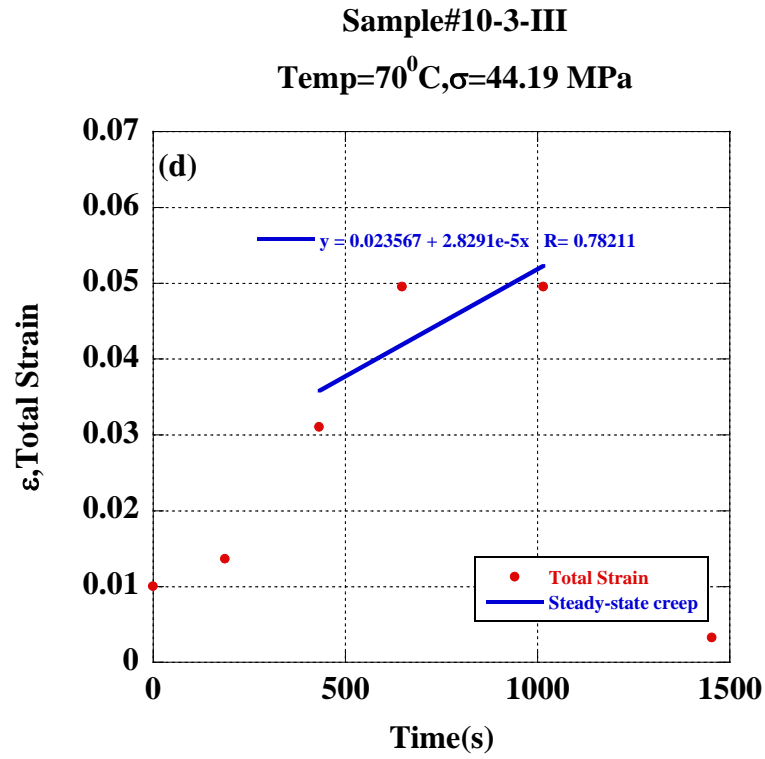
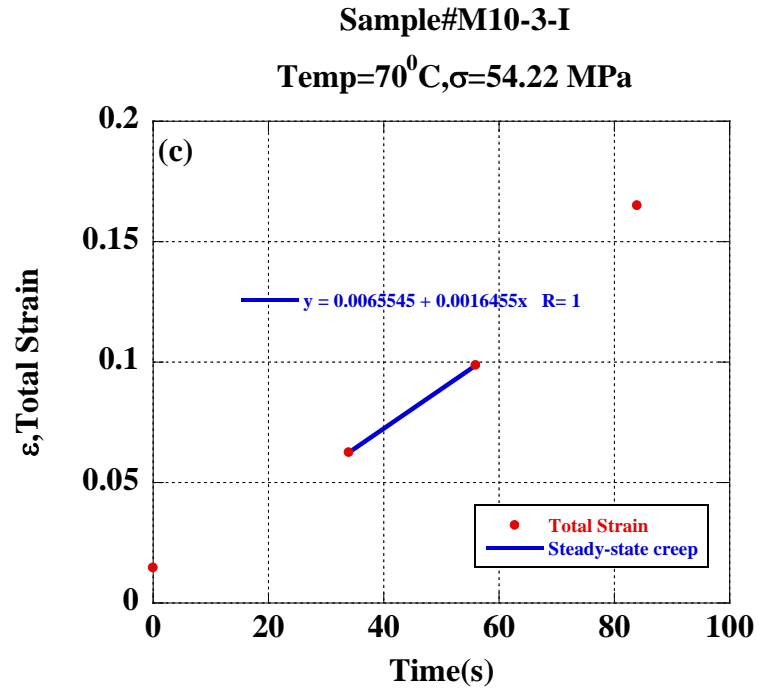


Figure A9-2a-d: Strain vs. time behaviour during creep under constant temperature of 20°C and constant load, hence constant engineering stress, and the steady-state of creep.





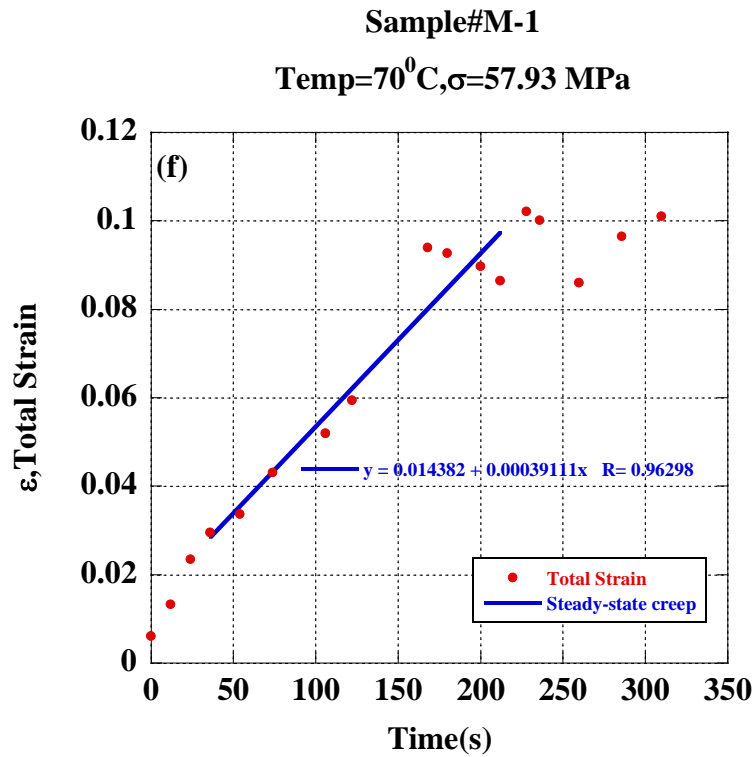
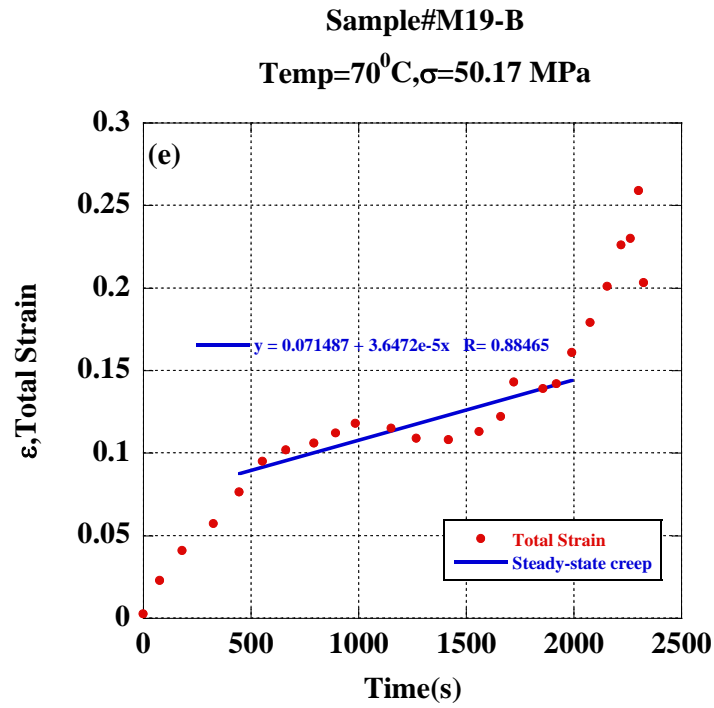
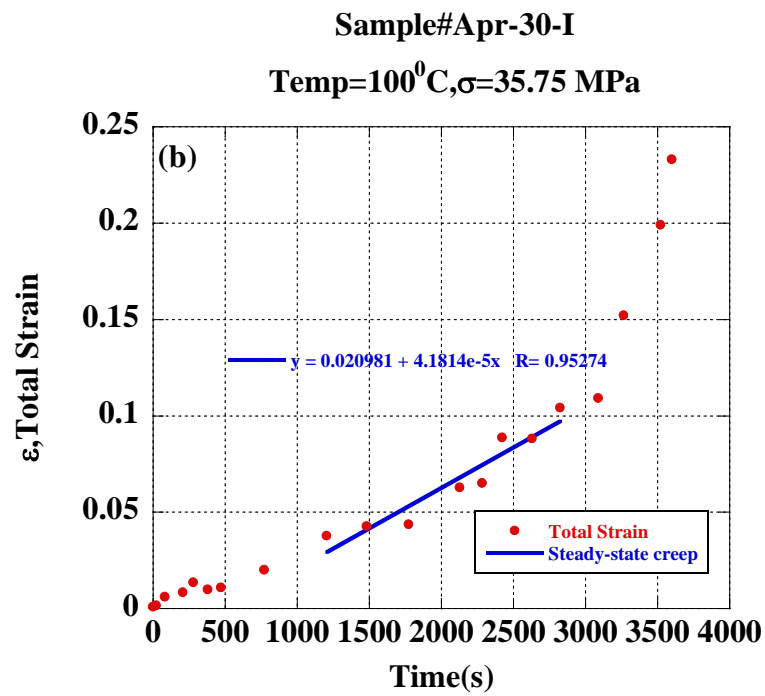
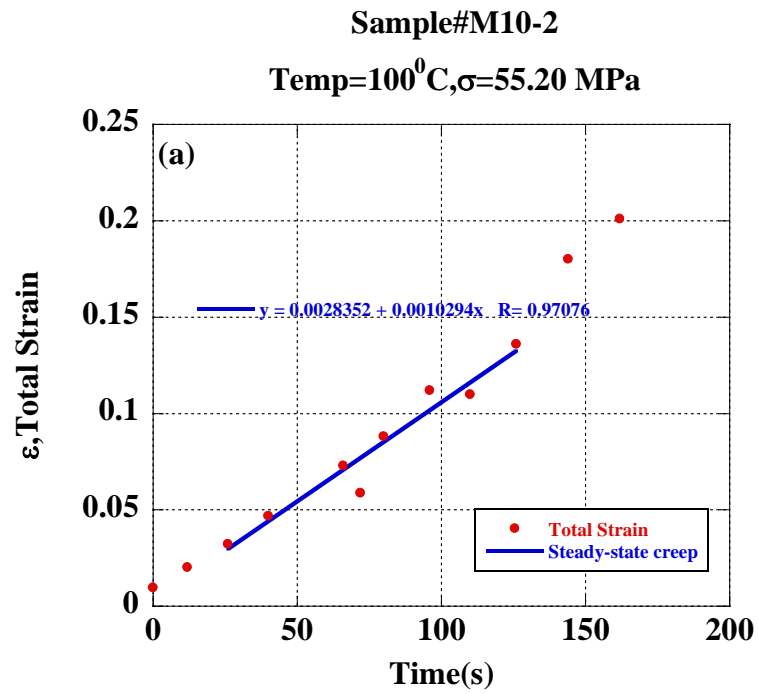


Figure A9-3a-f: Strain vs. time behaviour during creep under constant temperature of 70°C and constant load, hence constant engineering stress, and the steady-state of creep.



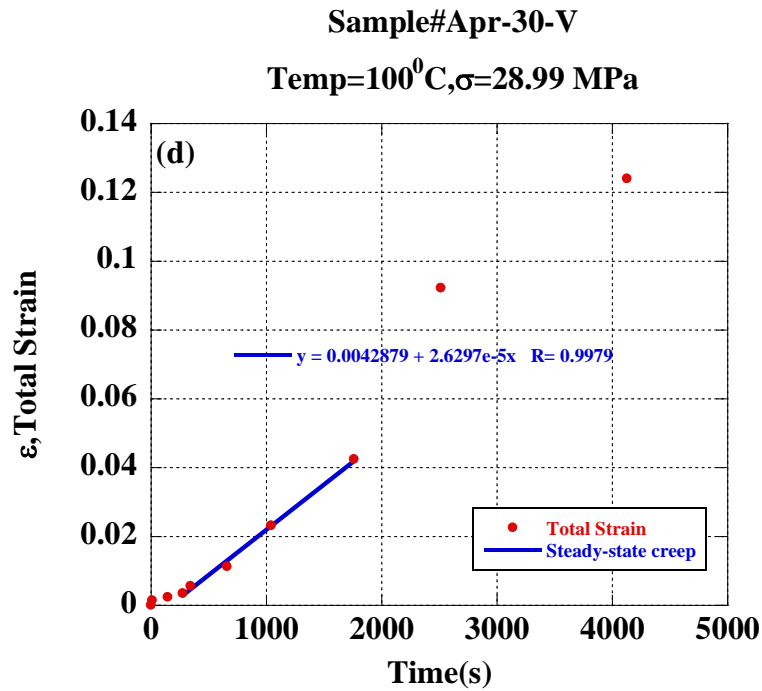
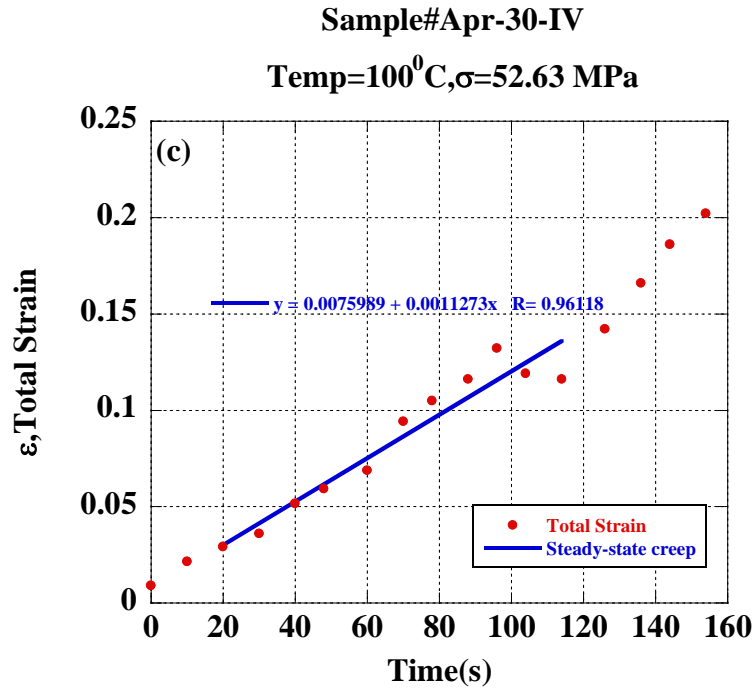
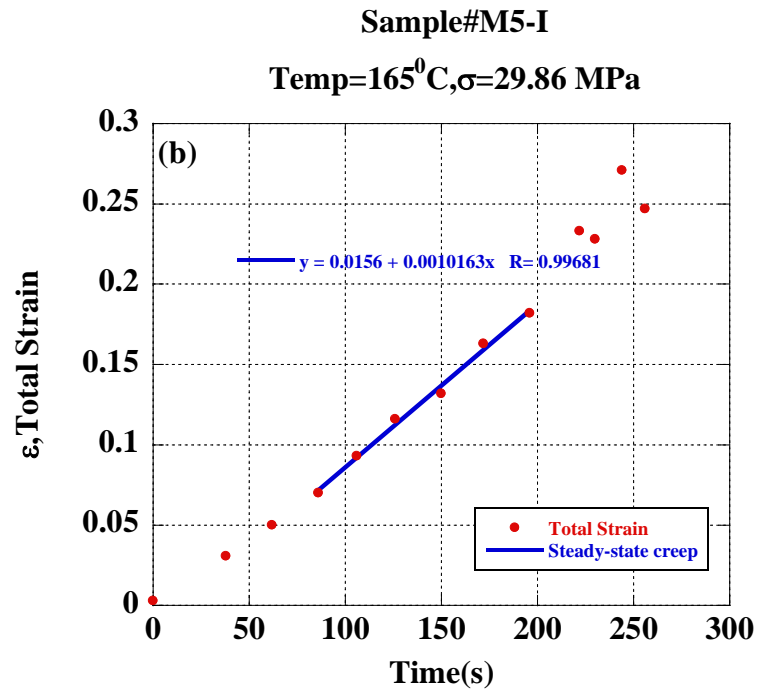
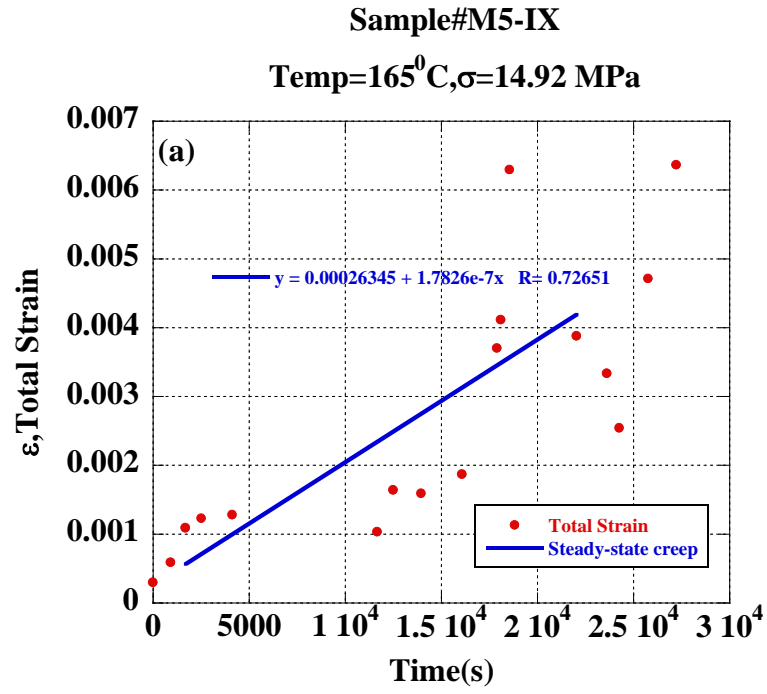


Figure A9-4a-d: Strain vs. time behaviour during creep under constant temperature of 100°C and constant load, hence constant engineering stress, and the steady-state of creep.



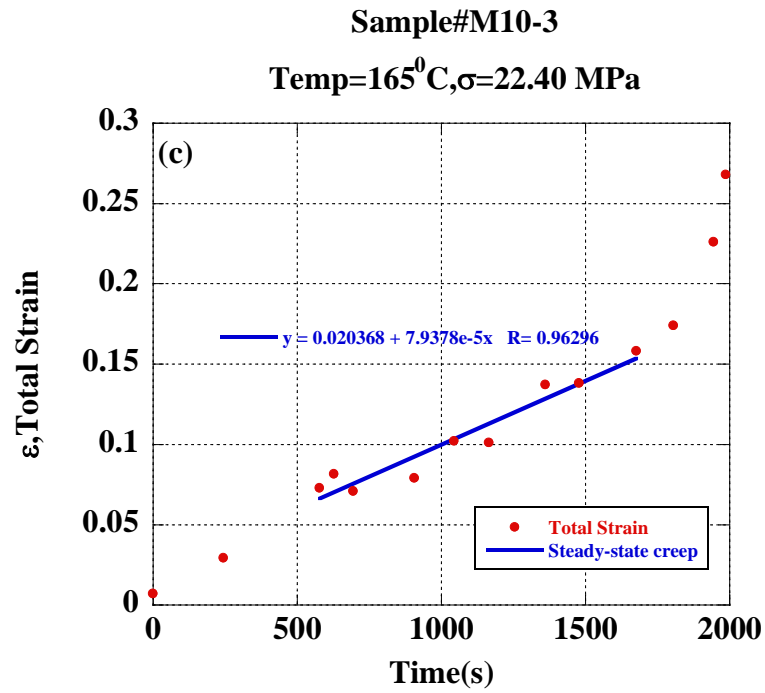


Figure A9-5a-d: Strain vs. time behaviour during creep under constant temperature of 165°C and constant load, hence constant engineering stress, and the steady-state of creep.

Matlab program for progressive method of defining creep parameters

```
a=[ Matrix of stress strain rate temp];

for i=1:21

    strs(i)=a(i,1);
    stn(i)=a(i,2);
    temp(i)=a(i,3);
end
strs=strs.';
stn=stn.';
temp=temp.';
b=1;
for Q=Q1:1:Q2
    for n=n1:.1:n2
        for C=C1:.1:C2
            for A=A1:.00001:A2
                Mm(b,1)=Q;
                Mm(b,2)=n;
                Mm(b,3)=C;
                Mm(b,4)=A;

                i=0;
                SSerr=0;
                Wsigma=0;

                for i=1:21
                    strn(i)=(C*(sinh(A*strs(i)))^n)*exp(-
Q/(8.314472*temp(i)));

                    dif(i)=(-stn(i)+strn(i));
                    SSerr=SSerr+((dif(i))^2);
                    Wsigma=Wsigma+stn(i);
                end

                Wmean=Wsigma/21;
                SStot=0;
                for j=1:21
                    diff(j)=strn(j)-Wmean;
                    SStot=((diff(j))^2)+SStot;
                end
                Rsquare=1-(SSerr/SStot);

                if b==1
                    mxR(b)=Rsquare;
                    r=b;
                else
                    if mxR(r)<Rsquare
                        r=b;
                        mxR(r)=Rsquare;
                    end
                end
                RS(b)=Rsquare;
                b=b+1;
            end
        end
    end
end
```

```

                                RS=RS.';
                                end
                                end
                                end

end
str=5;

Mmr=[Mm(r,1) Mm(r,2) Mm(r,3) Mm(r,4)];
for j=1:50
    str=str+2;
                                c=Mm(r,4)*str;
                                e=sinh(c);
                                f=e^Mm(r,2);
                                g=Mm(r,3)*f;
                                y(j)=g;
strm(j)=str;
end
    loglog(strm,y,'-');
    hold on

    y=y.';
    strm=strm.';

for j=1:21
xx(j)=a(j,1);
yy(j)=a(j,2)*(exp((Mm(r,1)/(8.314472*a(j,3)))));
end

loglog(xx,yy,'*');
hold on

xx=xx.';
yy=yy.';

```

APPENDIX10

Fatigue Damage Results

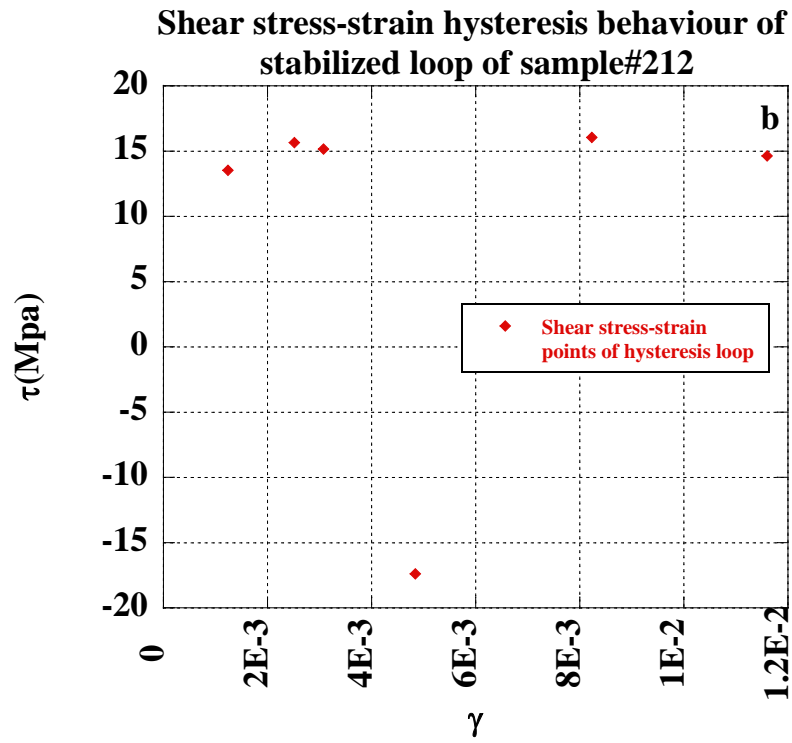
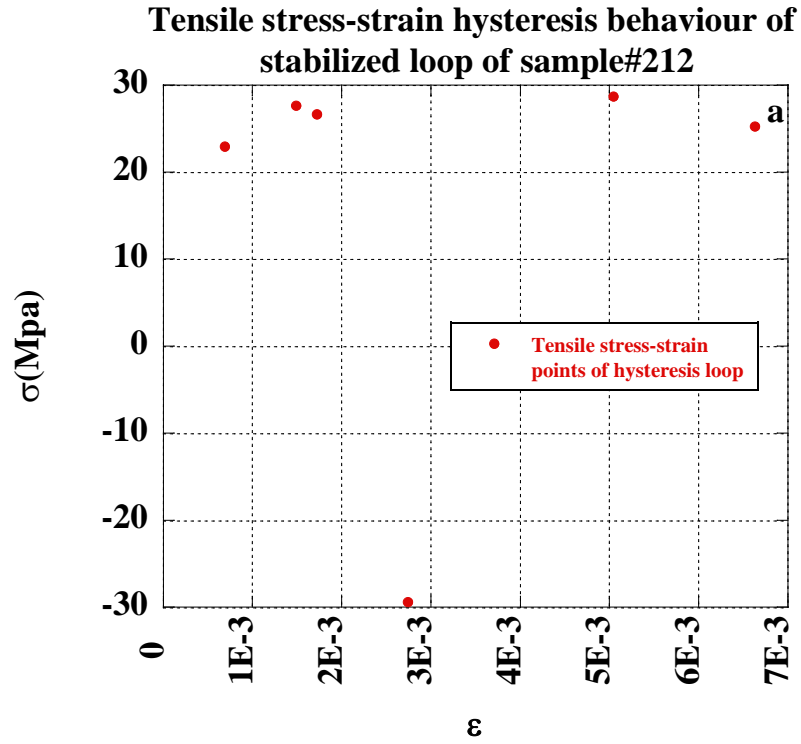


Figure A10-1: Stress-strain hysteresis behaviour of stabilized loop (seventh cycle) of sample#212 in a) Tensile condition and b) Shear condition.

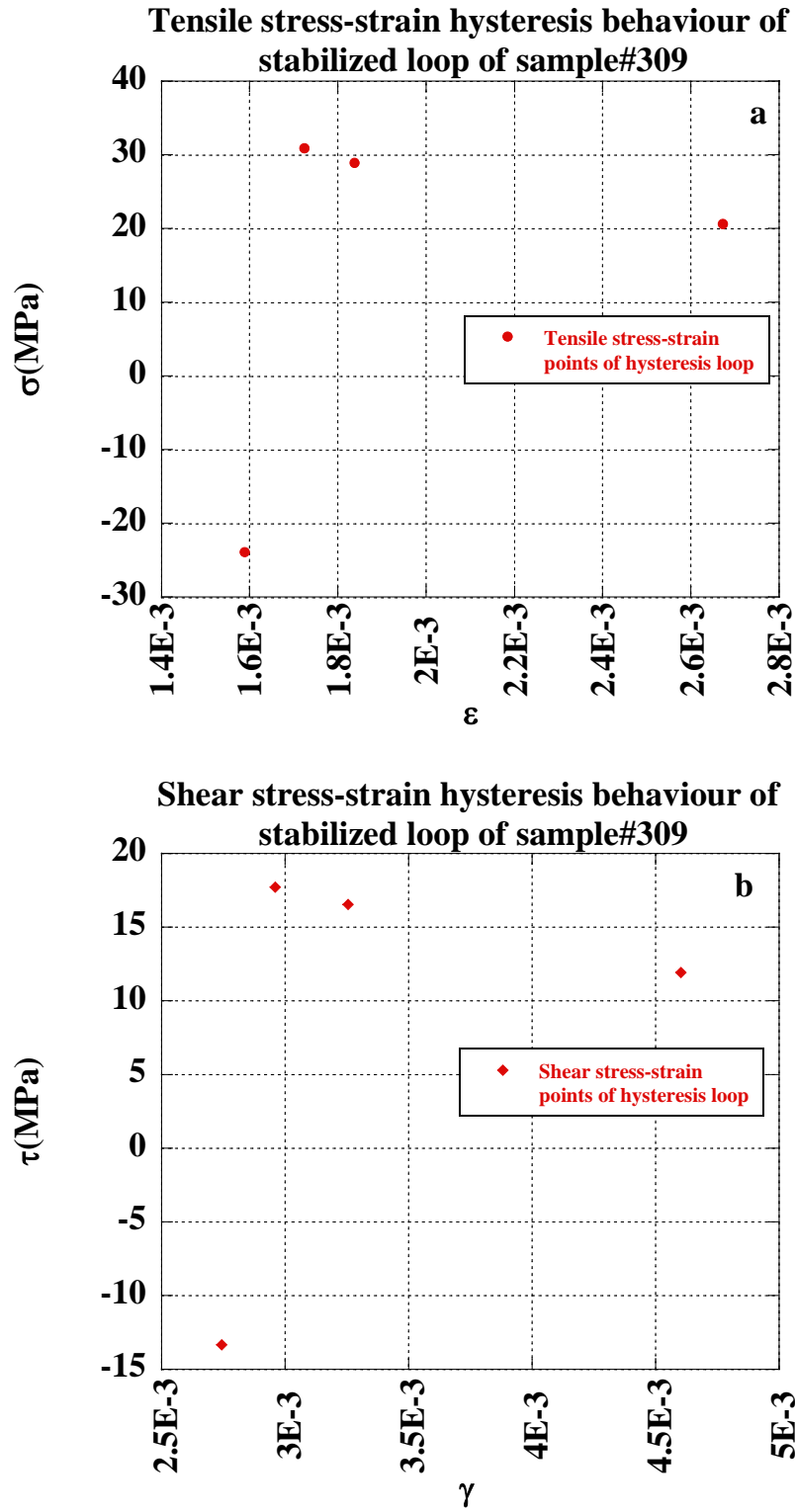


Figure A10-2: Stress-strain hysteresis behaviour of stabilized loop (seventh cycle) of sample#309 in a) Tensile condition and b) Shear condition.

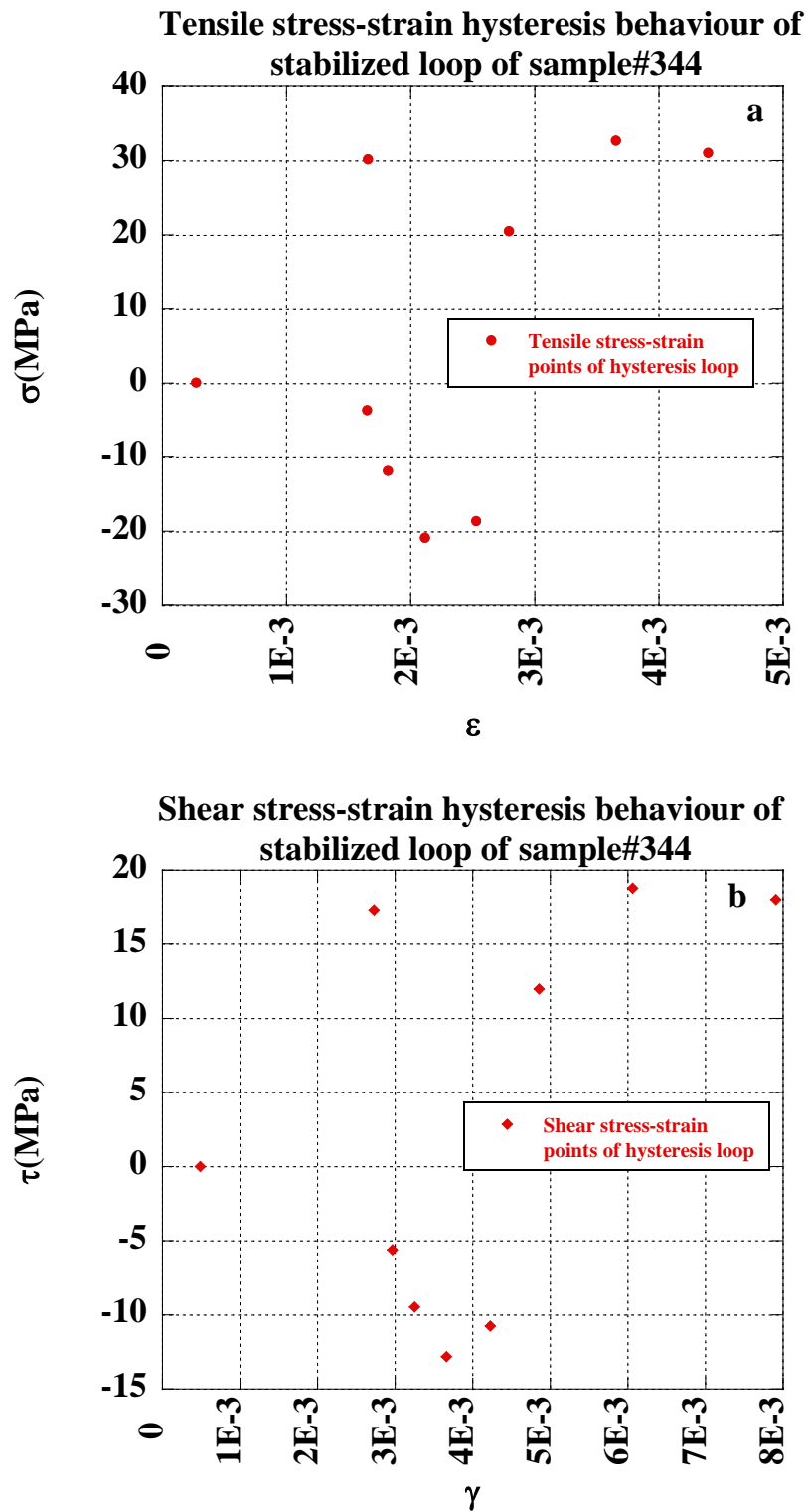


Figure A10-3: Stress-strain hysteresis behaviour of stabilized loop (seventh cycle) of sample#344 in a) Tensile condition and b) Shear condition.

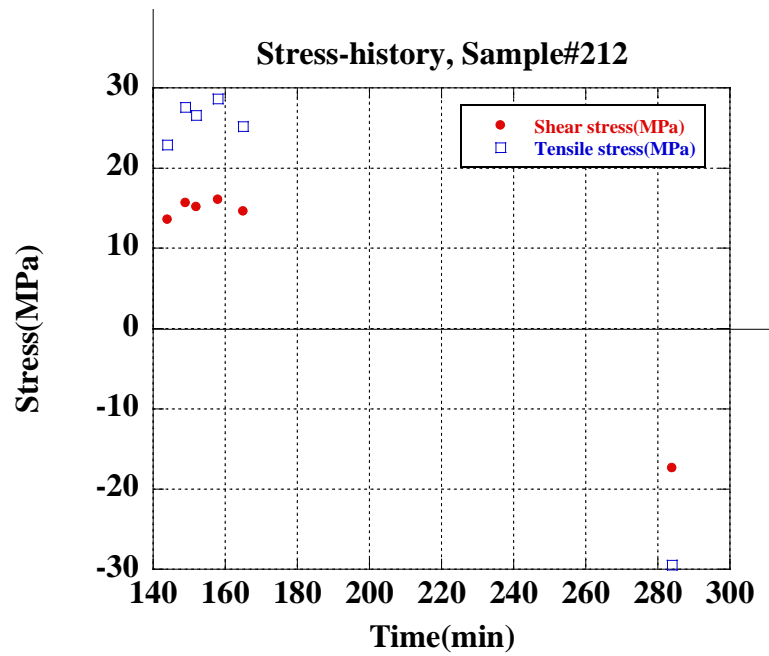


Figure A10-4: Results of proportional loading of tensile and shear stress for sample#212.

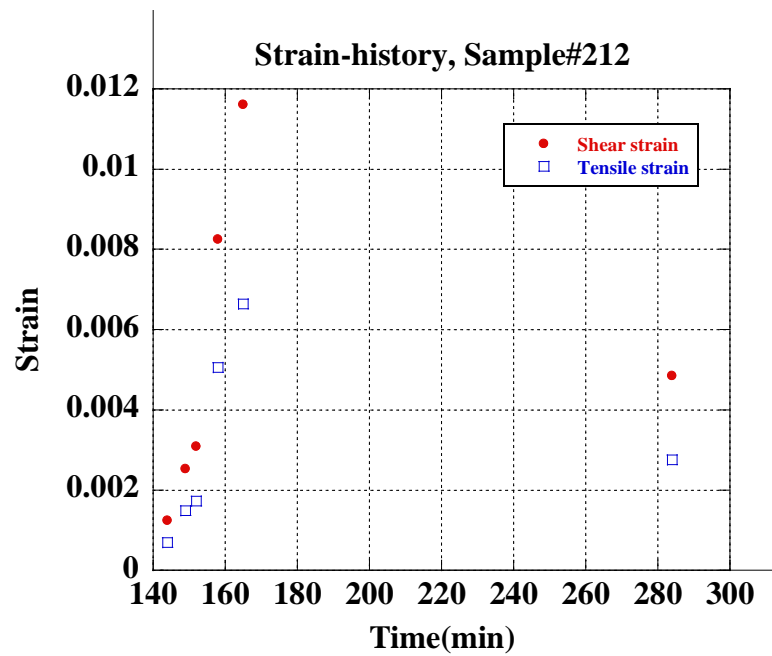


Figure A10-5: Results of shear and tensile strains with in-phase strain path for sample#212.

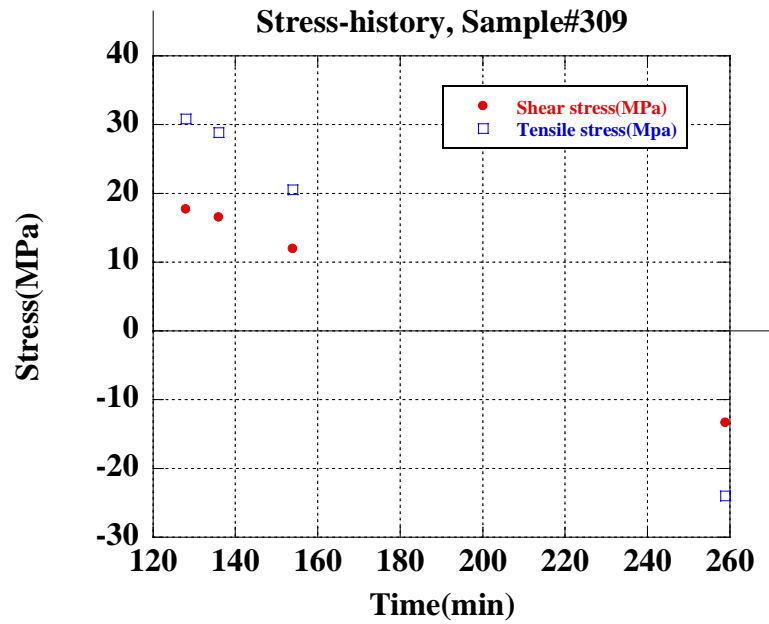


Figure A10-6: Results of proportional loading of tensile and shear stress for sample#309.

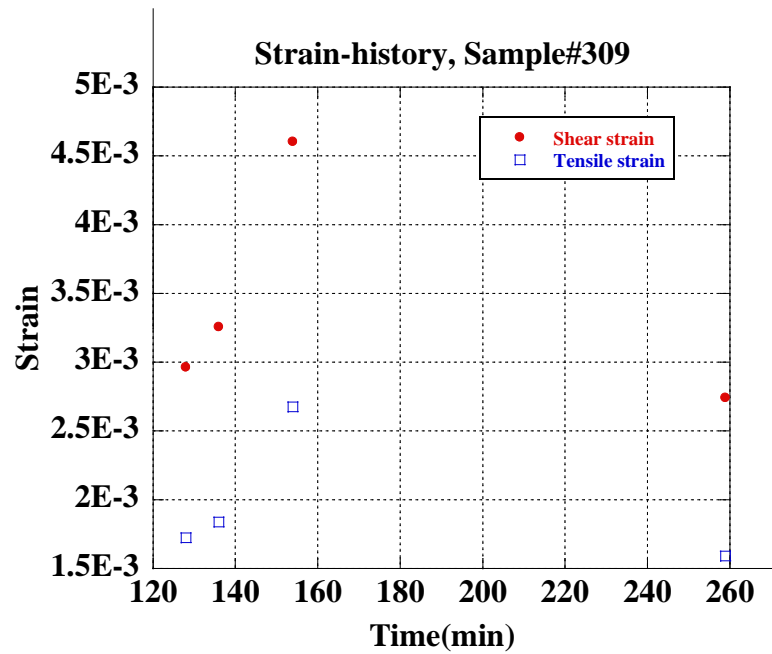


Figure A10-7: Results of shear and tensile strains with in-phase strain path for sample#309.

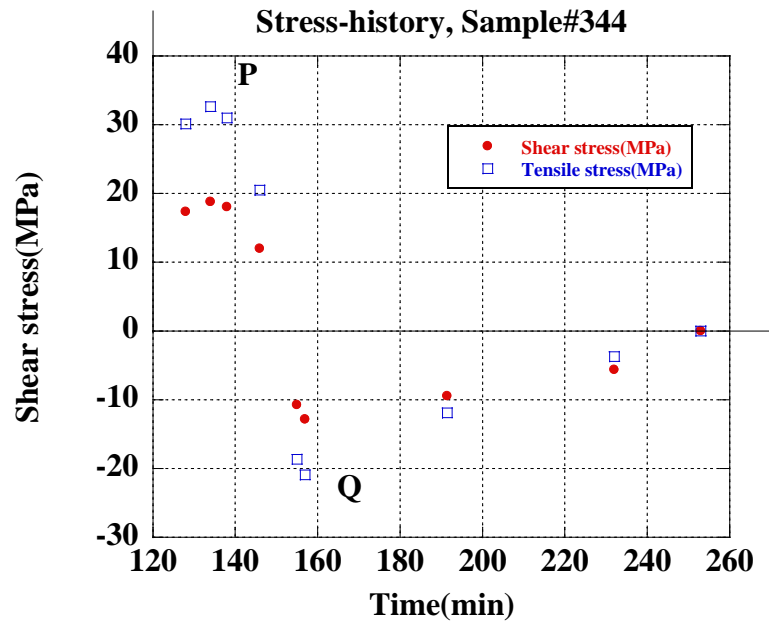


Figure A10-8: Results of proportional loading of tensile and shear stress for sample#344.

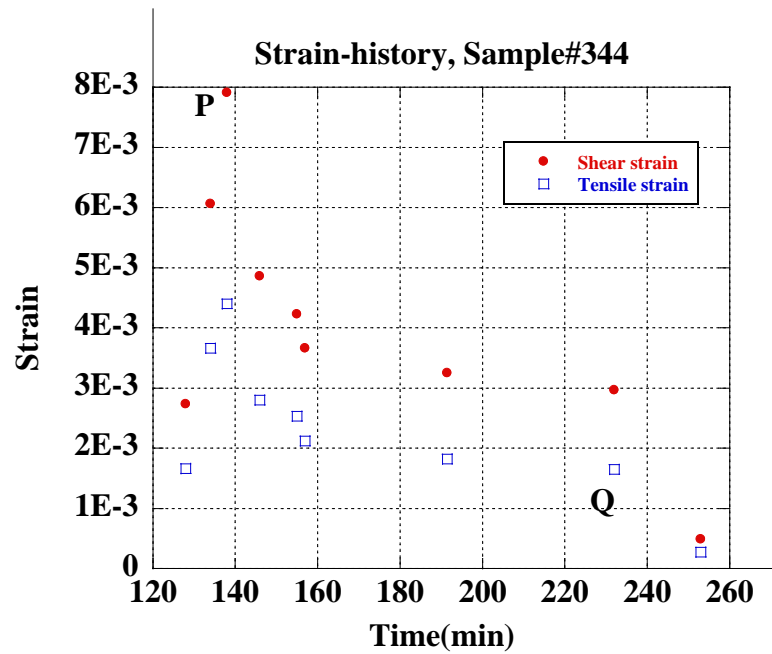


Figure A10-9: Results of proportional loading of tensile and shear strain for sample#344.

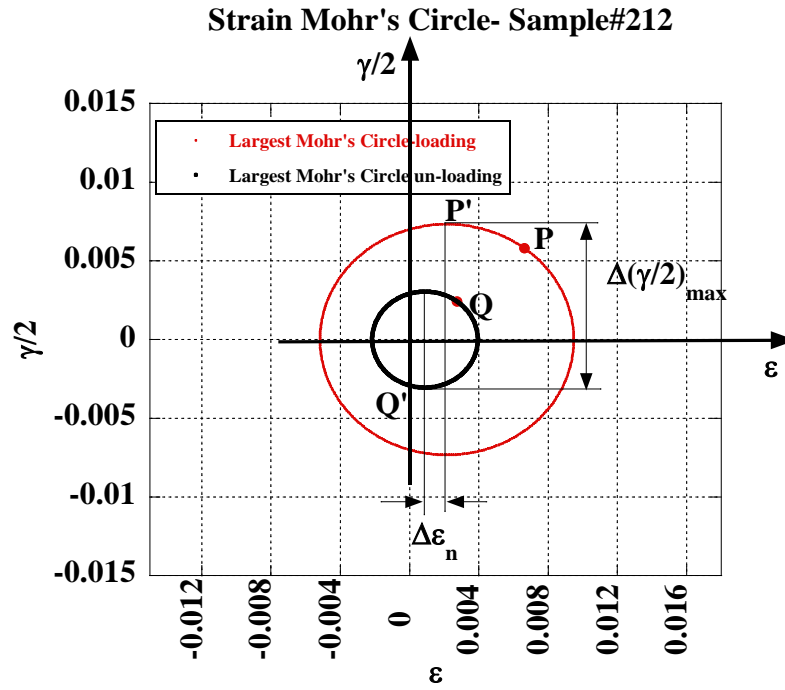


Figure A10-10: Strain Mohr's circle representing stress components of damage parameters for in-phase path for sample#212 during loading and un-loading of stabilized loop.

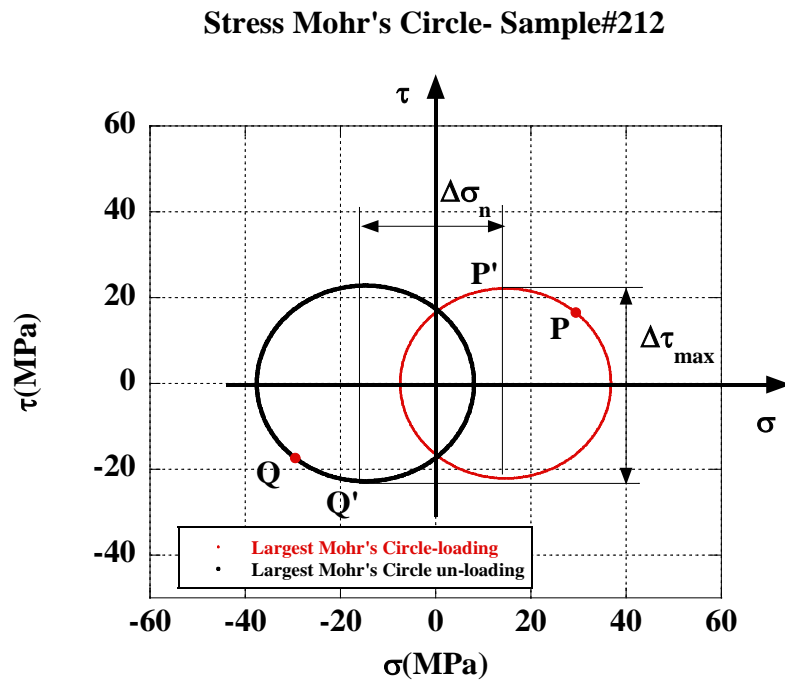


Figure A10-11: Stress Mohr's circle representing stress components of damage parameters for in-phase path for sample#212 during loading and un-loading of stabilized loop.

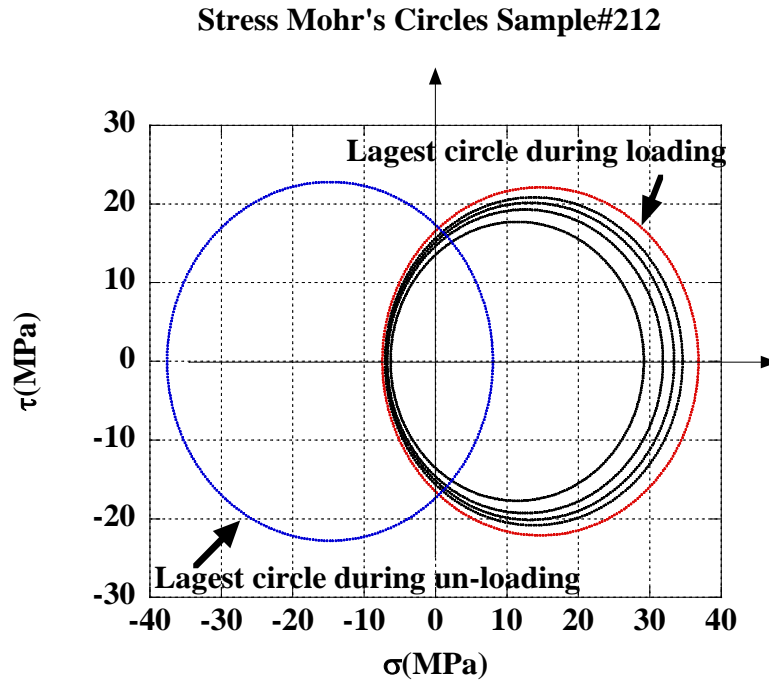


Figure A10-12: Stress Mohr's circle for in-phase path with mean-stress for sample#212 during loading and un-loading of stabilized loop

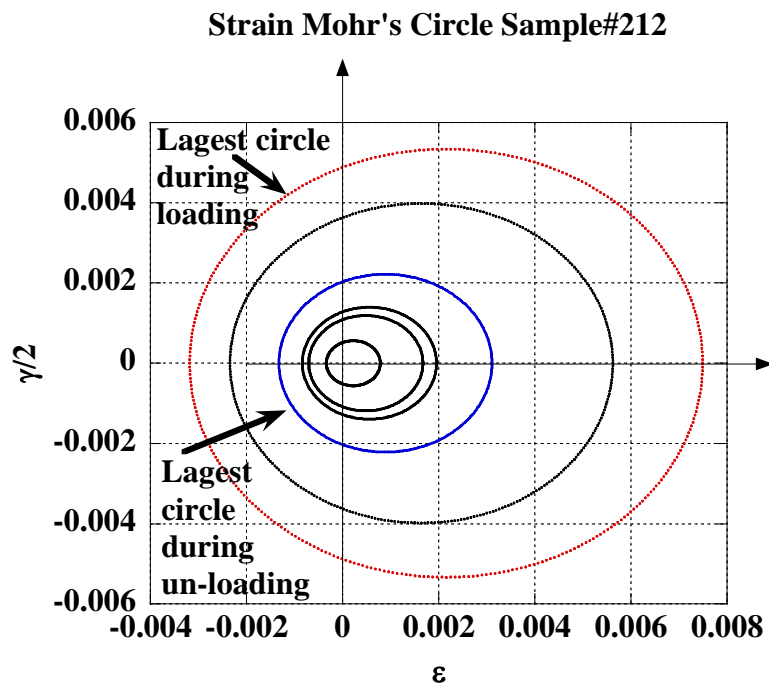


Figure A10-13: Strain Mohr's circle for in-phase path with mean-strain for sample#212 during loading and un-loading of stabilized loop.

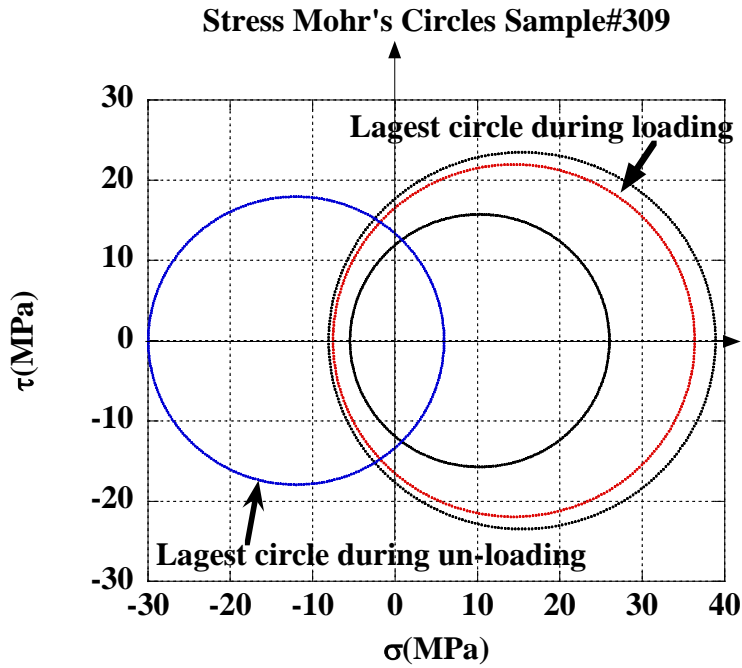


Figure A10-14: Stress Mohr's circle for in-phase path with mean-stress for sample#309 during loading and un-loading of stabilized loop.

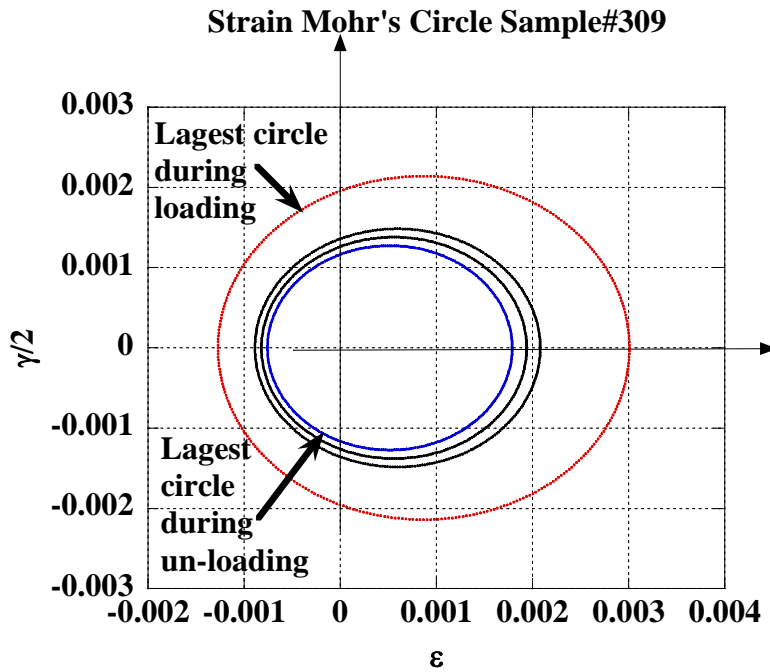


Figure A10-15: Strain Mohr's circle for in-phase path with mean-strain for sample#309 during loading and un-loading of stabilized loop.

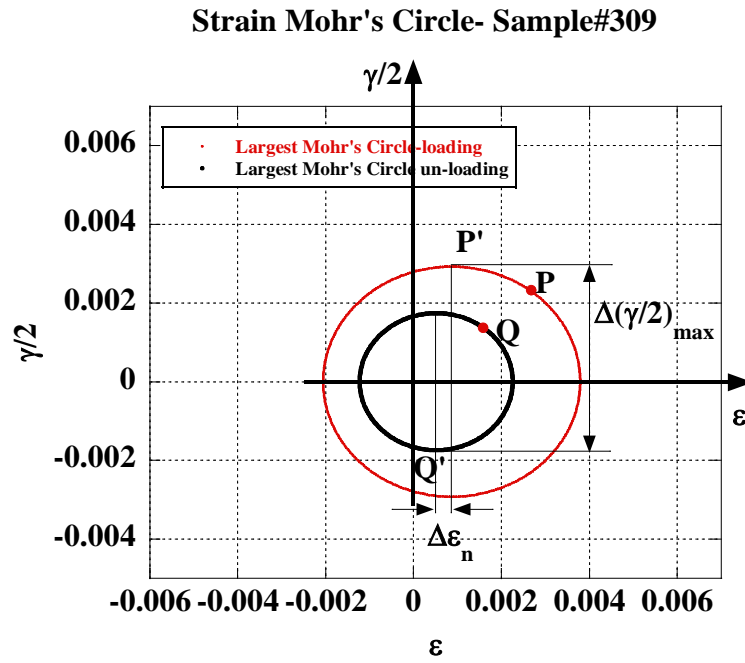


Figure A10-16: Strain Mohr's circle representing stress components of damage parameters for in-phase path for sample#309 during loading and un-loading of stabilized loop.

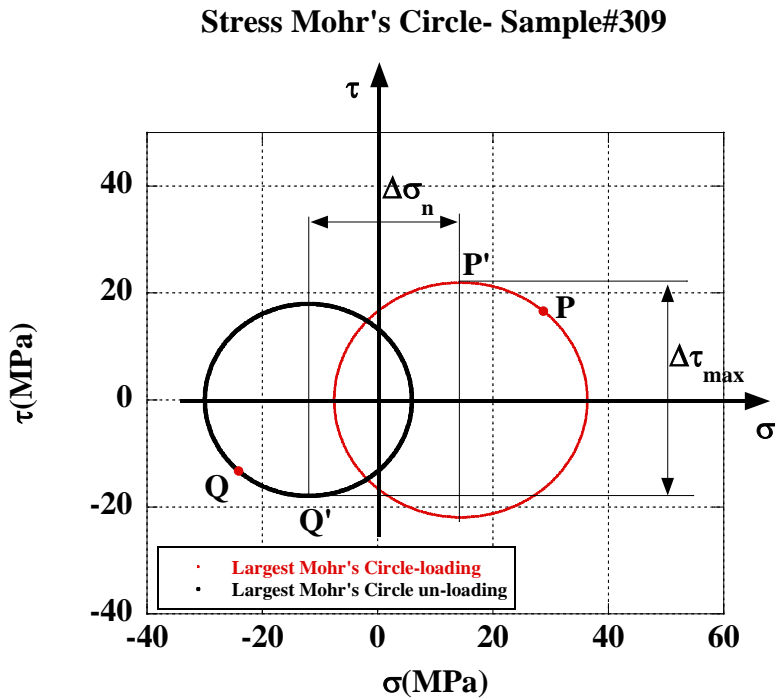


Figure A10-17: Stress Mohr's circle representing stress components of damage parameters for in-phase path for sample#309 during loading and un-loading of stabilized loop.

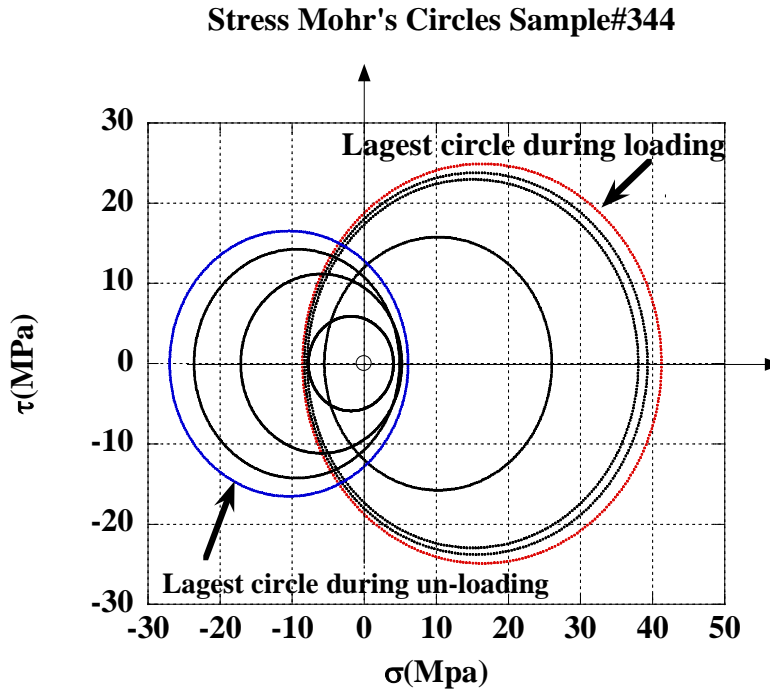


Figure A10-18: Stress Mohr's circle for in-phase path with mean-stress for sample#344 during loading and un-loading of stabilized loop.

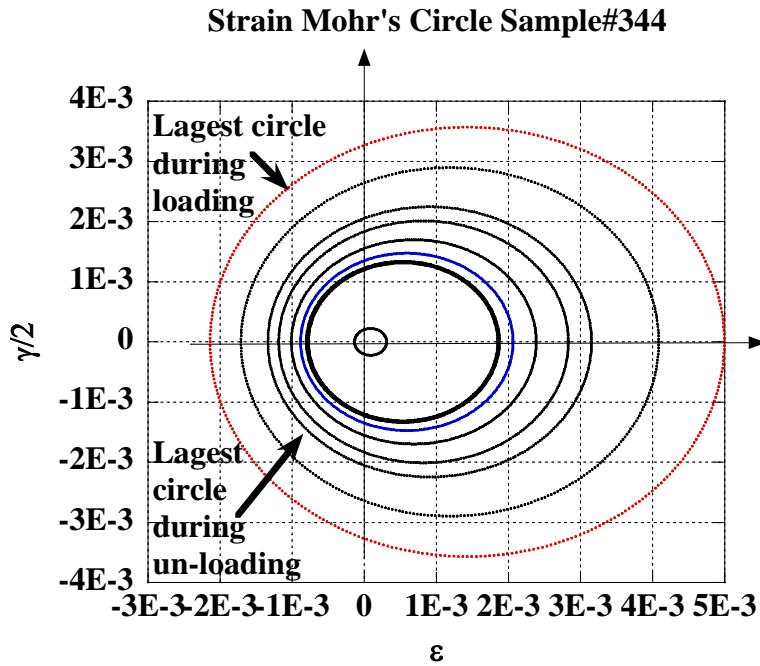


Figure A10-19: Strain Mohr's circle for in-phase path with mean-strain for sample#344 during loading and un-loading of stabilized loop.

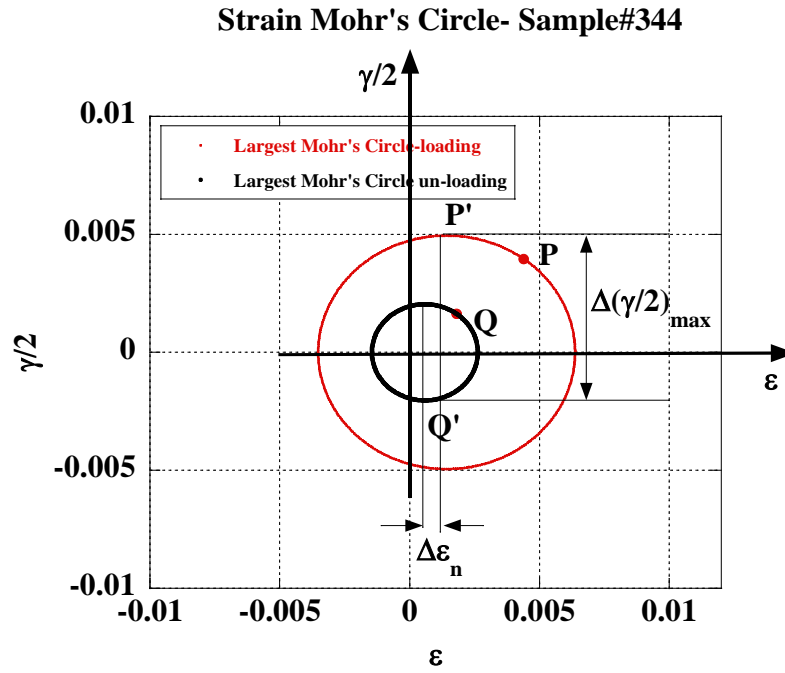


Figure A10-20: Strain Mohr's circle representing strain components of damage parameters for in-phase path for sample#344 during loading and un-loading of stabilized loop.

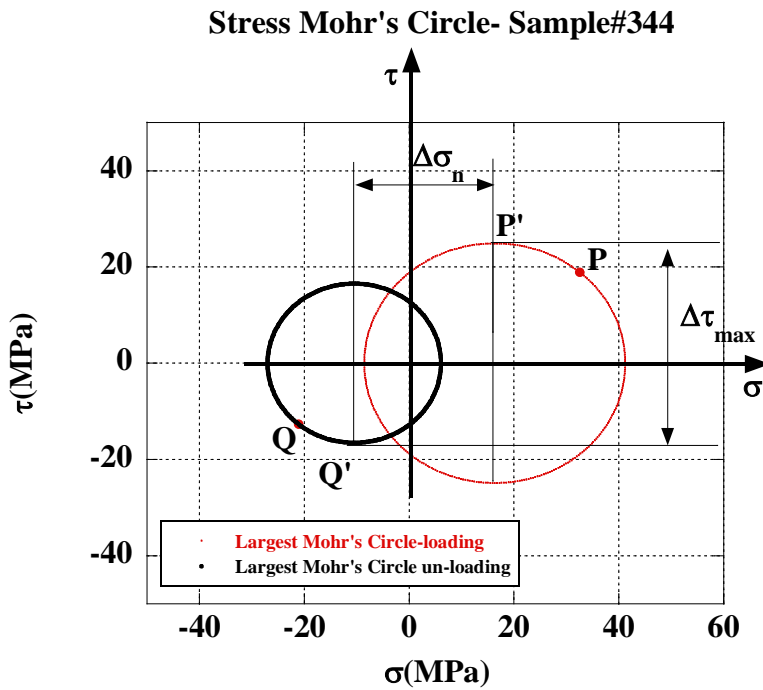


Figure A10-21: Stress Mohr's circle representing stress components of damage parameters for in-phase path for sample#344 during loading and un-loading of stabilized loop.

Matlab Program of Progressive Hysteresis Loop of Solder Joint

```
c4=C4;
alfa=Alpha;
n=n;
QK=Q;

G0=G0;
G1=G1;
v=v;

tmin=time0x2D212;

tsec=tmin*60;

T=temp0x2D212;

strn=strain;

N=length(T);

gt=0;
ge=0;
gp=0;
gccum=0;
gecum=0;
gpcum=0;
gcr=0;
gc=0;
tensile=zeros(N,1);
elastic=zeros(N,1);
plastic=zeros(N,1);
creep=zeros(N,1);
creepr=zeros(N,1);
creepcum=zeros(N,1);
GG=zeros(N,1);
EE=zeros(N,1);

%First cycle ramp up period until the maximum plastic strain

p=1;
i=1;

while p>=1

gt=0;
G=G0-G1*(T(i));
E=G*(2*(1+v));
```

```

Ta=(T(i)+27.3)/2;
tt=(tsec(i)-120*60);
m=1/(0.22-0.00053*T(i));
c6=(1/(130-.41*T(i)))^(m);
strs=1;

        while      gt<strn(i)
            strs=strs+.001;
            gc=tt*c4*((sinh(alfa*strs))^n)*exp(-QK/(273+Ta));
            gcr=c4*((sinh(alfa*strs))^n)*exp(-QK/(273+T(i)));
            ge=strs/E;
            gp=c6*((strs)^m);
            gt=ge+gp+gc;
        end

if T(i)<100
tensile(i)=strs;

mm(i)=m;
cc6(i)=c6;
gccum=gc+gccum;
elastic(i)=ge;
plastic(i)=gp;
creep(i)=gc;
creepr(i)=gcr;
creepcum(i)=gccum;
gecum=gecum+ge;
gpcum=gp+gccum;
GG(i)=G;
EE(i)=E;
i=i+1;
else

    p=0;

end

end

p=1;

j=i;
il=j

gp=max(plastic);

%First cycle until zero state stress

while p>=1

gt=0;

```

```

G=G0-G1*(T(j));
E=G*(2*(1+v));
Ta=(T(j)+T(j-1))/2;
tt=(tsec(j)-tsec(j-1));
strs=-40;
m=1/(0.22-0.00053*T(j));
c6=(1/(130-.41*T(j)))^(m);

    while      gt<=strn(j)
                strs=strs+.001;
                gc=tt*c4*((sinh(alfa*strs))^n)*exp(-QK/(273+Ta));
                gcr=c4*((sinh(alfa*strs))^n)*exp(-QK/(273+T(j)));
                ge=strs/E;
                gp=gp;
                gt=ge+gp+gc;

    end

if T(j)>100
mm(j)=m;
cc6(j)=c6;
tensile(j)=strs;
gccum=gc+gccum;
elastic(j)=ge;
plastic(j)=gp;
creep(j)=gc;
creepr(j)=gcr;
creepcum(j)=gccum;
gecum=gecum+ge;
gpcum=gp+gccum;
GG(j)=G;
EE(j)=E;
j=j+1;
else
    p=0;
end

end

%First cycle start of negative stress

p=1;
j2=j
while p>=1

    gt=0;
    G=G0-G1*(T(j));
    E=G*(2*(1+v));
    Ta=(T(j)+T(j-1))/2;
    tt=(tsec(j)-tsec(j-1));
    strs=0;
    m=1/(0.22-0.00053*T(j));
    c6=(1/(130-.41*T(j)))^(m);

```

```

while      gt<strn(j)
    strs=strs-.001;
    gc=tt*c4*((sinh(-alfa*strs))^n)*exp(-QK/(273+Ta));
    gcr=c4*((sinh(-alfa*strs))^n)*exp(-QK/(273+T(j)));
    ge=-strs/E;
    gp=plastic(j-1);
    gt=ge+gp+gc;

end

if T(j)>30
mm(j)=m;
cc6(j)=c6;
tensile(j)=strs;
gccum=gc+gccum;
elastic(j)=ge;
plastic(j)=gp;
creep(j)=gc;
creepr(j)=gcr;
creepcum(j)=gccum;
gecum=gecum+ge;
gpcum=gp+gpcum;
GG(j)=G;
EE(j)=E;
j=j+1;
else

    p=0;

end

end

%First cycle lower dwell until zero

p=1;
j3=j
while p>=1

gt=0;
G=(G0-G1*T(j));
E=G*(2*(1+v));
tt=(tsec(j)-tsec(j-1));
strs=0;
m=1/(0.22-0.00053*T(j));
c6=(1/(130-.41*T(j)))^(m);

while      gt<strn(j)
    strs=strs-.001;
    gc=tt*c4*((sinh(-alfa*strs))^n)*exp(-
QK/(273+T(j)));
    gcr=c4*((sinh(-alfa*strs))^n)*exp(-QK/(273+T(j)));

```

```

        ge=-strs/E;
        gp=plastic(j-1);
        gt=ge+gp+gc;

end
mm(j)=m;
cc6(j)=c6;
tensile(j)=strs;
gccum=gc+gccum;
GG(j)=G;
EE(j)=E;
elastic(j)=ge;
plastic(j)=gp;
creep(j)=gc;
creepcr(j)=gcr;
creepcum(j)=gccum;
gecum=gecum+ge;
gpcum=gp+gpcum;
j=j+1;
if j<=N
    p=1;
else
    p=0;
end

end

for i=1:N
    cr(i,1)=real(creep(i));
    crcum(i,1)=real(creepcum(i));
    pl(i,1)=real(plastic(i));
    el(i,1)=real(elastic(i));
end

plot(strn,tensile,'-r'), hold on

```